Observations of Dry Wear and the Development of an Improved Wear Law

Jure Aleksejev

Christ Church

University of Oxford

A thesis submitted for the degree of

Doctor of Philosophy

2021

CONTENTS

TABLE OF FIGURES

ABSTRACT

Unlubricated wear of metal components is a significant factor in the deterioration of various metal structures and assemblies and has been the focus of intensive research for several decades. Despite this, accurately predicting the quantity and development of wear from information about the geometry, material and loading of the wearing contact appears to be beyond the reach of engineering science at present. The development of more generally applicable, reliable wear prediction method ("wear law") would be of great benefit in terms of industrial practice and would also close a significant gap in the current state of tribological knowledge.

The research presented in this thesis establishes both the limitations of traditional wear prediction approaches based on two-body contact mechanics and/or Archard's wear law as well as a possible alternative in the tribological circuit approach, which was initially proposed by Berthier and then refined into a wear model for a closed contact geometry by Fillot, Iordanoff & Berthier. Through experimental research, a number of assumptions and questions put forward by these authors were examined; in particular the interaction between the debris ejection path length, surface profile and debris particle size was found to govern the ejection of wear debris and thus wear. The model was also found to predict a strongly non-linear dependence on normal force for an annular contact geometry, the same geometry in which exactly such dependence has been observed experimentally, but not yet explained. Additional experimental work revealed a tendency for the contact to eject debris along the shortest available path. With this knowledge, a mathematical expression for debris ejection in multiple directions was formulated. With it, the approach proposed by Fillot, Iordanoff & Berthier was expanded to an open contact geometry, successfully achieving a transition of a wear model between geometries. This would also indicate, that the approach studied could be a generally applicable wear model.

To aid the experimental work, a method for observing wear without disturbing it has been developed, using X-ray computed tomography. This is the first such application of X-ray CT to wearing contacts, the first instance of wear being extensively quantified entirely non-destructively (i.e. without dismantling the wearing contact for studies) and has been proven to be very successful as a tool for observing and quantifying wear. The success obtained can also serve as a powerful justification for further development of this approach and progress towards the observations of wear in-situ using penetrating radiation.

PUBLICATION LIST

During the preparation of this research work, the following scientific publications were produced:

- *Experimental investigation of debris entrapment in anular contacts* (1) was published in Proceedings of Institution of Mechanical Engineers, part J: Journal of Engineering Tribology in March 2020.

- *In-situ X-ray tomography of wear – A feasibility study* (2) was published in Tribology International in October 2020.

- *Use of synchrotron X-rays for imaging and diffraction studies of worn contacts: towards direct observation of wear damage in optically-opaque contacts* was submitted to Tribology International and is presently under review.

1 INTRODUCTION

Oxford English dictionary defines 'wear' as *'Damage, erode, or destroy by friction or use*'. In the sense of this definition, wear has accompanied mankind since prehistoric times, wearing out clothes, weapons and roads. Wear was of course also used constructively for purposes of craft, as attested by polished gemstones, swords and other objects. Unsurprisingly, wear eventually became an object of scientific study. P. I. Hurricks (3) attributed the first systematic examination of fretting wear to G. A. Tomlinson, who published a paper titled *The rusting of steel surfaces in contact* in Proceedings of Royal Society in 1927. However, Zmitrowicz (4; 5), has identified the work of Charles Hatchett as the earliest contribution to study of wear. Hatchett (in conjunction with Henry Cavendish, who, however is not directly credited as a co-author) studied wear of gold alloys for purpose of improving the quality of British coinage, publishing the results in Philosophical transactions of the Royal Society in 1803 (6). Hatchett and Cavendish engaged a certain Mr Cuthbertson to build a machine for rubbing coins against each other under pressure. The motion was applied along orthogonal axes simultaneously with a different frequency for each axis, giving very complex experimental conditions even by modern standards. In turn, Hatchett quotes a French report on wear of silver alloys published in Annales de Chimie in 1793, indicating that study of wear extends to at least late 18th century.

Wear became a topic of more concentrated research in the second half of the 20th century. The journal Wear was published for the first time in 1957, Tribology Transactions (originally ASLE Transactions) followed in 1958 and Journal of tribology (originally Journal of lubrication technologies) appeared in 1967. The term 'tribology' was introduced in 1966 by Jost (7) to describe the rapidly developing field of engineering science dealing with friction, friction mitigation and wear. Today, tribology is a large and diverse field, dealing with issues ranging from performance of artificial joints, to failures of spline couplings to longevity of nuclear fuel.

1.1 The motivation for this work

One of the major unsolved problems of tribology is reliable prediction of quantity and progress of wear. While a number of models have been proposed, it is presently impossible to reliably predict exactly how much wear will occur simply from taking into consideration the contact geometry, contact conditions and wearing materials. While laboratory tests can reveal useful information about general wear resistance of materials and the direction of influence of a certain parameter (i.e., does a change cause more or less wear), no method currently exists that would enable the *quantity* of wear to be calculated without extensive reliance on empirical data for that exact contact and operating condition(s).

This research project was sponsored by Rolls-Royce Plc with the general intention of advancing the understanding of wear in gas-turbine engine components. In a turbine engine, many parts are exposed to continuous or intermittent sliding and/or oscillating rubbing/fretting, leading to wear, pitting, accelerated oxidation or fatigue (Figure 1).

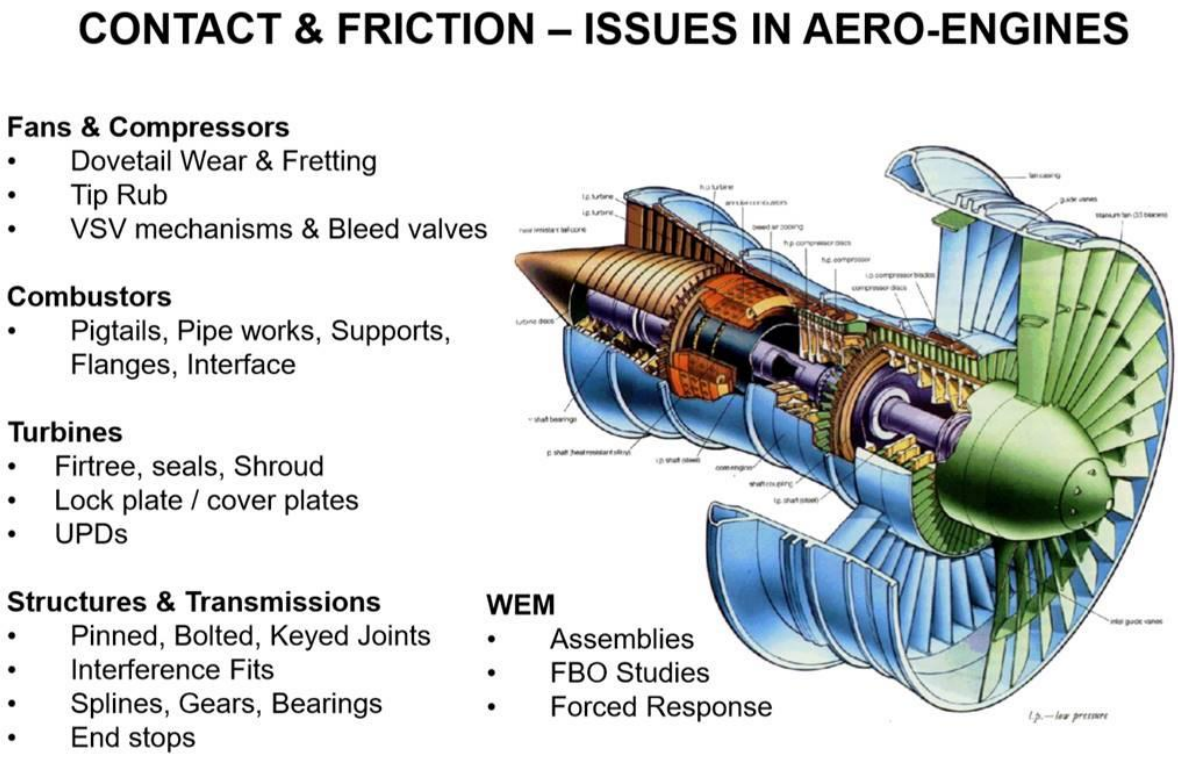

Figure 1: Wearing contacts in a typical passenger jet engine.

One of the components giving the sponsor concern is the anti-fret liner, sitting between the root of the compressor blade and the holding ring (Figure 2). The liner and the blade root wear in service, with the severity of the wear being irregular and unpredictable. This calls for relatively short inspection periods to either confirm that the components are still sound or provide for preventative replacement of components. Accurate prediction of wear would enable to safely extend the service intervals, reducing costs of engine down-time and replacement parts.

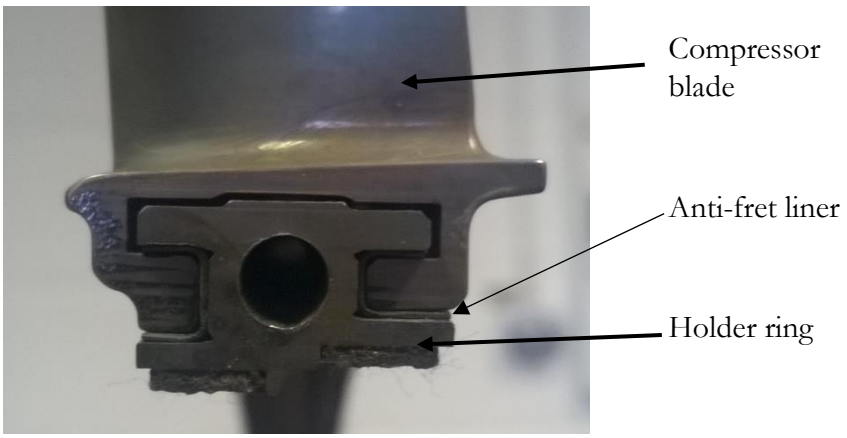

Figure 2: Compressor blade on the holder ring.

In the same engine it is possible to see wear ranging from insignificant, to total local consumption of the anti-fret liner. Examples of wear damage are in Figure 3 and Figure 4.

Figure 3: Scuffing marks on the anti-fret liner.

Figure 4: Wear on the compressor blade root.

The contact geometry consists of a series of rectangular patches (measuring 14x3 and 14x6 mm in size), pressed against a plane and reciprocating in the direction parallel to the longer side. The sponsor estimates the displacement to be of 0.1-0.5 mm range. The components are exposed to high-pressure air (environment pressures ranging from 2-4 MPa depending on the exact position in the engine and engine operation) at high temperatures (approx. 550°C peak). As there exists a pressure difference between the sides of the blade it is possible for there to be some air blow-by through the wearing contact. These highly complex conditions cannot be approximated using traditional experimental wear setups, such as pin-on-disc or ball-on-flat, as these have contact areas that are relatively small compared to their displacement and pressure distribution radically different to those seen in the blade root.

1.2 Desired outcome

The sponsor has invested considerable resources into attempts to predict the extent and development of wear damage through numerical modelling. From discussions with sponsor's engineers, it became apparent that they are looking for a relationship that would link the local stress field in the wearing contact with the local wear rate. This can then be used in a time-marching model to simulate wear: using the improved law, the local stress field is translated into local wear rate; the local wear rate is used to calculate the new (worn) surface profile, which is then used to re-calculate the local stress field and so on. As evidenced in the research performed, this appears to be an unreacheable goal, since wear is governed by both micro and macro-scale variables which cannot be simply separated. Predicting wear thus demands an integrated approach taking account of how macroscopic variables affect wear down to micro level. This requires, in the first instance, a mathematical description of wear that accounts for the interplay of microscopic and macroscopic variables and in the second instance a method for reliably inferring parameters for such a model from the geometry used in laboratory tests, even if the wearing contact in the engine is different.

1.3 Structure of the thesis

An extensive survey of available literature was made, indicating that the local wear rate depends significantly on the behaviour of the wear debris bed, which in turn is dependent on the macroscopic state of the contact (contact geometry, bulk temperature etc.) and can be influenced by external factors such as air flow through the wearing contact.

As a result, a more "global" approach was pursued; with the aim of producing (or at least open the pathway for producing) a mathematical description of wear for the entire contact, rather than some local wear law. While this would not enable the post-wear geometry to be precisely calculated, it would at least enable the prediction of the total quantity of material removed. A hitherto little used and relatively untested, but conceptually strong model was identified in the literature and made subject of extensive experimental and analytical study to explore how are its parameters influenced by contact geometry and how can this model be applied to different contact geometries.

To further aid research in this direction an approach for direct observation of the progress of wear through X-ray computed tomography was developed. This approach also enabled wear to be quantified without disassembling or otherwise disrupting the contact. This is an important development in itself, as it enables quantification of features that were previously difficult to assess (such as the real area of contact) and also testing of models predicting dynamics of the wear processes.

The discrete element method (DEM) was identified as a possible and hitherto little used method for simulating wear, without the need for an explicit wear law. While no attempt towards refining this approach was made (the work was predominantly experimental with no provisions for extensive programming/coding component) strong publications illustrating the approach were identified in the literature.

This thesis consists of 8 principal chapters:

- Chapter 2 presents a survey of available tribological literature concerning dry wear of metals under a variety of conditions. Its conclusions (section 2.4.1) list a number of observations concerning limits of existing knowledge and potentially fruitful directions of further research.

- Chapter 3 gives the details concerning the design of experimental equipment developed for the experimental work presented in this thesis.

- Chapter 4 presents an attempt to develop a wear modelling approach discovered in the literature and a systematic study of how do geometrical variables affect the parameters of this model.

- Noting severe limitations in studying wear with traditional methods of tribology, an approach based on X-ray imaging was introduced and proven through a pilot experiment (Chapter 0).

- In order to demonstrate the applicability of X-ray diffraction for examining worn samples without sectioning them, a pilot diffraction experiment was carried out (Chapter 6).

- Using these experiments as a base, an advanced X-ray imaging/diffraction experiment was carried out, demonstrating the possibility of observing, studying and quantifying wear without disturbing the contact (Chapter 7).

- In Chapter 8 an attempt was made to expand the approach studied in Chapter 4 to open contact geometries.

- Chapter 9 lists the conclusions of the research work, including possible wear mitigation strategies and areas of fruitful further research.

2 LITERATURE SURVEY

2.1 Fundamentals of wear.

Although wear processes had been known and exploited for millennia, systematic study of wear only became a regular occurrence after the first world war and started expanding rapidly in 1950s. The extent of the work performed during the past six decades is illustrated (but by virtue of its age no longer well represented) by the review of Meng & Ludema (8) who examined wear models published in the journal Wear and proceedings of Wear of Materials conferences between 1957-1992 and 1977-1991 respectively. A total of 5466 publications were surveyed, with several hundred distinct wear models identified and 182 selected for further study, which were in turn found to contain a total of 625 wear variables and empirical parameters.

Meng & Ludema were critical of state of the field, noting that despite the multitude of wear models, there is no generally applicable one, that existing wear models cannot be harmonised with each other and that there is little commonly shared terminology between researchers. The lack of commonality in approach is further illustrated by Blau (9) who lists in excess of 40 distinct metrics for assessing wear presented in two *Wear of Materials* conferences for only 8 types of wear.

In general terms, the observations of Meng & Ludema are still true. Despite extensive efforts, there appears to be no unified theory of wear and no common metric for measuring wear. No method is currently known by which wear in one geometry could be inferred from experimental results obtained in a different geometry. Many empirical correlations have been published, but each applies only within a narrow set of conditions or relies on coefficients that need to be measured on a case-per-case basis, making it very difficult to predict the extent of wear of some engineering component without extensive service/experimental data. As the influence of other factors is still unclear, predicting wear remains a significant challenge within the industrial context.

2.1.1 Types of wear

Typically, wear problems are categorized either by type of damage observed on the wearing surfaces or by the relative movement of wearing surfaces.

The simplest example of the former categorization was introduced by Archard & Hirst (10) who simply divided unlubricated wear of metals onto 'mild' and 'severe', with 'mild wear' meaning a regime producing small, heavily oxidized particles and low wear rates and 'severe' wear meaning a regime producing larger metallic particles and comparatively higher wear rates. This division appears to be losing popularity, but is still occasionally used (see for example (9; 11; 12))

More detailed categorisation by type of wear damage or wear process can be found in the review of wear mechanism maps by Lim & Ashby (13) who identified 6 types of metal-to-metal contact wear, namely ultra-mild wear, delamination wear, mild oxidational wear, severe oxidational wear, melt wear and seizure. However, the idea of wear maps in general and/or the approach of Lim & Ashby in particular were criticized by Godet (14) as well as Fillot, Iordanoff & Berthier (15) as misleading, since they equate the general wear process with the particle detachment mechanism, ignoring the behaviour of the wear debris bed.

Categorization by movement divides wear into unidirectional (surface moves only in one direction relative to another), reciprocating (movement changes direction) and fretting (reciprocating with very small amplitudes); with fretting being further divided into full slip, partial slip and fully stuck regime (16; 17; 18; 19; 20). In studies of fretting, it is common to express the relation between the tangential (shear) force trying to move one surface against the other and the displacement caused by this force in a diagram called a fretting loop (Figure 5). In the fully stuck regime, the shear force is insufficient to overcome the friction between surfaces and displacement occurs solely through elastic deformation of the bodies. In partial slip, a part of the contact surface slips, but a part remains stuck (due to local pressure and therefore the friction force being higher). In gross slip, the shear force overcomes friction completely, making the entire surface slip.

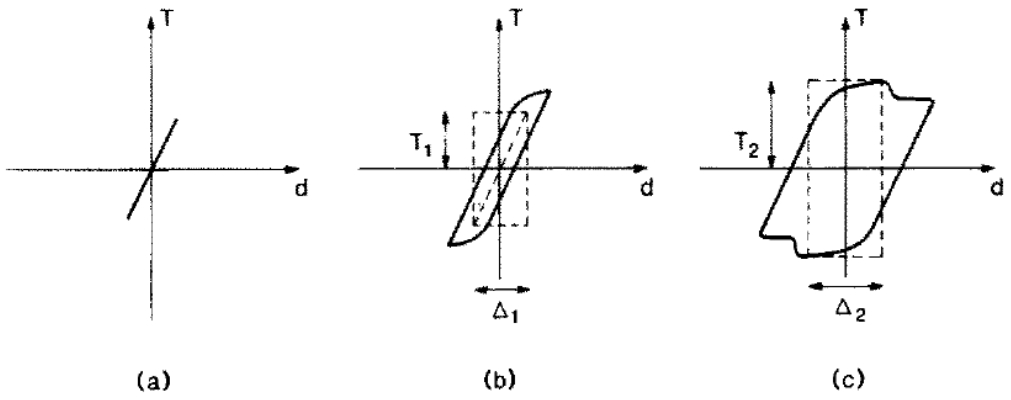

Figure 5: Fretting loops for the fully stuck (a), partial slip (b) and gross slip regime (c) according to Vingsbo & Söderberg (19). T denotes the shear force, d displacement, Δ1 the stuck-to-partial slip transition amplitude, Δ2 partial slip-to-gross slip transition amplitude.

Fouvry et al. (21) provide the following division for ball-on-flat contacts: The transition amplitude between partial and full slip (a_t) is given by Mindlin's (22) elastic expression (eqns. 1-2)

$$a_t = \frac{\pi r_G q_0}{8G^*} \quad \textbf{1}$$

$$\frac{1}{G^*} = \frac{1\text{-}\nu_1^2}{G_1} + \frac{1\text{-}\nu_2^2}{G_2} \quad \textbf{2}$$

Where r_G is the contact radius, q_0 is peak shear stress, G_1, ν_1 and G_2, ν_2 are shear moduli and Poisson ratios for the plane and ball materials respectively. If the amplitude is smaller than a_t, the contact is in partial slip. An empirical study of partial slip/full slip transition in Ti–6Al–4V alloy was produced by Fouvry, Duó & Perruchaut (23), which demonstrates the friction coefficient increasing with displacement in the partial slip region before falling to a slightly lower, but displacement-independent value.

The transition amplitude between full slip and reciprocating sliding is given as the sum: $a_t + r_C$; at this amplitude every part of the contact area is exposed (or 'opened') at least once during one cycle. This division considers only geometrical conditions. No evidence is given that the transition from full-slip to reciprocating sliding actually causes a change in wear to occur or that there are no further changes with displacement in the reciprocating sliding regime. Full-slip-to-reciprocation transition is discussed in somewhat more detail by Chen & Zhou (24), who linked the transition with a change in the wear mechanism, type of debris generated (fine, heavily oxidized in fretting, metallic in sliding) and identified a sharp increase in wear rate at the transition. However, they give no explanation as to which factors govern the appearance of this transition or by what mechanism they do so.

In any case, the above discussion applies only to Hertzian contacts. In a properly aligned annular contact, no pressure gradient is expected and it was believed that such contacts do not experience partial slip. However, Hintikka et al. (25) have demonstrated that in real annular contacts, elastic deformation of the cylindrical specimens causes a gradient of pressure to occur in the radial direction. Correspondingly, partial slip can occur in annular contacts. However, the pressure gradient and the motion occur in orthogonal directions, making the slip zones appear in parallel with the direction of the motion.

It should be borne in mind, that the classical contact mechanics approximation of a perfect elastic solid and perfect elastic half-space may not fully reflect the real contacting bodies, which have rough surfaces and locally an-isotropic properties. Through boundary-element analysis of rough surface contact Armand et al. (26) demonstrated that even in flat-on-flat contacts, the surfaces touch only in

small, randomly distributed spots, each with a unique pressure distribution, with pressure spikes being sufficiently high locally, to cause plastic yielding of the material.

2.1.2 Types of contacts

In contact mechanics, contacts are often divided into 'complete' where the contact area does not change with normal force (such as flat punches for example), 'incomplete' where contact area increases with normal force (such as ball-on-flat) and 'receding' where it decreases with normal force. In wear studies, a different division is typically used, although terminological differences exist between authors. In general, common contact geometries are divided roughly onto non-conforming (surfaces curve away from each other) and conforming contacts (surfaces are parallel to each other). In addition, contacts can also be divided into open contacts, where wear debris can escape by moving in the direction of the motion and closed contacts where this is not possible. For example, a ball sliding in a straight line on a plane would be considered an open contact, whereas a ball rotating against a plane around a normal through its centre would produce a closed contact.

2.2 Observation, quantification and charaterisation of wear

Different wear studies focus on different aspects of wear, be it the amount of material removed, the shape of the wear scar created, the chemical composition of wear debris or some other parameter that is deemed to be of importance. As the field developed, a number of techniques were introduced to enable the effects of wear to be observed and quantified (27).

2.2.1 How much wear?

The amount of material removed in wear is usually quantified using either change in mass or change in surface geometry. Weighing of wear samples before and after wear can establish the amount of material *removed from the worn bodies*. Since these amounts are often relatively small compared to the masses of the samples, suitably sensitive weight scales and sample handling protocols are required.

Changes in surface geometry can be established using profilometry. Budinski (28) for example used a line tactile profilometer to produce a pseudo-3D shape of wear scar. Optical profilometers can capture the topography of the worn area directly. The difference between the unworn profile (measured before experiment or idealized) and the post-wear profile represents the amount of material *removed from the worn area*. See for example (29; 30; 31). In cases where the worn area is difficult to reach or inconveniently shaped, X-ray tomography has been used successfully to obtain a high-resolution 3D image of the part pre- and post-wear in order to measure wear (32; 33; 34). Depending on the circumstances, relatively large differences may occur between these measurements, since not all material that has been displaced from its pre-wear position is actually removed from the sample.

Other options are also possible, although relatively rarely used.

As the bodies wear, their thickness decreases. By measuring the thickness of the wearing bodies, the amount of wear can be inferred. Belin et al. (35) report the use of X-ray attenuation for this purpose (since thinner samples attenuate less). The thickness of the wear sample can also be measured mechanically by equipping the wear machine with sensors that measure the movement of the sample components in the direction of the normal force; as reported by Živić et al. (36) and as was successfully attempted in this work as well (see section 3.2.2.3).

The use of radioactive materials is also reported. Warner et al. (37) studied wear of polyethylene doped with radioactive isotope against stainless steel, lubricated by water. Changes in radioactivity of the water and steel respectively were used as a measure of the amount of plastic worn away and re-attached to the steel surface or dispersed in the water lubricant as debris. Radioactive tracer technology (38) has been in use since 1950s for measuring lubricated wear of engine parts and has been expanded to other applications since, such as orthopaedic implants. The wearing parts are made radioactive through neutron irradiation or ion implantation and the radioactivity of the lubricating liquid measured through time to determine the accumulation of radioactive wear debris in the lubricant.

2.2.2 What is the temperature in wear?

In wear, we separate between the bulk temperature, which is the temperature of the wearing body measured far away from the worn area and flash temperature, which occurs at the contact of wearing bodies, as a result of energy dissipation through friction and plastic deformation. As wear depends on the material properties of the material, surface chemistry (oxidation, thermal degradation of lubricants, diffusion…) and material properties of the wear debris, all of which are at least to some extent a function of temperature, wear is governed by the interplay of both temperatures.

The bulk temperature of the wearing bodies is typically easily measurable and can be manipulated and controlled using furnaces, heating plates or induction heaters (29; 39; 40; 41). Flash temperature on the other hand is often difficult to determine in practice. A number of models for predicting flash temperature has been proposed, but when applied to the same case the results can vary significantly due to different assumptions and approximations; see discussion in (42; 43; 44). Experimentally, the flash temperature in contact between dissimilar metals can be measured by using the contact itself as the 'hot' joint in a thermocouple; this technique has been applied sporadically since at least 1925 (45; 46; 47) and has demonstrated that temperatures exceeding 1000°C can be reached, but that much lower flash temperatures also occur. In a homogenous contact (one where both wearing bodies are of the same material), this technique cannot be applied. Jin, Shipway & Sun

(30) used a series of thermocouples embedded into the wearing body to assess the heat flux, which can then be used to determine the temperature of the wearing interface. However, the result still depends on some assumptions and may not be the expression of the actual momentary flash temperature, but a time averaged value of flash temperature across the contact surface. Sutter & Ranc (48) used a thermal imaging camera to film the edge of sliding contact, inferring the flash temperature from temperature distribution in the high temperature streaks that occur as a result of friction in asperity contact. Ghasemi, Furey & Kajdas (49) used an infra-red microscope to image the fretting contact of a steel ball and a sapphire plane, with temperature being inferred from the IR radiance of the hot spots. Very low temperature rises (<40°C) were measured.

Flash temperature could play a significant role in wear; as explained by Barber (50) localized heating causes the asperities to increase in prominence through thermal expansion. Since the asperity wears 'hot' its size post-wear depends not only on the material removed, but also on shrinkage upon cooling. Grigoriev et al. (51) present an idealized mechano-thermal model of sliding wear which indicates that for a material with a negative coefficient of thermal expansion wear can be effectively eliminated at sufficiently low nominal contact pressures, since the asperities shrink upon frictional heating, thus 'retracting' from contact, reducing localized stresses.

2.2.3 Tribologically transformed structure (TTS)

In wear of metals, a layer termed tribologically transformed structure (52; 53; 54; 55) is formed directly underneath the worn area (Figure 6). This structure is formed during or immediately after, the very initial stage of the wear process (rapid creation of TTS in titanium alloy in the first 50 wear cycles is reported by (52), with as little 10 cycles being reported as sufficient in AISI 316L stainless steel (56)). Some authors report that a certain (comparatively small) amount of frictional energy needs to be expended, before TTS is formed (21).

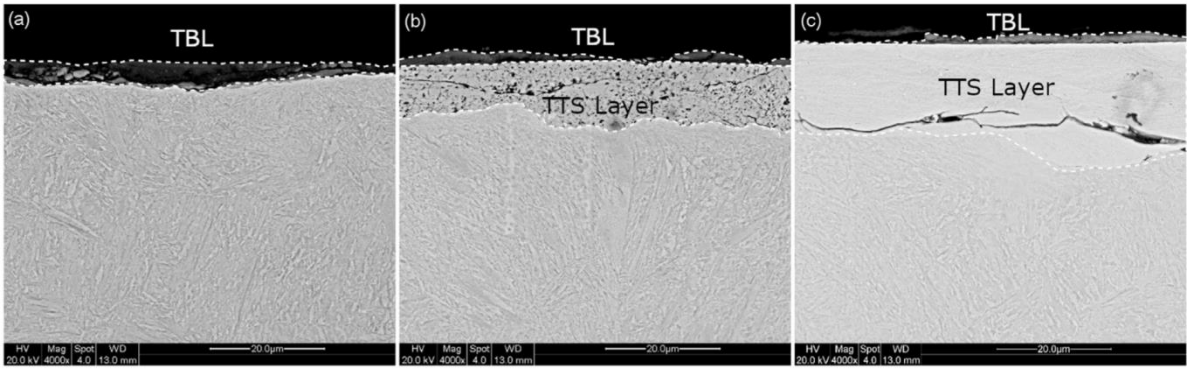

Figure 6: Different forms of TTS formed in fretting BS S132 steel (cylinder-on-plane geometry). (57)

Typically, the observation of this structure utilizes traditional metallography: the wear sample is mechanically sectioned, polished, etched and subjected to optical (58) or scanning electronic microscopy (57; 59). More advanced techniques, such as transmission electron microscopy with electron diffraction (52; 60) or electron backscatter diffraction (61; 55; 62) can also be applied, usually done ex-situ.

A concise explanation for occurrence of TTS is given by Zhou et al. (54). After observing that TTS is formed in wear of metals, regardless of contact conditions and the exact composition of metals in contact, they dismiss the possibilities of TTS being formed through temperature-induced phase transformation (since there is evidence that the occurring temperatures are not sufficient to cause this, as separately shown by (49; 47); in addition to TTS also forming in wear of pure metals (63)), TTS being formed through mechanical alloying (as it also forms in homogenous joints and even in wear of metal against non-metallic minerals (64)) or through incorporation of elements from the atmosphere into the material (as TTS is found to have the same chemical compositions as bulk material). They propose that TTS is formed through intense, localized plastic deformation. This is supported by successful creations of TTS-like structures without the use of wear through the use of extreme plastic deformation under compression-torsion (65; 66; 67; 68) or impact conditions (69).

Further evidence for creation of TTS through plastic strain is provided by Mahato et al. (70) who studied deformation of pure aluminium sliding against a single wedge. As seen in Figure 7 a single pass of the wedge can create significant, but localized strain, the distribution of which appears very similar to the appearance of TTS (Figure 6). The strained material also contained cracks running roughly parallel to the surface. These cracks can connect with each under in subsequent passes so that: "*When a second sliding pass was made over the folded surface created by a prior pass, platelet-type particles were observed to detach from the surface.*"

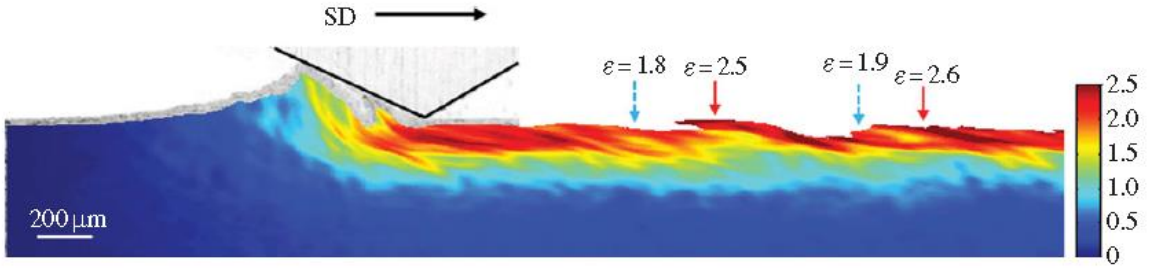

Figure 7: Strain distribution in aluminium subjected to localized plastic deformation due to sliding. (70)

TTS is of importance, since it is the TTS, not the bulk material that disintegrates in wear (TTS being created on/underneath the surface of the wearing bodies). TTS possesses different mechanical properties than bulk material, being harder (71; 62) and due to significant strain and related strain hardening, less ductile (52). If TTS is indeed created by plastic deformation, this process also absorbs energy, which could be relevant, especially in the initial stage of wear. Liu, Liskiewicz & Beake (72) also proposed the replacement of bulk hardness in the Archard's wear model (see section 2.3.1) with TTS hardness to make the model better reflect the properties of the material actually undergoing wear. As discussed above, TTS is also prone to formation of cracks running roughly parallel with the surface, which can lead to particle detachment (73; 62). This cracking pattern could be the result of the TTS formation mechanism or a combination of the TTS formation mechanism and the extremely fine-grained structure created.

2.2.4 Observing wear in-situ

As wear is a phenomenon taking place between surfaces, observation of wear in-situ is possible, if at least one of the wearing bodies is transparent to the frequencies of the electromagnetic radiation used. Most commonly, visible light is used, which requires one of the wearing bodies be made of optically transparent material; with artificial sapphire (74; 49), various glasses (75; 76; 77; 78) and polymers (79) being typical choices.

Between 1996 and 2000 a number of publications (80; 81; 82; 83) were made by researchers at Nanyang Technological University concerning in-situ imaging of wear through X-ray radiography. In this fashion it is possible to obtain results equivalent to using a transparent counter body, but with a metal-metal contact. The researchers have demonstrated that the real area of contact can be observed (but have not attempted to quantify it). Despite an extensive search for other studies, these were the only works found to describe observation of the wear process in-situ not relying on optically transparent bodies. They appear to be little known in the wider tribological community and are rarely cited.

This lack of further study presents a significant research opportunity. Traditional methods of tribology mostly provide an insight only into the end state of wear, with the exact progress of wear and mechanisms influencing it, being inferred/extrapolated from a large number of different experiments and mathematical models. On the other hand, X-ray methods enable wear to be observed directly (as presented in the works cited above), while modern X-ray computed tomography enables the observation of features down to micrometre scale (32; 33; 34; 84). This indicates that wear could be observed in-situ and essentially in real time, especially when using a very bright source, such as a synchrotron, enabling further understanding of wear to be generated. In

principle, X-ray imaging can be paired with other X-ray methods, such as diffraction to study wear-induced changes in material structure and chemical composition. Further development of X-ray methods for studying wear appears to be both possible and valuable as a research tool. This thesis presents attempts made in this direction (chapter 0, chapter 6 and chapter 7).

2.2.5 Coefficient of friction in wear

In order to move the contacting surfaces against each other, a force needs to be applied parallel with the contacting surface, shearing the interface. The coefficient of friction in wear is typically reported to increase rapidly in the initial part of the experiment, reaching maximum and then slowly decreasing to a steady-state value. Consider for example similarities between the works of Mulvihill et al. (85), Hintikka, Lehtovaara & Mäntylä (86) and Pearson et al. (87).

Mulvihill et al. used full and segmented annulus-on-plane contacts made of Udimet 720 nickel alloy. The object was to determine whether the friction behaviour observed in linear fretting tests was the product of leading/trailing edge effects or the contact surface itself. The value of the friction coefficient grows rapidly at the start of the experiments, before falling again, but with only small differences between full and segmented cases (Figure 8).

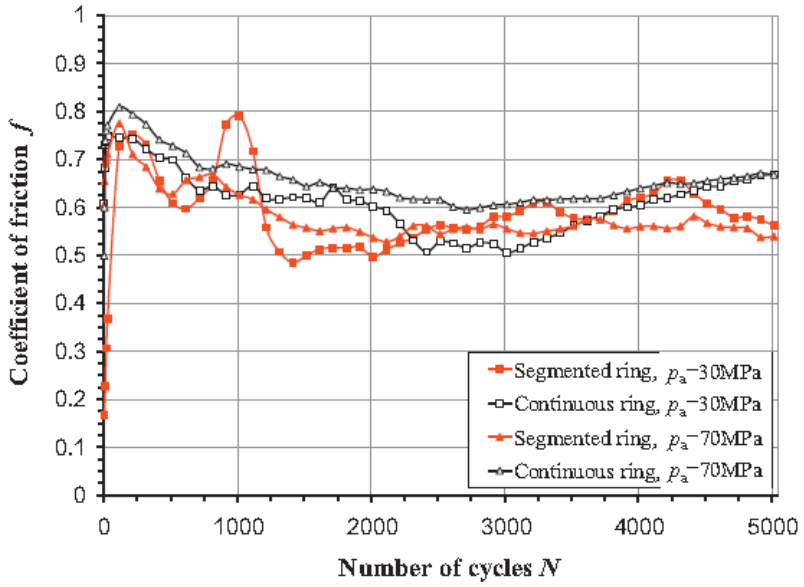

Figure 8: Composite of average friction coefficients for all four experiments of Mulvihill et al. (85).

A similar progression was observed by Hintikka, Lehtovaara & Mäntylä (86), but using a lower pressure (10 MPa vs 30 and 70 MPa), different material (EN 10083-1-34CrNiMo6 steel) and different frequency. The trajectory of the coefficient's development follows the same pattern and is only weakly dependent on the displacement imposed (Figure 9). Pearson et al. (87) studied the effect of bulk temperature on fretting of Super CMV steel. The coefficient of friction was found to follow a similar trajectory below 300°C, but also to decrease with increasing temperature (Figure 10).

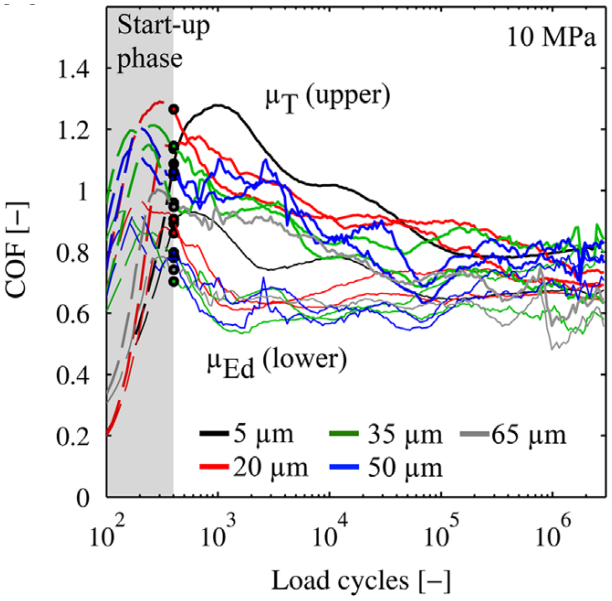

Figure 9: Higher and lower limit of the coefficient of friction as a function of displacement and number of cycles according to Hintikka, Lehtovaara and Mäntylä. (86)

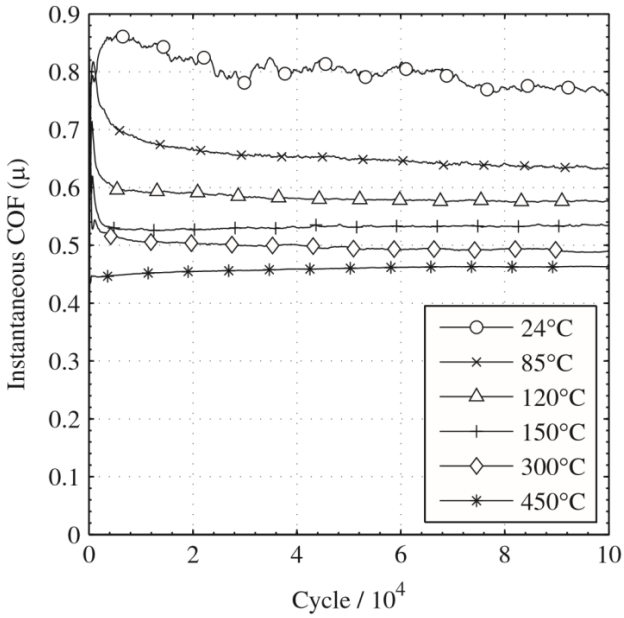

Figure 10: Friction coefficient for Super CMV steel at different temperatures as a function of total number of fretting cycles. (87).

It should be remembered that wear debris is produced as wear progresses. As discussed in more detail in section 2.2.8, this leads to a wear debris bed being produced, separating the surfaces. The high steady-state friction coefficients observed therefore no longer represent the friction between the surfaces (indeed, Suh & Sin (88) report that the friction coefficient *decreases* significantly, after the experiment is interrupted and the debris bed removed) but some gross resistance of the *entire* contact to relative motion and should therefore be properly called gross friction coefficient of contact. This can also explain the variations of friction with temperature observed by (87), as elevated temperatures affect the physical and chemical properties of the debris bed, changing the resistance to relative motion. However, there is currently little understanding as to exactly how properties such as particle shape, particle size, particle-to-particle friction and particle-to-particle adhesion translate into macroscopic debris bed behaviour. This thesis discusses the measurement of coefficient of friction, its oscillations during the wear cycle and its relation to wear debris bed in section 4.3.2.4., DEM modelling of the wear debris behaviour is discussed in section 8.4.

2.2.6 Effect of atmosphere on wear

Jet engine parts may operate in environments significantly different from those commonly encountered. At altitude of 10000 m the atmospheric air pressure is only approximately ¼ that at ground level; inside the engine a range of pressures may be encountered, while combustion consumes oxygen and produces carbon dioxide, water vapour and other compounds, including corrosive SO_2 and NOx. Systematic studies of wear as a function of atmosphere were published by

Feng & Rightmire (89), Mishima (90), Velkavrh et al. (39) and Cai et al. (91), using a range of materials and contact geometries.

Feng & Rightmire (89) studied wear of an annular contact of SAE 1018 steel in air, CO_2 and helium. Wear was measured through mass loss. In dry air, an oxidized debris bed appears quickly leading to steady state wear. In carbon dioxide, the transition to steady state takes much longer, with extensive surface-to-surface metal transfer. However, the losses of material are 20-25% greater than in dry air. In helium, material transfer becomes the principal wear mechanism, with material shifting from one surface to another. This leads to extensive surface damage (Figure 11), but very little mass loss.

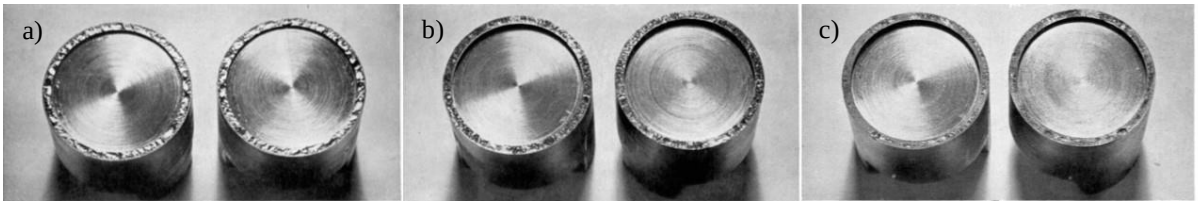

Figure 11: Montage of annular samples of Feng & Rightmire worn in helium a), CO_2 b) and dry air c) (89).

Mishima (90) studied six pure elements (Fe, Ti, Co, Ni, Zn, Au) in dry air, pure oxygen and pure nitrogen at a range of pressures, using a pin-on-disk geometry and assessing wear through mass loss. When there is a chemical reaction between the wearing material and the atmosphere, the wear rate depends strongly on atmospheric pressure, reaching a maximum at some low pressure (see for example Figure 12, Figure 13) and then decreasing significantly with pressure reaching minimum at atmospheric pressure. On the other hand, if there is no chemical reaction the wear takes place as in high vacuum.

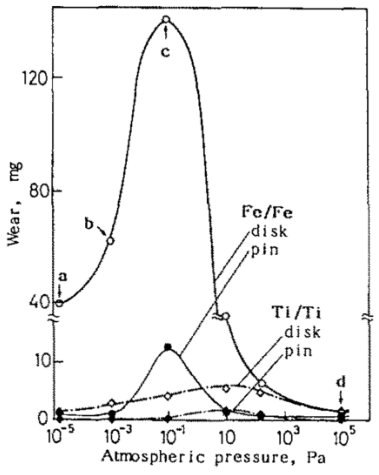

Figure 12: Wear of Fe and Ti in dry air as a function of pressure according to Mishima. (90)

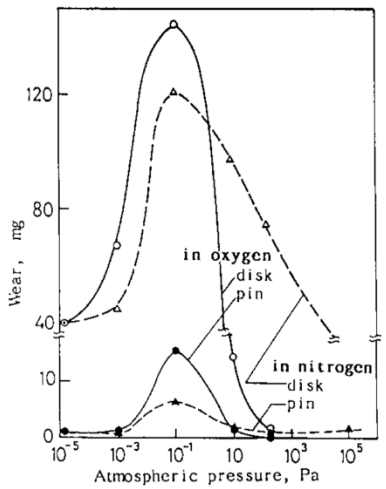

Figure 13: Wear of Fe in oxygen and nitrogen as a function of pressure according to Mishima. (90)

Velkavrh et al. (39) used steel (DIN 100Cr6 steel) ball reciprocating on flat in atmospheres of air, Ar, N_2 and CO_2 at two temperatures (20°C and 200°C) Wear was assessed by 3D profilometry. Their results are in Figure 14.

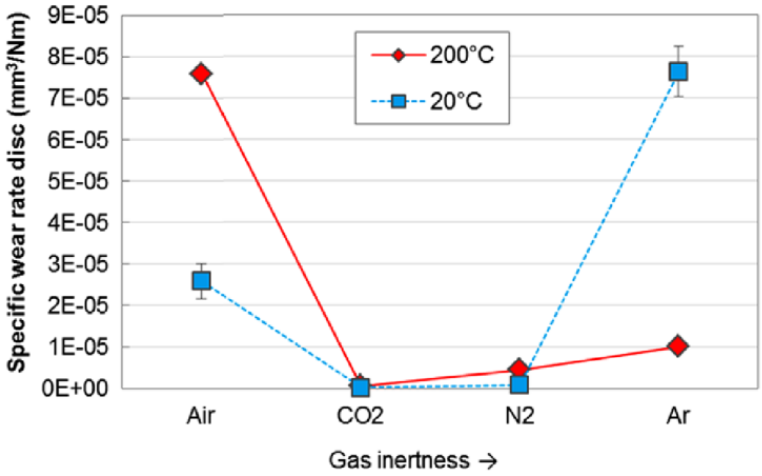

Figure 14: Specific wear rates as a function of atmosphere according to Velkavrh et al. (39)

Cai et al. (91) used a ball (AISI 52100 steel) against flat (LZ50 steel), but with the ball reciprocating torsionally, not longitudinally. Wear took place in the atmosphere of air and dry nitrogen at a variety of rotational displacements. Wear was assessed by measuring the depth of the wear scar in the flat body. The authors concluded that wear is always greater in nitrogen than in air, with the difference between them increasing significantly outside the partial slip regime (Figure 15).

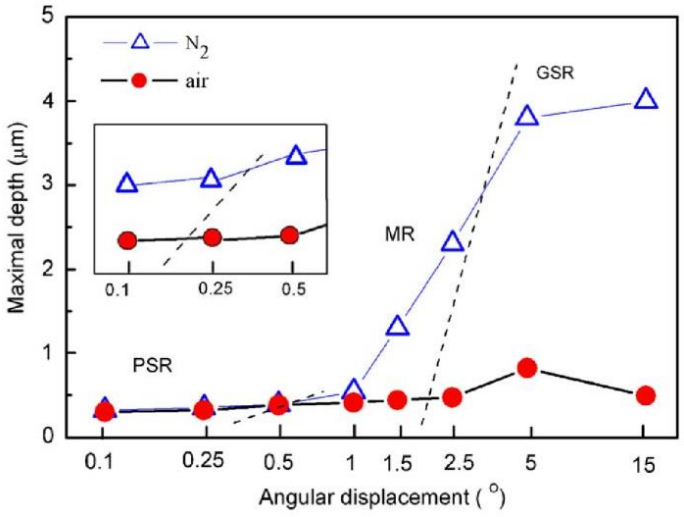

Figure 15: Wear in air and nitrogen as a function of angular displacement according to Cai et al. (91).

The results presented are highly incongruous. According to (89) wear of steel in CO_2 takes place similarly as in air, but is more severe, whereas in He there is only material transfer, but no mass loss. In (39) a CO_2 atmosphere supressed wear strongly and there was extensive loss of material

in Ar (an inert gas, like He). Similarly, (90) reports that wear of iron is similar in air, oxygen and nitrogen. (39) on the other hand, reports steel wearing significantly less in nitrogen than in air, whereas (91) reports the opposite effect.

Given the inconsistencies, pursuing a detailed study of experimental effects on wear might seem to be a productive course of action. However, without a general wear law, linking the atmospheric effects, properties of the bulk material and the wear debris with the progress of wear, the observations collected would be just that: independent observations with little relevance to the general understanding of wear outside the experimental conditions used. It was therefore decided to focus experimental efforts onto more fundamental questions of wear.

2.2.7 Effects of temperature on wear

Many jet engine components operate at elevated temperatures, requiring detailed understanding of their tribological properties at these temperatures. Study of wear at elevated temperatures has attracted many researchers over the years, producing a comprehensive body of work.

As material properties of metals (hardness, yield point, creep resistance etc.) generally decrease with rising temperature it would be intuitively expected that higher temperatures will cause more severe wear. However, the consensus of the scientific community is that the opposite is the case, at least when wear takes place in oxidative atmospheres. This is explained through the following mechanism: increase in either bulk or flash temperature promotes the generation of oxidized wear debris; oxidized debris forms a debris bed protecting the surface from further damage; at high temperatures, the debris particles sinter together, forming a compacted bed called a glaze, which offers maximum protection (12).

Pearson et al. demonstrated (87) that wear of Super CMV steel in air (other conditions being equal) decreases with increasing bulk temperature, despite the softening of the steel. Higher temperatures also lead to narrower wear scars. A glaze layer is formed at approx. 150°C. The same material was studied by Hayes and Shipway (92). Keeping other parameters constant, the bulk temperature was increased from room to 250°C. Wear decreased with bulk temperature, but was also affected by the contact geometry; when the contact area was smaller, the wear rate reduced quicker with rising temperature. This indicates that the glaze formation depends on the interaction between bulk temperature (which is set by the researchers directly) and the flash temperature (which depends on the frequency, size of the contact area and other factors). In all cases studied, glaze layer was fully formed at bulk temperature of 150°C.

Jin, Shipway & Sun (30) examined wear of 304 stainless steel as a function of bulk temperature and fretting frequency. Increasing the frequency from 20 to 200 Hz reduced wear, with the effect being the most pronounced at room bulk temperature. This is explained through the increase in fretting frequency increasing the frictional energy dissipation, promoting the formation of a protective debris layer. Increasing the bulk temperature also reduced wear, with wear rate at 275°C being less than 1/10 that at room temperature. This is also explained through oxidized debris forming more readily at higher temperatures. Coefficients of friction on the other hand, were relatively unaffected.

Rybiak, Fouvry & Bonnet (93) studied fretting of Jethete M152 steel against A268 stainless steel at a number of temperatures, using a flat-on-flat contact. They concluded that wear decreases sharply (by factor of 10-11) at bulk temperatures above 200°C, dividing the wear into the low and high temperature regime, with variations in wear in either regime being minimal in comparison. Based on this, they designed an experiment where the bulk temperature was oscillated between 200°C and 400°C. Change of temperature caused the wear rate to change significantly, with no long-term effects being carried from the low to high temperature wear or vice versa.

Hirsch & Neu (94) studied fretting wear of 301 stainless steel against a 52100 steel counterbody at room and elevated temperatures and also observed a sudden decrease in wear rate at approximately 200°C. They ascribe this transition to a chemical change in the iron oxides formed in wear. At lower temperatures, Fe_2O_3 is formed, whereas a higher temperatures Fe_3O_4 is formed which offers greater protection against wear. Again, only one frequency was used.

The easiest way to study the effects of flash, not bulk temperature on wear is to vary the relative speed of the moving bodies, with higher speeds giving higher flash temperatures. As discussed in section 2.3.1 (see eqns. 5, 6) Dréano, Fouvry and Guilloneau (40; 41) as well as Baydoun et al. (95) determined that wear decreases with fretting frequency to the power of either -0.3 (95) or -0.5 (40) when in a stable wear regime (i.e. the glaze layer is either absent or fully formed).

2.2.8 Wear debris bed

As explained by Zmitrowicz (5) the characteristic length-scale of the debris particles produced in wear is small compared to that of the contact, leading to the debris particles being trapped between surfaces and exposing them to mechanical, thermal and chemical influences. Depending on the mechanism of their creation and the influences they suffered, debris particles may take a variety of shapes and sizes (see Figure 16 for examples).

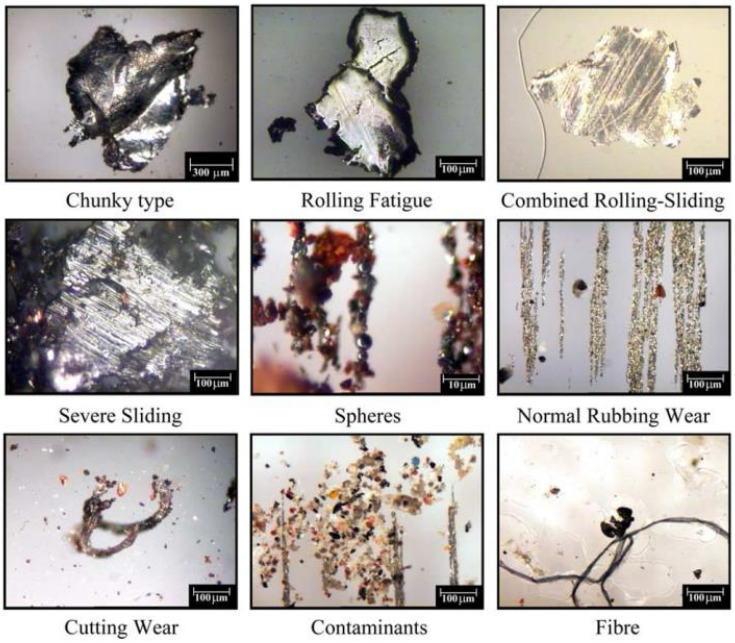

Figure 16: Gallery of different wear particles by Raadnui. (96)

The resulting layer of wear particles, known as a debris bed, is universally reported to be of great influence on the wear process. Godet was first to explicitly include the study of wear debris beds into the study of wear and introduced the commonly used term 'third body' (97; 98) to describe material separating the wearing surfaces (which belong to the 'first bodies') in a wearing contact. The wear debris bed supports (or contributes to the support of) the normal load (98) and aids in the accommodation of relative velocity (99). The usual two-body contact mechanics thus cease to apply. This is illustrated by the discussion in section 2.2.7 of reports of many researchers that wear decreases (possibly to a very significant degree) at elevated temperatures or higher fretting frequencies (18; 30; 12; 93; 87; 100). This might appear illogical, given that yield strength, hardness, creep resistance and other mechanical properties of metals tend to deteriorate with temperature, but only if the behaviour of debris is not considered. At higher temperatures, sintering of debris particles creates a protective layer of 'glaze', whose presence significantly inhibits wear.

Somewhat similarly, researchers modelling wear report that finite element models struggle to predict wear correctly, if the debris bed layer is not taken into account, their explanation being that the presence of the bed changes the local stress field and therefore local wear rate. See for example (101; 102; 103). However, the connection may be indirect. As discussed in greater detail in section 2.3.3.1 such simulations use a localized wear law, which needs to be calibrated with an experiment. As experiments inevitably involve entrapped debris, the global wear coefficient

obtained in the experiment cannot simply be applied on a local level in the simulation, unless debris is also taken into account.

2.3 Wear equations and numerical modelling of wear

In its most basic form, a wear equation (also frequently termed "wear law") is a mathematical statement linking wear (expressed as an accumulated volume, mass or either a momentary or average wear rate) to conditions under which the wearing contact operates. As discussed earlier in chapter 2, many such equations were proposed with different ranges of claimed applicability and containing a large number of variables. By far the most commonly cited wear equation is the Archard's wear law. Due to its prominence, a more detailed discussion of its properties, limitations and proposed modifications is merited.

2.3.1 Archard's wear law

Published in 1953 (104) the Archard's law gives a simple formula for quantifying wear volume V:

$$V = \frac{F_n \cdot L}{h} \cdot k \qquad 3$$

where F_n is the normal force, L the total distance slid, h the hardness of the softer material in the joint and k is a dimensionless constant, frequently also referred to as the wear coefficient. For a chosen contact geometry, materials, sliding speed, amplitude, frequency etc. k is expected to be the same, regardless of the variations in values of F_n, L and h. According to Archard (104; 10) the law should apply regardless of the nominal size of the contact.

Archard's law has been derived using asperity contact models for unidirectional sliding wear, which raises questions as to its applicability to fretting wear. The derivation of Archard's law (104) is based on the shearing of originally spherical asperities that are deformed and then sheared by collision with asperities from the opposite surface. However, in cases of fretting, not all of the contact surface may be experiencing slip. As Archard's wear law has been derived for moving surfaces, the partial slip-gross slip transition could be taken as the lowest possible limit to which this law can apply to fretting, as below it, parts of the contact area are not experiencing relative motion.

In practice, extensive issues with the Archard's wear law have been observed. For Hertzian and flat-on-flat contacts in reciprocating sliding, several researchers noted that at constant normal force, the wear accumulated in some constant number of cycles increases roughly with the square of imposed displacement, whereas the Archard's law predicts only a linear increase (on account of the total distance accumulated in N cycles being proportional to displacement and

wear being proportional to the total distance). This was observed independently and for a variety of material combinations by Kusner, Poon & Hoeppner (105), Waterhouse (106), Elleuch & Fouvry (107; 108), Baydoun et al. (95), Dréano, Fouvry and Guillonneau (40; 41). Several non-Archard empirical wear models were proposed, based on the observations cited:

Elleuch and Fouvry (107) reasoned that variation in displacement causes a proportional variation of debris ejection, promoting wear at larger displacements. They proposed a wear model which weighs the Archard's wear law with a ratio of average displacement in the experiment and some arbitrary length:

$$M_{total} \propto \frac{\overline{D}}{D_{ref}} \sum_{i=1}^{N} 4F_{Ni}D_i \qquad 4$$

Where M_{total} is the total mass of material worn away, F_{Ni} the normal force in the ith cycle, D_i the displacement in the ith cycle, $\overline{D}$ the average displacement over the course of the experiment and D_{ref} an arbitrary, but fixed length.

Baydoun et al. (95) studied wear of 35NCD16 steel contacts in an open flat-on-flat geometry. The contact was submitted to a wide range of frequencies, normal forces and displacements with the following equation derived as the best fit for the experimental data:

$$V_{total} = K_e \left(\frac{p}{p_{ref}}\right)^{0.6} \left(\frac{f}{f_{ref}}\right)^{-0.3} \frac{1}{D_{ref}^{0.7}} \cdot 4NF_N D^{1.7} \qquad 5$$

Where V_{total} is the total wear volume, K_e is the wear coefficient, p the nominal contact pressure, p_{ref} an arbitrarily chosen reference pressure, f the fretting frequency and f_{ref} an arbitrarily chosen frequency. It would appear that p_{ref}, f_{ref} and D_{ref} are introduced predominantly to make the respective variables p, f and D dimensionless.

Dréano, Fouvry and Guillonneau (41) studied wear of a cylinder-on-cylinder contact of a cobalt alloy and alumina under a variety of conditions, observing a quadratic dependence of wear on displacement, but only linear with respect to F_N. For the case where there is no variation of displacement, frequency and normal force during the experiment, they proposed the following equation for calculating the volume loss:

$$V_{total} = V_{initial} + K_{0x} f^{-0.5} e^{\frac{-E_a}{2RT}} F_N D^2 N \qquad 6$$

Where $V_{initial}$ is the volume of material worn away in the initial stage of wear, when the wear rate deviates from the steady-state rate, K_{ox} the wear coefficient, E_a the activation energy for oxidation, R the gas constant and T bulk temperature.

Zhu, Shipway & Sun (31) report that the wear rate of a cylinder-on-flat contact is inversely proportional to the length of the wear scar in the direction of sliding, all other parameters being the same. This contradicts Archard's conclusion of wear being independent of contact area.

In annular contacts of tempered steel, Hintikka, Lehtovaara & Mäntylä (86; 109) observed no dependence of wear on normal load, but have determined that wear can be increased significantly by cutting notches into the annulus. The change in wear increases with the number of notches, which is qualitatively consistent with the later observations of Zhu, Shipway & Sun (31).

Several researchers have noted that wear is not simply inversely proportional to hardness. Studying steels of similar hardness, but different microstructures (pearlite, pearlite/ferrite, globular cementite) Zambrano et al. (110) identified the yield strength, not the hardness as the property indicating wear resistance. Similarly, Moore (111) concluded: '*Bulk hardness is not a direct measure of the wear resistance of ferritic materials, but…for materials of similar structure but different composition, linear relationships exist between bulk hardness and wear resistance.*' Ojala et al. (112) and Valtonen et al. (64) studied commercial wear resistant steels of different grades and microstructures and also concluded that hardness is not a sufficient proxy for wear resistance.

A comprehensive study of effects of hardness on wear in cylinder-on-flat contacts was published by Lemm et al. (29). Steels of five different levels of hardness were used. Results for homohardness pairs are in Figure 17. Contrary to Archard's model wear changes only within a small range and initially increases with increased hardness.

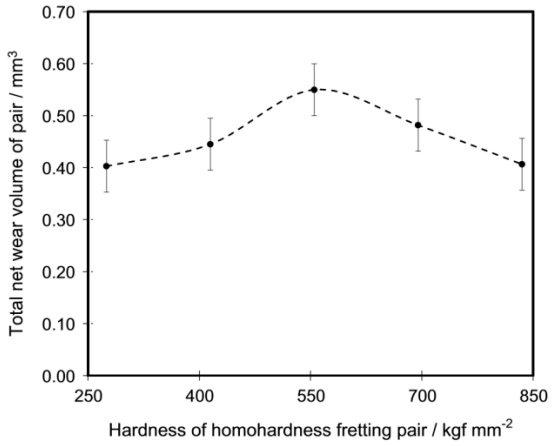

Figure 17: Wear at constant normal load, frequency and displacement as a function of hardness according to Lemm et al. (29)

Wear can also show sensitivity to position: Hiratsuka and Muramoto (11) for example demonstrated that Archard's wear coefficient and the transition between severe and mild wear depend on the orientation of the experimental machine.

2.3.2 Mass balance in wear

The Archard's wear law is not concerned with what happens *after* an asperity has sheared off. The presence and possible influence of debris bed (see section 2.2.8) are not considered. In other words, Archard's formulation ignores the *global* functioning of the wearing contact. To account for this, Berthier (113) developed the concept of a tribological circuit, building upon Godet's third body approach. The circuit includes the debris bed layer and the flows carrying particles in and out of it (Figure 18).

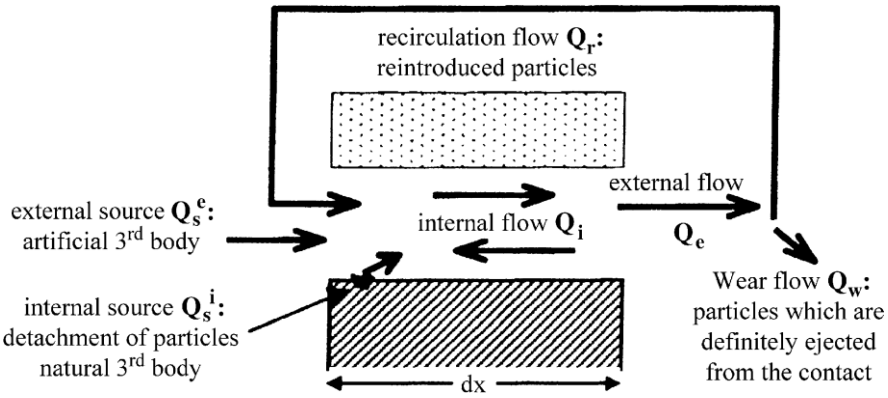

Figure 18: Tribological circuit. (114)

Conceptually, the tribological circuit illustrates that wear is more than merely the particle detachment mechanism: in a steady state, the sum of all the mass flows in the circuit must be zero, as required by the principle of mass conservation. Changing parameters which govern one of the flows must have an influence on other flows as well, otherwise the steady state will not

reappear, causing the wear debris bed to either completely disappear (not possible as this would require infinite particle velocity in the contact) or thicken to infinity.

This explains frequent observations that promoting debris ejection leads to an increase in wear. For example, Hintikka, Lehtovaara & Mäntylä (109), carried out three series of experiments:

- 'Sta' series: Annular samples were fretted at three different levels of normal force;
- 'Cle' series: Samples were fretted at two levels of normal force, with fretting interrupted 13 times to clean the contact surfaces;
- 'Gro' series: Radial notches (or grooves) were cut into one of the samples elements in order to facilitate the ejection of wear debris. Gro_6 denotes experiments with six notches, Gro_{12} with twelve.

Results of (109) are presented in Figure 19 and Figure 20. The results marked 'Sta' are for full annuli without cleaning. The 'Cle' series had the contact cleaned periodically. In accordance with the Archard's wear law, the wear volume (in this case mass) should rise with proportionally with the normal force and should not be affected by the cleaning of the contact (since there is no 'cleaning constant' in the law), but this was not the case. The 'Cle' series tests exhibited a higher rate of wear than those of 'Sta' series at both levels of normal force and the change in the normal force had no significant effect on wear.

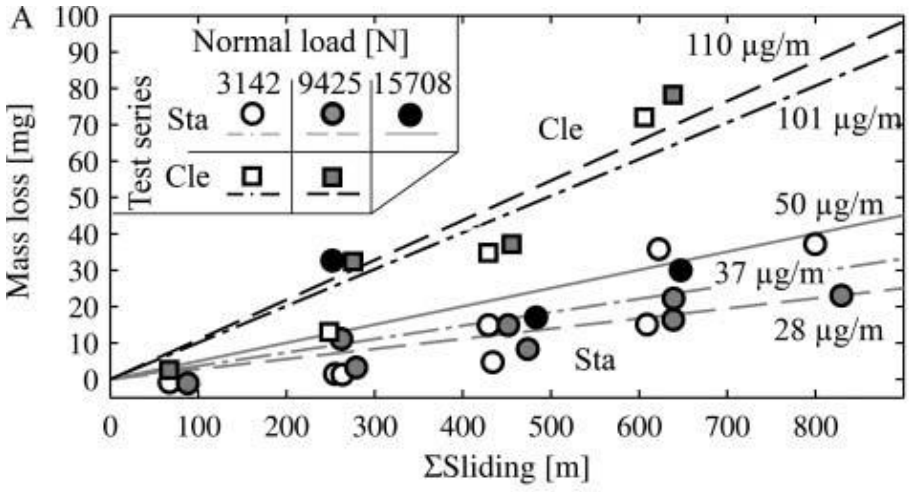

Figure 19: Comparison of fretting in an annular contact without (Sta) and with (Cle) periodic cleaning of the contact. (109)

Figure 20 shows wear mass loss with and without notches. The addition of the notches increases wear (other factors being equal), with increase being larger with a larger number of notches.

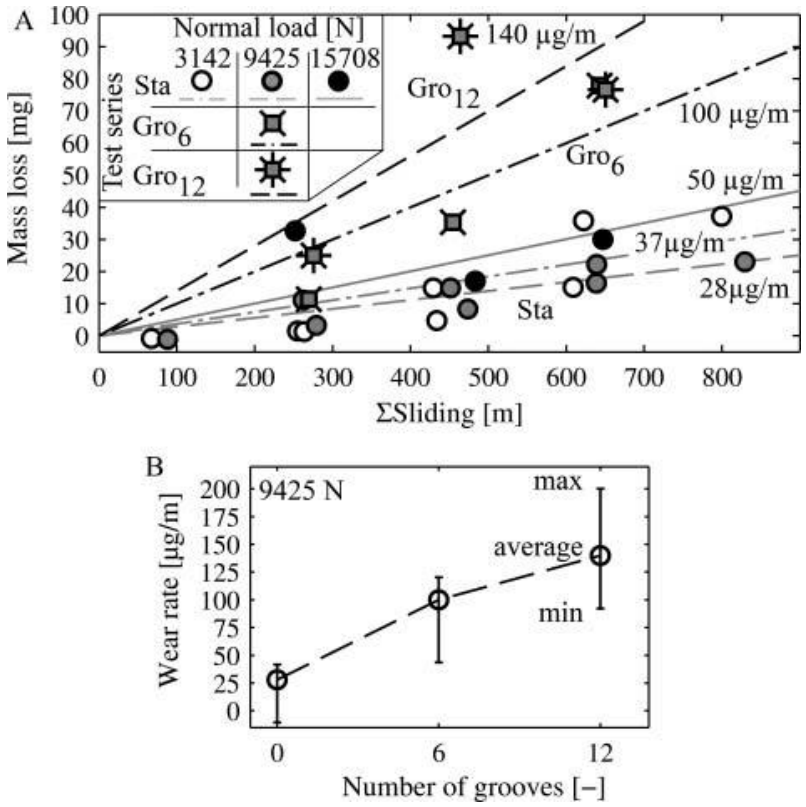

Figure 20: Notched samples results. Wear volume as a function of accumulated sliding distance A), average wear coefficient as a function of notch number B). (109)

The same principle is shown in the work of Leheup & Pendelbury (115). An annulus-on-flat contact was fretted in air, with the central cavity pressurized to the desired pressure (0.39, 0.25, 0.12 or 0.08 MPa). The total distance slid was 1500 m in all cases. Two levels of normal force (310 N and 110 N) were used. The pressure differential caused a leakage of air through the contact, which promoted the ejection of wear debris and increased wear. In both 310 and 110 N cases the application of pressure differential increased wear by approximately a factor of 10. The nature of the debris was also affected: '*Without air flow…the cup's annular wear scar is brown (Fe_2O_3) and nonreflective. Since the imposed motion is an arc, wear debris must move transverse to the motion direction in order to escape - to the exterior, or into the cup…where it becomes somewhat aggregated by the jostling action. With an air flow…no debris is found in the cup. All debris escapes to the exterior in the flow direction, and the cup's worn surface is reflective and metallic.*' (115)

Similar results are reported by Gordelier & Skinner (116), who studied unidirectional sliding wear of nuclear graphite. The graphite sample was hollow, enabling nitrogen to be blown into the centre of the contact area. Introduction of the gas has caused a significant increase in wear, with the increase being roughly proportional to the nitrogen's overpressure relative to the atmosphere.

The work of transforming the idea of tribological circuit into an explicit wear law was performed (at least on a conceptual level) by Fillot, Iordanoff & Berthier (117; 15). By simplifying the tribological circuit to particle detachment flow, particle ejection flow and internal flow and writing appropriate mass balance equation, they arrived at a wear law fully taking into account both particle generation as well as particle ejection:

$$Q_d(t)=C_d\left(H_{max}-H(t)\right) \quad (7)$$

$$Q_e(t)=C_e H(t) \quad (8)$$

$$\varrho S\frac{dH(t)}{dt}=Q_d(t)-Q_e(t) \quad (9)$$

where Q_d is debris generation rate, Q_e debris ejection rate, C_d generation constant, C_e ejection constant, H_{max} maximum debris bed thickness, H debris bed thickness, S nominal contact area and ϱ debris density. While it seems possible that debris collected after ejection would have different density than the one in the debris bed (since it is not exposed to contact pressure), a single value of density can still be used, since any change happens immediately after the moment of ejection, not before it. Assuming $H(0)=0$ as a boundary condition the steady state debris bed thickness ($H_{stab}=H(\infty)$) is given as:

$$H_{stab}=\frac{C_d}{C_d+C_e}H_{max} \quad (10)$$

While the debris bed development is described by:

$$H(t)=H_{stab}\left(1\text{-}e^{\frac{-t\,(C_d+C_e)}{\varrho S}}\right) \quad (11)$$

In steady state debris generation and ejection rates are:

$$Q_d(\infty)=Q_e(\infty)=\frac{H_{max}}{\frac{1}{C_e}+\frac{1}{C_d}} \quad (12)$$

This wear law comes close to satisfying to Meng & Ludema's general recommendations for obtaining success in wear studies: '*Abandon efforts to model wear in terms of the current list of wear mechanisms. These terms only serve to diverge thinking on real wear processes. It is not surprising that the long-standing wear mechanisms are still in use; however, there are few alternatives. Develop full descriptions of the evolution of macroscopic events on sliding surfaces. This must include a description of the formation and movement of fragmented particles in the interface region.*' (8) Unlike Archard's law, it takes account of the debris

bed, debris ejection and models wear as a series of mutually-acting processes rather than merely the particle detachment process.

It is of note that expressions very similar in mathematical form have been proposed by other authors using independent and radically different methods of reasoning. In the study of Warner et al. (37) an almost identical wear model was derived for the particular case under study (water-lubricated wear of polyethylene against steel) entirely empirically; while Hanief & Wani (118), using analytical reasoning by analogy with an electrical circuit, proposed an equation for development of wear rate with time identical to the expression for particle detachment flow in the Fillot, Iordanoff & Berthier. This gives additional credibility to this model. However, Fillot, Iordanoff & Berthier provide little guidance on how can the parameters Q_d, H_{max} and Q_e be determined. Without a way to reliably determine these parameters independently, eqns. 7-12 are of limited use as a predictive tool.

2.3.3 Numerical modelling of wear

With development of computing technologies, many attempts were made to produce numerical computer models capable of predicting wear rates and wear scar morphology as well as other tribological phenomena (119; 120). This may seem to be an incongruous pursuit, since a numerical simulation requires a comprehensive mathematical formulation of the wear phenomena, which does not appear to exist at present. On the other hand, Fillot, Iordanoff & Berthier (117) developed their wear law with the aid of numerical simulations.

Numerical modelling of wear can use at least three *main* approaches, based on solid continuum mechanics, fluid continuum mechanics or discrete elements.

2.3.3.1 Modelling wear through solid mechanics

This is a very common approach with many variations reported in the literature. Typically, the work follows the following general pattern:

- Calculation of local stresses and strains in the contact area using finite elements (FE) or some similar numerical method
- Application of a wear law linking local stresses/strains with mass loss
- Adjustment of the mesh geometry to reflect the local mass loss calculated
- Repetition of the above

Wear laws used in such models are typically Archard's wear law (121), or an energy wear law (mass loss is proportional to the energy expended (101; 103)) although other possibilities are also used. Building on the work of Kapoor (122), Elleuch & Fouvry (107) developed a model linking mass loss to total plastic strain. Ghosh, Leonard & Sadeghi (123) used Voronei tessellation to simulate the crystal grains and postulated that wear occurs through inter-granular cracking and then simply deleted any grain than has separated from all of its neighbours.

The approach suffers from a significant weakness, namely it needs to pre-suppose a wear law, but there are no generally applicable wear laws currently known. As a result, the parameters and coefficients of the wear law used need to be determined empirically for the exact contact geometry and material pair that is being simulated, meaning that the simulation can extrapolate the results beyond the duration of the physical experiments or be used for testing of different wear law, but is of limited utiliy for other purposes, until a more generally applicable wear law is developed.

2.3.3.2 Modelling wear through fluid mechanics

In this approach, the contact surfaces are modelled as porous surfaces through which fluid (representing the wear debris) flows, forming a fluid film (debris bed). In steady state, the 'outflow' through the sides of the contact (ejection of wear debris) needs to equal the 'inflow' through the surface (creation of wear debris).

As the fluid flows through the film, a pressure gradient appears, which is a function of local fluid velocity, fluid rheological properties and fluid film thickness. The gradient must be such as to exactly balance the normal force pushing the surfaces together (otherwise the film must either increase or decrease in thickness). This permits only certain combinations of fluid flow rate and fluid film thickness. In addition, the relative motion of surfaces shears the fluid film, with the shear force depending on the speed of the sliding, the thickness of the film and the rheological properties of the fluid. If rheological properties, shear force and normal force are known, the fluid film thickness can be calculated from the shear force relation and then inserted into the pressure gradient relation, giving the steady state fluid flow rate, which is the steady state wear rate.

A general mathematical description for a quasi-fluid powder with relevant boundary conditions is given by Heshmat (124). Alternatively, Haff (125) and Zhou & Khonsari (126) applied kinetic theory to particulate matter, deriving equations for compacted particle flow. The first case is relevant where the debris behaves quasi-fluidly and its rheological properties have been determined empirically. The second where the debris is highly uniform in size and particle-to-

particle interaction is known. As a result of difficulties of determining either, this modelling approach has seen very little use in the wear community, but far more in studies of powder lubrication (127; 128; 129; 130), where powders are produced separately and have repeatable, well-characterized properties.

2.3.3.3 Modelling wear using discrete elements

The Discrete Element Method uses discrete particles (or elements) to simulate both continuous (particles are linked to each other) and discontinuous (particle interact when they contact) bodies. The ability to simulate the disintegration of solid bodies and flow of particulates makes this approach well-suited for modelling wear.

Fillot, Iordanoff & Berthier produced a series of progressively sophisticated models, modelling a 'degradable body' composed of bonded particles pressed against a 'non-degradable surface' made of fixed particles, first in 2D (131; 132) and then in 3D (117; 15; 133). Particle shape was assumed to be spherical. Periodic boundary conditions are applied to surfaces perpendicular to the direction of sliding. As the body slides over the surface, spheres are detached from it, becoming third-body particles (Figure 21)

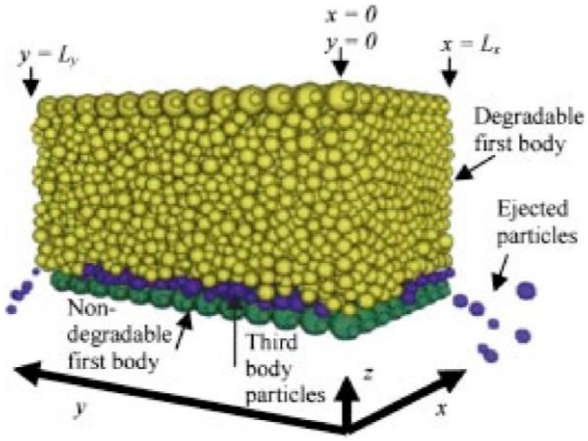

Figure 21: The model of Fillot, Iordanoff & Berthier (117). Normal force is applied in the –z direction, sliding is unidirectional in the x direction.

Further exploring the effects of particle cohesion on wear on a conceptual level (133) Fillot, Iordanoff & Berthier reached the conclusion that particle cohesion promotes both debris creation and debris entrapment. Where geometry of the contact also promotes debris entrapment, increased particle cohesion has a wear-retarding effect and the reverse, whereas geometry favours debris ejection. In either case, the authors did not attempt to simulate a real material and used particle bond and interaction parameters that were arbitrary or computationally convenient.

DEM is also applicable to multi-phase materials; see for example the work of Champagne, Renouf & Berthier (134) who present a 2D simulation of solid two-phase material and study the effect of normal force and particle interaction on wear and surface damage. Like (133) they conclude that increasing adhesion between debris particles increases debris creation and leads to thicker debris beds, but do not comment on ejection effects, since the boundary conditions of the simulation prohibited ejection of wear debris.

Using spheres to simulate the first and third bodies may appear to be an excessive simplification given the irregular shape and size of both crystal grains in metals as well as wear debris particles. Mollon (135) produced a DEM model simulating wear of polycrystalline material with realistic grain shape, but did not introduce realistic particle bond or interaction laws in it.

Can DEM be used to model a practical wear case? If the particle-to-particle bond parameters are chosen correctly, the bulk response of the bonded assembly might be made similar to that of a real material. Similarly, if the particle-to-particle interaction model is chosen correctly, the behaviour of loose particles can be made similar to real debris. In this fashion it should be possible to simulate a real-life wear case. The greatest practical limitation appears to be the incorporation of plasticity into the model; having been used primarily for studies of brittle minerals and granular material transport, there has been relatively little research in simulating bulk ductile behaviour using DEM.

An attempt in the direction of realistic simulation of wear by means of DEM was made by Li et al. (136) who simulated wear in a roller bearing. In order to determine the parameters of the particle interaction models, a uniaxial compression of a block of bonded particles was simulated and the parameters adjusted until the simulated macroscopic Poisson ration, Young's modulus and yield point corresponded to the real material in question. The finite element method was used to calculate the local stresses in the bearing and these then applied to a 2D DEM model to study wear on a local scale. Phan et al. (137) studied abrasive resistance of oxide layers forming on high-speed steel rollers in rolling mills. In preliminary simulations they simulated micro-tensile and indentation tests in order to obtain particle bond parameters that gave bulk material response similar to real oxide. This information was then used to simulate scratch tests on oxides in 3D. For additional discussion on techniques for obtaining realistic bulk material response in DEM see André et al. (138), Chen, Schott & Lodewijks (139) and Jerier & Molinari (140). In this work some DEM modelling was used to study the behaviour of thick wear beds. This is presented in section 8.4.

2.4 Literature survey - Outcomes

Wear has been a subject of continuous scientific interest for several decades with a large volume of literature published. However, there is a general lack of congruence with no single metric or method for assessing wear, nor a generally applicable wear law. A number of wear simulation techniques exist, but practical industrial application remains challenging, since the wear laws used require empirical 'tuning' to each particular case under simulation.

In some cases, it appears impossible to extract any solid conclusions from the available research, consider for example the discussion about the influence of atmosphere on wear in section 2.2.6 (refs (89; 90; 39; 91)) where there is little common ground between the authors. A similar conclusion is voiced by (141).

Archard's wear law remains both widely discussed and widely used in the wear research community, despite a general agreement that there exist many more variables affecting wear than merely three and despite evidence that variations of those three variables (hardness, normal force and displacement) give responses different than those predicted by the law (see (29; 110; 111; 112) for effects of hardness, (86; 109) for effect of normal load, (105; 107; 95; 40) for effect of displacement).

Ultimately, Archard's wear law accounts only for the creation (or more accurately, one of the possible ways of creation) of debris particles. For a complete description of wear, events taking place after debris creation need to be considered as well. Empirically, the importance of wear debris behaviour is demonstrated by a number of observations:

- formation of protective glazes at higher temperatures which significantly decrease wear (see (92; 30));
- decrease or even total suppression of wear through prevention debris ejection (15)
- increase in wear rate through stimulation of debris ejection, for example by cleaning (109), changes in contact geometry (109; 18) or an intra-contact flow of some medium (115).

A practical wear law needs to account for these observations. Conceptually, the inter-relation of particle detachment, debris bed formation and particle ejections is represented by the tribological circuit introduced by Berthier (113). By applying DEM simulation to the tribological circuit Fillot, Iordanoff & Berthier developed a set of equations describing wear in terms of mass balance (117) and successfully tested it empirically (15). Apparently unbeknownst to either

research group, a similar expression has also been formulated independently by Warner et al. (37). Unfortunately, no method for determining the parameters this wear law requires is currently known, apart from measuring them empirically on a case-per-case basis. If a method for determining these parameters independently were to be developed, a powerful wear law could be obtained, as it would take into account wear particle generation, entrapment and ejection.

Many attempts at modelling wear have been made and published, most commonly coupling the finite element method with an assumed wear law, linking the local stress/strain state with the amount of material lost. As there are no generally applicable laws of wear, the wear law chosen needs to be experimentally calibrated to suit the geometry, material and other conditions being simulated, with the simulation thus mostly extrapolating experimental measurements to different durations of wear. In the absence of a widely applicable wear law, this method does not appear to be useful for predicting wear and degradation of parts in an industrial context.

Several authors have tried simulating wear in contact of solids using discrete element simulation. This method automatically takes into account the creation of debris particles and their entrapment between the surfaces. By its nature it does not require any pre-defined wear law to be applied, but it does require particle-to-particle bond and particle-to-particle interaction models that give realistic responses. Attempts in this direction have already been made (see (136; 137) for realistic first body properties, (135) for realistic first body structure and wear particle shape). Further research in this direction appears to be promising.

2.4.1 Lessons and opportunities

The information from the previous sections informed the development of research presented in this work. At present, a large portion of publications dealing with dry wear concentrate either on application of various solid mechanics models to the wearing contact or on performing experiments to study wear of a particular material combination using a small range of contact geometries or a single contact geometry.

Treating wear as a two-body contact problem appears to be reaching its limits as a research/modelling approach, since the results are not only significantly sensitive to the approximations used (see for examples the inclusion of surface roughness and effects of plasticity (26), as well as discussion in (142) which shows that in partial slip, wear cannot continue indefinitely without the wear bodies deforming plastically), but the very core of the approach may be insufficient to tackle the problem. No methods through which local stress fields could be reliably translated into wear has been discovered. A number of authors argue that the behaviour of the debris bed needs to be accounted for, not merely as a cohesive third body

(as done by (101; 102; 103)) but as a quasi-fluid entity, whose properties and flow depend on an array of variables, beside the local stress field. The model proposed by Fillot, Iordanoff & Berthier (117) treats wear as a pair of mutually opposed processes of debris generation and ejection, which are coupled through their dependence on the debris bed. This is a conceptually strong model, but implied in it is the importance of both local and global conditions: the detachment of an individual particle is the result of the local condition (collision with another particle/asperity with a sufficient force and in appropriate direction), but the number and outcome of such events are influenced by global conditions, such as debris ejection being physically prevented at the edge of the contact. In other words, points in the wearing region can 'feel' the effects of changes occurring far away from them.

On the other hand, the ever-increasing body of experimental results has failed to produce any universal or even widely-applicable model of wear. While empirical models can be successfully fitted to results of a specific experiment or experimental series, none have been found that would have a wider applicability without extensive 'refitting' to other cases. While the qualitative effects of certain wear parameters appear to be established with a degree of reliability: in metals, wear decreases with bulk temperature and rising frequency (sections 2.3.1 and 2.2.8), increasing hardness also contributes to wear resistance, but the effects are not linear and depend significantly on the microstructure, not merely on the value of hardness (section 2.3.1). There is evidence that reducing the grain size and coefficient of thermal expansion also function as a wear-reducing mechanisms (143; 63; 51). However, reliable quantitative predictions remain elusive, for the time being.

In the light of this, the primary objective of this work was formulated as an attempt to develop a more widely applicable macroscopic model of wear (i.e., one taking into account contact geometry, normal forces, amplitudes, material properties etc.) based on the concept of tribological circuit of Berthier (113), since this approach accounts for behaviour of the debris wear bed. The model of Fillot, Iordanoff & Berthier (117; 15) was taken as a starting point, since it is stated in general terms, strong conceptually and was (as of 2018) mostly untested in practice. This law however is only a global wear law and can only be used (at least in its present state) for predicting the total quantity of wear, but not for predicting the shape of the wear scar. As of 2018 it was unclear how and if parameters of this law could be reliably predicted without recourse to tedious measurements. Also, the original authors provided no pathway for expanding this law to other geometries.

The work presented was experimentally driven, but the experiments were not designed to study wear of a particular material in a particular geometry and under such and such set of conditions, but to study wear *as wear*, the focus being less on how much wear there was, more on the process that created the output. As a result, the materials studied were chosen with respect to their convenience of use, rather than as examples of real wear-facing materials.

2.4.2 Use of Annular Contacts

Annular contacts were chosen as the preferred contact geometry. Annular contacts have appeared sporadically in literature for decades (see (89; 109; 25; 62)) but remain relatively rarely used. However, for many purposes of this work, they were ideal, due to a number of properties:

- Contact pressure and contact area

In a ball-on-flat or cylinder-on-flat contact the initial distribution of contact pressure and the size of the contact area are given by Hertz's analysis as a function of geometry of the contact bodies, their elastic properties and the normal force. This makes it difficult to separate the influences of individual variables. If the normal load is changed, the contact pressure distribution changes (at least in its magnitude, if not its form) and the contact size will change too. If different materials are tested, it may prove impossible to have the same contact area and pressure distribution in all cases due to the interplay of properties. In an annular contact, the size of the contact area is independent of normal load, known in advance and does not change significantly with wear (excluding possible plastic deformation of samples), causing little/no change in nominal contact pressure. In an annular contact, area, pressure and material thus become independent factors varied by the experimentalist as desired.

- Lack of leading or trailing edges

Edges of the contact act as stress concentrators, capable of causing significant increases in local stress, raising the question to what extent are the observed wear phenomena the result of such edge effects. In a properly aligned contact of two identical annuli, both the inner and outer edge are common, meaning that there is no stress concentration at the edges. Since the common edges run parallel to the direction of movement, no part of the surface will cross an edge during wear.

- Simplified dimensional relations

The length of the annular contact in the direction of sliding is infinite. Dividing any contact dimension (annulus width, average particle size, imposed displacement etc.) by contact length thus always gives zero. This significantly decreases the number of geometrical relations applying to the contact. Particle size, annulus width, displacement, grain size and surface roughness parameter remain as the length scales most likely to influence wear.

- Simplified simulation and analysis

The annular contact is relatively easy to analyse/simulate. Heat transfer can be treated as straightforward 1D conduction through a homogenous wall from the contact surface (heat source) to the sample mount (heat sink). In contrast, Hertzian contacts require significantly more complex models, generally taking into account the contact size and the time-dependence of both location and magnitude of the heat source (see for example (30)).

An annular contact can be easily approximated by two blocks with periodic boundary conditions applied to the surfaces perpendicular to the direction of the sliding, making any CFD, DEM or other types of simulation relatively straightforward. For the same reason a full annulus-on-annulus contact is a good physical representation of the idealized model of Fillot, Iordanoff & Berthier (117; 15; 133), making it ideal for testing and expanding this particular model.

The benefits mentioned above do come at a price, however. In an annular contact there will always exist a radial gradient of sliding displacement (and as a result also sliding speed). This is minimized by increasing the radius of the annulus, but this results in relatively large samples. Larger samples require more material to make (which could result in significant costs in some cases), larger sample masses lower the resolution of mass loss measurements and finally, large annuli have relatively large surface areas, requiring large normal forces to reach representative surface pressures. This in turn requires sufficiently powerful and heavily-built wear machines which might not be easily accessible. Another significant issue with annular contacts is the question of alignment. Angular misalignment will cause an uneven distribution of contact pressure around the circumference, axial misalignment will cause an edge (and associated stress concentration) to appear. Special precautions need to be taken when designing experimental rigs and machining the samples to minimize these effects.

2.4.3 X-ray imaging in tribology

Noting the earlier successes of X-ray imaging in tribology, attempts were made to create a technique for in-situ imaging of wear through X-rays, which could open a path to practical means for direct observation of wear in (pseudo)real-time. This could enable a greater insight into the initiation and progress of the wear process, as well as the ability to monitor the condition of the contact without disassembly, which could have practical industrial uses. Experimental results presented in chapters 0 and 0 show that wear can be imaged using X-rays without dismantling the contact, indicating that true in-situ imaging is possible with the right equipment. X-ray methods enable the progress of wear to be viewed from unworn to completely worn conditions, the worn surface profiles to be visualized and quantified, as well as the real area of contact and contact porosity to be estimated. This approach also enables the detailed observation of the wear debris bed. Real-time observations of wear and debris ejection were not attempted due to technical limitations, but appear to be possible, at least if using only 2D radiography and a sufficiently powerful X-ray source. Some estimation of the thickness of the wear-deformed region in the material of the wearing bodies is also possible through X-ray diffraction.

3 METHODOLOGY

During the course of this project, 8 main parts of experimental work were performed for the purpose of providing data needed to formulate an improved model of wear. Most of the experimental equipment used was developed specifically for the task at hand and manufactured within the department workshops. The first part of this chapter describes the general thrust of the modelling work performed. The second part of this chapter presents the details of the mechanical design and practical use of the experimental equipment used. As such, it functions primarily as a repository of engineering and experimental design details and might be less of an interest to a reader interested primarily in questions of tribological science. Chapters discussing the results of the experimental work make references to the relevant sections of *Methodology*, so that the reader may find the details relating to individual experiment, if and when desired.

3.1 How to approach the development of a new wear model?

As discussed in section 2.1, upon reviewing several thousand wear models Meng and Ludema (8) concluded that the models published do not enable reliable prediction of wear and that the models published cannot all be correct, since they are not based on some common principle or theory of wear. In particular, they suggested that if a truly general law of wear is to be produced, it: "*…must include a description of the formation and movement of fragmented particles in the interface region.*" This is consistent with the third body approach proposed by Godet (98; 14). However, at the time of writing there is no generalized model of wear available. As discussed in section 2.3.3.1, the majority of computer wear modelling is done using some variant of Archard's wear law. Since the wear constant in such models cannot be predicted in advance, the usability of such models is severely limited; in addition, wear does not always conform to Archard's formalism (41; 40; 95; 86; 109) and it is not fully clear why, how or when do these deviations occur.

While a very large number of empirical wear models have been published, these do not give much opportunity for extrapolating results across geometries and material combinations. The most effective method for predicting wear of a component in service remains the use–of approximations of real-world contacts (144; 145; 146; 147). This however, is resources intensive and does not directly lead to understanding the physical principles of wear, understanding without which computer modelling of wear is not feasible.

How can a generalized wear law, especially one based on "*a description of the formation and movement of fragmented particles*" be developed? A strong attempt in this direction was made by Fillot, Iordanoff and Berthier (denoted FI&B in the continuation for brevity) between 2003 and 2007 (131; 132; 117; 15; 133). Using the discrete element method, first in two dimensions and then in

three, they studied wear of perfectly brittle material and associated formation and behaviour of wear debris beds. From their numerical experiments, they obtained a mathematical description of wear. Unfortunately, the original authors did not continue their work significantly past the stage of their publications in 2007 (148).

The modelling strategy in this work focuses on exploring the applicability and practicality of using the approach of Fillot, Iordanoff & Berthier to generate a model capable of predicting the amount of material removed in wear. For this purpose, three preliminary goals were set:

- Exploring the mathematical implications of the FI&B model to determine, whether its predictions are consistent with the experimental data available and whether some additional understanding of wear could be obtained through it (see sections 4.3.2.2 and 8.1, as well as discussion in 9.2). Experiments aimed at measuring the development of wear rate and testing dependence of wear on normal force were carried out to provide data for mathematical analysis.

- Testing an assumption stated in (117) about effects of geometry on debris entrapment and generally trying to improve the understanding of forces and mechanisms responsible for the values of constants in the FI&B model (see sections 4.2.2.2, 4.2.3, 4.3.2.4). Experiments aimed at measuring wear as a function of geometry and measuring the properties of the debris bed were conducted to generate relevant data.

- Expanding the approach to different contact geometries. FI&B only studied wear in one geometry, but proposed a wear model stated in very general terms. If this model is indeed a general model of wear, there should exist a way for stating the three constants of the FI&B model as a function of any geometry, thus predicting wear in contact of any shape. As a start, work focused on open flat-on-flat contacs. After experimental observations helped to refine assumptions about the direction of debris ejection (see section 8.2.2) the derivation of FI&B was retraced with new assumptions, specific to this contact geometry to obtain a functioning wear model (section 8.3).

3.2 Main wear rigs

This section deals with two separate wear rigs that were used for the majority of experimental wear work in this project. In this context, the term 'rig' refers to the sample holders, mounting brackets and other parts that hold the wear sample. The wear rig is operated by a loading frame, which applies compression and torsion, as required for the experiment with an annular contact. The first rig was inherited from the research work of Z. Clark (149) and was designed to be

operated by the Zwick-Roell Z100 loading frame. The second rig was originally designed to be used with an Instron loading frame, which offers (in principle) superior data sampling and storage capability, as well as the ability to utilize external position sensors. However, a series of practical issues demanded a return to the use of Zwick-Roell loading frame, which necessitated modifications to the design. Both rigs used annular samples as their unique properties (discussed in section 2.4.2) make the uniquely useful for experimental studies of wear.

3.2.1 First wear rig

The first rig (Figure 22) was designed to utilize an annular sample with an internal diameter of 66 mm and external diameter of 70 mm. Being readily available, it was used in the initial part of the experimental work. One of the issues with using the annular contact is the question of contact alignment; if the contacting surfaces are not parallel, the contact pressure will vary around the circumference of the sample, with local plastic deformation being possible in extreme cases. A special mechanism to avert this was incorporated into the design. Whereas the top sample element was simply mounted on a large steel bracket (using three pins for positioning and three bolts for holding the sample in place) the bottom sample element was mounted on a wobble plate, which rested on a steel bearing ball. The centre of the ball lies on the plane of worn contact. As the sample elements are pressed together, the bottom sample can pivot around the ball to make the wearing surfaces parallel.

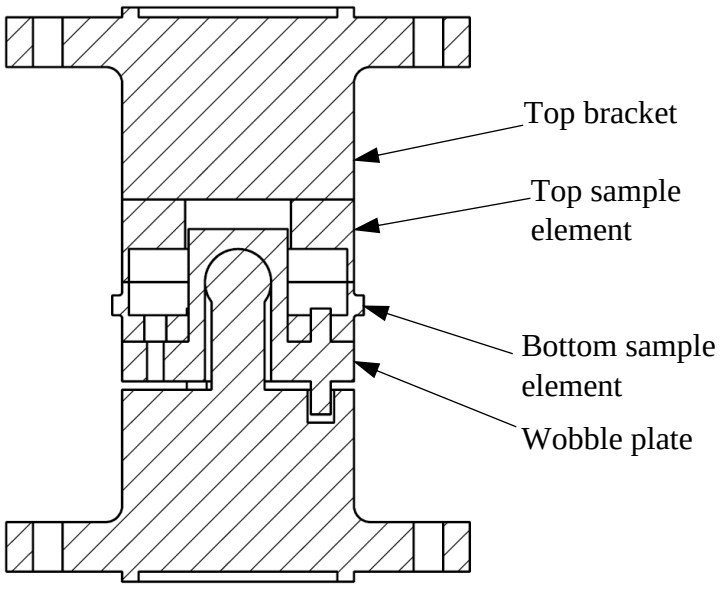

Figure 22: Cross-section through the first wear rig.

The torque is transmitted from the bottom mounting bracket to the wobble plate by a set of three steel pins, riding in oblong holes.

Figure 23: First wear rig: wobble plate, pins and disk spring visible

Figure 24: Wear sample mounted on the first wear rig

During the use of the rig, it was discovered that the normal force oscillates (on occasions quite violently) during the progress of the experiment. These oscillations were found to decrease, if the pins were greased and a set of disk springs inserted between the wobble plate and the bottom bracket (Figure 23).

The wear rig is operated by the Zwick-Roell Z100 loading frame, which applies compression and torsion as demanded by the test sequence. The loading frame enables compressive loads of up to 100 kN and torques of up to 1000 Nm to be applied. Normal force is applied by means of a pair of electrically-driven leadscrews. The load frame also measures the applied compressive force, the applied torque, angular and axial position of the sample to give data required to produce wear loops or calculate the steady state wear rate. Values are recorded to six places. Under uniaxial compression, the accuracy of normal force measurement was ±15 N or less.

3.2.2 New sample design and wear measurements

As discussed in section 2.2.1, there exist several different metrics for assessing wear which in turn can be measured in different ways. The most common options are measuring the mass loss through weighing the wear samples on precision scales and calculating the volume displacement through comparing the pre- and post-wear surface profile. The properties of these two approaches are summarized in Table 1. Many different variations for measuring profiles are reported in the literature (28; 31; 32; 34) ranging from technologically simple such as tactile profilometry to highly advanced like ex-situ X-ray CT tomography.

Operation	Weighing of wear samples	Profilometry
Preparation of sample (brushing, washing…)	Comparable	
Measuring procedure	Simple	Intermediate to complex
Measuring time	Very short (s to min)	Intermediate to very long (min to h)
Data processing time	Instantaneous	Intermediate to long
Data processing complexity	Very low	Intermediate
Issues	Mass loss is small compared to sample mass → possible resolution issues	Potentially labour and time intensive. Volume displacement does not always match the mass loss.
Additional information gained	None	Substantial (line surface profiles, pre- and post-wear roughness)

Table 1: Comparison of weighing and profilometry as a wear measuring tool.

In this study, profilometry was initially chosen to measure wear, since it was assumed that the mass losses from wear were too small compared to the mass of the sample (approx. 250 g for the bottom and 320 g for the top sample element) to be measurable by weighing. This was proven incorrect, but the resolution of the weight scales available was only 0.01 g at such high masses. For profilometry, the Alicona InfiniteFocus optical profilometer (Alicona, Austria) was chosen as it is highly adaptable to different surface contours and the measurement of 3D profiles over large areas. To provide a fixed reference surface for volume displacement calculations, a shoulder was added to the bottom wear sample (Figure 25). The surface of the shoulder is not affected by wear and thus forms a reference plane; the volume between the contacting surface and the reference plane can be calculated from the 3D profile data, giving the volume change caused by wear. Both the top and bottom sample have an annulus 10 mm tall and originally 2 mm wide. The sample elements were positioned using 3 6 mm H7 locating pin holes and fixed using M6 bolts.

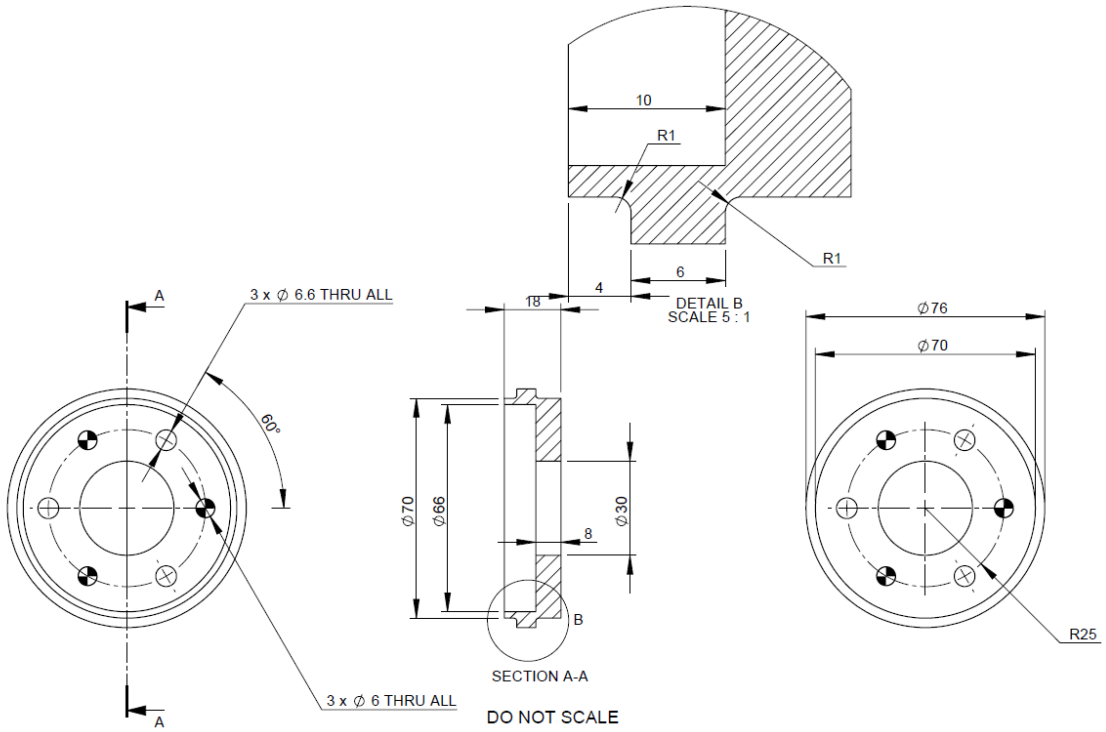

Figure 25: Drawing of the improved bottom sample element.

The preliminary work was performed using samples with a 2 mm wide annulus, which were made from EN1A steel. For experiments with different annulus widths (results published in (1)), two more sample geometries were designed, both having an internal diameter of 66 mm and external diameters of 68 and 74 mm, giving a 1 mm and 4 mm wide annulus respectively.

3.2.2.1 Wear measurements through profilometry

Unlike a cylinder-on-flat or a ball-on-flat contact wear geometry, where the wear scar is relatively small and can be easily examined in its entirety, the surface of the annular contact is very large, making profilometric assessment of the entire contact surface a challenge. As result it was decided to limit profilometry to a relatively small section of the surface and extrapolate the results. This required a method of positioning the sample on the profilometer with great repeatability, to ensure that the same surface was examined before and after wear. For this purpose, an octagonal mounting jig was made, enabling the bottom sample element to be accurately positioned with regard to the Alicona (Figure 26), by sliding the jig against a pair of brass rails on the sample table, which formed a 90° angle. The mounting jig thus had to have two orthogonal sides to mate with the rails, which in turn limited the possible number of scans to multiples of 4, with 8 scans per sample being chosen as the best compromise between the quantity of data and the speed of data acquisition. Before and after wear, the bottom sample element was thus scanned in eight places, obtaining 8 3D profile patches.

Each patch was divided into a reference surface and wear surface part (Figure 27). The profile data from reference surface is used to create an idealized reference plane. The change in volume between the wear surface and reference plane is the volume of material displaced by wear. The 8 values obtained are averaged and then extrapolated to the entire sample to obtain the wear volume. Depending on the settings, the scanning of each patch took between 20 to 60 minutes.

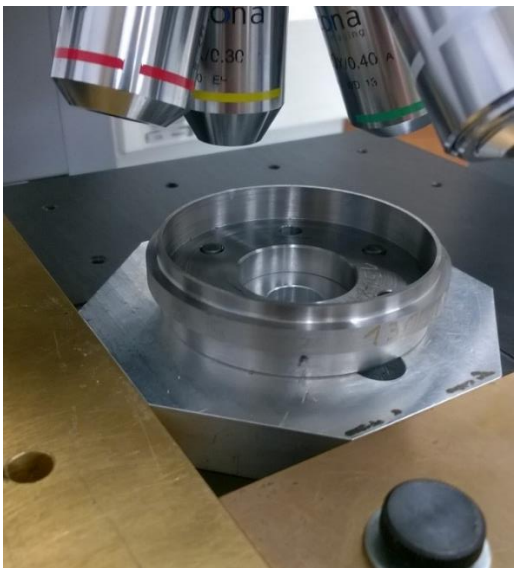

Figure 26: Sample being scanned.

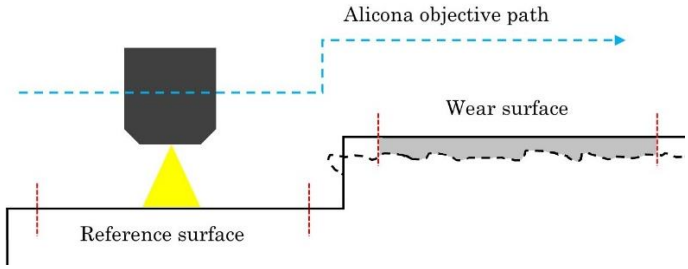

Figure 27: Diagram of a patch being scanned. The Alicona objective moves radially (blue dashed line) scanning the reference surface and the wear surface (solid line for pre-wear shape, dashed black for post wear shape). From the scan, two regions, marked with dashed red lines are isolated. The grey area represents the measured volume displaced. Some of it has been detached, the remainder forms burrs.

During the progress of experimental work, it was discovered that the mass loss caused by wear can be established through weighing with adequate accuracy (see the discussion in section 4.2.2.1). With this, it was also revealed that the mass of material corresponding to the volume change measured is often significantly larger than the mass loss measured. To test the possible cause of this, one of the samples was weighed and then carefully machined to remove any burring formed during the wear, before being weighed again. The difference in mass corresponded to the difference between the mass of the material displaced according to the Alicona and the mass lost in wear. This demonstrates that some of the material removed from its original position still remains attached to the sample, but elsewhere.

3.2.2.2 Surface profiles and roughness metrics

The Alicona optical profilometer can of course be used in a more traditional capacity to assess the worn surface texture. The Alicona software enables the user to extract surface profiles in any orientation relative to the 3D dataset collected.

The raw (unprocessed) surface profile is called "primary surface profile" or also "form" as it is the actual exterior shape of the object studied. Its shape is the combination of two factors, commonly named waviness (deviations of surface from ideal form that have a relatively long

wavelength) and roughness (deviations with shorter wavelength). Depending on which factor is of interest, the primary profile is filtered to remove the unwanted components. For this purpose, a Gaussian filter and a specific cut-off length are used, with waviness having larger and roughness smaller wavelengths than the cut-off. Alicona software will automatically set the cut-off length to the value recommended by ISO 4288 standard, depending on the length of the profile being studied (150). In this study the cut-off length was 80 μm for profiles measuring up to 1.25 mm in length (as found in 1 mm wide annuli discussed in sections 4.2.2.1, 4.2.2.3, 5.4.3 and 250 μm for profiles measuring up to 4 mm in length (which are typical for the 2 and 4 mm wide annuli studied).

In machine practice, roughness is usually of greater interest, since it relates to surface finish, while waviness is typically small and tightly controlled. In tribology, matters are more complicated. While the rubbing components are usually machined to a good finish before wear, the worn surface might be heavily damaged. Examination of worn surfaces on samples worn for this thesis showed that primary profile deviations were of the same order of magnitude than the largest debris particles. It therefore seemed appropriate to focus on examination of the primary (unfiltered) profiles.

To assess how flat (or non-flat) a surface profile is, a number of standard profile metrics exist. While the equation used for an individual metric is the same, the meaning of the metric changes depending on if and how the primary profile has been processed: use of the primary profile gives primary profile roughness metrics, the use of high pass filtered profile roughness metrics. Each profile is evaluated with respect to the mean line, which represents the perfectly smooth shape of the surface. Methods for calulcating the mean line are given in standard ISO 4287.

Three of the most common profile metrics are:

- Arithmetical mean deviation of the profile (denoted Ra) is calculated as the average mean of the absolute deviations of the profile from its mean line.
- Root mean square deviation of the profile (denoted Rq) is calculated as root mean square of the deviations from the profile and its mean line.
- Average height of the profile (denoted Rz) is calculated as the arithmetic mean of the absolute values of deviation from the mean line for the five highest and five lowest points of the profile.

In this thesis, the term 'roughness' is generally used to denote primary profile roughness, unless stated otherwise.

3.2.2.3 On-line measurement of wear

Profilometry can only reveal the total amount of wear (as volume displaced), after the completion of wear. However, wear can also be monitored in real time, by observing the relative position of the wear sample elements. This is of particular importance for establishing the wear rate and its change(s) during the experiment. Post-mortem observations can only give the average wear rate. This is insufficient, since the wear model this work focuses on, predicted a specific development of the wear rate, which needed to be confirmed or infirmed thorugh experiments. In this work, the vertical position of the sample elements was monitored using the sensors on the loading frame; enabling plots of vertical position against time (typical example in Figure 28) to be produced. Since the worn surfaces are rough, the vertical position oscillates as the loading frame is adjusting the position of the element to ensure constant normal force. In most cases, the lowest points are reached at the end of the wear stroke, making the frequency of the oscillation equal to the frequency of the reciprocating motion. A low pass filter was applied to remove this oscillation (see the breakout in Figure 28). Full normal load is applied at the start of the experiment, and the wear motion starts in point A. Wear reaches steady-state in point B and the experiment ends with point C. The difference in vertical position between points A and C multiplied with the nominal contact area (which in an annular contact does not change with wear) gives the amount of material detached from the first bodies during the course of wear. From the same data set, the steady-state wear rate can be determined, by fitting a linear trend line to the 'filtered position' dataset between points B and C. The slope of the trend line represents the rate at which the sample is thinning; multiplying with the nominal contact area gives the steady-state wear rate.

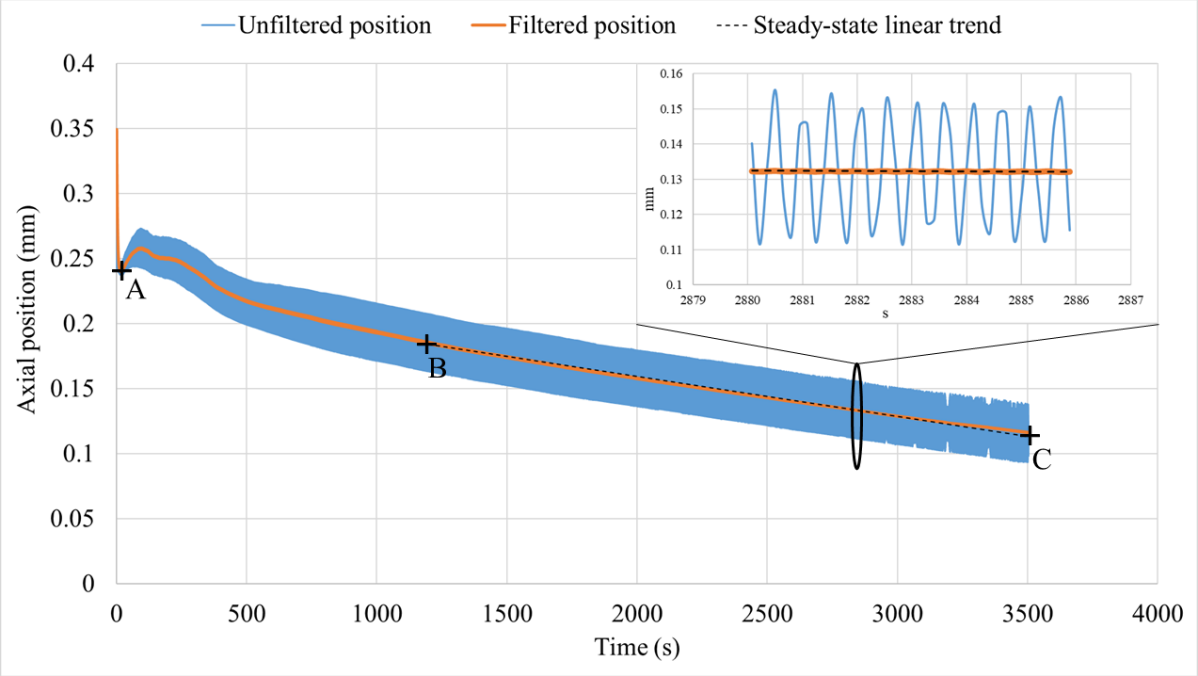

Figure 28: Axial position of the bottom sample as a function of time. The breakout view shows 11 stead-state wear cycles in greater detail.

3.2.3 Tubular sample and sample holder

As the work with the first rig continued, several issues became apparent. Namely, the use of the Alicona was extremely time-consuming (6-8 h of scanning per sample, with 1-2 h of data processing in Excel), the rig had significant backlash on account of clearances between the pins and the slots, while the samples used were complicated and therefore expensive and slow to produce. If any significant number of experiments was to be made, a simpler sample and a more time-efficient experimental approach was needed.

It was apparent that switching to measuring wear by weighing would give significant times savings. However, this creates conflicting requirements for sample design, since the sample would need to as light as possible (to maximise resolution of weighing) but also as large as possible (to minimize radial gradients). These diverging requriements were satisfied with by designing a tubular sample, measuring 80 mm in internal diameter, 84 mm in external diameter and 20 mm in height (Figure 29). Significant weight savings were made, with an aluminium tubular sample weighing only about 10% of the old steel samples. This shape can also be relatively easily machined out of commercially available bar/tube stock, expediting manufacture and reducing costs.

Figure 29: Tubular sample.

Having no mounting or fixing holes of any kind, the tubular sample requires a special sample holder, which is made of high strength steel. The sample fits around the central arbor with a H7/j6 fit (Figure 30), which ensures good repeatability in positioning of the sample.

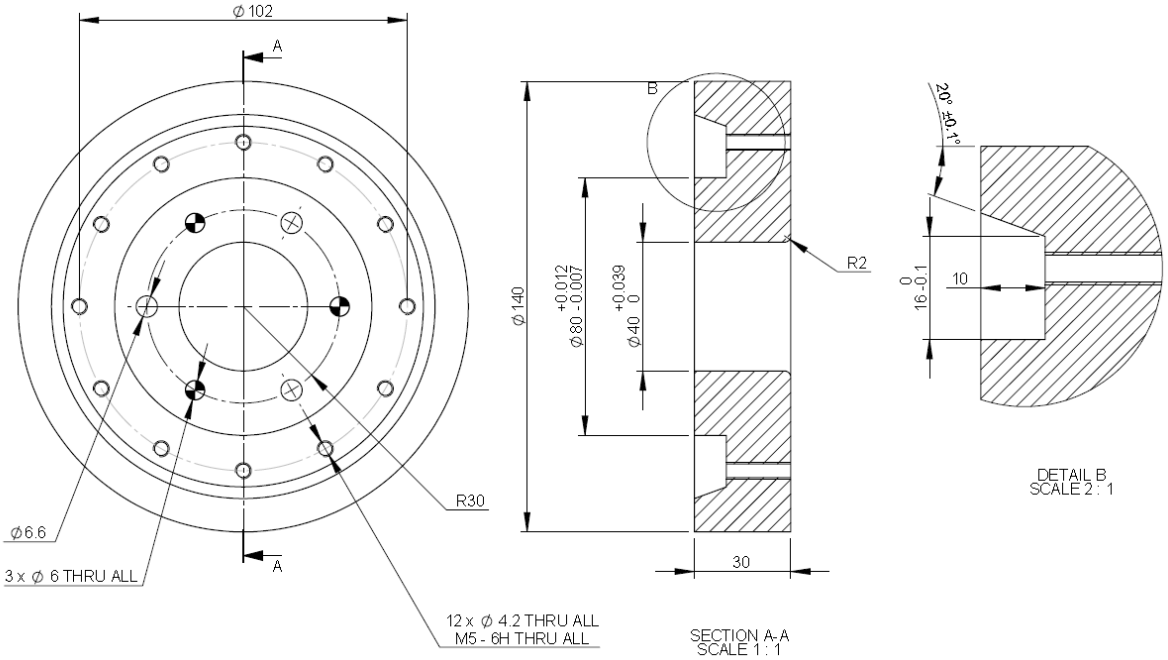

Figure 30: Tubular sample holder.

The sample is held in place using 6 chucking blocks (Figure 31-Figure 33). When installed, the blocks together act as a collet, exerting pressure onto the sample in the radial direction, preventing the sample from rotating around the arbor. Each block is shaped as a segment of a ring, with the outer edge tilted 20° from vertical. Each block is bolted down with a pair of M5

bolts, grade 12.9. As the outer side of the block is angled, the axial push of the bolts is translated into a radial push, pressing on the outer side of the sample.

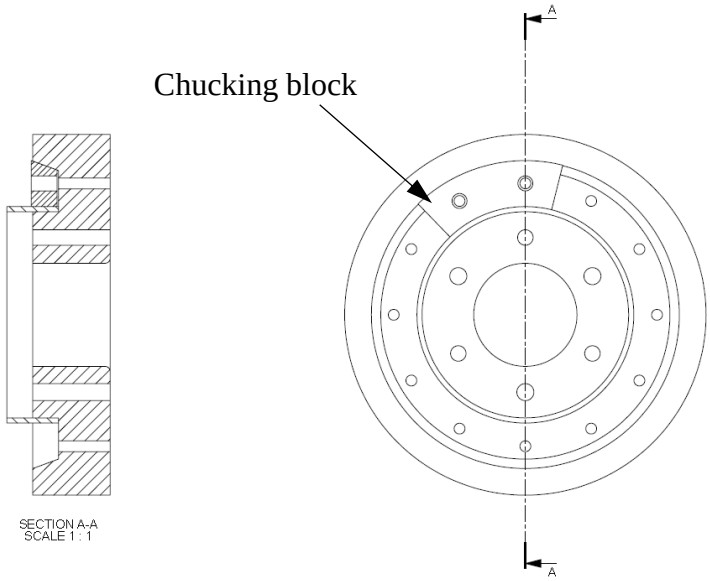

Figure 31: Sample element in the sample holder with the chucking block.

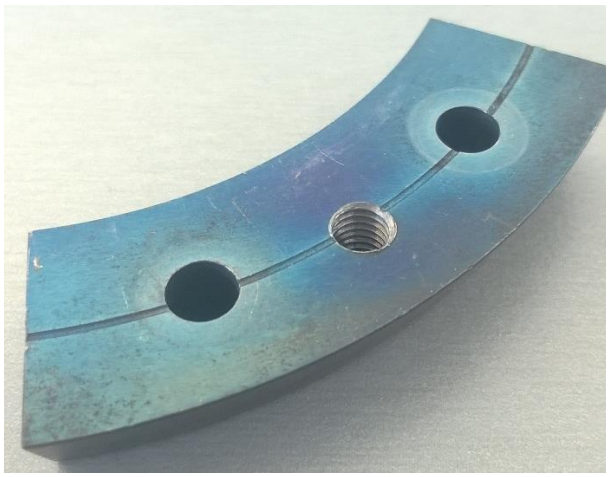

Figure 32: The threaded hole is used to facilitate the removal of the block after experiment.

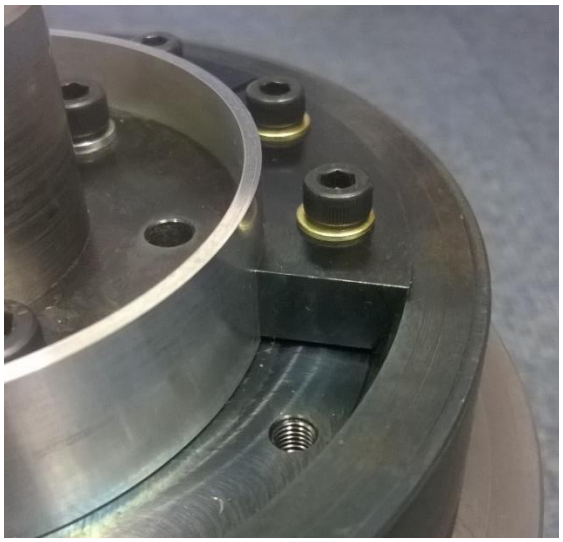

Figure 33: Sample mounted on the sample holder, showing the chucking block.

To protect the sample holder and chucks from corrosion, these pieces were blued, by heating them in an oven to 310°C. To further enhance the protection, the sample holders were then rubbed with linseed oil and left to cure for 2 weeks. When mounting the sample, the bolts holding the chucking blocks are tightened with a torque wrench to torque of 6 Nm.

According to (151) the force F_s exerted by each screw can be calculated as:

$$F_s = \frac{M_s}{\tan(\alpha+\varrho')\frac{d_2}{2}+\mu_P\frac{d_m}{2}} \quad (13)$$

The nominal values of relevant parameters are given in Table 2:

Tightening torque	M_s	**6000 Nmm**
Pitch diameter	d_2	4.480 mm
Helix angle	α	3.253°
Effective friction angle	ϱ'	10.5°
Bolt-washer friction coefficient	μ_P	0.1
Median bolt head diameter	d_m	6.75

Table 2: Nominal thread dimensions for the normal M5 metric thread according to ISO 724:1993.

The value of F_s is thus 6.8 kN. A special bolting sequence was developed for installation of chucks (Figure 34) to ensure repeatability. Firstly, a chucking block is placed into one out of the twelve possible positions around the circumference of the sample and tightened. A second block is placed opposite it and tightened. The third is then placed to either left or right of the first block and the fourth block opposite the third block.

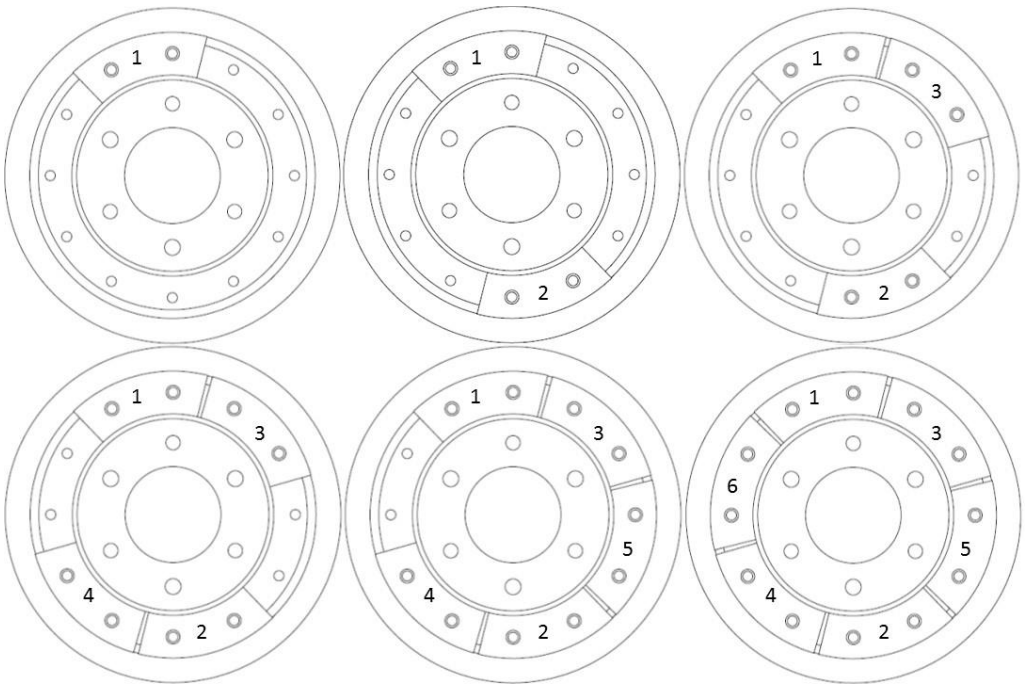

Figure 34: Bolting sequence of the chucks.

Using a straightforward balance of forces (Figure 35) and assuming that the coefficient of friction ν between the chucking block and the sample holder is 0.25, the value of radial force F_R can be calculated as 20.2 kN per chucking block.

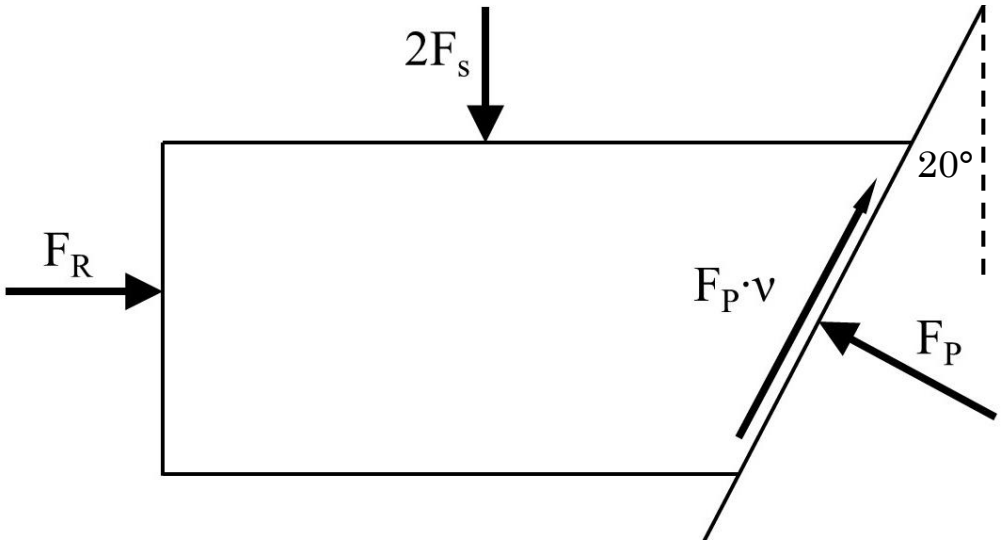

Figure 35: Forces acting on the chucking block.

3.2.4 Second wear rig

The new sample holder was designed in conjunction with the new wear rig. The primary objective of its design was to replace the pin-and-slot mechanism from the first rig with an alternative that did not suffer from significant backlash and would not slowly wear in service, as the pins were found to be doing. Reducing the backlash was of vital importance as backlash would interfere with plotting the wear loops thus making calcultions of effective displacement more complicated (see discussion in section 8.3). Since it was desirable to keep the wobbling action (to reduce/eliminate angular misalignment of the sample), a mechanism capable of transmitting torque (up to 1000 Nm) but maintaining a degree of angular compliance was needed. These features are satisfied by a bellows coupling. Coupling BK1-1500 made by R+W (152) was obtained and the wear rig designed around it. The dimensions were suitably increased, since the larger sample diameters called for the use of higher compressive forces. As before, a wobble plate-and-ball arrangement was used.

Initially, the new wear rig was intended to be used with an Instron 8854 loading frame located in Begbroke Science Park. It was hoped that this frame will provide a more precise control over the axial force and allow for a higher data sampling frequency and data storage memory. The loading frame is equipped with hydraulic collets designed to grip shafts up to 60 x Φ30 mm in size. The wear rig was thus designed in two parts: at the top a simple turned bracket (Figure 36) is used which fits into the Instron jaws, to which the top sample holder is bolted; at the bottom a central post is used to transmit the axial force, with the bellows coupling sitting around it and the wobble plate carrying the bottom sample holder. To ensure a close fit between the ball and the

socket on top of the post, the socket was manually polished using a spare ball and valve lapping compound. The cross-section of the new rig is shown in Figure 37.

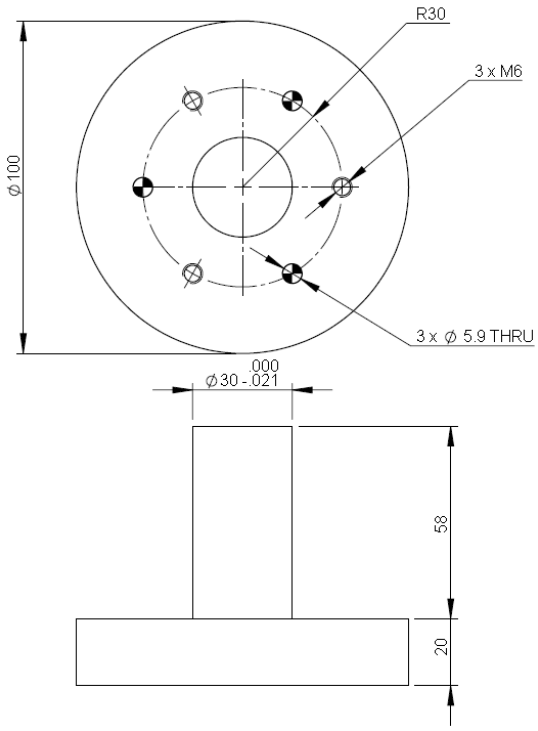

Figure 36: Bracket for the top sample holder - Instron loading frame compatible.

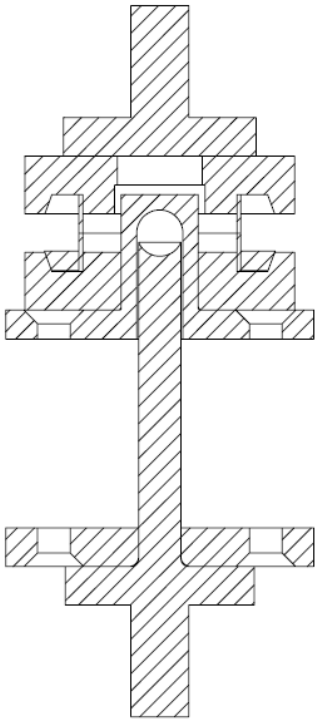

Figure 37: Cross-section of the new sample rig - Instron loading frame compatible.

Three elements of the design require special examination with respect to stresses occurring in service.

The central post is expected to carry a large axial force, but being relatively slender, possible buckling needs to be considered. The post has a cross-section A=314,16 mm^2, second moment of area I=7854 mm^4 and least radius of gyration i=5mm. The slenderness λ is therefore:

$$\lambda=\frac{2\cdot 154 mm}{\sqrt{\frac{7854\ mm^4}{314.16\ mm^2}}}=61.6 \qquad 14$$

According to (151) for λ<105 the following critical stress (σ_B) equation is to be used:

$$\sigma_B=335-0.62\lambda=297\ MPa \qquad 15$$

Using a safety factor of 2 (this is not a safety critical part), the maximum permissible compressive force is 46.6 kN which is above the maximum compressive forces used in this work (maximum force tried was 30 kN, largest used in experiments was 22 kN).

Secondly, the wobble plate experiences tensional stress as the sample holder is pushed downwards, while the socket presses against the ball. This tensional load is carried by an annulus having an internal diameter of 24 mm and external diameter of 40 mm, giving a total cross-section of 804.2 mm^2. Assuming the maximum permissible stress of 200 MPa (the material's yield point being approx. 550 MPa) the maximum permissible compressive load from the wobble plate perspective is therefore 161 kN.

Lastly, the contact pressure between the ball and the socket in the post is considered. Assuming sinusoid repartition of pressure, the maximum contact pressure caused by applying an axial compressive force of 45kN can be calculated as being 182 MPa. As this is less than 50% of the yield strength and since the rig is not operated at normal forces beyond 30 kN the contact pressure is deemed to be sufficiently low.

The assembled bottom half of the rig is presented in Figure 38.

Figure 38: The new wear rig prepared for testing with the Instron loading frame.

3.2.5 Use with Instron compression-torsion loading frame

While the Instron loading frame is superior to the Zwick-Roell with regard to the ease of programming the test sequence, sampling frequency and available memory, two significant issues were observed in actual testing:

- A crescent area of unworn surface was observed on each sample element, measuring approx. 0.2 mm at the widest point. This indicated an axial misalignment of the loading frame, which the wear rig was not designed to accommodate.

- During the wear tests, the Instron grips were seen swaying side-to-side, imposing not only rotational but also transversal movement to the sample, which is highly undesirable.

Initially it was assumed that these problems are linked, the axial misalignment causing an uneven distribution of pressure, which in turn leads to the torque needed to overcome the frictional force appear eccentrically, relative to the axis of the rotating grip. The axial misalignment was removed by the Instron staff. However, the swaying of grips was still observed during repeated tests. This raised concerns over possible fatigue damage to the loading frame with prolonged use and further experiments were halted until a solution could be found. However, soon after the loading frame was put out of commission in an unrelated incident. In order to avoid serious delays to the project, it was decided to revert back to the use of the Zwick-Roell loading frame.

3.2.6 Use with Zwick-Roell compression torsion machine

In order to mount the new wear rig onto the Zwick-Roell loading frame, the stubs designed to fit into the Instron hydraulic grips (see Figure 36) were shortened to 55mm in length and had a M30x2mm fine thread cut into them. This thread was chosen because it is compatible with the diameter of the parts, while having particularly high thread friction on account of very small pitch. The mounting brackets from the first rig were repurposed, machining M30x2mm threaded holes into their centres (Figure 39).

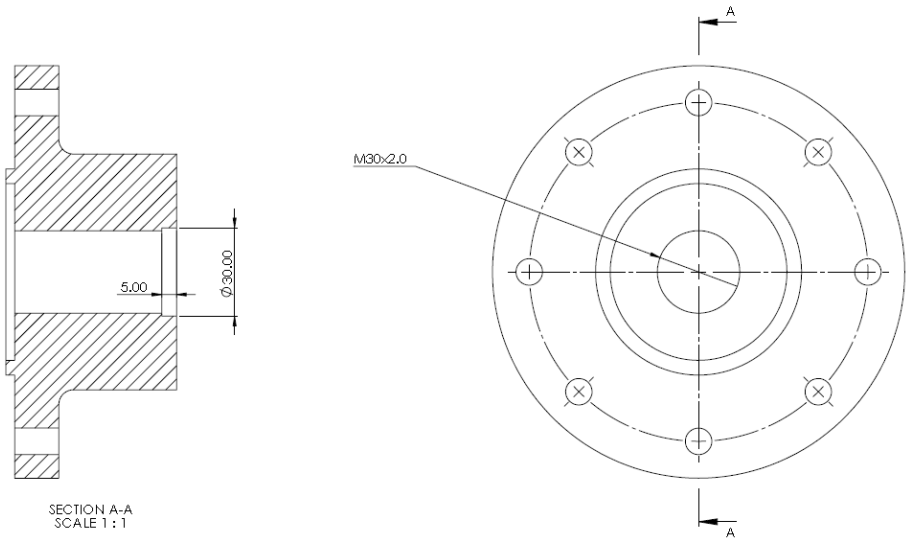

Figure 39: Mounting bracket modified with a central threaded hole. Note that only the hole dimensions are stated, as this is an extant part, not being made from scratch.

This enabled the new wear rig to be made compatible with the Zwick-Roell frame. When torque is applied clockwise to this assembly, the screw mount tightens and when counter clockwise, the loosening is resisted by a normal force of several kN (while having a thread profile with very high friction and therefore resistance to unscrewing under load).

To further fix the components in place, Loctite 638 threadlocking compound was employed; with parts cured at 50°C for 24 hours after application. According to the manufacturer, this compound obtains a compressive shear strength of 29 MPa, increasing to approx. 35 MPa with the above curing regime (153). Taking into account the surface area of the threaded joint and assuming the shear strength of the compound as 29 MP, the break-free torque of the entire joint is 2200 Nm, which is well in excess of what the loading frame can generate. This assembly, while perhaps not conventional, has stood up to over a year of extensive use without issue.

Figure 40: New wear rig on the Zwick-Roell loading frame.

3.2.7 Alignment bearing addition

In order to ensure adequate rig alignment at all times an alignment bearing was incorporated into the design to insure coaxiality of the top and bottom sample element. An alignment needle bearing RPNA 30/47 was chosen as it offers the smallest profile while enabling angular misalignment to be accommodated, requiring the least material to be removed from the parts. A

socket was machined into the top sample holder and the bearing inserted with an interference fit (Figure 41). The top of the wobble plate was shaved down, to become the shaft of the bearing.

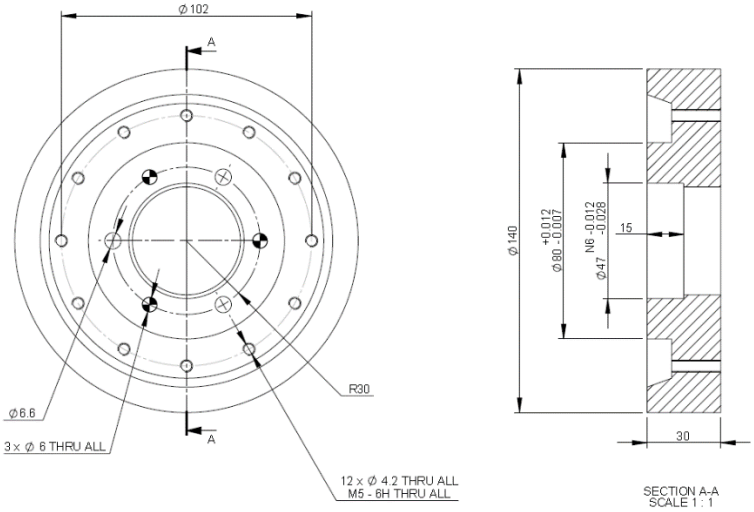

Figure 41: The top sample holder with bearing socket.

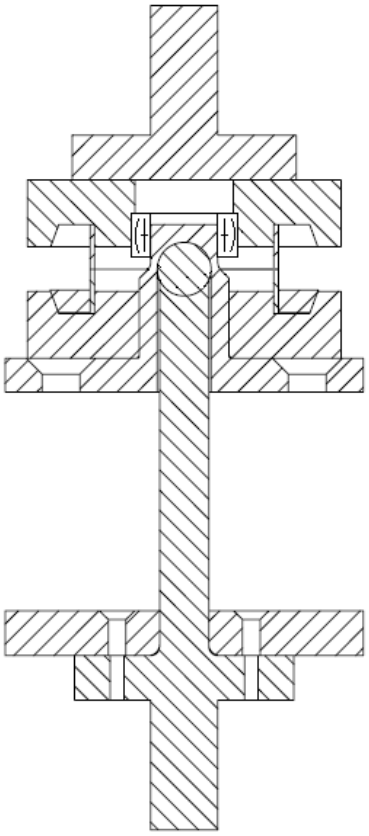

Figure 42: Cross-section of the wear rig with the alignment bearing. Mounting brackets and bellows coupling not shown.

3.2.8 Debris entrapment rings

To study the effects of debris entrapment on wear, debris need to be entrapped somehow, to a degree beyond the entrapment capacity of the contact itself. Fillot, Iordanoff & Berthier (15) have successfully used flat-on-flat contact surrounded by tall metallic walls. It would be impractical to use metal entrapment elements in this study, since tight-fitting elements would wear against the sample, disturbing the mass loss measurements, while any clearance (which would be necessary to both prevent wear and enable the disassembly of the worn contact after experiment) would enable the egress of the wear debris. These issues were not significant in (15) due to the unique combination of materials and geometry used by the authors. In this study, the perfect material for entrapment elements would be one that would cause minimum wear to the aluminium sample, while being sufficiently elastic to be easily installed and removed. A decision to use plastic rings was thus made. The wearing contact is encased into a pair of tight-fitting rings, surrounding the contact on both sides (Figure 43-Figure 44).

Figure 43: Debris entrapment rings in position, showing the worn surface buried between them.

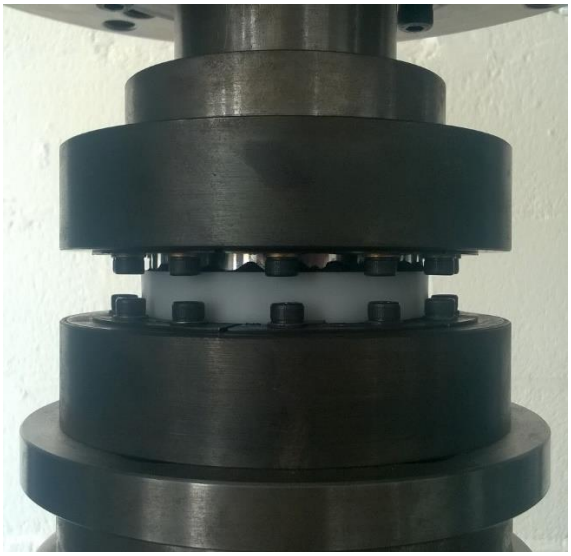

Figure 44: Debris entrapment rings in position.

For measuring the debris bed thickness, a special measuring method was developed. After the completion of the main wear experiment, the wear elements were separated, cleaned by brushing and vacuuming the wear debris, before being loaded back to the full normal force used in the experiment. The vertical position of the bottom sample element was monitored with the difference between the vertical positions at the end of wear and after cleaning corresponds with the wear debris bed thickness. In essence, the loading frame itself is used as a measuring calliper.

To test the repeatability of this approach, a separate experiment was carried out: a worn sample was installed and loaded 10 times with identical normal force, with the sample elements being separated to a distance of 150 mm for 5 minutes after each loading cycle to represent the cleaning process to observe the variation in the vertical position caused by gross movement of the loading frame. This was performed at normal forces of 2, 5, 10, 15 and 20 kN. The standard errors of the vertical position measured in each experimental run were 0.398 μm, 0.323 μm, 0.973 μm, 0.304 μm and 0.177 μm respectively. Since the debris beds studied are about two orders of magnitude thicker, this is considered acceptable repeatability.

3.2.9 Use of segmented samples

As the wear modelling work required tests on an open contact geometry, a way for obtaining such a geometry with the existing wear rig was needed (since rigs specifically designed for using open contacts were not easily available). By machining a number of slots into the annular sample element, and wearing such an element against a full annulus, the sample is effectively divided into a number of independent flat-on-flat open contacts. While such arrangements were used before (86; 85) they were viewed by their creators as 'enhanced' or 'modified' annular assemblies; it apparently went unnoticed that wearing such an assembly is essentially running a number of open-contact wear experiments *in parallel* on the same wear machine! As it may be imagined, running one experiment and obtaining results which are equivalent to the aggregate results of 10 or even 20 separate experimental runs represent a significant economy of time and resources, doubly so, since the equipment used can also use full annular samples. In this work, segmented samples were used to enable the study of wear in open contacts, using the new wear rig described in sections 3.2.6-3.2.7 without the need for additional wear machines.

Originally, 5 mm deep cuts were made in the sample, the exact shape and placement were varied depending on the objective of the experiment. Figure 45 shows a sample element with rotationally symmetric relief cuts measuring 5 mm deep and 5 mm wide, dividing the sample into 16 contact areas. Such samples were used in tests where the imposed displacement of movement was varied.

For tests where the sample geometry was varied, the contact surface was divided into 6, 12, 24 or 48 equally-sized segments, with every second one milled away, again, originally to the depth of 5 mm. This gave elements with either 3, 6, 12 or 24 contacts of different sizes (Figure 46).

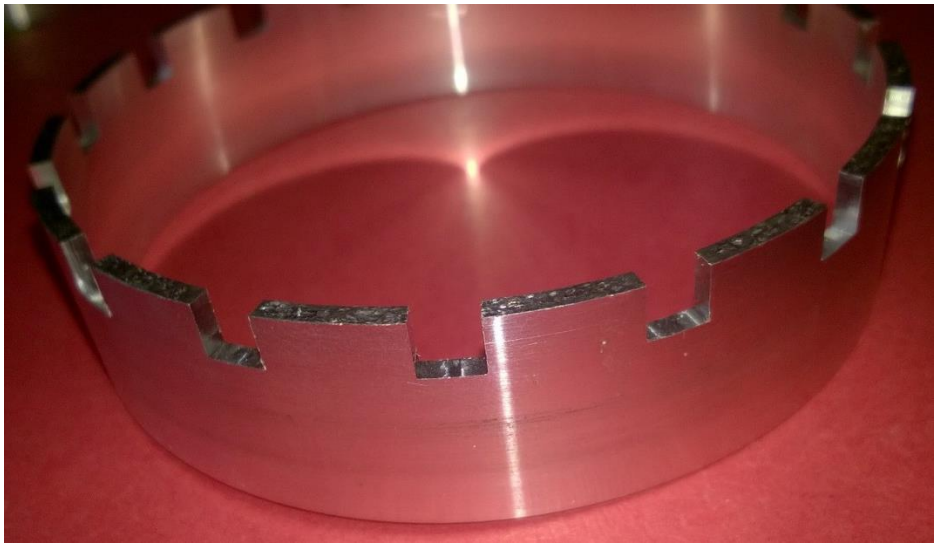

Figure 45: Segmented sample element after wear.

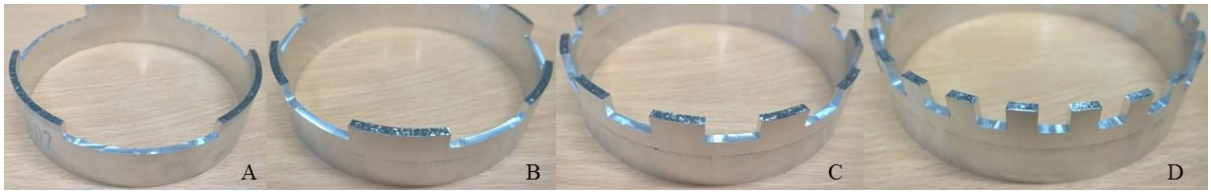

Figure 46: Segmented sample elements showing different geometries used: Element with 3 contacts (A), six contacts (B), 12 contacts (C) and 24 contacts (D).

In practice, samples from Figure 46 have shown a serious weakness, namely that the 'teeth' of the sample bend during wear, reducing effective displacement during wear. This issue increases with the number of contacts, since the contacts are narrower and thus less stiff. A new set of samples was made with segments given a 'ziggurat' shape to make them stiffer (Figure 47). This shape was chosen as a compromise between the necessity to 'buttress' the contact patch from the side and the relative difficulty of machining a sloped, rathern than a stepped side to each 'tooth'. The contact patches have the same shape as before.

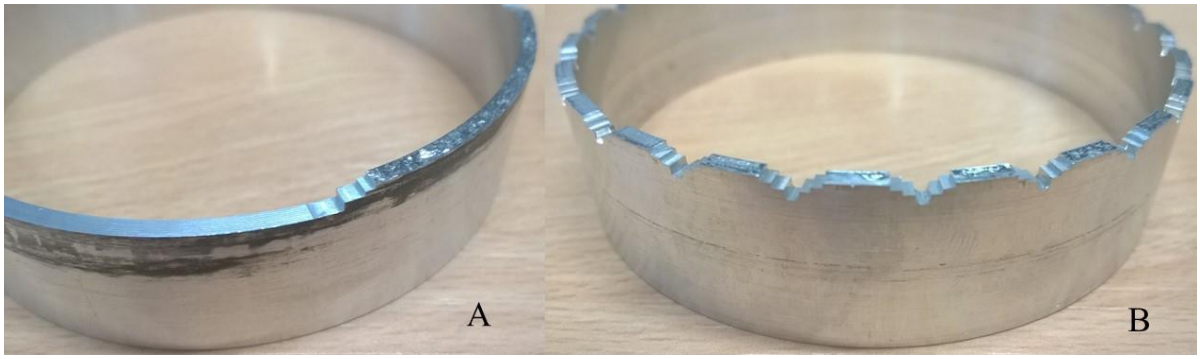

Figure 47: Segmented samples with the revised segment shape. Detail of the sample with 3 contact patches (A), sample element with 24 contacts (B).

3.3 Pilot X-ray work

Taking inspiration from a seminar which presented the use of X-ray computed tomography for observing the growth of stress-corrosion cracks in-situ, the idea of using a similar approach for imaging wear processes had been formed. Despite extensive survey of the literature, no prior studies of this precise nature were found and the ability to observe the worn contact without disturbing the wear process seemed to be of great importance, not only for this project, but to the general field of tribology. A decision was made to produce a proof-of-concept study of application of X-ray methods to wear. Two pilot experiments, one using X-ray CT imaging and one using X-ray diffraction were carried out.

X-ray CT imaging was carried out at Oxford, while a short diffraction experiment was successfully proposed to Diamond Light Source

3.3.1 Pilot tomography sample assembly

Pilot tomography work was conducted using the Zeiss XRadia Versa X-ray microscope. As this is a laboratory machine, the intensity of X-rays generated is relatively low (the peak brightness of bremsstrahlung-based X-ray tubes can be up to 9-10 orders of magnitude less than what is achievable at a synchrotron facility (154)), dictating a number of experimental parameters. The volume containing the contact had to be small to give practical imaging times and the weight of the sample was limited to 20 mm. An annular contact of external diameter of 4 mm and internal diameter 2 mm was used (Figure 48, Figure 50A), to satisfy not only the geometrical constraints, but also because the axisymmetric annular geometry lends itself to simple image processing. In addition, annular geometry has unique properties compared to more common incomplete contacts (86; 109; 25; 58) and has been the subject of increased interest in the tribological community. To minimize imaging time further, the samples would need to be made of low-density material to reduce X-ray attenuation. As discussed in section 2.4.1, the emphasis of the work was on the process of wear as such, rather than study of a particular engineering material. Consequently, a common aluminium alloy (6082T6) was chosen as sample material, as it is available and does not present significant challenges with regard to machining or handling, while satisfying the requirement for low density. Each sample element was cylindrical, with the wear annulus located on one of the bases and an M6 threaded hole made into the opposite base.

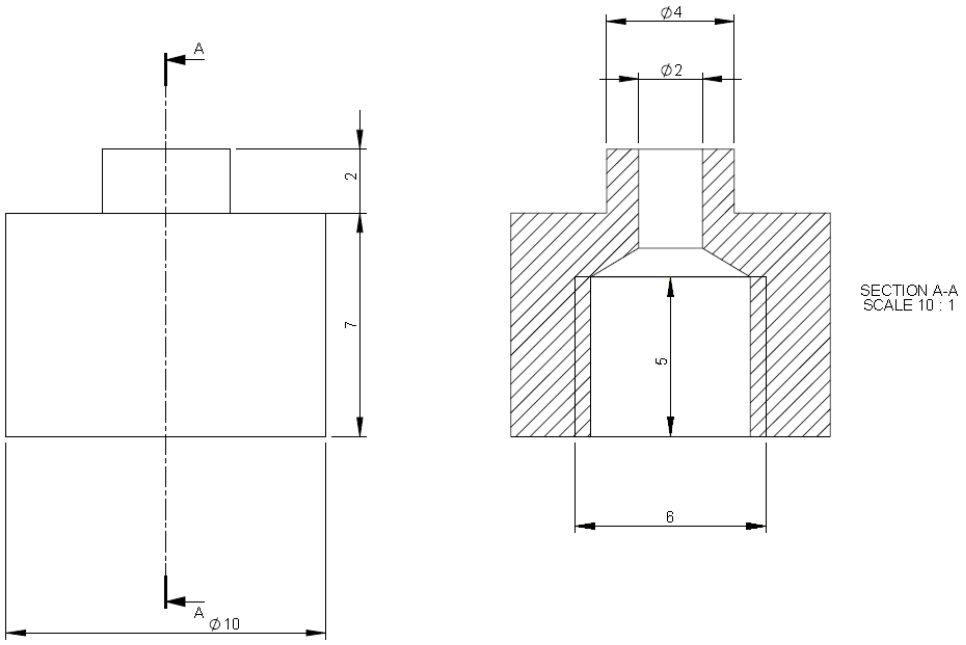

Figure 48: Design of the sample elements used in pilot tomography experiments.

Building an Xradia-compatible wear rig would be a highly complex endeavour; for an initial proof-of-concept study the wear condition was preserved by clamping the wear sample after imaging, so that wear could be examined undisturbed, despite the wear and imaging processes being carried out separately. To minimise the effects of the clamp on imaging a polycarbonate clamping tube was devised. The inside of the tube was reamed to ensure a close fit with the cylindrical part of the sample element. The tube was given 8 incisions on each side to increase flexibility.

Each sample element was screwed to a sample holder, which was a hollow steel tube with an external diameter of 10 mm using a grub screw. When the sample elements are pressed into contact with the annular wear surface and one is rotated counterclockwise relative to the other, both elements tighten against the sample holder, inhibiting further rotational movement. The clamping tube slides over the sample elements (Figure 49, Figure 50B) with a pair of small jubilee clips then used to compress it around the sample elements (Figure 50C).

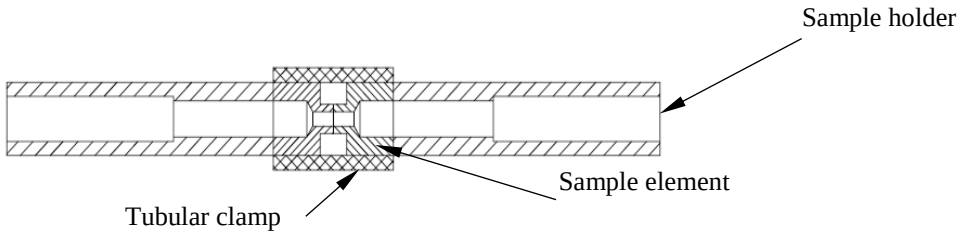

Figure 49: The pilot wear assembly. Grub screws not shown.

After the completion of the experiment, the sample elements were first clamped together, before the assembly was removed from the sample holders by unscrewing the grub screws through the holes in the sample holders. This design enables the clamped sample assembly to be removed without any force being transmitted through the sample post wear. This is important to prevent the worn contact being upset while the sample is being removed from the sample holder.

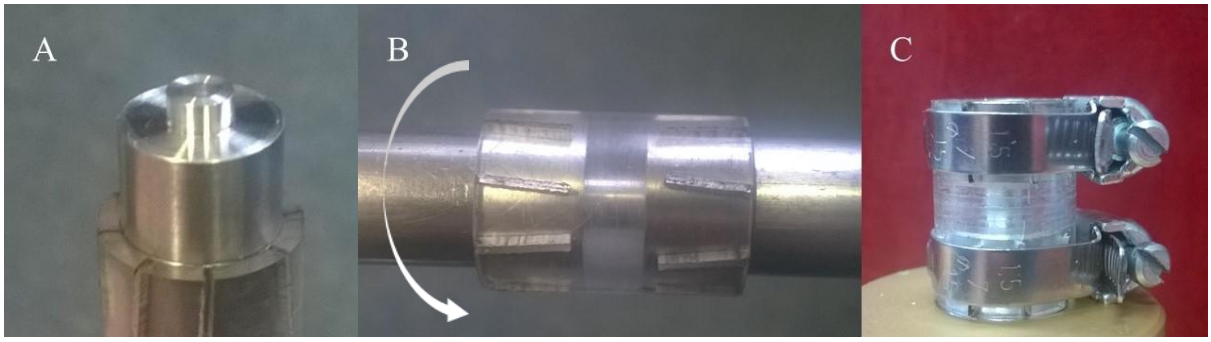

Figure 50: The wear sample. (A) Unworn sample element showing the annular contact surface (B) Sample elements mounted in contact, with the clamp in position, but without clips. The direction of rotation is shown. (C) The fully clamped sample after wear and tomography.

3.3.2 Pilot tomography wear procedure

In order to wear the sample, a rotational motion was applied to one of the sample elements, whilst the other was held still. In addition, the sample elements were pushed against each other using approximately constant axial force. This combination is possible through the use of an ordinary lathe, with one of the sample holders being held in the chuck and the other in the tailstock. To apply a constant normal force, a weight was hung from the handle of the tailstock wheel (Figure 51).

Figure 51: The weigh on the tailstock wheel.

The axial force of the tailstock spindle (assuming the handle being in the 3 o'clock position) is given by:

$$F_A = \frac{mgr2\pi\sigma}{L} \quad (16)$$

Where m is mass of the weight, g the gravitational acceleration, r the radius of the tailstock wheel, σ efficiency of the spindle and L the pitch of the spindle screw (in mm per turn). For the lathe used r was 5 cm, L was 4 mm/turn. σ values for lead screws are typically around 0.1. Two weights were used, weighing 568 and 1645 grams respectively. Given the imprecisions in measurement of r and uncertainty as to the value of σ, the calculated values of F_A were rounded to 45 and 130 N respectively. Using a lathe as a wear machine is a rather crude approach, but has proven itself to be quite sufficient for the purposes of a pilot study.

The experiments were conducted according to the following experimental sequence:

- The lathe speed is set to 40 rpm (the lowest available on this particular model).
- The sample elements are attached to respective sample holders and manually tightened.
- The sample holders are clamped into the chuck and the tailstock respectively.
- The clamping tube is slid over one of the samples, followed by both jubilee clips.
- The tailstock is gently moved forward, until the sample elements touch. The handle is then slowly rotated to the 3 o'clock position and the tailstock locked in place.
- The weight is slid onto the tailstock wheel handle.
- Lathe is started and allowed to run for a set period of time.
- The clamping tube is slid over both sample elements and the clips tightened with a screwdriver.
- The tailstock sample holder is unclamped, releasing the axial force from the assembly.
- The entire assembly is removed from the chuck.
- One of the sample holders is clamped in a vice and the grub screw is removed. No torque is transmitted through the worn contact, since the grub screw is located within the clamped holder. This is repeated with the other holder, leaving behind the clamped sample, shown in Figure 50C

During the wear and fitting of the clamping tube, the aluminium elements are compressed with the axial force F_A. As the axial force is released, the elements expand, putting the plastic tube in tension, until equilibrium is reached. From the dimensions and elastic moduli of the sample element and clamping tube materials, the stiffness of the components can be calculated. From this it may be established that approximately 20% of the initial F_A, is retained after clamping.

3.3.3 Pilot X-ray diffraction experiment

X-rays can be applied to more than just imaging; X-ray diffraction is a well-established technique for studying crystal structure of metals, making the pairing of X-ray CT imaging and diffraction for in-situ investigations of wear a logical and potentially powerful investigative approach. However, it was not clear what information X-ray diffraction could gather, if applied in such a manner. A research proposal for an ex-situ diffraction experiment was successfully submitted to Diamond Light Source, with the intention of applying X-ray diffraction to a geometry similar to an in-situ wear experiment to study the practicality of such an approach. Some of the steel samples used in either preliminary research work or the study of contact width (section 4.2) were sectioned, to make diffraction samples. To approximate the actual wear set-up, each diffraction sample consisted of a pair of annular sections, stacked with the worn surfaces touching, thus creating an assembly geometrically identical to the one used during wear.

The diffraction samples (as well as the reference samples, 4 references using CeO2, 4 using Si) were retained the sample holder to ensure repeatable positioning. The reference samples are supported in brass discs measuring Φ20x2mm with a Φ5mm central hole. The hole is filled with a mixture of reference material and glue. The reference samples are fixed in place using adhesive tape; since the density and thickness of the reference material are large compared to the plastic foil of the tape, the majority of diffraction occurs within the volume of the reference sample.

The sample holder mounted on the beam table is shown in Figure 52. A pair of legs was attached to the sample holder using shoulder screws. Each leg had a pair of countersunk M6 bolt holes for attaching the assembly to the sample table. In combination, the self-centering nature of countersunk screws and the tight tolerances of the shoulder screws gave a highly repeatable positioning to the holder. However, the geometrical imperfections of the samples (such as burring at the worn edges) were found to influence the position of the sample *within* the holder, tilting the sample from vertical.

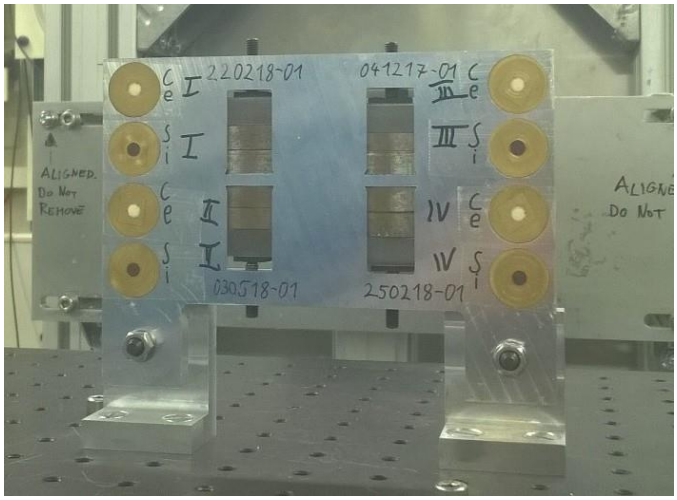

Figure 52: Sample holder as seen from the detector side. Note the brass discs containing the reference samples and the four diffraction samples.

The sample holder needs to be of appropriate dimensions so that all sample positions fit within the range of movement of the sample table (155). Preferably the diffraction region in each sample should be at the same distance from the detector. To achieve this, a plate-shaped holder was designed (Figure 53), with the samples resting in windows so shaped that the 'nose' of the sample was flush with the front face of the holder plate, as are the faces of the reference samples.

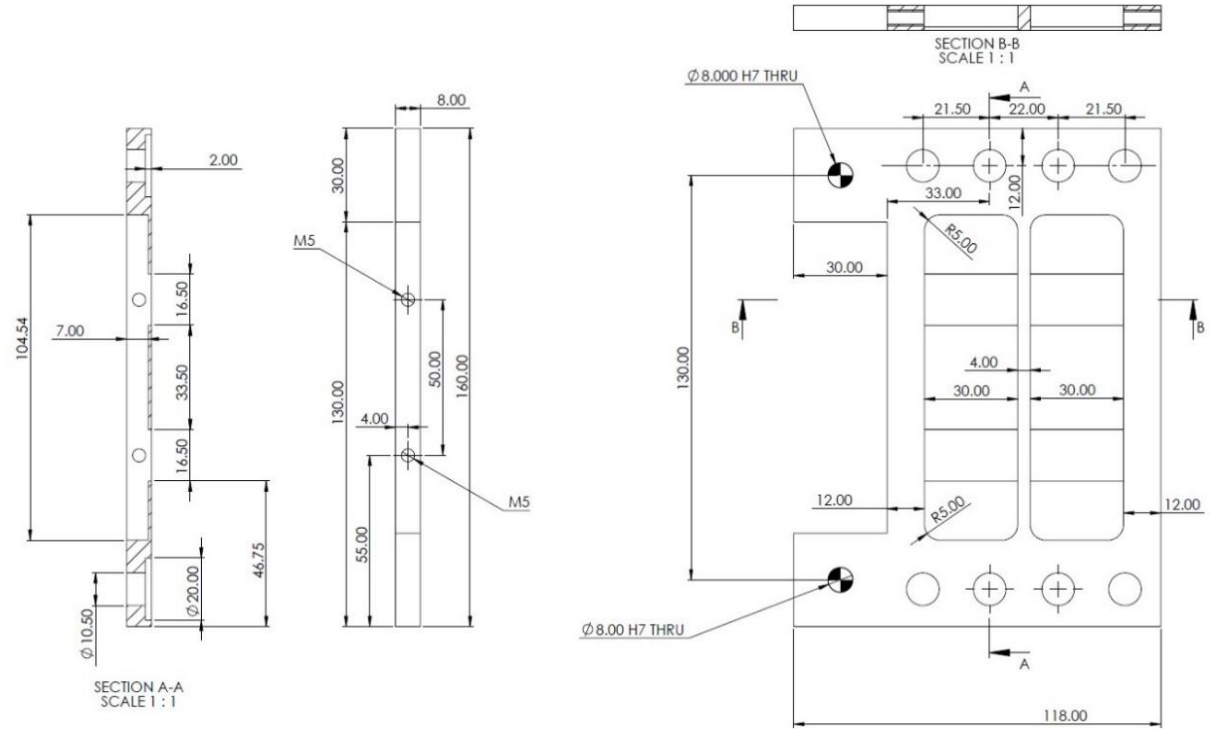

Figure 53: Design of the diffraction sample holder.

3.4 X-ray imaging rigs

After the success of the pilot X-ray experiments, a larger experiment was planned with the intention of applying diffraction and tomography simultaneously at a synchrotron facility. A special wear machine would be used, to wear the sample on the beamline, thus creating a true in-situ experiment, observing the progress of wear on a single sample.

3.4.1 Planned experiment at Diamond

Three days of beam time at the I12 beamline were awarded for late June 2020. An agreement was reached with University of Manchester to use their Deben CT10kN loading frame. The frame was to be shipped to Diamond, mounted into experimental hutch 1 and experiment carried out. The intention was to carry out 5 experimental runs at different normal loads, each with approx. 20 data points, observing the worn zone as it develops from unworn to steady state wear condition. This experiment was cancelled by Diamond Light Source after the COVID19 outbreak as incompatible with the changed working and site-access policies. Since many fittings made for the planned experiment were repurposed for the replacement X-ray work at Diamond, a short discussion of their design and development is included.

When designing the sample and sample holders the capacity of the beamline needs to be taken into account. Tomography module 3 at the I12 beamline can only accommodate volumes of up to 8x8x8 mm. This module was judged to be the best available, due to its balance of tomography resolution and field of view size (module 2 would require very small samples and module 4 would give a resolution judged too poor for the purpose of this research). This dictated the sample to use an annulus measuring 7.5 mm in external diameter and 5.5 mm in internal diameter. The design of the sample holder needs to ensure great repeatability of sample positioning, hold the sample tightly and enable a quick and simple change of the sample elements. In machine practice, Morse taper is used for holding accurate and reliable mounting of tools that experience axial and torsional forces. Tools for machining Morse tapers are widely available. As a result, the sample elements were given the shape of Morse taper #1. Figure 54 shows the cross-section of the sample, as originally designed.

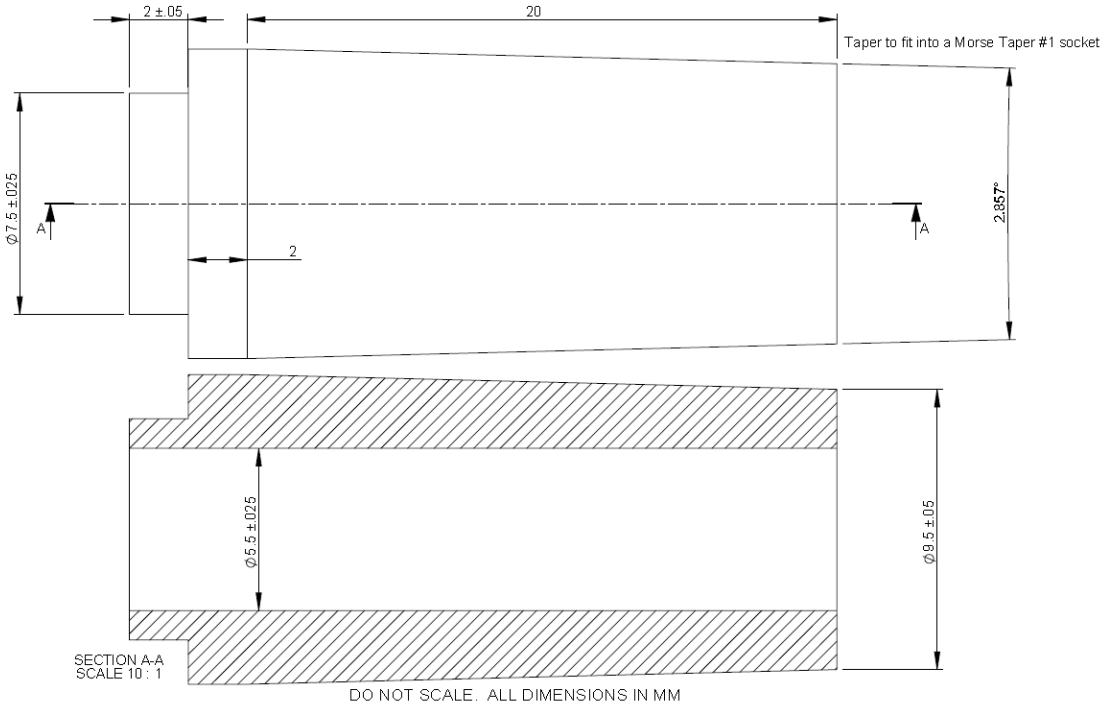

Figure 54: Wear samples for the Diamond Light Source Experiments.

Special sample holders (Figure 55, Figure 56) were designed to fit the Deben CT10kN loading frame. The design is based on the proprietary jaws, the drawings of which were supplied by Deben, which were used as a base for the design. The limited clearance of the frame prevented the use of a more complex wobble plate mechanism, as used in the larger rigs described in 3.2.4.

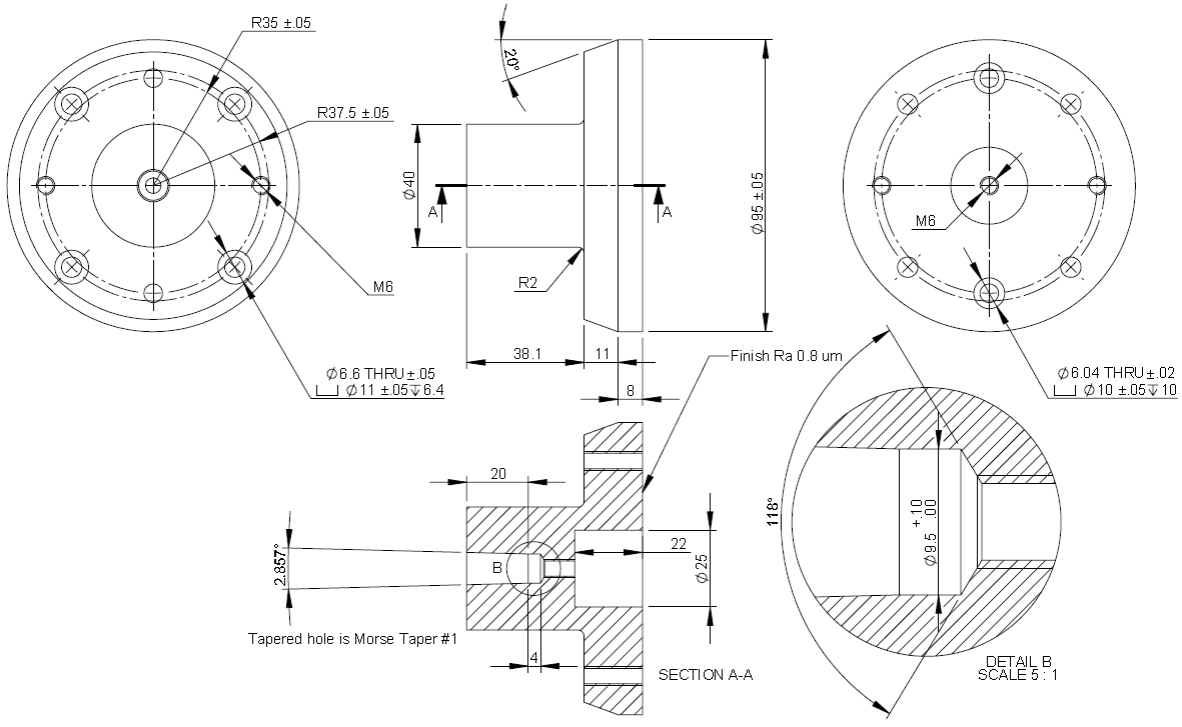

Figure 55: Top sample holder for the Diamond experiment.

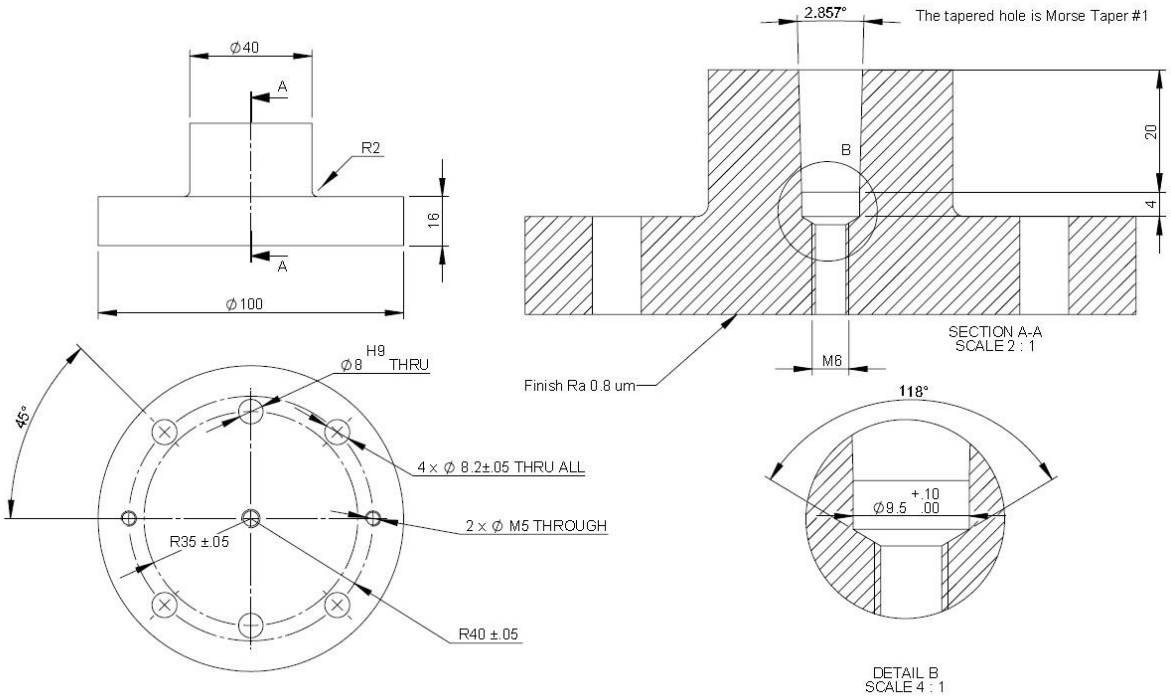

Figure 56: Bottom sample holder for the Diamond experiment.

In use, the sample holders would be attached to the loading frame, centred and fixed in place. The sample elements would be inserted into the holders and a pre-load applied to seat them fully, before the experiment began. Sample elements are removed by inserting an Allen key through the hole in the sample and turning the ejection screw at the bottom of the hole.

Figure 57: Sample holder with sample as originally produced.

3.4.2 Use of Zwick-Roell compression torsion machine in preparation of samples for ex-situ Diamond Light Source Experiment

While a complete in-situ experiment at Diamond Light Source was made impossible by external circumstances, the success of the pilot work still merited a replacement study to be carried out, both to explore the practical possibilities and limitations of the approach and strengthen the case for acceptance of future research proposals. An experiment dividing the wear and X-ray

observation into separate parts was possible within the strictures of COVID19 regulations, which would enable the progress of wear to be observed through the use of several samples. This would enable to demonstrate the applicability of X-ray computed tomography to the observation of wear more strongly than the pilot work and with enough data points, preliminary observations about thickness of the wear debris bed layer, worn roughness and size of wear debris could still be made. In principle, diffraction data could also reveal information about the thickness of the tribologically transformed structure and possibly lattice strain. A proposal for ex-situ tomography-diffraction experiment using 15 samples was successfully submitted to Diamond Light Source.

The Zwick-Roell machine was used to apply the compression and torsion needed for wear. A total of 15 samples were worn to varying degrees in laboratory in Oxford, then encased in an epoxy putty (UniBond Express Repair) under load to preserve the wear condition as closely as possible before being sent to Diamond for further processing. A pair of adapter plates were made to enable the mounting of sample holders onto the Zwick-Roell machine.

The following experimental procedure was used:

- The sample elements are inserted into respective holders.
- The test sequence is initiated, applying first the pre-load to securely sit the elements, then the axial and torsional load required (Figure 58A).
- At the end of the experiment, the samples remain in contact and under load. Epoxy putty is applied around the contact and compressed using a sleeve and a zip tie.
- Putty is left to cure for 24 hours (Figure 58B).
- Still under load, the screws holding the top sample holder are removed.
- The assembly is lowered and the top sample holder removed. The screw in the bottom sample holder used to lift the wear sample.
- A 2.5 mm hole was drilled into the sample region radially, to enable the diffraction beam to pass through one side of the sample unobstructed (Figure 58C; this was necessary since otherwise, the beam would diffract on both sides of the annulus, complicating/corrupting data).

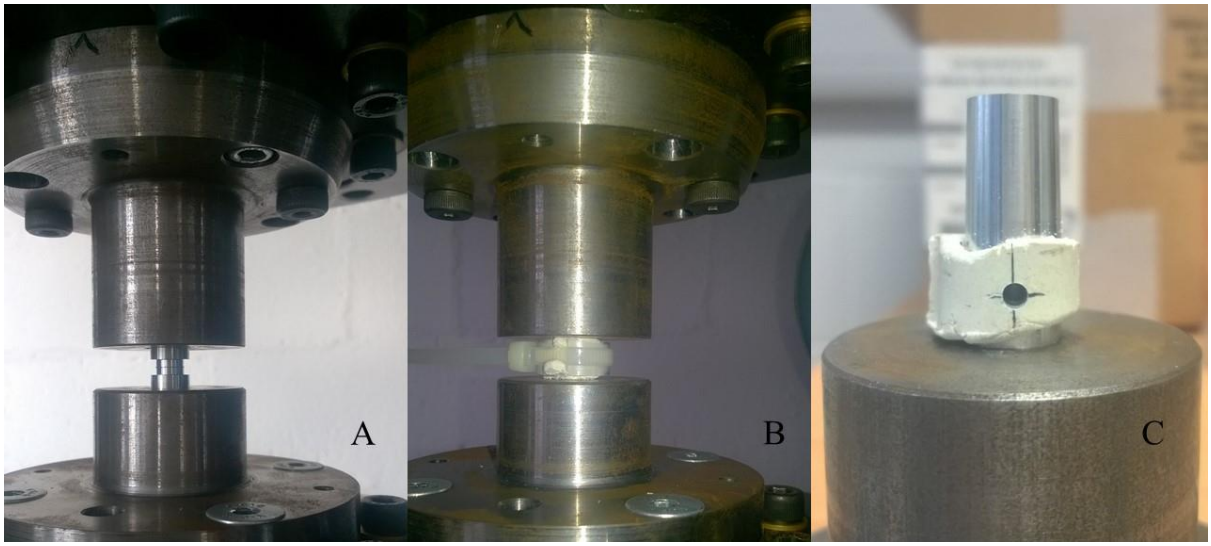

Figure 58: Ex-situ sample preparation. Wear sample mounted in the wear machine (A) Putty curing (B) Wear sample with radial hole showing (C)

The samples were conveyed to Diamond Light Source where the imaging and diffraction study was carried out.

4 TOWARDS A NEW WEAR MODEL

As discussed in sections 2.3.2 and 3.1 Fillot, Iordanoff & Berthier introduced a conceptually powerful model of wear, which was chosen for further examination and study, due to its novel way of modelling wear as a combination of parallel, interconnected, but opposing processes of debris generation and entrapment. In this section, the model and its application to an annular contact geometry are discussed and explored in greater detail.

4.1 The model

In the final and most mature incarnation of their approach (15; 133) FI&B use a discrete element code to simulate unidirectional sliding of a block made from bonded particles against a rough surface. Periodic boundary conditions are applied perpendicular to the direction of sliding; effectively making the block infinite i.e. the setup simulates an annular contact of infinite radius. Friction between particles of the block and that of the surface causes individual bonds to break, eventually 'liberating' a particle or a group of particles, which thus form a wear debris bed. By application of suitable boundary conditions, the particles can be permanently prevented from exiting the contact; in this manner, the authors determined that when a sufficient quantity of wear debris accumulates, the damage to the wearing body stops. This led the authors to formulate the concept of the maximum debris bed thickness (H_{max}) which occurs when no debris ejection is allowed.

They also determined that the debris ejection rate linearly increases from zero with debris bed thickness H, while the debris generation rate linearly decreases from maximum with debris bed thickness, reaching zero at some maximum thickness (denoted by H_{max}). The difference between debris generation and ejection rates causes debris bed thickness to increase or decrease. The core relations of this model have already been given by eqns. 7-12 and are restated:

$$Q_d(t) = C_d\left(H_{max}\text{-}H(t)\right) \quad 17$$

$$Q_e(t) = C_e H(t) \quad 18$$

$$\varrho_d S\frac{dH(t)}{dt} = Q_d(t)\text{-}Q_e(t) \quad 19$$

where ϱ_d and S denote the debris density and contact area respectively. C_e is the ejection constant; larger values indicate more rapid debris ejection. C_d being the debris generation constant; larger values indicate more rapid debris generation. In the steady state, the debris bed thickness become stable ($H(\infty)=H_{stab}$) and debris creation and ejection rates become equal.

Steady state debris bed thickness and steady state wear rate (for initially clean and perfectly flat surfaces) are given by:

$$H_{stab} = \frac{C_d}{C_d + C_e} H_{max} \quad (20)$$

$$Q_d(\infty) = Q_e(\infty) = Q_{stab} = \frac{H_{max}}{\frac{1}{C_e} + \frac{1}{C_d}} \quad (21)$$

Equations 17-21 enable the calculation of both steady-state and instantaneous wear rates as well as establishing the total detached and ejected masses, by integrating the expressions for rate over time. As the conservation of mass must apply, regardless of wearing materials, geometry, atmosphere etc. this is a general description of wear (albeit containing case-specific parameters) which conforms to the requirements established by Meng & Ludema (8), as well as Berthier (113). This is therefore a conceptually strong model of wear which requires only the knowledge of three parameters, C_d, C_e and H_{max} to operate. In practice, C_d and C_e are almost always positive making $H_{stab}<H_{max}$. In principle, the H_{stab}/H_{max} ratio could take any value between 0 and 1 (values above 1 violate the fundamental premise of the FI&B model). Using a special material combination which gave a very predictable debris particle size, Fillot, Iordanoff and Berthier have succeeded in reaching $C_e \approx 0$, by mechanically restricting the ejection of wear debris (15), enabling them to generate $H_{stab} \approx H_{max}$ thus enabling them to measured H_{max} directly. The original authors do not provide any guidance on how to establish C_d, C_e and H_{max} outside empirically measuring them on a case-by-case basis (15). This chapter presents attempts to investigate some of the ways in which contact geometry, pressure and material influence C_d, C_e and H_{max}.

4.2 Debris ejection constant and contact geometry[1]

Fillot, Iordanoff & Berthier speculated (117) (but did no publish any evidence) that the width of the contact influences the entrapment of wear debris, namely that ejection decreases (C_e becomes smaller) the wider the contact is perpendicular to the direction of sliding. This is consistent with the argument separately made by Zmitrowicz (5) who explained the phenomenon of entrapment as a consequence of disparity between the characteristic dimension of the contact and the much smaller characteristic dimension of the debris particle. In a contact studied by FI&B debris is ejected perpendicularly to the direction of motion, making the width of the contact a sensible choice for the characteristic dimension affecting entrapment.

[1] **Section 4.2 is based on paper of Aleksejev et al. (1)**

Annular contacts naturally lend themselves to testing the above assumption, as they are real world manifestations of the idealized geometry studied by FI&B. Using annular contacts of different widths, the expected inverse dependence of debris ejection (and therefore wear) on annular width can be tested. In addition, although systematic studies on how contact pressure (86), atmosphere (89) and intra-contact flow (115) affect wear in annular contacts have already been published, the influence of annular width does not appear to have been explored in previous studies, making this exercise valuable in itself. To test the hypothesis that the ejection path length controls debris entrapment, two experimental series of tests were conducted, one on steel and one on aluminium samples, varying the annular width while maintaining other parameters constant in each experimental series. The focus of the study was on the effects of annulus width and not the response of a particular engineering material. Hence the steel and aluminium samples were chosen for ease of availability and manufacture. The observed variations in total wear and steady state wear rate were then interpreted using a simple model of debris entrapment and by considering the worn surface roughness.

4.2.1 Debris ejection constant and contact geometry - Experimental strategy and set-up

The first experimental series was performed using EN1A steel samples, the second one (done to test the mathematical model developed to explain the results of the first one) using 6082T6 aluminium alloy samples.

In each experimental series, the nominal contact pressure, amplitude and total distance slid were held constant. The annulus widths tested were 1, 2 and 4 mm; see Table 3 for additional details. Note that the tangential displacements used are of the order of ~1mm, rather than >0.1 mm typical of fretting, making this closer to reciprocating wear rather than fretting wear.

	Experimental series					
Material	EN1A			Al 6082T6		
Annulus width (mm)	1	2	4	1	2	4
Internal annulus diameter (mm)	66	66	66	80	80	76
Number of cycles	1700	1700	1600	3500	3460	3550
Angular amplitude (°)	2			1		
Frequency (Hz)	1			1		
Nominal contact pressure (MPa)	9.35			15.0		
Accumulated sliding distance (mm)	8000			9800		
Initial surface roughness (µm)	Ra = 0.8, Rz = 5.5			Ra = 0.7, Rz = 4.4		
Material hardness	189 HV			101 HV		

Table 3: Experimental parameters for both experimental series. Note that the cycle numbers were varied to compensate for changes in median sample radius, the keeping the accumulated slid distance constant in each experimental series.

Samples were subjected to wear using the following procedure: The bottom and top sample elements were cleaned with an isopropyl alcohol-based degreasing agent and dried. The sample elements were weighed and then mounted on the loading frame (Zwick-Roell, Z100, Germany). Special sample grips are used to hold and align the sample elements; for detailed description please see section 3.2.1 (steel samples) and sections 3.2.3-3.2.4 (aluminium samples). The loading frame imposes and controls axial and angular position and can maintain constant axial load using feedback from a load cell. The test rig moved the bottom sample axially and applied angular motion to the top sample element as required. The machine also measured and recorded torque, angular and axial displacement, normal force and computed the accumulated wear work. To initiate the test sequence, the sample elements were brought into contact at a speed of 0.05 mm s^{-1} in the axial direction, until 50% of the nominal contact pressure was reached. The full contact pressure was then applied and the cyclic angular displacement imposed.

After each test, the sample elements were separated and removed from the test machine, brushed and wiped clean, ready to be weighed again, providing the measurement of total mass loss. Weighing of the steel samples was done using a Sartorius Digital Scale (Sartorius Lab Instruments, ENTRIS2202-1S, Germany) for steel samples (required by the high mass of the steel samples) and an analytical balance (Mettler-Toledo, XS105 DualRange, USA) for aluminium samples.

In addition to the total mass loss, the steady state wear rate was determined using the axial position of the bottom sample element, which gradually changed during the test, due to material removal from the sample elements. The axial position data was low-pass filtered to remove measurement noise and the linear portion of the data identified (see description in section 3.2.2.3 for details). The linear rate of change of axial displacement was multiplied with the nominal contact area and the density of the material to give the steady-state wear rate.

4.2.2 Debris ejection constant and contact geometry - discussion

4.2.2.1 Steel experimental series

Figure 59 shows how the total mass lost is distributed between the top and bottom sample elements in this series. The split is mostly even, as is expected in light of the geometrical symmetry, but in 4 mm annuli there is a tendency for more mass to be lost from the top element.

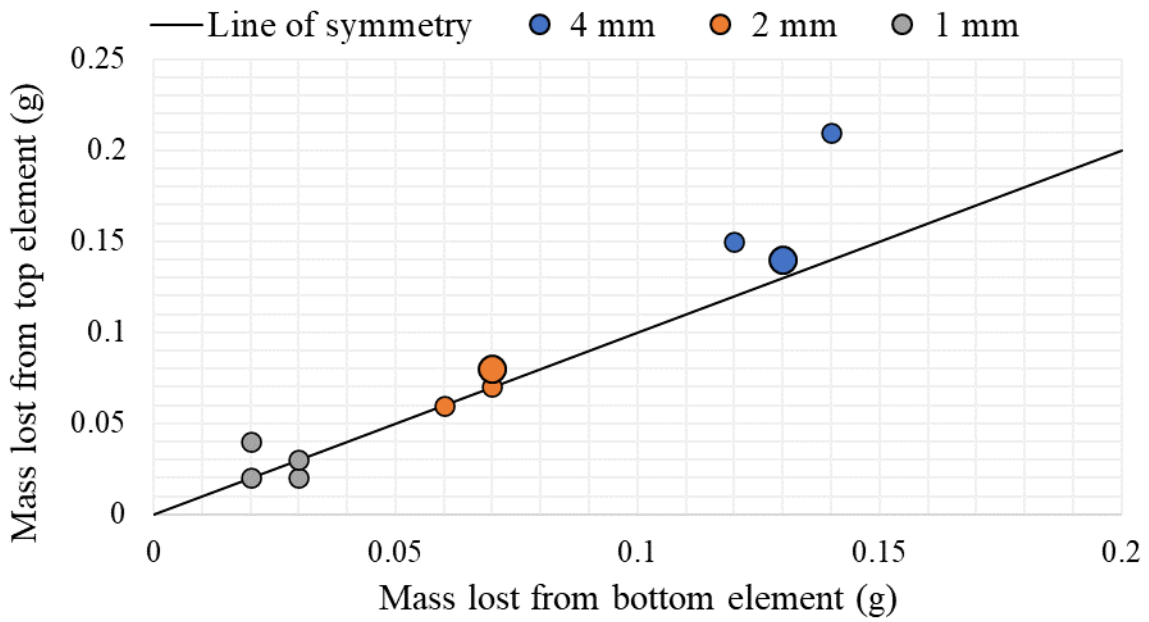

Figure 59: Distribution of mass lost between the top and bottom sample elements for the first cycle of experiments. Line of symmetry represents perfectly even split of total mass lost. Enlarged markers indicate two tests with identical results.

When the lost mass is plotted against the amount of work expended in wear, the points fit well to a straight line

Figure 60). Linear regression analysis gives an R^2 value of 0.89 when all the data points are included. If the largest outlier is excluded (marked with a red circle) R^2 raises to 0.99. Linear increase of wear volume with accumulated energy for identical contacts is frequently reported in the literature (see (156; 157; 158; 86)). However, in this case the linearity exists *between* contacts of different sizes.

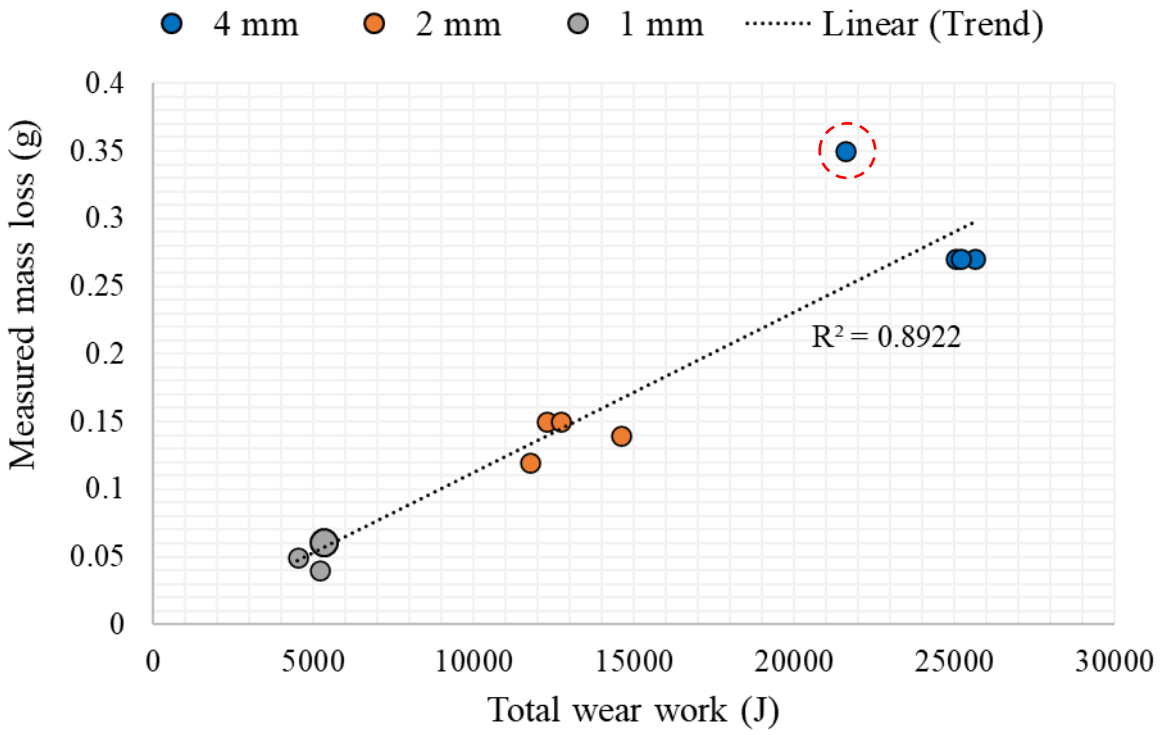

Figure 60: Lost mass as a function of wear work and annulus width in the steel series. A red circle marks an outlier. Enlarged markers indicate two tests with identical results.

The principal purpose of this study was to establish whether an increase in the width of the annulus increases wear debris entrapment (other variables being the same) or not. Increased entrapment should manifest itself through a decrease in wear. There are currently no standardized methods for measuring the exact magnitude of debris entrapment and as of 2018 there were no methods to observe the debris bed between metal bodies. Entrapment therefore had to be inferred qualitatively from observed wear damage. However, contacts with larger contact areas can be expected to lose more material in total. To account for this, the total mass loss and the steady state wear rate were normalized with respect to nominal contact area. Normalized total mass loss for the steel experimental series is shown in Figure 61. By excluding the largest and the smallest value (marked with red circles; both of these tests were conducted

before the addition of the spring discussed in section 3.2.1 and shown in Figure 23 the values fall into a range of 0.24 to 0.35 mg/mm^2. No clear trend in wear versus annulus width is observed.

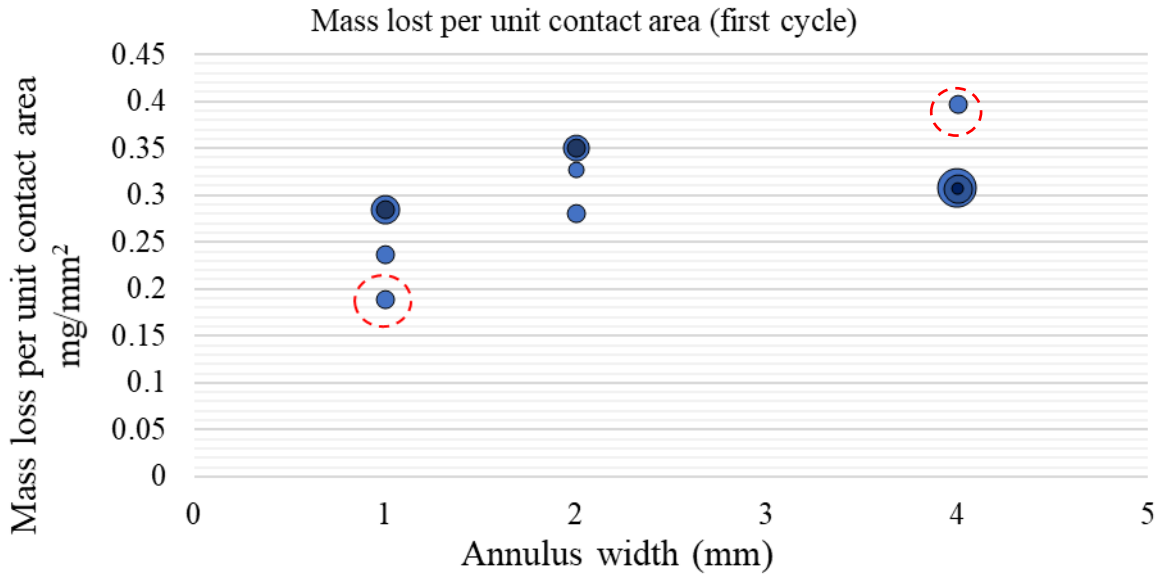

Figure 61: Total mass losses per unit contact area as a function of annulus width for the steel experimental series. The largest and smallest values are marked with red circles.

Steady-state wear rate normalized with respect to contact area is shown in Figure 62. There is significant scatter between tests and no specific trend is observed. As with the total mass loss, the steady state wear rate is not decreased by increasing the width of the annulus.

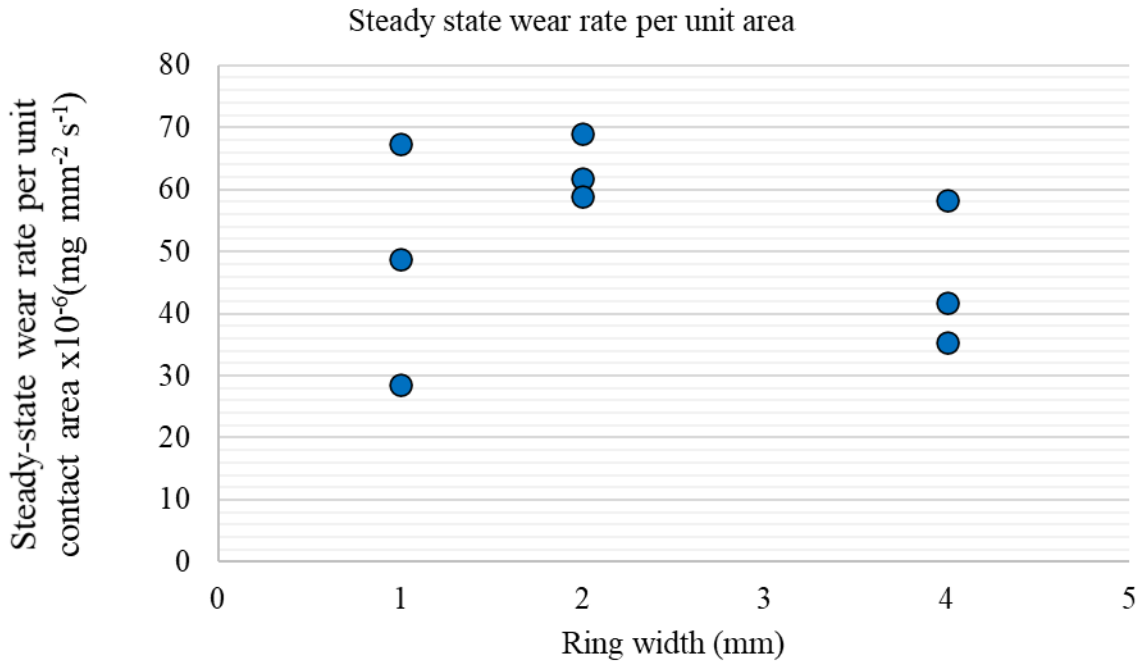

Figure 62: Steady state wear rate per unit contact area as a function of annulus width for the steel experimental series.

The results obtained with steel samples show that wider annuli do not wear less, even relatively, much less absolutely, which indicates that wider annuli do not have a smaller C_e. Therefore, it must be concluded that wider annuli do not show an increase debris entrapment. This is quite an unexpected outcome, which requires an explanation. By applying the mass conservation principle to radial debris flow in a simplified contact it can be demonstrated that annulus width may not influence entrapment under certain conditions.

4.2.2.2 Debris bed mass flow analysis and entrapment

Entrapment of debris is defined as containment of the debris between wearing surfaces (159; 98). This is commonly assessed qualitatively; however, to compare the extent of debris entrapment it is desirable to have a quantitative measure. The debris ejection constant of FI&B is not fully appropriate, as it expresses the magnitude of the debris ejection flow, which may depend on factors such as the shape and size of the contact area and does not measure simply the capacity of the contact to entrap. For this reason, the average time needed for a debris particle to escape from the contact after its release into the debris bed has been adopted as the measure of debris entrapment (the same concept has been independently proposed by researchers from University of Nottingham in (31)).

Consider the debris mass flow in a radial cross-section of the annular contact, as shown in Figure 63. As the annulus width is small compared to the radius, the contact can be approximated by a pair of infinitely long straight walls, of width $2L$, separated by a debris bed layer of thickness H. As it has been demonstrated that larger values of H decrease wear (117; 15) and since wear observed in steel annuli scales simply with contact area, it is assumed as a first approximation that H is independent of L. In addition, H is most likely to be influenced by contact pressure, which has also been kept constant. It is also assumed that mass is removed uniformly across the contact surface, with mass loss rate per unit area M. The contact is symmetrical with respect to a central vertical plane (distance L away from either edge) and it is assumed that there is no net mass transfer across this symmetry plane.

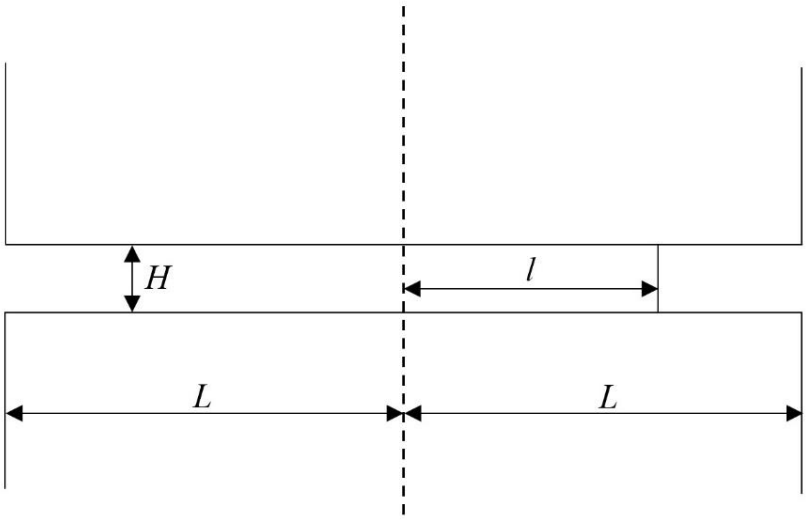

Figure 63: Cross-section through an idealized annular contact. The slip direction is in/out of the page.

In steady state, the mass flux of debris in the radial direction, m', per unit depth, at some horizontal distance l from the central plane can therefore be written as:

$$m'(l) = 2lM \qquad 22$$

The debris flows through the gap between the surfaces of the first bodies. Using eqn. 22 and denoting the bulk density of the debris ϱ, the radial velocity of the flow, v_r, is:

$$v_r(l) = \frac{m'}{H\varrho} = \frac{2lM}{H\varrho} \qquad 23$$

It is assumed that each particle removed from the first bodies immediately obtains the radial velocity of the flow at that position. A particle travelling with the speed v_r travels a distance dl in time dt. Using eqn. 23 we obtain:

$$v_r dt = dl = \frac{2lM}{H\varrho} dt \qquad 24$$

Hence

$$dt = \frac{H\varrho}{2M} \frac{dl}{l} \qquad 25$$

The quantity $HQ/2M$ defines a characteristic time t^* which is taken to be a constant. Solving eqn. 25 gives

$$\int_0^{t_e} \frac{dt}{t^*} = \int_l^L \frac{dl}{l} \quad \textbf{26}$$

$$t_e = t^* \ln \frac{L}{l} \quad \textbf{27}$$

Where t_e is the time between release of a particle into the debris bed, at position l, and ejection of the same particle over an edge of the contact. The average time particles spend in the contact can therefore be calculated as:

$$\bar{t}_e = \frac{t^*}{L} \int_0^L \ln \frac{L}{l} \, dl = t^* \quad \textbf{28}$$

Eqn. 28, identifies the characteristic time t^* as the average time debris particles spend in the contact. This time is independent of the width of the annulus. On the other hand, C_e does increase with the width of the contact, since the quantity of material ejected increases linearly with the contact area and the debris bed thickness is assumed to remain the same. The independence of average ejection time on geometry is in line with the observations gathered on steel samples. According to eqn. 28 the average ejection time is independent of material properties (apart from debris density) as well as from the wear contact conditions such as pressure, displacement or sliding velocity. Increasing the width of the annulus still further should therefore have no entrapment effects. It is also therefore expected that the independence of entrapment of width of the contact will be observed in other contacts. To test this, the aluminium experimental series was carried out using different pressure, displacement and material, but varying only the annulus width within the series. This directly tested the independence of wear predicted by eqn. 28.

4.2.2.3 Aluminium experimental series

In the aluminium experimental series, the mass loss was equally split between the top and bottom sample elements, as was the case for steel samples (Figure 64). However, the total mass loss is smallest in 4 mm wide rings, as opposed to being the largest, as was the case in steel rings. This may appear paradoxical, but it should be born in mind that total mass loss represents the effect of the entire process of wear: the initiation of surface damage, galling of surfaces, generation of the wear debris bed and finally steady-state wear.

When using aluminium rings, the number of cycles needed to reach steady state wear increases roughly in proportion with the size of the contact area, meaning that while a steady-state was reached in all cases, this required more cycles in wider rings, eventually causing less wear to be accumulated over-all. This explanation is further supported by the fact that total mass loss in 2 mm aluminium rings is less than twice that in 1 mm rings, indicating that the run-in period of the contact was longer. In the steel rings, the stead-state was reached much more quickly, making the steady-state part of wear mask the transient wear phenomena. The reasons for the difference are not fully clear; we speculate that the most likely explanation is that aluminium, possessing higher ductility than steel, required more energy to be expended (and hence more cycles to be accumulated) in order to initiate wear and establish a tribologically transformed structure.

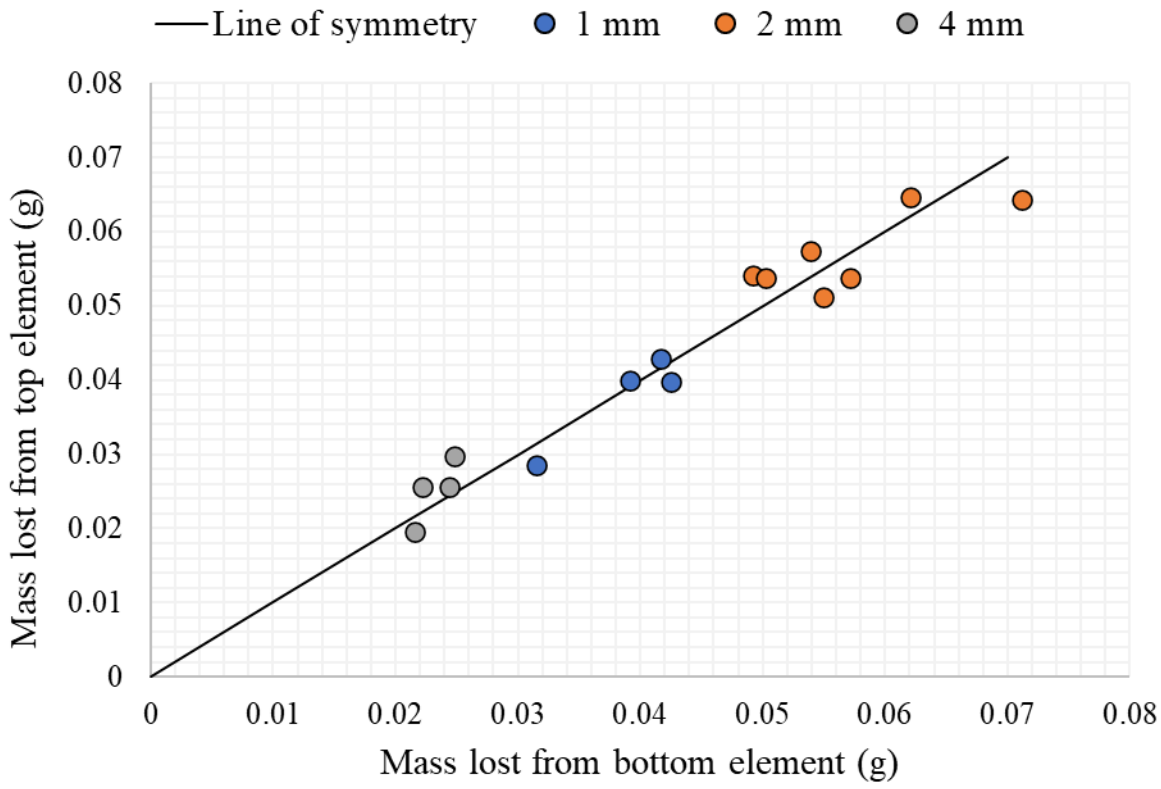

Figure 64: Distribution of mass lost between the top and bottom sample elements for the aluminium experimental series. Line of symmetry represents perfectly even split of total mass lost.

When the total mass loss is plotted against accumulated wear work, no particular trend is observed between annuli of different widths (Figure 65).

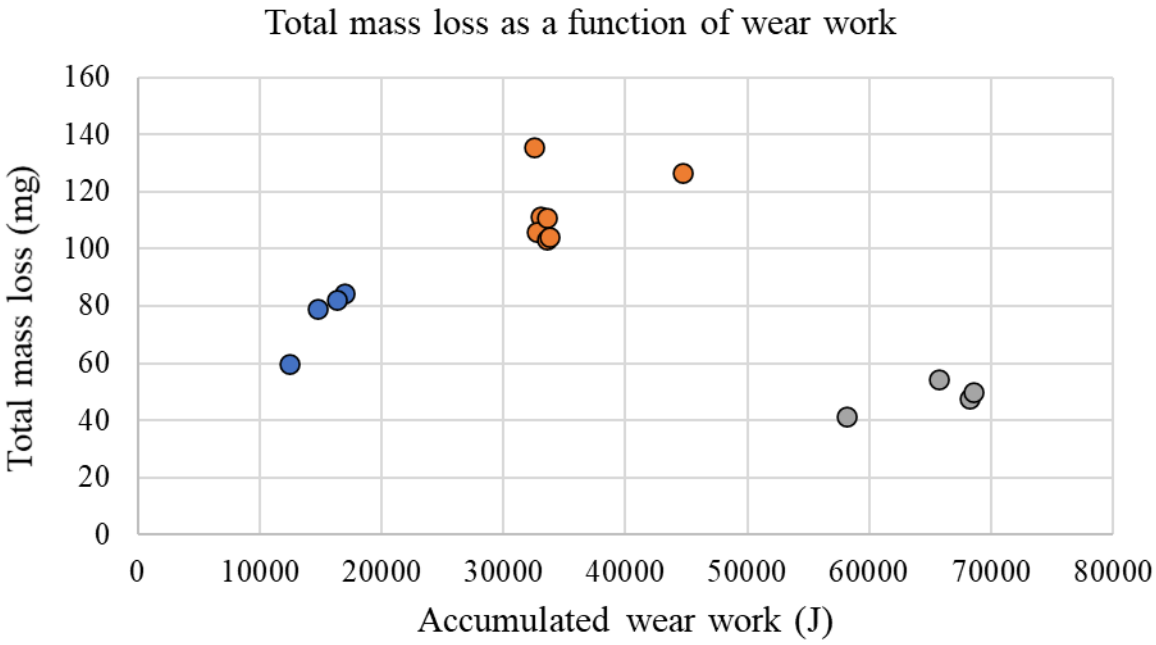

Figure 65: Total mass loss as a function of accumulated wear work in aluminium experimental series.

When normalizing the total mass loss with respect to contact area a clear negative trend is observed, with the normalized mass loss decreasing with annulus width (Figure 66).

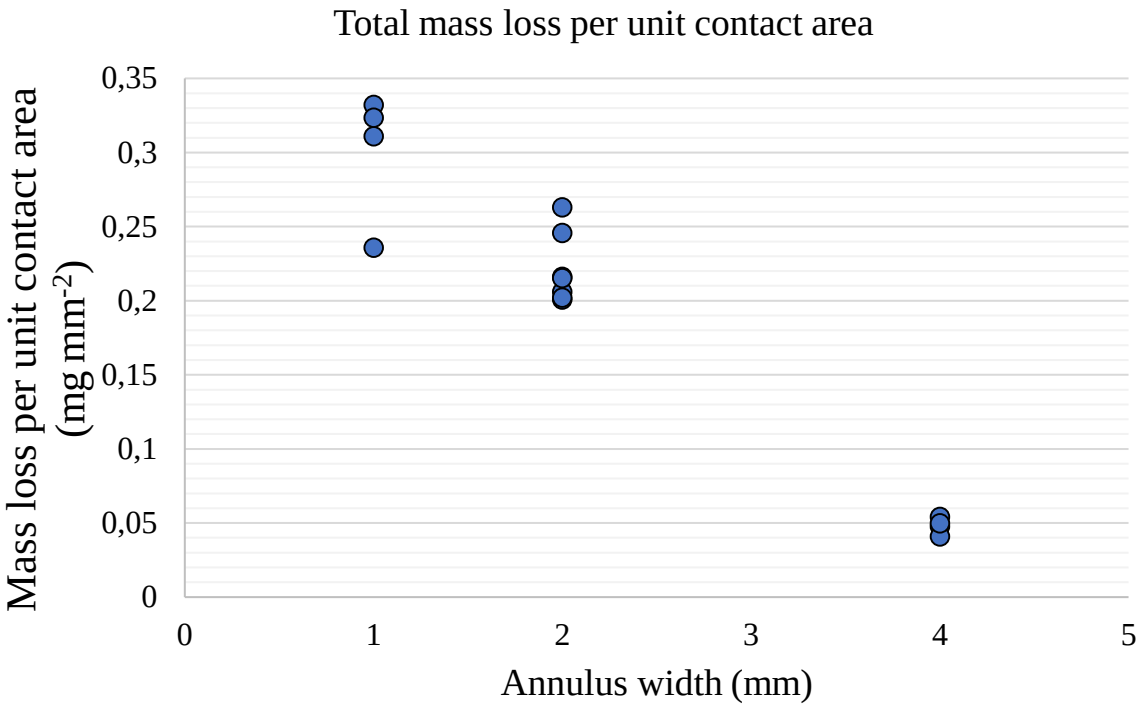

Figure 66: Total mass loss per unit of contact area as a function of annulus width in the aluminium experimental series.

The same trend is observed when the steady-state wear rate is normalized with respect to the contact area, as seen in Figure 67.

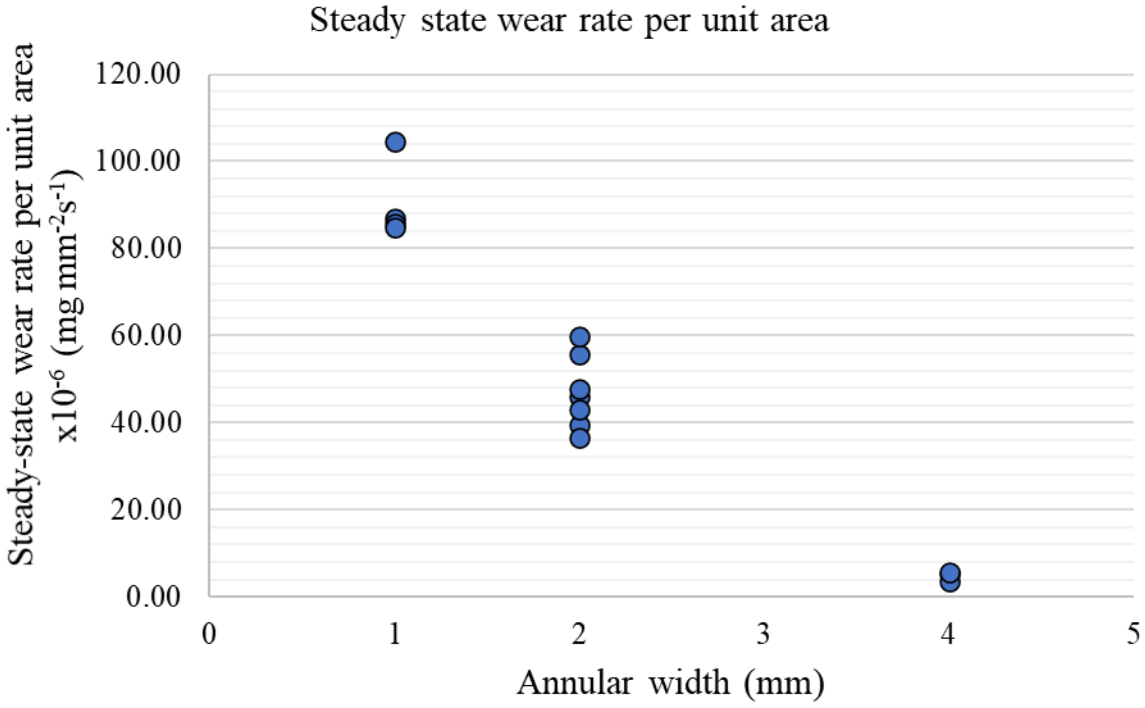

Figure 67: Steady state wear rate per unit area as a function of annular width in the aluminium experimental series.

The aluminium experimental series shows that wear (as measured by total mass loss or steady state wear rate) decreases with annulus width, which is consistent with an increase in wear debris entrapment. This contrasts with the steel experimental series, where the wear was almost independent of annulus width.

In both experimental series powdery wear debris was produced. A scanning electron microscope (Zeiss, EVO LS 15, Germany) was used to observe and study the wear debris particles (Figure 68). When steel was used, the debris accumulated inside the bottom sample and was easily collected for further study. When aluminium was used, this was not practical, so an adhesive tab was applied directly to the contact surface after wear to collect the wear debris. Collecting wear debris for the purpose of weighing was impractical, since the sample holders were not design to retain the debris, while collection through vacuuming or some similar method would probably waste portion of the debris particles too small to be reliably captured by the filters.

The steel debris particles are mostly flake-shaped, ranging in size from 2 μm - 300 μm, with 10 μm - 20 μm being typical. The flake thickness is estimated at 5-10% of its diameter. There were no visually discernible differences between the particles obtained from contacts of different widths. The aluminium debris was also in the form of flakes, in a similar size range of 2 μm – 200 μm. Debris collected from the 1 mm aluminium rings consisted primarily of relatively large flakes (over 50μm across and approximately 5μm in thickness), with wider rings tending to produce smaller debris particles (although some larger ones were still found).

In a separate experiment, the wear debris from the steel and aluminium contacts was placed between a pair of flat steel plates and compressed with clamps. The thickness of the assembly was measured using a micrometre screw, to determine how much can the debris layer be compressed. The observed debris layer thicknesses were 0.09-0.100 mm, showing the likely limiting value for the thickness of the debris bed in wear.

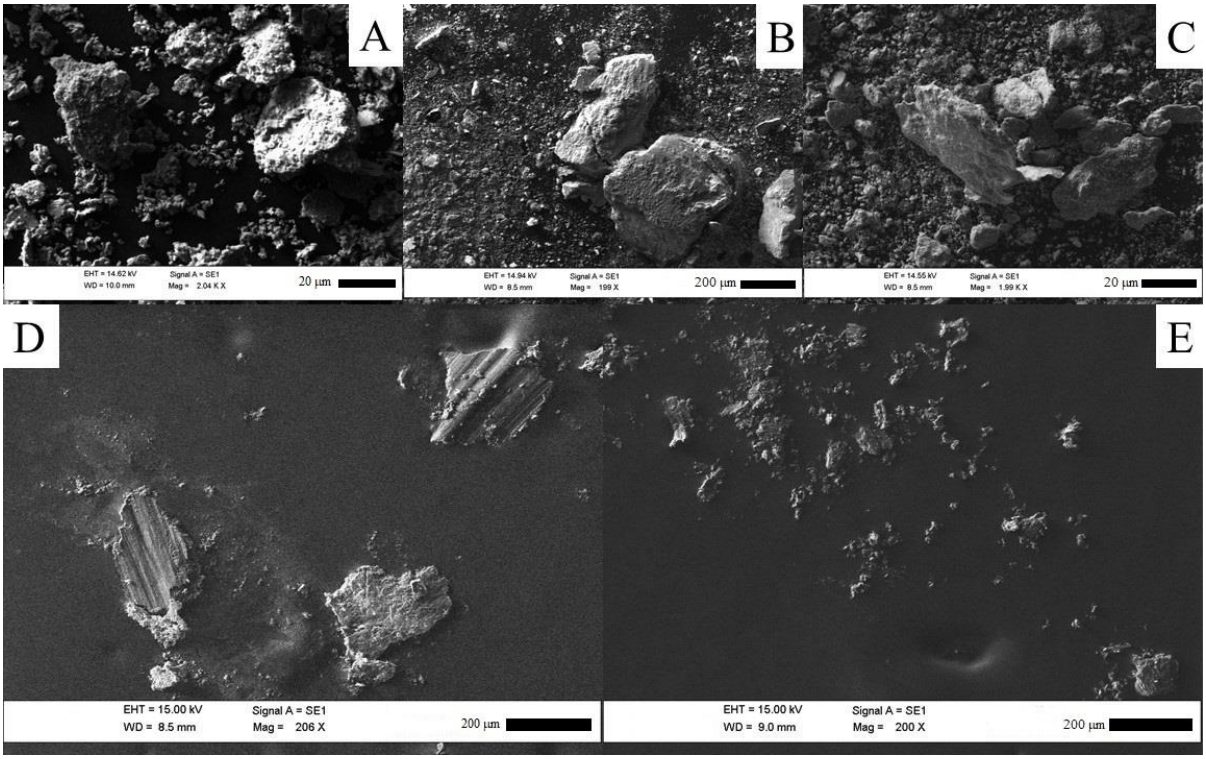

Figure 68: Wear debris particles. 1 mm wide steel A) 2 mm wide steel B) 4 mm wide steel C) 1 mm wide aluminium D) 4 mm wide aluminium E).

The difference in wear behaviour observed suggests that debris entrapment is influenced by factors other than the width of the annulus. However, the annulus width was the only geometrical parameter varied in the experimental design of each series. This indicates that a self-establishing length scale may affect the entrapment process. In this case, varying the width of the annulus is not sufficient to deconvolute the factors influencing debris entrapment.

Some observations concerning what this length scale might be can still be made. One possibility is that the worn surface roughness could differ between the two experimental series. To test this, an optical profilometer (InfiniteFocus, Alicona, Austria) was used to examine the worn surface profiles. Profiles were taken in the radial direction with start and end points approximately 100 μm away from the inner and outer edge of the annulus. It was determined that the worn aluminium surfaces were considerably rougher than the worn steel surfaces. This is illustrated in Figure 69, which shows a comparison between representative primary radial surface profiles in 2 mm wide annuli. For brevity, only two profiles are shown for each material, but they illustrate a general trend observed on several profiles in all three contact geometries.

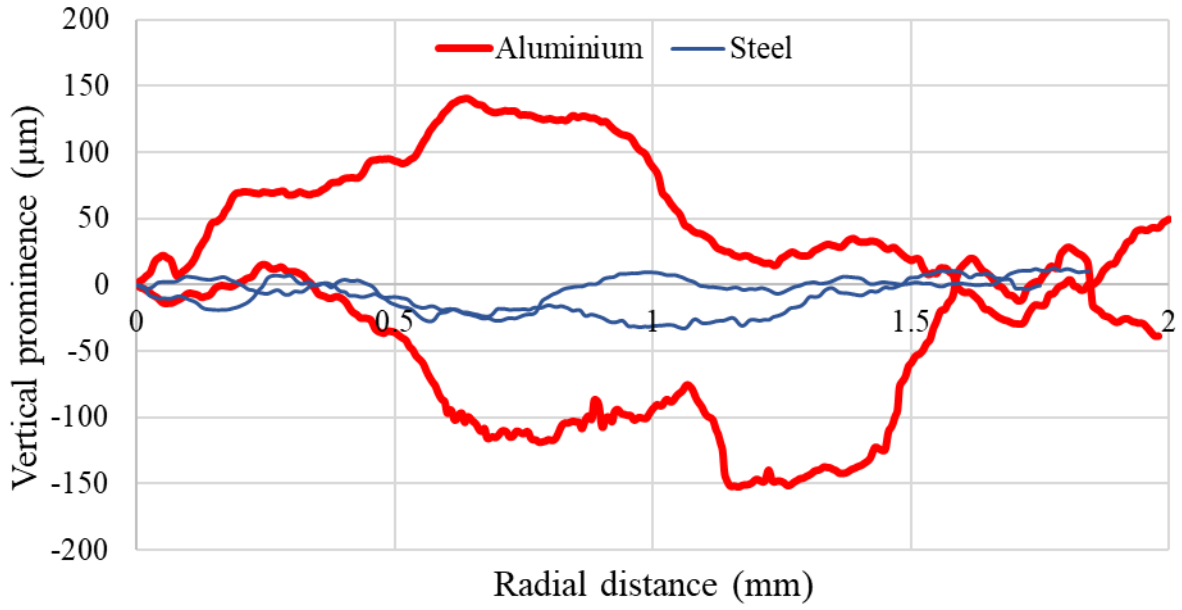

Figure 69: Four randomly chosen radial primary surface profiles from 2 mm wide annuli (2 from steel and 2 from aluminium samples).

A more detailed roughness analysis shows that the primary worn surface profiles are consistently rougher in the aluminium annuli and also that the profile roughness increases with annulus width (see Figure 70).

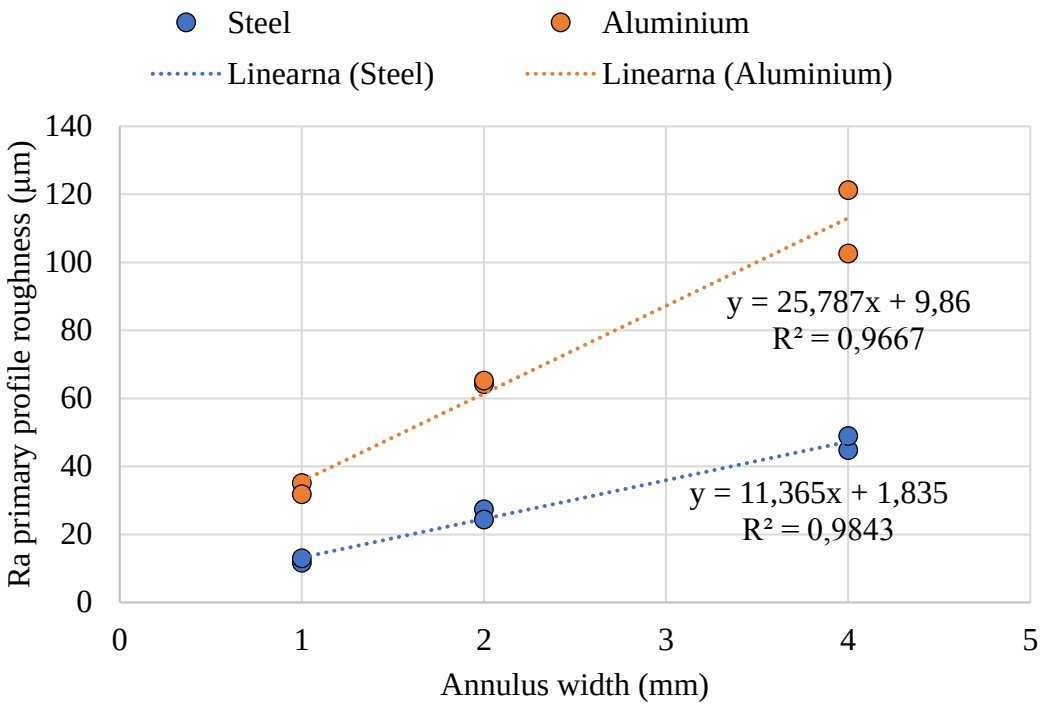

Figure 70: The relationship of Ra primary profile roughness and annulus width in steel and aluminium experimental series.

The derivation of eqn. 7 assumes a 'steady' flow of debris through the debris bed. It is possible that the rougher worn surfaces occurring in the aluminium annuli disturb the flow of debris. In the steel annuli, no systematic dependence of wear was observed and the worn surface was relatively smooth with the largest particles observed (Figure 68) having diameter several times larger than the vertical prominence of the worn profiles meaning that they essentially 'prop' the contacting surface apart, allowing smaller debris to pass more easily. The argument developed in section 4.2.2.2. could then be expected to apply at least to some degree. In the aluminium annuli, however, the surface wears to a much rougher profile, invalidating the assumptions of the simplistic mass-flow explanation that led to eqn. 28. Comparing the roughness profiles in Figure 69 with the debris sizes noted from Figure 68, it is evident that the scale of roughness established in the aluminium specimens is capable of locally accommodating even the largest debris particles with room to spare. Debris particles are thus forced to 'pool' in large voids or are blocked by large asperities.

The notion that surface roughness can affect debris entrapment has been proposed in prior studies (160; 161), with a threshold effect observed, where roughness effects only occur when the roughness parameter of the surface is large enough compared to the size of the wear particles. Taking this into account, the differences observed between the two experimental series can be explained in terms of material propensity to wear into a particular morphology under the experimental condition used.

4.2.3 Debris ejection constant and contact geometry - summary

Wear of annular contacts made of EN1A steel and 6082T6 aluminium alloy was studied to test whether wider annuli entrap wear debris to a greater degree, changing the debris ejection constant as formulated by FI&B. The experimental results in steel rings showed no particular trend in wear as the annulus width was changed. To explain the independence of wear on annulus width, a simple model of the radial debris flow velocity profile was developed. In this model, the average time from particle creation to ejection was found to be independent of annulus width. Taking this time as a measure of debris entrapment explains the experimental observation in steel rings. A second experimental series using aluminium alloy rings and a different set of wear conditions was performed to test whether the model assumptions are more generally applicable. The normalized wear in the second series showed a clear trend of decreasing with the ring width. Based on measurements of the worn surface profiles we conclude that the most likely explanation for the different wear behaviours observed is that the aluminium rings wear into a much rougher surface profile, which influences the flow of debris to a greater extent, than the relatively smooth worn profile of steel samples. This would cause the debris entrapment to increase significantly with ring width in the case of aluminium alloy annuli, but not so in the case of steel annuli. It should be noted that the worn-in surface roughness is not a controllable experimental variable, but rather a self-determined length scale likely to affect wear. A predictive understanding of the factors affecting the worn in surface roughness is desirable, but not currently available.

The work presented highlights the significance of both debris flow in wear and the worn surface roughness affecting debris entrapment. To conclusively determine the influence of these factors, it would be advantageous to observe the debris flow during wear in-situ; at the time of writing, no mature experimental approach for doing so in metal-metal contacts existed.

4.3 Debris bed thickness and contact conditions

Having established that C_e may depend on the interaction between debris particle size, surface roughness and (at least in some circumstances) the length of the debris ejection path, we may try to progress to questions concerning H and H_{max}. Since the work of FI&B is relatively little known, no studies on the factors influencing H_{max} appear to have been made. Yet, this is an important parameter in the model. Indeed, it is not even what the physical interpretation of H_{max} is. Is this the debris bed thickness at which point the largest asperities can no longer come in contact? Or the one where the internal friction of debris particles dissipates all energy and there is none left to erode the first bodies? Or yet some third option? There are also no data available on how do contact conditions, such as contact pressure, affect H and H_{max}.

4.3.1 Debris bed thickness and contact conditions - Experimental strategy and setup

Two sets of experiments were planned, with the experimental setup and approach identical to the one described in 3.2.6 and 4.2.2.3. In the first series, full aluminium rings were worn at different levels of contact pressure to observe the total wear mass loss, the steady state wear rate and measure the steady state debris bed thickness H_{stab}. In the second series the same wear conditions were used, but the number of cycles increased and the wear contact encased with a pair of debris entrapment rings to deter debris ejection and thus hopefully enable the contact to accumulate a debris bed of thickness close to that of H_{max}. Two different ring widths (2 and 4 mm) were used. The parameters of the tests are given in Table 4. Constant frequency was used, as the effects of frequency on wear have been studied to some degree and it was not expected that frequency would be the most important factor influencing H_{stab} or H_{max}. The number of cyles was chosen so that the contact would spend an appreciable amount of time in steady-state, which was necessary for stead-state wear-rate measurements. Without debris entrapment rings, steady-state wear was generally achieved in 2000-2500 cycles, showing the choice to be appropriate.

	Experimental series			
Debris ejection	Free		Restricted	
Annulus width (mm)	2	4	2	4
Internal annulus diameter (mm)	80	76	80	76
Number of cycles	5000	5000	10000	10000
Angular amplitude (°)	1		1	
Frequency (Hz)	2		2	
Nominal contact pressure (MPa)	4.95, 10.1, 14.9, 21.4	5.17, 9.95, 15.4	4.95, 10.1, 14.9	5.17, 9.95, 15.4
Accumulated sliding distance (mm)	14300		27925	
Initial surface roughness (µm)	Ra = 0.7, Rz = 4.4			
Material hardness	101 HV			

Table 4: Experimental conditions used in investigations of *H*.

4.3.2 Debris bed thickness and contact conditions - discussion

4.3.2.1 Unrestricted debris ejection

In the works of Hintikka et al. (86; 109) it was reported that in annular contacts, the total amount of material removed does not increase linearly with normal force. The same result was observed in preliminary work performed during this project in 2017. It was therefore expected that a similar pattern will be observed again, as it indeed was.

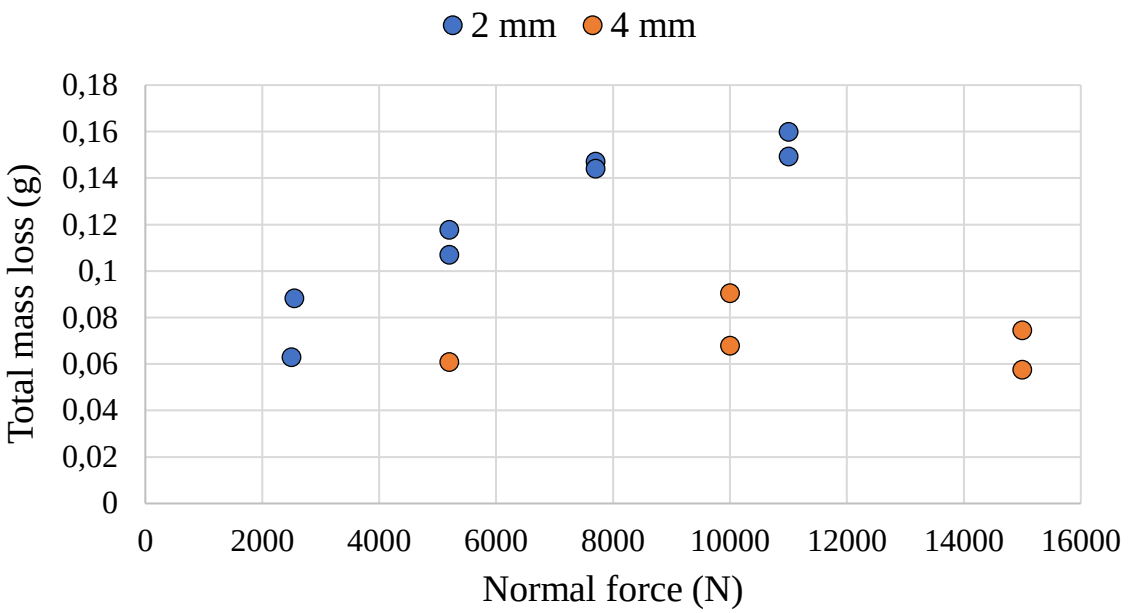

Figure 71: Total mass loss as a function of normal force (debris ejection unrestricted).

As may be observed in Figure 71, the total amount of material removed does increase with normal force, but only up to a point. Increasing the normal load causes smaller and smaller increases in the amount of total wear, with wear becoming independent at sufficiently high levels. Since the total mass loss represents the loss in both steady-state and non-steady wear regimes, this could be conceivably attributed to the change from one regime to the other occurring at different times, thus causing different quantities of material to be removed, but this seems somewhat far-fetched: it is expected that the momentary wear rate is higher in the initial stage of wear than in the steady-state and it seems profoundly unlikely that the onset of steady-state changed with normal load exactly so, as to balance the contribution of steady and non-steady parts to give comparable values of total wear for the exact length of experiment. This expectation is confirmed when examining the steady-state wear rates shown in Figure 72.

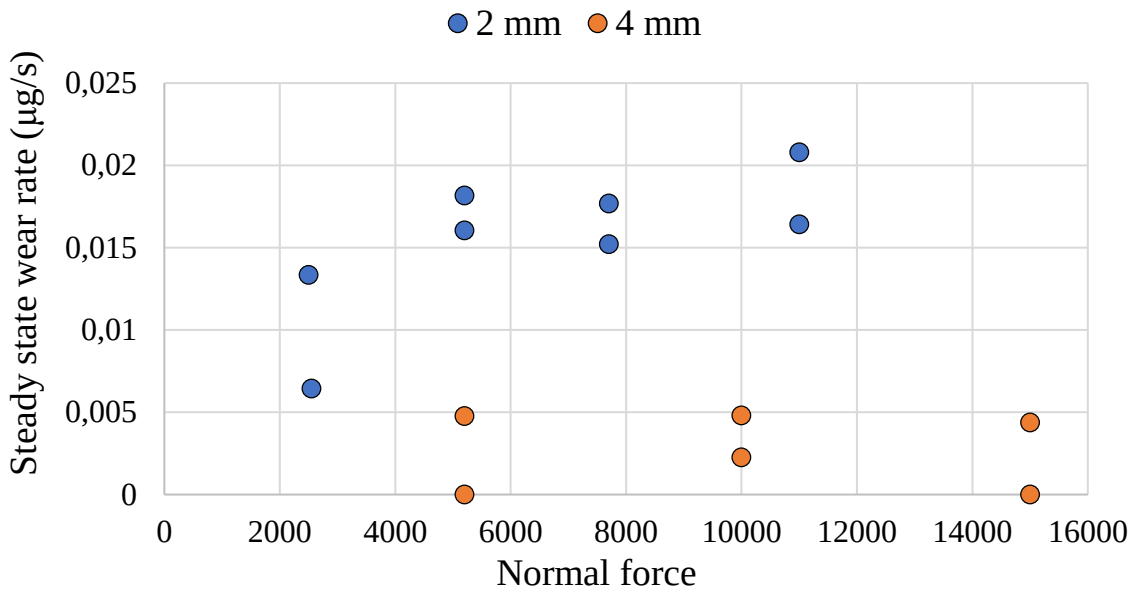

Figure 72: Steady-state wear rate (debris egress unrestricted).

As may be observed, the steady-state wear rate exhibits the same behaviour as the total mass loss. In annular contacts, beyond a threshold, the wear does not seem to increase with normal force. This was first observed by Hintikka and co-workers (86; 109), but in the course of this project it was also observed for EN1A steel, 6028 aluminium under a variety of wear conditions, indicating that this is a general property of annular contacts. This requires explanation.

4.3.2.2 Dependence of wear on normal force – mathematical explanation

The law of Fillot, Iordanoff & Berthier can provide such an explanation. Let the expression for Q_{stab} be written as a function of wear parameters, assuming a full annular contact with a fixed median radius. FI&B argue that if $C_e >> C_d$, $Q_{stab} = Q$ and is described by the Archard wear law. As $C_e >> C_d$ makes $C_e^{-1} + C_d^{-1} \approx C_d^{-1}$ eqn. 21 may be rewritten as:

$$Q_{stab}(C_e \gg C_d) = C_d H_{max} = k F_N v_r \qquad 29$$

Where k is the wear constant (it equals the Archard's wear coefficient, divided by material hardness), F_N the normal force and v_r the relative sliding velocity of the wearing bodies. From this, the constant C_d can be can be expressed as

$$C_d = \frac{k F_N v_r}{H_{max}} \qquad 30$$

Thus, the expression for steady-state wear rate can be produced, by uniting eqns. 29 and 30 with eqns. 20 and 21 obtaining:

$$H_{stab} = \frac{\frac{kF_N v_r}{H_{max}}}{\frac{kF_N v_r}{H_{max}} + C_e} H_{max} = \frac{kF_N v_r}{\frac{kF_N v_r}{H_{max}} + C_e} \quad (31)$$

$$Q_{stab} = H_{stab} C_e = \frac{kF_N v_r C_e}{\frac{kF_N v_r}{H_{max}} + C_e} \quad (32)$$

The dependence on normal force F_n can now be investigated. It is obvious that the magnitude of other parameters will have a significant effect on the behaviour, making it necessary to establish the ranges in which these are most likely to occur. In the experiments presented in 4.2.2.1, 4.2.2.3 and 4.3.2.1, the steady-state total wear rates observed in aluminium are in the range of approximately $5 \cdot 10^{-9}$-$2.5 \cdot 10^{-8}$ kgs^{-1} (Figure 67, Figure 72). There is a high certainty that steady-state debris beds measure 10^{-5}-10^{-4} m in thickness, as ascertained by compressing the expelled debris between steel plates and direct measurements. Ranges typical for laboratory fretting experiments are listed in Table 5.

Parameter	Typical range	Source/explanation
C_e	10^{-5}-10^{-2} (m)	
k	10^{-10}-10^{-5}	(104; 10)
v_r	10^{-3}-10^{0} (m/s)	(95; 29; 31; 30)
L	10^{-4}-10^{-2} (m)	(1), other authors used similar values (85; 89; 86; 109)
F_N	10^{2}-10^{4} (N)	(1) and experiments in section 4.3.2.1 used forces of several 10^{3} N; also (95; 40; 108; 30; 109)
H_{max}	10^{-4} (m)	Debris bed thicknesses measured are in 10^{-2}-10^{-1} mm range.

Table 5: Typical ranges of experimental parameters in laboratory fretting wear experiments.

Inserting the general order of magnitude values into eqn. 32 enables the dependence on F_N to be tested; a number of different combinations has been tried, with the values used shown in Table 6 and resulting dependencies shown in Figure 73.

Line	k	v_r	H_{max}	C_e
A	10^{-6}	10^{-2}	10^{-4}	10^{-4}
B	10^{-6}	10^{-2}	10^{-4}	$2{\cdot}10^{-4}$
C	10^{-6}	10^{-2}	10^{-4}	$4{\cdot}10^{-4}$
D	10^{-9}	10^{-2}	10^{-4}	10^{-4}
E	10^{-8}	10^{-2}	10^{-4}	10^{-4}
F	10^{-7}	10^{-2}	10^{-4}	10^{-4}
G	10^{-8}	10^{-2}	$2{\cdot}10^{-4}$	10^{-4}

Table 6: Magnitudes of parameters used in traces in Figure 73.

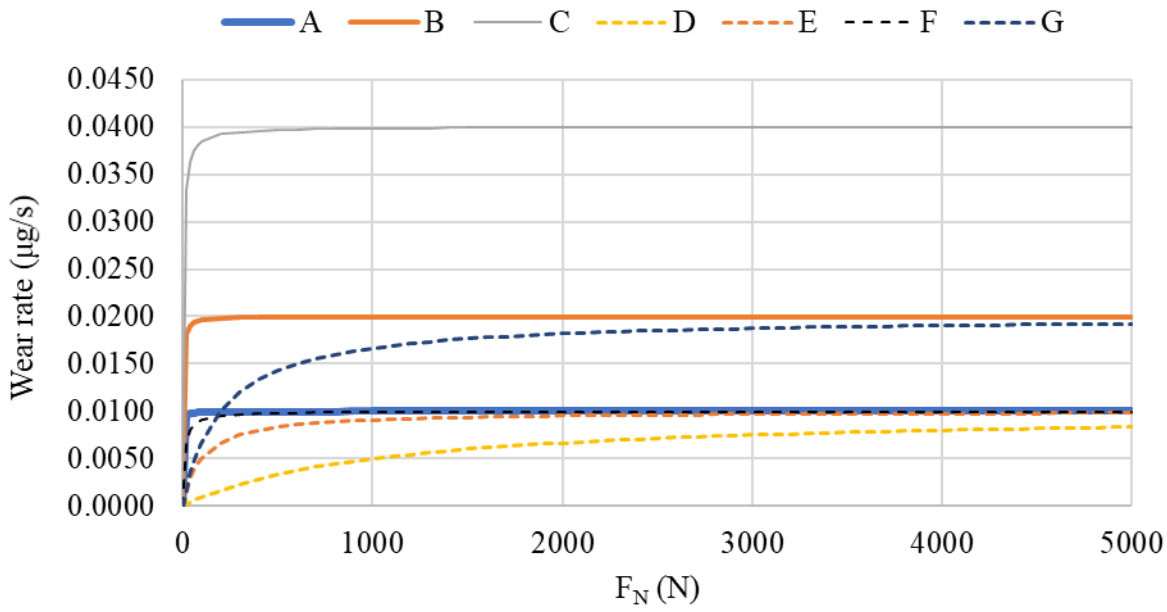

Figure 73: Steady state wear rate as a function of normal force according to eqn. 32 with the parameters from Table 6.

Note the general similarity with the trend shown in Figure 72. In all cases, the wear rate increases asymptotically until reaching a value independent of normal force. In other words, the empirically observed and hitherto unexplained independence of wear in annular contacts on normal force can be explained in terms of principles of Fillot, Iordanoff and Berthier, with wear parameters typically encountered in laboratory conditions being of such order of magnitude to produce a near-flat response to normal force at force levels typically used in the experiments hitherto published. It can also be observed that the value of the asymptote is governed by the interplay between H_{max} and C_e, with larger C_e (other things being equal) causing a higher wear rate. This is consistent with observations presented in Figure 67 and discussed in section 4.2.2.3.

4.3.2.3 Restricted debris ejection

The experiments described in section 4.3.2.1 were repeated, but with a higher number of cycles to maximize the time the contact spends in steady-state and with the use of plastic debris entrapment rings in order to restrict (and hopefully completely prevent) ejection of wear debris. The entrapment rings had to satisfy a list of contradictory requirements: the fit between the ring and the sample had to be tight enough to prevent ejection, but not enough to cause wear, the entrapment ring had to be either extremely wear-resistant or disposable, the ring had to be elastic to enable removal after experiment should there be any burring of the samples. It was decided that polyethylene rings are the most convenient, as the material could fit snugly over the sample, but would not wear down the sample material by friction on account of being much softer. Plastic was also judged (and proven in practice) to be sufficiently pliable to enable removal of the ring after experiment.

Just as in section 4.3.2.1 the total mass losses and steady state wear rates were obtained. A smaller number of samples were studied, since experiments running at relatively low or relatively high normal loads repeatedly failed to run to completion. Despite extensive investigation, the cause could not be identified. Total mass losses are shown in Figure 74, steady-state wear rates in Figure 75. The final debris bed thicknesses, which are assumed to be close to H_{max} for this material, are shown in Figure 76.

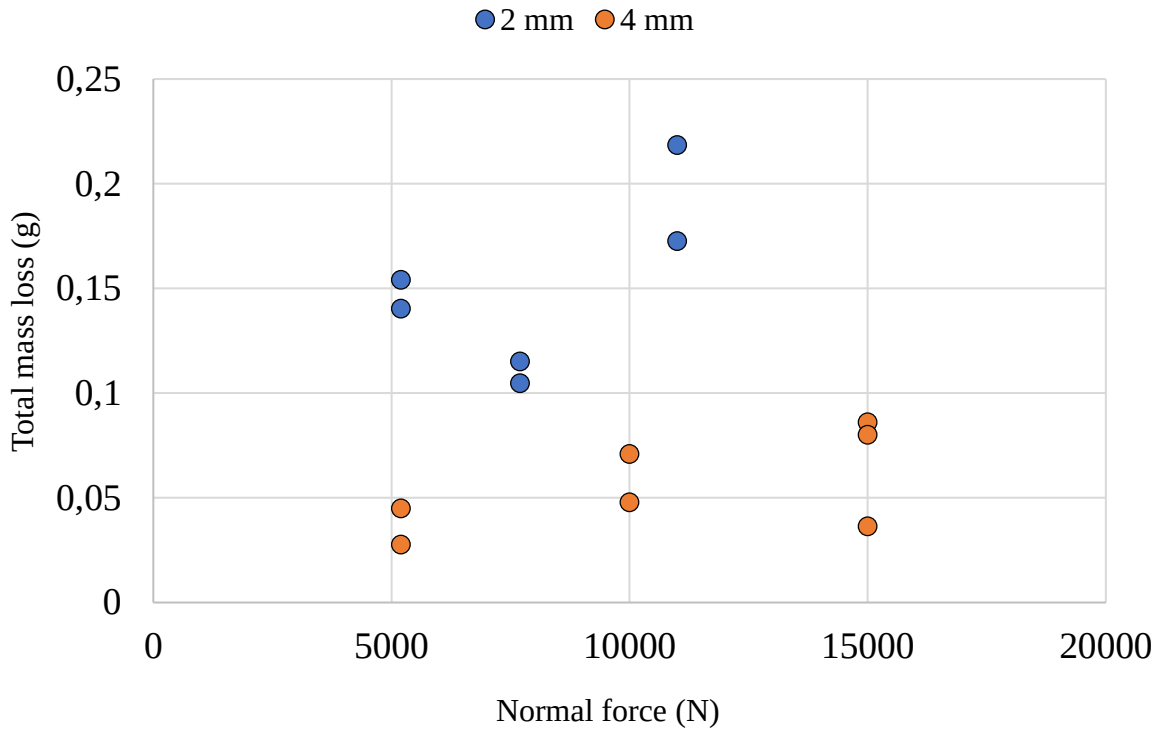

Figure 74: Relationship between normal force and total mass loss in wear (debris ejection restricted).

As before, the total mass lost in wear is not increasing linearly with normal load, however, the number of data points is small. The fact that steady state wear rate (Figure 75) appears to decrease with normal force could be explained by higher normal forces leading to smaller vertical oscillations of the sample. It is suspected that vertical movement of the sample against entrapment rings contributed to leakage of wear debris. There appears to be little difference in terms of total wear mass loss or steady-state wear rate compared to the experiments in section 4.3.2.1. This could indicate that the entrapment rings were not very efficient at entrapping the wear debris.

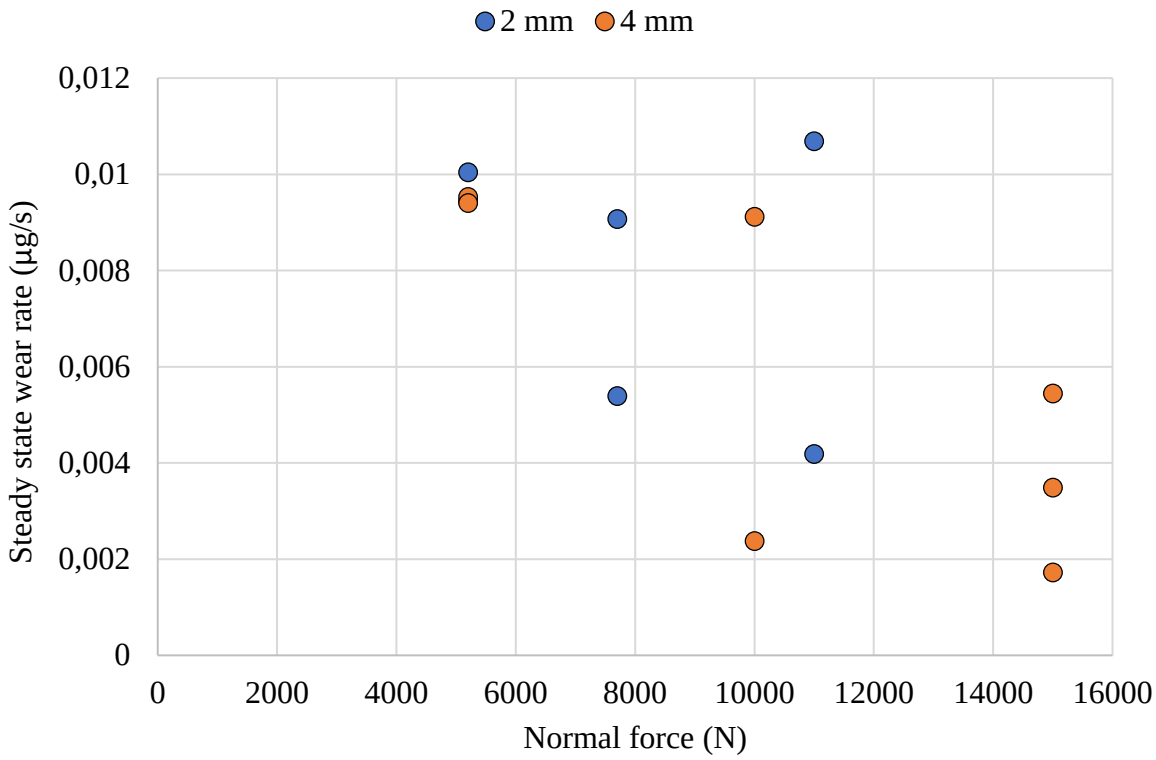

Figure 75: Steady-state wear rates (debris ejection restricted).

The debris bed thickness was measured using the approach described in 3.2.8. The measured values are shown in Figure 76. Since the measured thickness depends on the extent of entrapment obtained, the scatter of data can be explained through the variations in debris leakage through the entrapment rings, which would depend both on condition of the ring, the geometrical tolerances between the wear samples and the entrapment ring and possibly also on oscillations of normal force mentioned earlier.

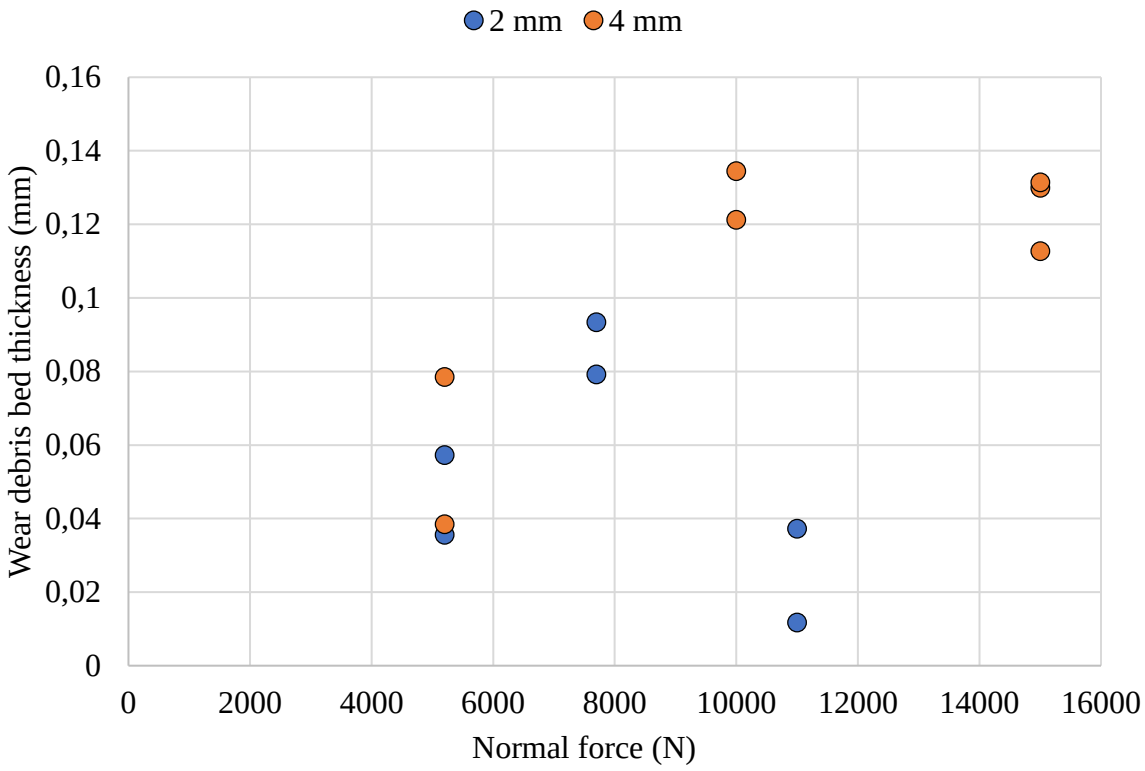

Figure 76: Debris bed thickness at the end of experiment (debris ejection restricted).

4.3.2.4 What governs the maximum debris bed thickness?

H_{max} is the debris bed thickness at which no further particle detachment occurs (i.e. wear, defined as damage to the wearing bodies is totally supressed). The energy flowing into the contact in the form of mechanical motion is thus completely dissipated in ways that do not cause damage (delamination, cracking, plastic straining, oxidation etc) to the wearing bodies. Since the model of Fillot, Iordanoff & Berthier has received little attention in the tribological community no previous studies on what dictates the magnitude of H_{max} have been identified. The original authors demonstrated that wear does decrease linearly towards zero with increase in debris bed thickness H, but did not elaborate on the process or mechanism causing this behaviour to occur.

Some hypotheses can be put forward however.

At least early as Archard's work (104) wear was interpreted as the result of collision and shearing of asperities. As the debris bed grows, the asperities are eventually unable to collide, since the thickness of the wear debris bed is larger than the combined vertical prominence of asperities on both wearing bodies. Based on this reasoning, it can be hypothesized that there exists a connection between the roughness of the post-wear profile and the debris bed thickness. This hypothesis is easily tested by plotting the debris bed thicknesses measured as a function of

surface roughness parameters. The results for the 2 mm wide rings are shown in Figure 77, results for 4 mm rings in Figure 78.

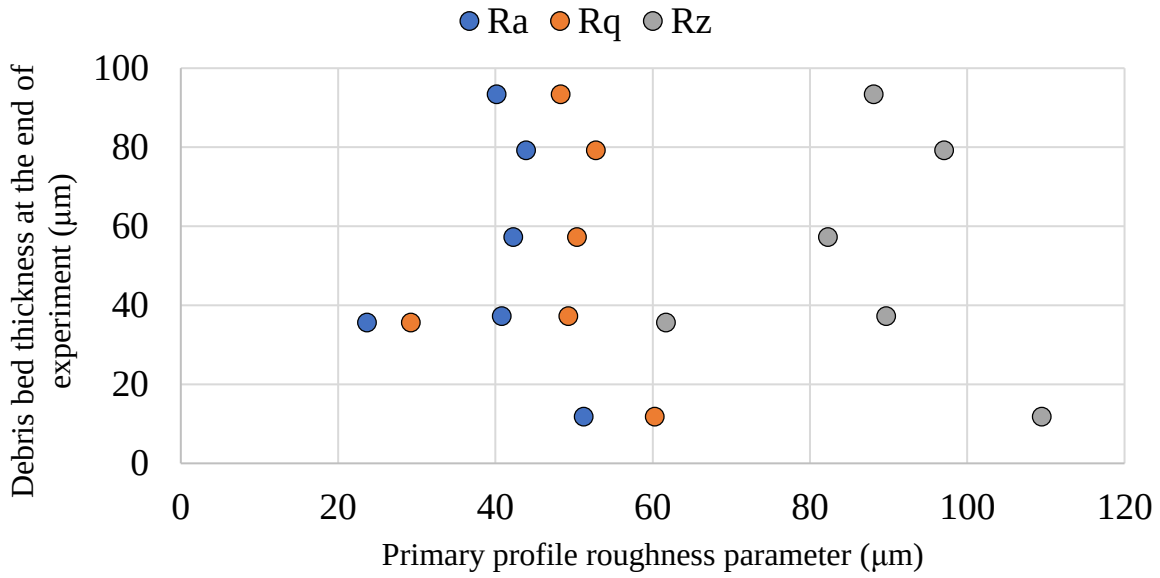

Figure 77: Debris bed measured (restricted debris egress) vs post-wear primary profile roughness for 2 mm wide rings.

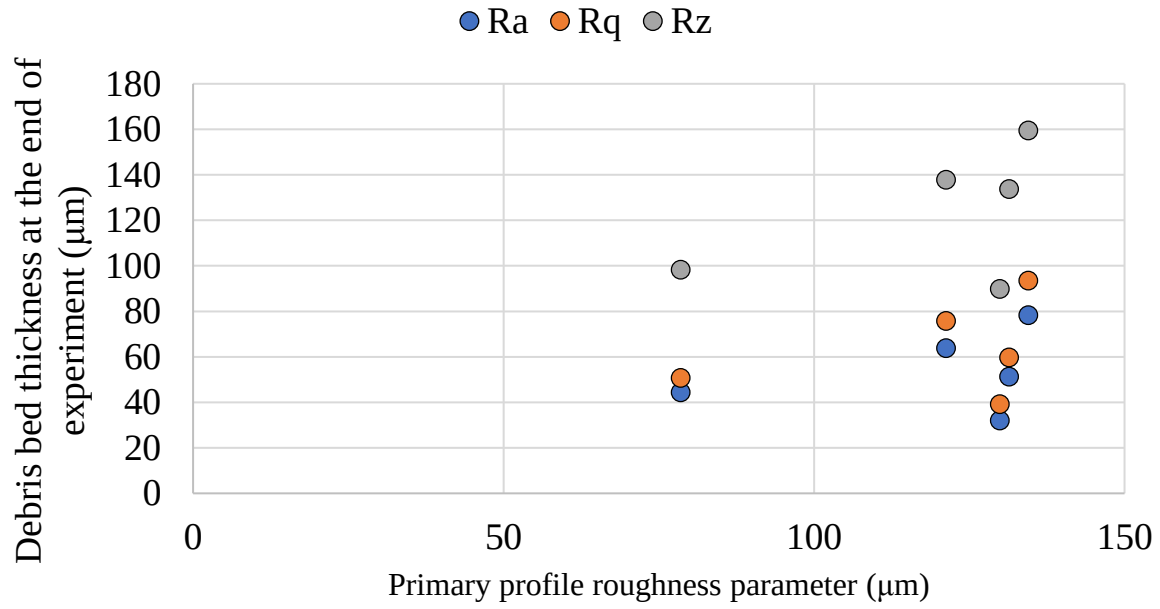

Figure 78: Debris bed measured (restricted debris egress) vs post wear primary profile roughness for 4 mm wide rings.

The results are at best inconclusive; in 2 mm rings (Figure 77) no trend is observed. In 4 mm rings (Figure 78) four data points for each parameter are bunched in a loose group, but there is also a significant outlier in each case. The 'separation of surfaces' hypothesis cannot be confirmed at this point.

The second hypothesis begins with the observation of sub-surface cracking patterns. Nurmi et al. (62) provide an excellent example of subsurface cracks in steel growing at an angle to the worn surface, eventually forming double-wedge like structures, measuring some 100 µm in size (Figure 79). Similar development is reported by (16).

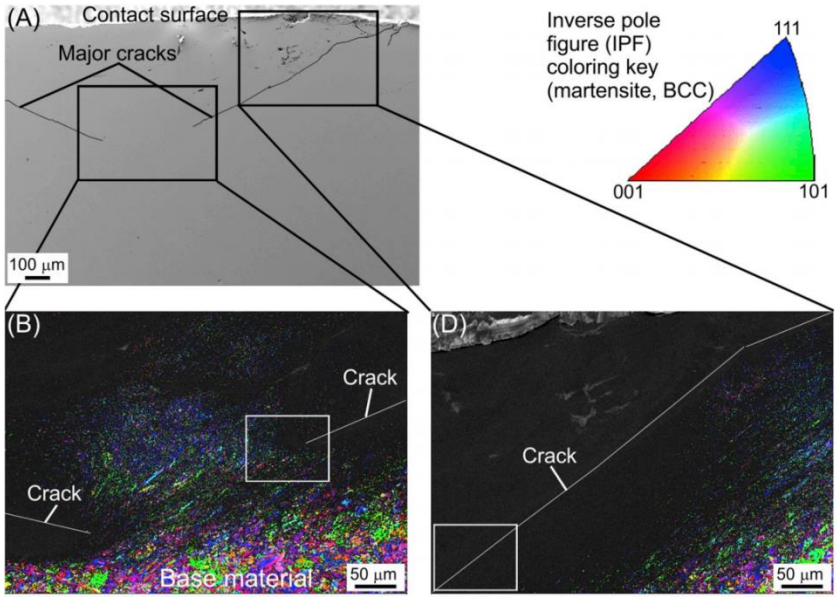

Figure 79: Subsurface cracking in steel (62). Main crack A), zoom to crack tips B) Zoom to the crack C).

In principle, if the frictional force acting on the surface of such double wedge is large enough, the particle will lift itself up the incline against the contact pressure and be swept into the debris bed. Consider an idealized example of a wear debris particle shaped like symmetrical double wedge (Figure 80). In order for the particle to slip out of position, the distributed shear traction ν must overcome the contact pressure p_N and the static friction between the particle and the first body (f) (friction force only applies to one sloped surface, since the particle is pushed away from the other surface. Once the particle moves, it lifts itself into the debris bed, which can then sweep it away.

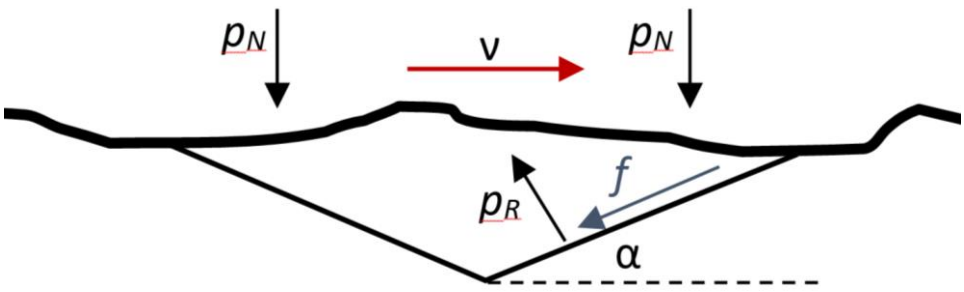

Figure 80: Schematic of a double wedge wear particle.

The balance of forces is given by the vector inequality (f_s being the coefficient of static friction, f_C being the coefficient of friction for the wearing contact):

$$\begin{bmatrix} \nu - p_R \frac{\sin\alpha}{2\cos\alpha} - p_R f_s \frac{1}{2} \\ -p_N + p_R \frac{1}{2} - p_R f_s \frac{\sin\alpha}{2\cos\alpha} \end{bmatrix} \geq \begin{bmatrix} 0 \\ 0 \end{bmatrix} \quad \textbf{33}$$

Expressing the distributed shear traction as $\nu = p_N f_C$ following inequalities can be written:

$$p_N f_C \geq \frac{p_R}{2}\left(\tan\alpha + f_s\right) \quad \textbf{34}$$

$$\frac{p_R}{2}\left(1 - f_s \tan\alpha\right) \geq p_N \quad \textbf{35}$$

Expressing p_N from eqn. 34 and inserting into eqn. 35 the slip condition for the particle:

$$\frac{p_R}{2}\left(1 - f_s \tan\alpha\right) \geq \frac{p_R}{2f_C}\left(\tan\alpha + f_s\right) \rightarrow f_C - f_s - \tan\alpha\left(f_C f_s + 1\right) \geq 0 \quad \textbf{36}$$

From eqn. 36 it follows that particles will only be removed from the points of their generation at certain combinations of f_C, f_s and α. The limit case is an infinitely thin flat particle ($\alpha = 0$), which will move only if the coefficient of friction for the contact is larger than the coefficient of static friction for the material. In short, wear can only take place if $f_C > f_s$. Real values of α are larger than zero, requiring larger values of f_C for wear to progress.

Detailed examination of this hypothesis is quite complex. While the coefficient of friction in the contacts studied changes over the duration of the experiment in line with commonly observed pattern (see discussion in section 2.2.5), it also changes over the course of one wear cycle. Due to the roughening of the surface, the normal force oscillates as the surfaces slide against each other and the loading frame is trying to compensate the vertical positioning accordingly. Every time the direction of rotation is reversed, the residual elastic strain in the sample and wear rig needs to be overcomed. This hysteresis causes the magnitude of the shear force to dip after each reversal. This is shown in Figure 81.

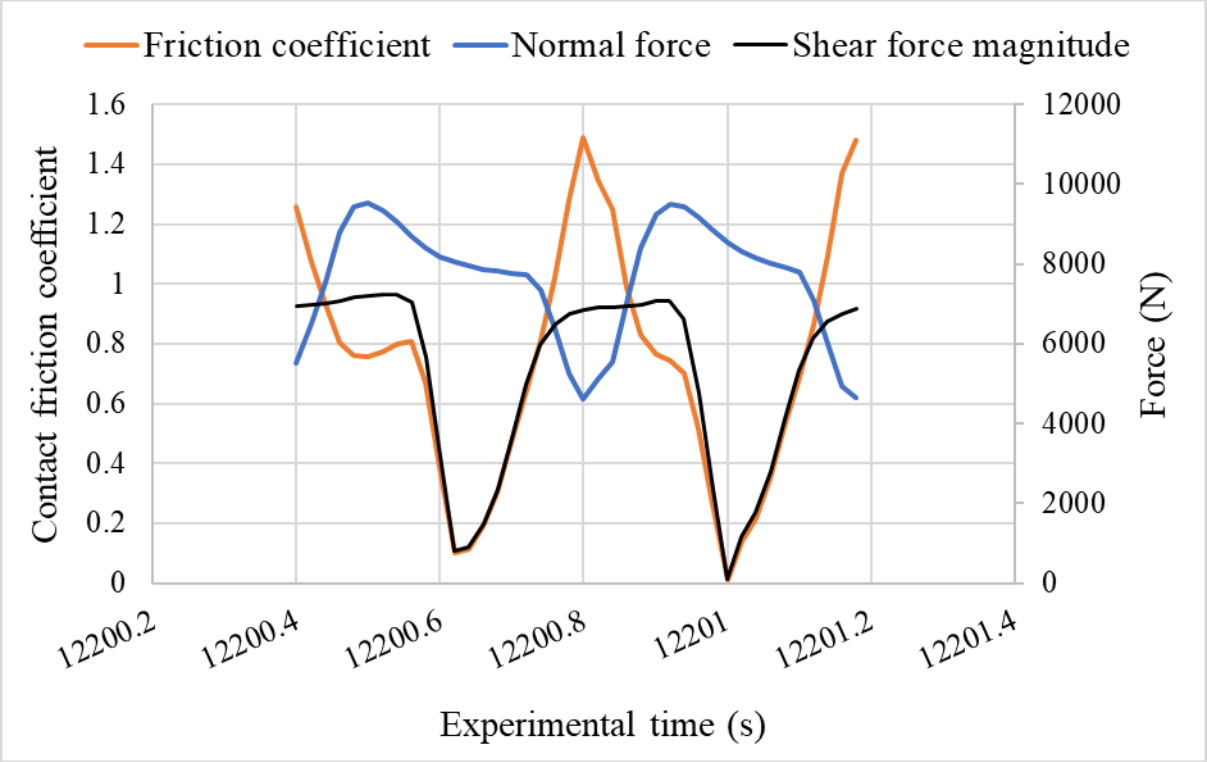

Figure 81: Variation in normal force, shear force and friction coefficient in one steady-state wear cycle for a 2 mm ring at nominal normal force of 7700 N.

In order to test the hypothesis, the friction coefficient values measured in the final 1000 cycles of each experiment were averaged; results are shown in Figure 82.

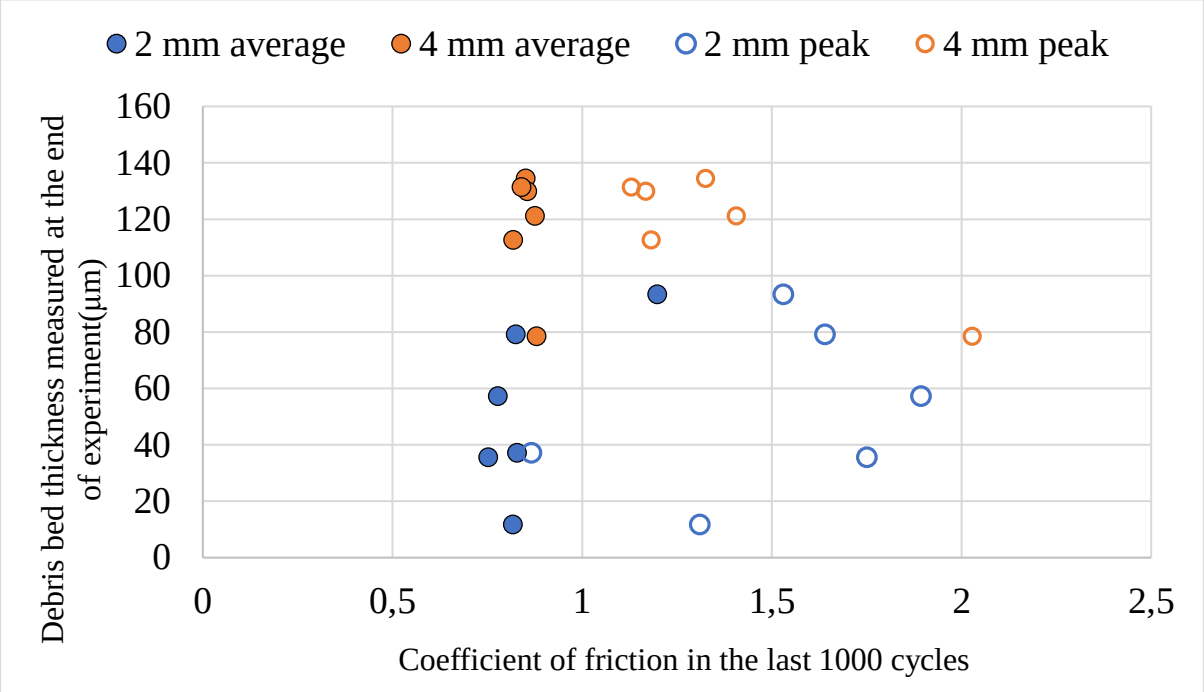

Figure 82: Debris bed thickness, average and peak coefficients of friction for the final 1000 cycles. Debris egress restricted.

The average coefficient of friction over 1000 cycles is usually approximately 0.85, apart from three outliers. However, the corresponding values of debris bed thickness vary considerably, indicating that the magnitudes might not be linked. The peak coefficients of friction found in the same set of cycles are however much larger, with only one value smaller than 1 (also shown in Figure 82). Most sources also agree that the coefficient of static friction between aluminium surfaces is of the 1.05-1.4 range (162; 163; 164; 165), which is significantly above 0.8. According to the hypothesis, wear ought to be completely suppressed. However, examinations of the vertical position indicate that wear continues, albeit at a low rate. The large peak values of the friction coefficient help to explain this contradiction: the wear rate is low, because the contact spends a portion of time in a regime, where the coefficient of friction is sufficiently low, to prevent the particles from being dislodged. The results are congruent with the hypothesis. There even exists a weak linear relation between the peak coefficient of friction in the last 1000 wear cycles and the steady state wear rate (Figure 83).

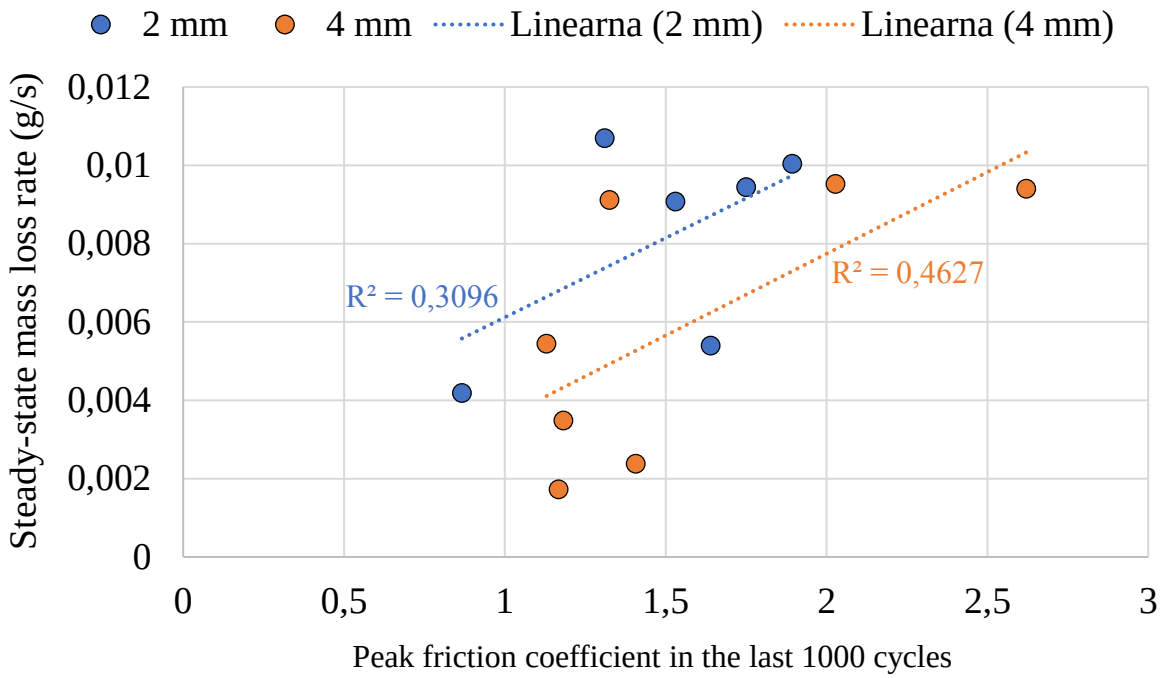

Figure 83: Peak coefficient of friction and steady-state wear rate in 2 and 4 mm wide annuli (debris egress restricted).

4.4 Towards a new wear model – outcomes

Noting the conceptual strength of the Fillot, Iordanoff & Berthier model, a series of experiments was designed to examine their assumption that the length of the debris ejection path influences debris entrapment. In the process, the concept of average debris ejection time was introduced as a quantitative measure of debris entrapment (section 4.2.2.2), which is to a degree a novel development, since entrapment was more commonly described only qualitatively, not quantitatively. It was demonstrated that debris entrapment depends on the interplay of ejection path length (which is linked to the contact geometry) and worn surface roughness and debris particle size (which are self-establishing lengthscales). The importance of worn roughness as a wear-regulating parameter does not appear to be stressed or explored to any significant degree in previous published works. According to an extensive study of available literature, this is also the first systematic study of wear in annular contacts of different widths.

Focusing on the question of debris bed thickness, a series of experiments were carried out determining the thickness of the wear debris bed and noting that wear is not linearly dependent on normal force, an observation in line with several independently published works on annular contacts (86; 109), but so far lacking explanation. Applying the model of Fillot, Iordanoff and Berthier, it was demonstrated that the model reacts in a manner similar to the observed trends at the values of parameters typical in experimental studies. This not only gives additional credence to the model, but also appears to be the first explanation proposed for the non-linear behaviour observed.

It was hypothesized (based on published observations of under-surface cracking in wear (62)) that the maximum debris bed thickness could be caused by the growth of the wear debris bed limiting the dislodgment of debris particles due to reducing friction. The experiment was impeded by imperfect debris entrapment (debris egress was restricted, but not completely prevented), but the friction coefficient was found to oscillate between the 'wear' and 'no wear' values. This is consistent with the low wear rates observed and could indicate the hypothesis is correct.

The experiments presented are limited by typical limitations of traditional tribological methods. Each data point requires a separate wear experiment, which is conducted using samples of slightly different composition, crystal structure and hardness and in different environmental conditions, such as temperature and air humidity. This makes the process slow, resource intensive and gives opportunity for many sources of experimental noise to appear.

5 PILOT IN-SITU OBSERVATIONS OF WEAR[2]

The in-depth investigation of wear in annular contacts presented in chapter 4 opens a number of questions. While the thickness of the wear debris bed plays a crucial role in the FI&B model, no real information was gathered about how the bed actually looks like, how are the particles created or changed in it, what its local thickness might be etc. Likewise, FI&B model predicts only material removal and ejection rates, but does not provide information about where the wear might initiate or what the worn surface profile would be. Indeed, given the importance of the surface profile on debris entrapment, identified in section 4.2.2.3, a method for observing the profile while the wear is ongoing would be very valuable from the experimental standpoint. In short, the outcomes of the experiments described in chapter 4 indicate that additional understanding of the processes involved could be obtained by observing the progress of wear, without disturbing it.

5.1 The need to observe wear

In chapter 4 wear was studied mainly through ex-situ, post-mortem quantification, with the addition of on-line measurements of the forces and displacements involved, enabling steady-state wear rates and coefficients of friction to be established. This was a very conventional approach: combining profilometry, microscopy, metallography and other techniques (27) to reveal the end state of an individual wear experiment is typical for the field. To study the *process* of wear, repeated experiments are usually required with the wear process interrupted at different stages, which is time-consuming, costly and presents issues of repeatability (as indeed is demonstrated by significant scatter in the data discussed in sections 4.3.2.1 and 4.3.2.3).

Seeing things that profilometers and weight scales cannot capture is therefore of great importance to tribological studies and could change the very nature of the experimental approach from wearing many samples to observe their respective end-states to observing the progress of wear on one sample. As discussed in section 2.2.4, the most common method for real-time in-situ *observations* of wear and other tribological phenomena is the use of transparent counter-bodies (79; 78; 74; 166) and Godet attributed his observations of wear of chalk against glass as fundamental to the formulation of the third-body concept (97; 77; 76). Use of optically transparent wear bodies, however, introduces new variables associated with the material of the counter-body and inevitably changes the nature of the contact.

[2]Chapter 5 is based on paper of Aleksejev et al. (2)

5.2 Utilization of penetrating radiation

X-ray imaging methods provide a potential alternative solution to this problem by enabling non-destructive measurement with appropriate resolution. This was demonstrated by researchers at the Materials Research Laboratory, Nanyang Technological University (80; 81; 82; 83) who used X-ray microscopy to investigate in-situ the wear scars and wear debris beds in a variety of contacts. Unfortunately, their works appears to have passed unnoticed in the general tribological community and have not been developed further since.

Over the past twenty years X-ray computed tomography has been put to a variety of uses in tribology, including ex-situ measurements of worn profiles in 3D (33; 32; 34), in-situ observation of Couette flow in granular materials (167), ex-situ (168; 169; 170; 171; 172) and in-situ (173; 84; 174) investigation of fretting and rolling fatigue crack form and propagation. However, there appears to have been no attempt to use X-ray tomography to image the actual wear zone with the wearing bodies in contact. The closest studies found in the literature are by Cornuault & Carpentier (175) who obtained post-weld tomographs of the welded zone in linear friction welds and by Mandard et al. (147) who used X-ray tomography to observe the change in porosity of an abradable porous layer caused by sliding wear and also to observe the morphology of individual wear debris particles. However, this was done ex-situ and no attempt was made to image the wearing bodies in contact or observe the particles before they were ejected from the debris bed.

Based on the successes of imaging cracks, ejected debris particles and similar small features using X-ray computer tomography (CT) it seemed very likely that the worn surface can be resolved in-situ using this technique. From the literature and from previous experimental experience it was known that the worn surfaces are typically much rougher than the virgin surface (see sections 4.2.2.3 and 4.3.2.4) and the debris particles produced range from tens to hundreds of micrometres in size (176; 57). Since features on such scales have been resolved using X-ray CT before, success seemed certain. In order to conclusively demonstrate the feasibility of using X-ray CT for collecting observations of wear and strengthen any future research proposals for an in-situ tomographical imaging experiment at a synchrotron facility, a small-scale imaging experiment was devised using an Xradia Versa 510 micro CT system (Zeiss, Germany).

5.3 The experiment

The details of the experiment design and operation can be found in sections 3.3.1 and 3.3.2. Samples with an annular contact of external diameter of 4 mm and internal diameter 2 mm were used (Figure 50A), as the relatively low brightness of the X-ray source necessitated small dimensions while the axisymmetric annular geometry lends itself to simple image processing and has been used extensively throughout this work. To minimize imaging time further, a material with low X-ray attenuation (aluminium alloy 6082T6) was chosen. This material is unlikely to be used in any industrial application where significant wear is expected, but as this is a laboratory-scale proof of concept study, the direct applicability of results is not required.

5.3.1 The sample

Sample design is described in detail in section 3.3.1. Each sample element was mounted on the sample holder using a grub screw. Sample elements are locked together using a polycarbonate clamping tube and a pair of small jubilee clips (Figure 50C).

5.3.2 Experimental parameters

In total, five experiments were conducted, using the parameters shown in Table 7. The experimental parameters provide variation of normal load, and distance slid (distance calculated at the mid radius of the contact) which are two key parameters believed to influence wear in accordance with Archard's law (104). The expectation was that these parameters may influence the morphology of the worn region.

Axial force (N)	Sliding time (s)	Total distance slid (mm)
45	300	1884
45	900	5652
130	60	377
130	300	1884
130	900	5652

Table 7: Experimental parameters.

5.4 Imaging

The clamped sample was imaged using an Xradia Versa 510 micro CT system (Zeiss, Germany)[3]. The voxel size of 2.47μm was chosen as the smallest realistically possible with the setup and time available; tube voltage was set to 100 kV (tungsten target) and exposure time to 8 seconds per projection to give a good balance of image brightness and imaging time. The total exposure time was approximately 8 hours, with the output volume occupying approximately 2000x2000x2000 voxels.

5.4.1 Image processing

Image processing and 3D rendering was performed using Aviso 9.7.0 (ThermoScientific, USA) and FIJI (177) image processing software.

Using Avizo software, a 3D representation of the worn contact can be made, as seen in Figure 84. The tomograph consists essentially of two regions, 'metal' and 'air'. By supressing the 'air' region, the shape of worn sample is revealed. The resolution of the tomograph is sufficient to show the extensive burring and scuffing, as well as particulate matter attached to the surfaces. The 3D render provides an overview of the exterior of the worn sample.

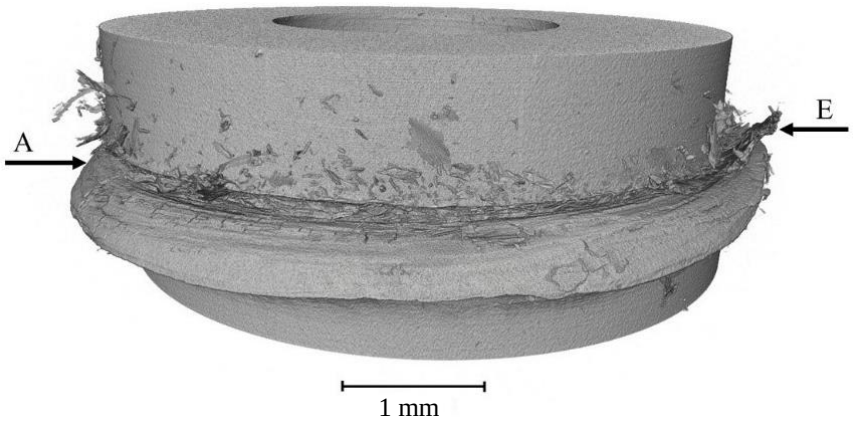

Figure 84: 3D render of the worn sample (axial height approximately 560 slices or 1.38mm). Normal force: 130 N, sliding time: 300 s. A and E mark the positions of two axial slices, which are 300 μm apart.

[3]**XRadia Versa was operated by Yijun Lim, then student in the Department of Materials, University of Oxford.**

5.4.2 Axial slices, the wear scar and plastic deformation

Axial cross-sections reveal the shape of the wear scar and the wear debris particles entrapped. In Figure 85, an axial slice is superimposed on the 3D render of the worn sample, which has been made translucent in order to show the relationship between the axial slice and the sample geometry. Figure 86 shows a series of axial slices giving an insight into the structure of the debris bed; the positions of slices A and E relative to the sample are marked in Figure 84.

Axial slice A is taken just below the wear scar and clearly shows the local increase in diameter due to plastic deformation near the contact, despite the nominal contact pressure being *below 10% of the yield stress* of the 6082T6 alloy. Separate tests using reciprocating annular contacts have indicated that the extent of plastic deformation increases strongly with accumulated sliding distance and increasing displacement amplitude. The extreme plastic deformation observed is therefore credited to the use of unidirectional sliding in the experiments dicussed here, rather than small-amplitude reciprocation/fretting. Given the already low nominal contact pressure it is unlikely that using smaller normal loads and longer accumulated distances would make a meaningful difference in reducing the extent of plastic deformation.

Also visible in slice A are small cracks developing in the plastically deformed fringes of the sample. Slices B-D are taken from close to the centre of the worn region and show deep pits in the worn surface, which appear across many slices. Also visible are wear debris particles that are trapped in the wear scar. Slice E is taken from above the wear scar, where the slice geometry is almost unaffected by wear. Thin slivers of material can be seen outside the main body of the sample; these appear to be the edges of thin burrs connected to the sample. A series of axial cross-sections can also be joined into a video showing the debris bed from the perspective of an observer moving along the central axis of the contact.

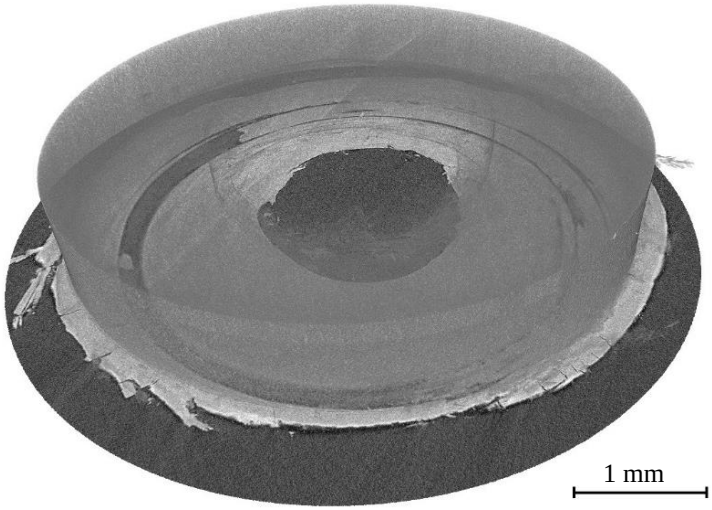

Figure 85: Axial cross-section in Avizo. Normal force: 130 N, sliding time: 300 s, sample elements made translucent for clarity.

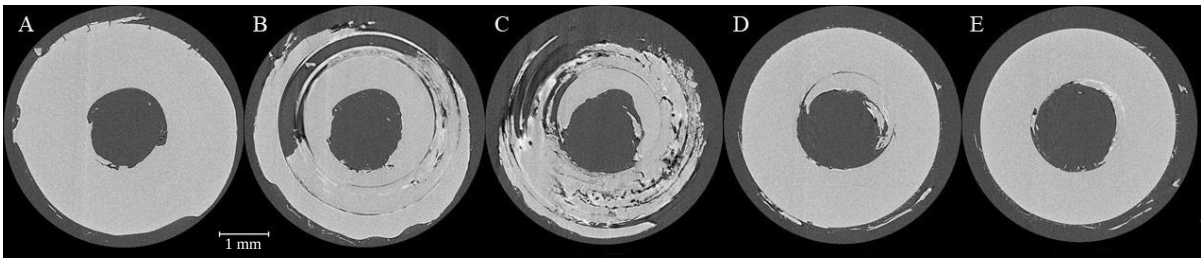

Figure 86: Axial cross-sections through the worn region; sections A and E correspond to positions shown in Figure 84. Lighter areas represent metal, darker areas air. Axial distance between sequential slices is 74 μm. Normal force 130 N, sliding time 300 s.

By examining each axial slice, the uppermost and lowermost point at which mechanical damage to the surface of each sample element appears, can be determined. The axial distance between these two slices defines a total depth of wear scar, that is, the axial distance between the bottoms of the deepest surface pits on either of the contact surfaces. The total wear scar depths measured in this way are shown as a function of normal force and sliding distance in Figure 87. The total depth of the wear scar represents an upper bound on the debris bed thickness. Locally, the debris bed thickness can vary from zero (first body contact) up to the total depth of the wear scar. The wear debris bed thickness is of great significance in the FI&B model (section 2.3.2) however, measuring the debris bed thickness without interrupting the wear process remains challenging with traditional techniques (see section 4.3.2.2).

In Figure 87, a generally increasing trend of wear scar depth with distance slid can be seen; somewhat unexpectedly lower normal load also led to a much larger total wear scar depth in one case, however, as only limited quantity of data was collected, no specific relationship can be determined.

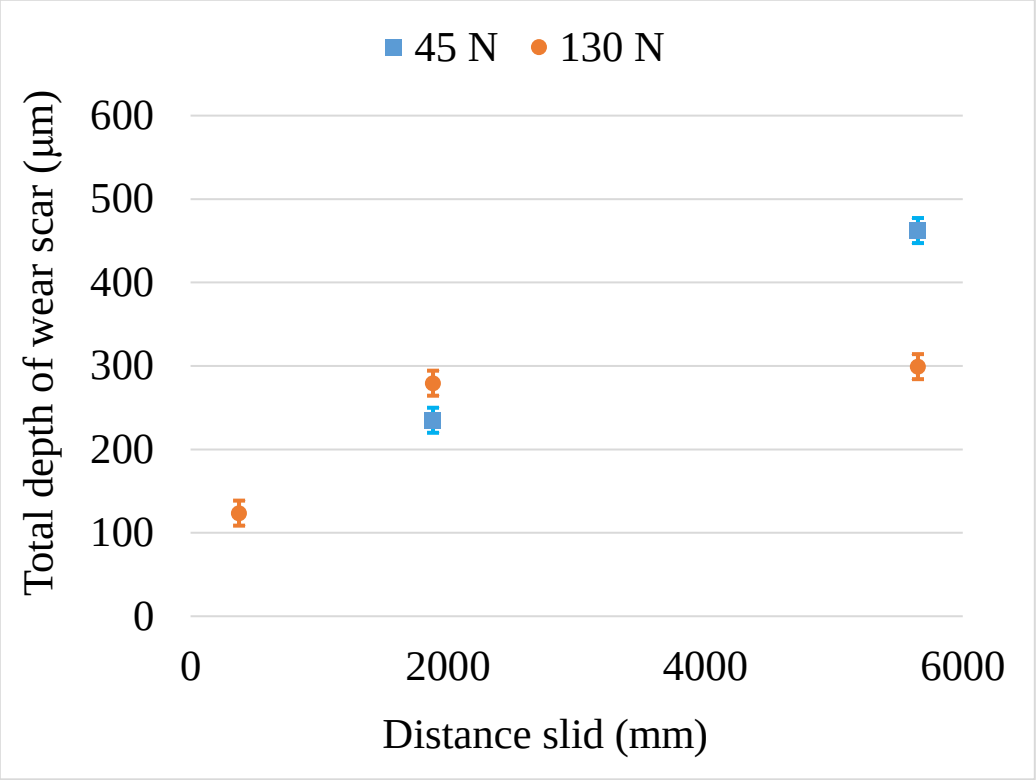

Figure 87: Total depth of wear scar as a function of normal force and sliding distance. Error bars show the absolute error of measurement.

Extensive plastic deformation can be observed near the edges of the contact zone, with the edges curling outwards. To study the extent of this deformation, axial slices are examined one by one. Far from the wear region, circles are fitted to the outer and inner diameter of the samples. The slices in the worn zone are examined and the diameter of the circles adjusted so that the extreme edge of the metal region touches the edge. The change in diameter of both circles thus gives a measure of maximum plastic deformation that has occurred at the inner and outer edge of the contact. The results are shown in Figure 88.

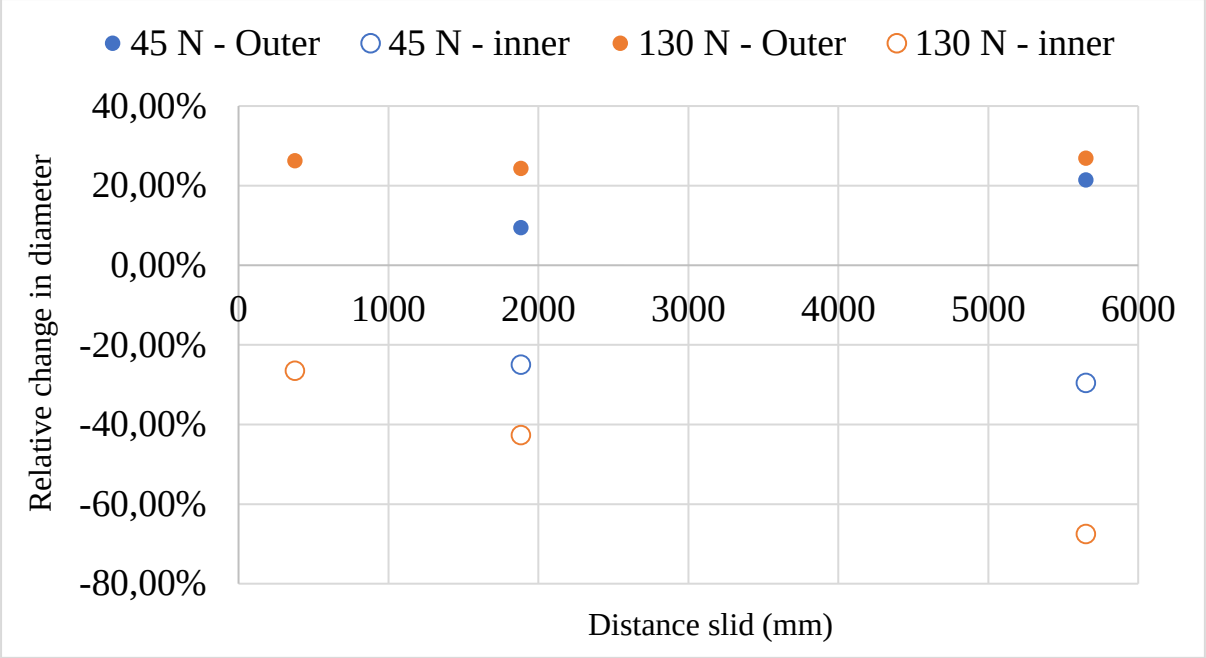

Figure 88: Maximum plastic deformation at the contact edges as a function of normal force and distance slid.

Such significant deformation is remarkable given the low nominal pressure.

5.4.3 Radial slices and radial surface profiles

Figure 89 shows a radial slice through the worn region superimposed on the 3D render of the sample. Radial slices can be made in any number and in any orientation, revealing the material entrapped between the surfaces of the first bodies and severe roughening of the surfaces. Figure 90 and Figure 91 show examples of typical radial slices. Figure 90 also shows the lines representing the total depth of the wear scar on that slice, to help visualize the concept referred to in section 5.4.2.

An advantage in comparison to conventional metallography is that every part of the sample can be viewed without damage to the debris bed or the sample. To give a direct comparison between tomography and metallography, a sample element (worn at normal force of 130 N for 900 s) was sliced using a diamond saw, mounted in resin and wet ground with abrasive papers up to 2500 grit. Figure 92 shows the optical metallographs obtained alongside a corresponding tomography slice from the same sample, displaying excellent agreement between the two.

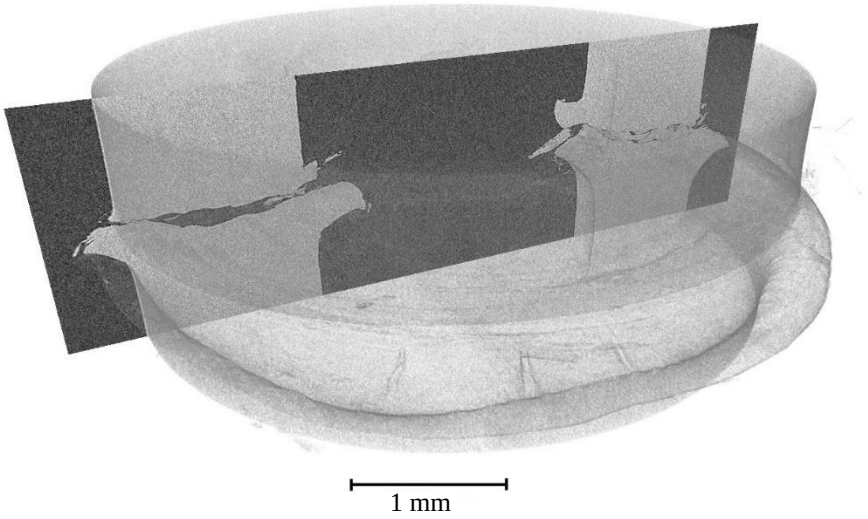

Figure 89: Radial cross-section in Avizo. Normal force: 130 N, sliding time: 300 s. Sample elements made translucent for clarity.

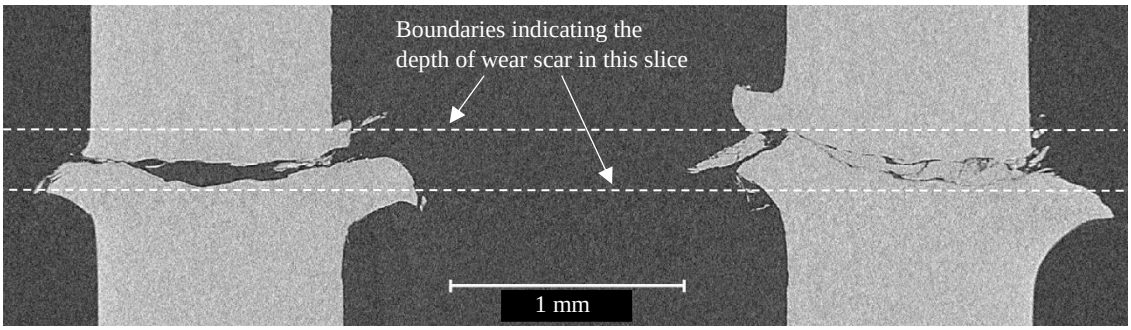

Figure 90: Radial cross-section of the worn annulus. Normal force 130 N, sliding time 300 s. Depth of the wear scar shown is less than the total wear scar depth, which is the difference between the highest and lowest point in the entire contact.

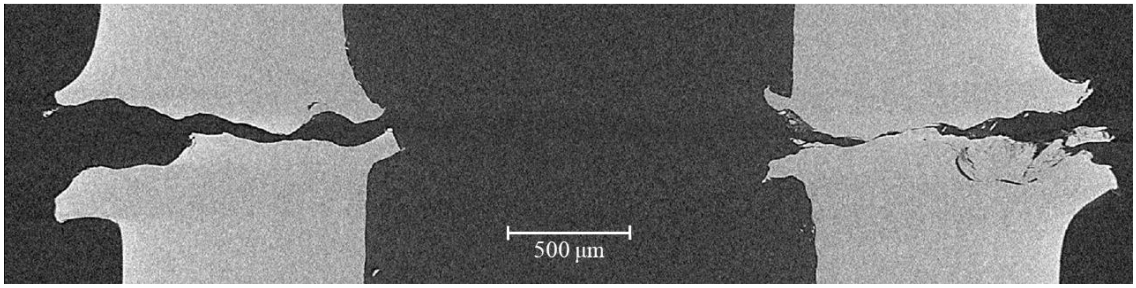

Figure 91: Radial cross-section of the worn annulus. Normal force 45 N, sliding time 900 s.

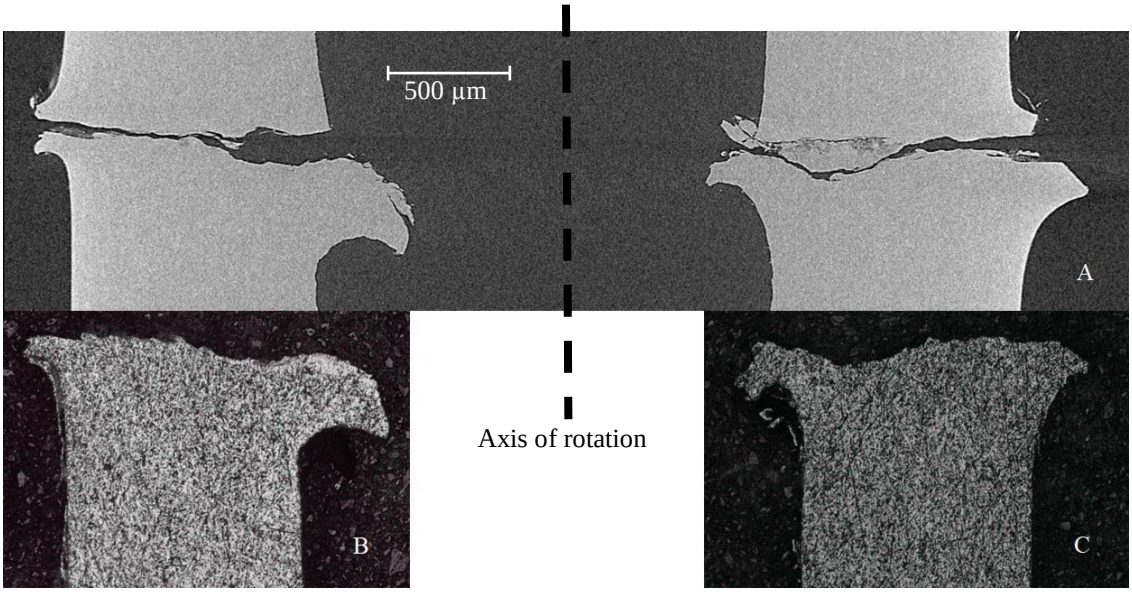

Figure 92: Section comparison. Radial tomography slice (A). Optical metallographs of the same sample element (B, C). Normal force 130 N, sliding time 900 s.

Radial cross-sections enable the direct visualisation of the wear debris bed in a fashion not even accessible to experiments with transparent counter bodies. While the concept of debris bed thickness features prominently in the model of Fillot, Iordanoff & Berthier, Figure 90-Figure 92 reveal a rather complex picture; often the large gouges in the worn surface are simply empty, sometimes the first bodies touch directly (local debris bed thickness being zero in both cases, even if the surfaces are dozens of µm apart!), sometime the debris bed is shown to be comprised of several large pieces filling the space between the first bodies etc.

From radial cross-sections, the primary surface profiles in the radial direction can be extracted, by tracing the outline of the metal region, extracting the trace as a coordinate set and trimming the set to only the contact surface. The resulting coordinate set can then be, at least in principle, processed to give standard roughness measurements. However, the resolution of the tomograph was only approximately 2.5 µm, making it impossible to detect surface features significantly smaller than that. In a practical sense, this limited analysis only to the assessment of primary profile roughness. Higher resolutions are in principle possible, but require longer imaging times and/or more advanced equipment.

To obtain each roughness estimate, several profiles were taken and the average of their roughness values computed. To compare the results with a conventional technique, two samples were disassembled and the sample elements scanned on an optical profilometer (InfiniteFocus, Alicona, Austria), taking eight radial profiles in arbitrary positions on the relevant surfaces, and the individual values averaged. Figure 93 shows the roughness values measured for tests using normal force of 45 N and a comparison with the Alicona data. This shows excellent agreement between the two measurement methods, indicating that tomography can provide reliable primary roughness data. Figure 94 provides similar results for the tests using normal force of 130 N, however agreement with the Alicona is less good in this case. For brevity only Ra roughness values are shown, although other measures (Rq, Rz) can be readily obtained as well. The 'lower' and 'upper' labels in Figure 93 and Figure 94 refer to the position of the worn surfaces with respect to the Xradia machine.

Based on this limited data set, it appears that the roughness tends to increase with distance slid, and hence, the development of the wear process. In contrast, changing the applied load did not greatly affect the surface roughness.

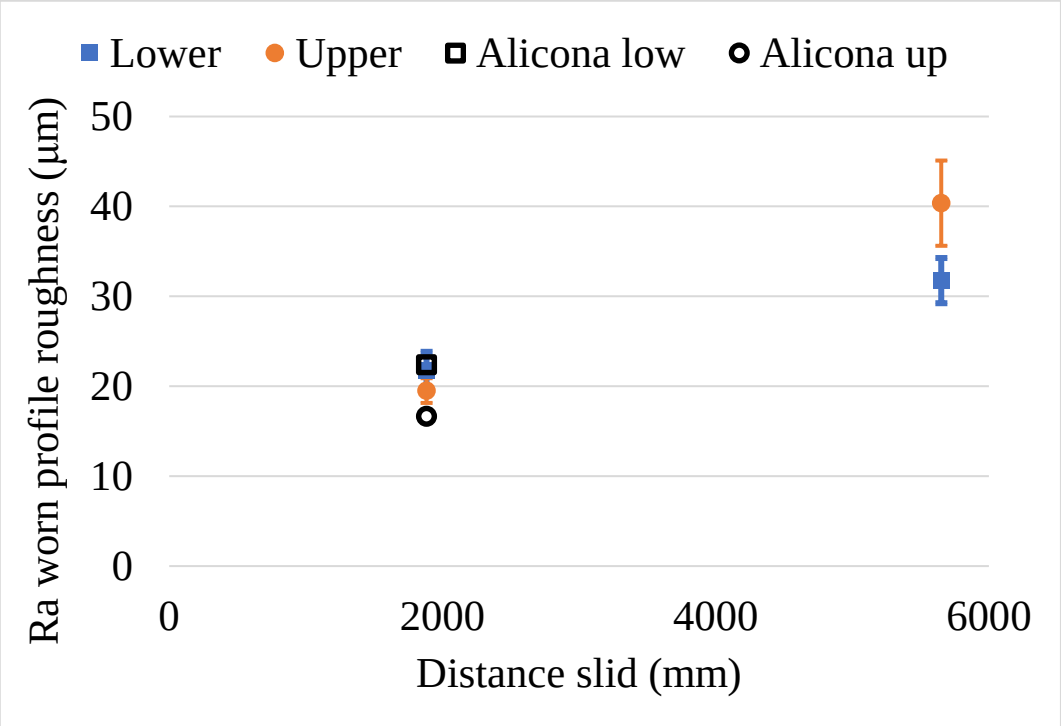

Figure 93: Worn Ra primary profile roughness obtained at normal force of 45 N. Error bars show standard error.

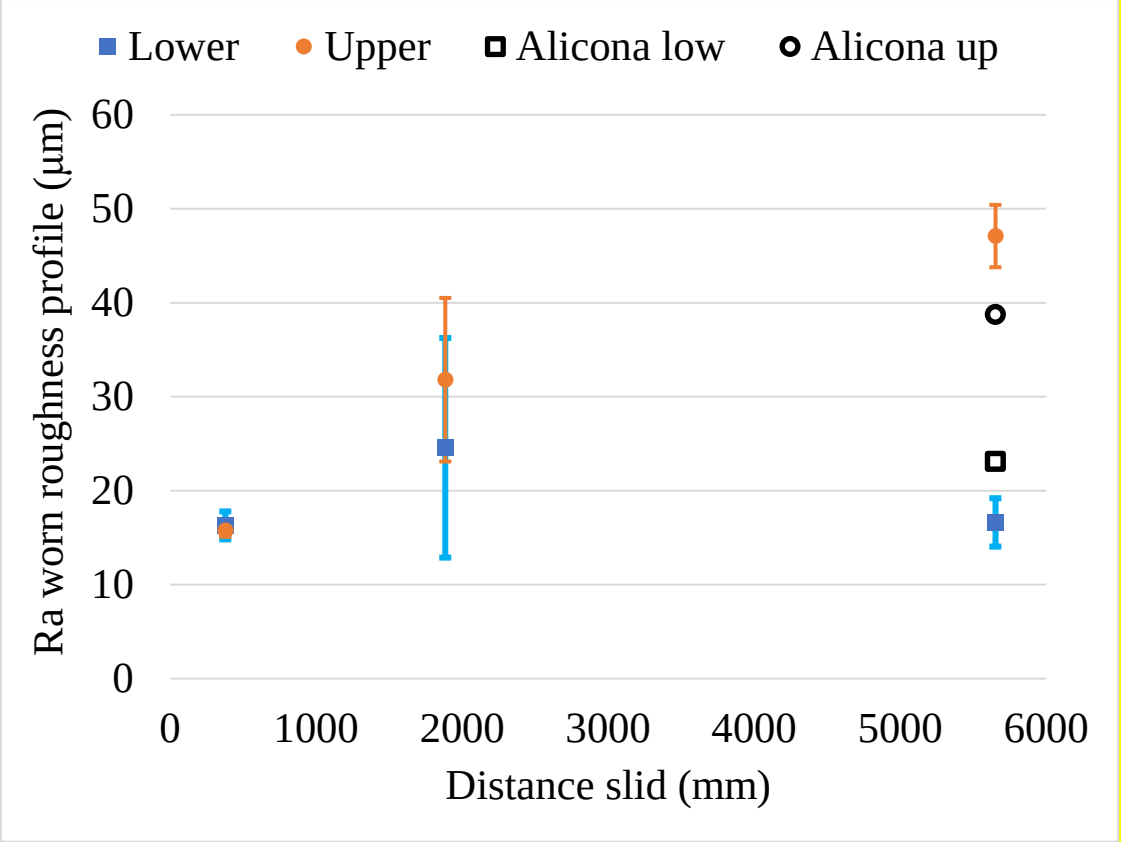

Figure 94: Worn Ra surface roughness obtained at normal force of 130 N. Error bars show standard error.

5.4.4 Real area of contact

The real area of contact is of importance in wear as the location of greatest local stresses and heat generation (178; 179; 180; 181). In electrical contacts, the real area is of importance to contact resistance (182; 183).

How is the real area of contact to be assessed? The real area of contact represents a contact between the first bodies. Finding the real area of contact therefore involves finding the area(s) where there exists continuity of the first body material (in this case metal) along the vertical axis of the contact. Viewing the 'air' region of the tomograph along the axis, should therefore reveal the area where there is no air i.e. the metal continues straight through the wear zone. A similar approach was developed independently by Fu et al. (81) and Zhang et al. (184), but was unknown at the time of the experimental work.

The process for obtaining the real area of contact is the following:

- The 'air' tomograph region is obtained (Figure 95A)
- The region is rotated so that it is viewed axially (Figure 95B). A number of irregular-shaped openings in the air region may be observed.
- A screenshot is captured and trimmed into a square with borders tangential to the edge of the blue region.
- The corners are filled in with a shade similar to that of the air region.
- Thresholding in FIJI was used to isolate the areas representing the real area of contact Figure 95C.
- The size of the black areas was calculated using FIJI as percentage of the entire picture.
- As the area of the picture is known, the real area of contact can be expressed in mm^2.

Note, however, that the limited resolution of the tomograph prevents accurate interpretation of features smaller than approximately 2 μm. Since the limit of resolution could cause either thin air gaps or sufficiently small points of contact to be misinterpreted, the computed area of contact could be either an underestimate or an overestimate. Contact regions smaller than 2 μm, yet spanning the typical wear scar depth seem relatively unlikely given Ra surface roughness of tens of microns. In contrast, air gaps of thickness less than 2 μm are more likely to occur because any gap located close to a contact region is likely to be thin. This positive contribution increases with the length of the contact area boundary. Given this, the resolution-related inaccuracies are likely to increase the apparent size of the contact area. In addition, cases where a surface asperity is so shaped, that the contact with the opposite surface lies outside the base of the asperity would not be identified by this process, and similarly with certain convoluted surface geometries (see discussion in (185)). The contribution of this effect to the total inaccuracy cannot be established conclusively, however repeating the imaging at several different resolutions could result in the real area of contact observed showing an asymptotic trend, giving an indication of what the true value might be. However, it should be kept in mind, that the contact area is also likely to depend on load applied to the contact.

Despite such limitations, X-ray tomography appears to be the only reliable method for directly estimating the real area of contact between rough/worn metallic bodies currently developed. Although a variety of computational methods for predicting contact area has been proposed (186; 140; 187), they require experimental validation and quantitative area measurements to verify their accuracy. This is reasonably straightforward for cases where the surface texture is known and the surfaces otherwise clean, but difficult in the presence of wear debris and without detailed knowledge of surface topography.

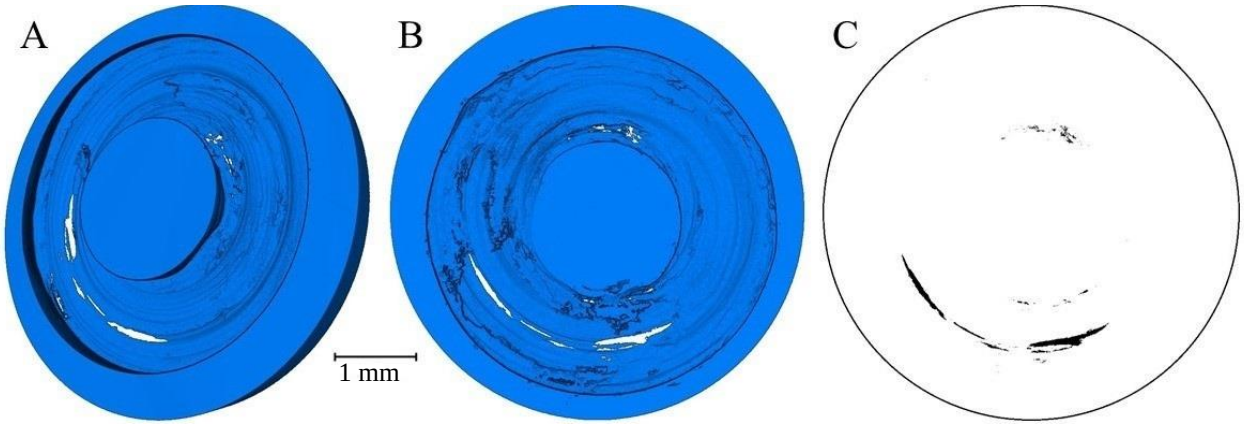

Figure 95: Views of the air region (A) 3D render of the air-region showing its general shape. (B) Axial view of the air region; white areas correspond to axial holes in the air region. (C) Post-processed image showing locations of direct contact between metallic surfaces; the circle represents the external diameter of the air region. Normal force 45 N, accumulated sliding distance 1884 mm.

The real contact area estimates (normalized with respect to the nominal contact area) are shown in Figure 96. In most cases, the real contact area is less than 4% of the nominal area and the distribution shown in Figure 95 is typical in that the majority of the real contact area is located in a crescent shaped cluster of patches. We note that increasing the load increases the measured contact area, though with limited data there is no observable trend in contact area versus accumulated sliding distance. The results obtained are in line with the widely held expectation of the real area of contact being small compared to the nominal area. Small contact areas are consistent with the FI&B model, which postulates that the wear process separates the wearing bodies through the creation of the debris bed layer.

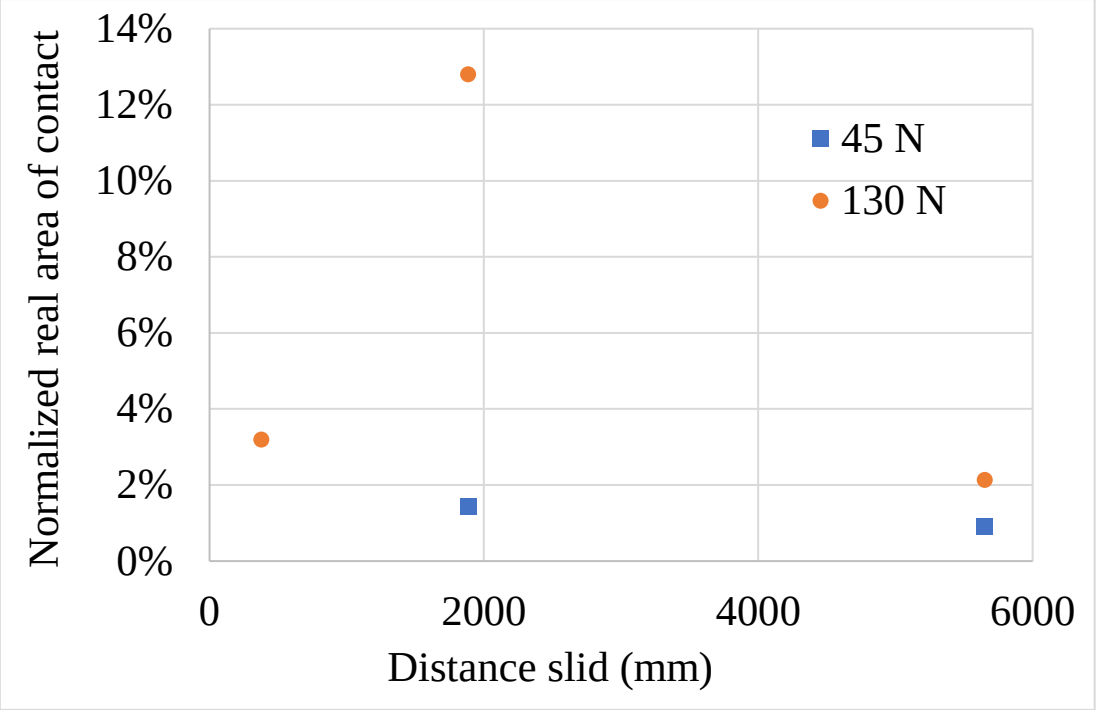

Figure 96: Normalized real area of contact as a function of normal force and sliding distance.

5.5 Pilot X-ray work - outcomes

The purpose of this work was to investigate and demonstrate the ability to collect observations of wear of metallic components without disturbing the wearing contact. This was successfully accomplished using X-ray tomography and the resulting data-set was shown to provide measurements of total wear scar depth, surface profile, roughness, and real area of contact. Despite the evident advantages of X-ray tomography in this application and extensive survey of available literature, no previous studies of this type were identified.

It was demonstrated that the profile and roughness measurements were consistent with conventional post-mortem examination techniques, which is especially significant, since measuring the worn surface roughness without disturbing the wear process is not possible through traditional methods. This approach opens the possibility to study the development of surface roughness with wear (roughness being identified as a potentially significant parameter in section 4.2.3). It would appear that such knowledge is vital for developing models predicting the development of roughness with wear. Other data, which are difficult to obtain otherwise were also collected; in particular, the total depth of the wear scar was assessed. By measuring the growth of the wear debris bed and observing the behaviour of wear particles under different conditions it would be possible to test mathematical models of debris bed development and study the effects of wear conditions on bed behaviour in greater depth. Measuring the total

depth of the wear scar during wear is challenging with traditional techniques but readily accessible by X-ray tomography.

Zhang et al. (184; 185) have independently proposed the use of X-ray tomography for measuring the real area of contact between rough metal surfaces, but the work in this chapter appears to be the first application of this technique to contacts roughened by wear. Establishing what the real area of contact is, how it changes with wear and how it varies through the wear cycle is of interest in studies of electrical and heat conductivity through the contact. Observing where and how quickly the wear process intiates in the contact and how it spreads through the contact area is also of great interest and nearly impossible to positively determine in any other way but through imaging, which (in case of metal-metal contacts) requires the use of penetrating radiation.

In principle, observing the real area of contact also has applications in studies of lubrication, since the transitions between lubrication regimes are defined in terms of the area of contact between the lubricated surfaces. However, even with a very bright X-ray source such as a synchrotron the imaging times needed for a full tomography are estimated to be of several minutes (subsequently confirmed in practice, see section 7.2), which is impractical for such an application. For the same reason, it is unlikely that a single cavitation event in lubricant film could be observed, but time-averaged distributions of vapour fractions in macroscopic cavitating flows have been collected successfully (188; 189; 190).

In total, the outcome of this chapter is of immense importance as it indicates, that with appropriate experimental equipment it would be possible to observe the progress of wear in one wear sample, thus avoiding repeatability issues mentioned in section 4.4. Since X-rays are already used, it would be relatively straight-forward to expand the experiment using X-ray diffraction to study wear-induced changes within the sample material. This would produce a very powerful approach for studying wear and in particular for testing of models describing wear debris transport, debris bed growth, TTS development etc. The following two chapters describe the expansion of the experimental techniques described here.

6 PILOT X-RAY DIFFRACTION

The approach described in the chapter 5 enables observations of geometrical changes in wear (surface roughness, burring of the edges etc.) to be made. However, other changes also occur in wear, namely the creation of the tribologically transformed structure (TTS). As discussed in section 2.2.3, the TTS consists of fine-grained recrystallized material and can measure over 100 μm in thickness. Its creation and behaviour in wear on the other hand appear to remain a matter of contention. Zhou et al. (54) argue that TTS creation starts, when the product of surface pressure, surface shear traction and displacement increases beyond critical value. Since the coefficient of friction in wear can easily increase by a factor of three or more in the initial onset of wear, this would correspond to TTS starting to grow (perhaps very quickly) during the initial stage of wear. Sauger et al. (52) on the other hand associate TTS formation with an energy threshold: once a sufficient amount of frictional energy is expended 'the TTS layer is suddenly generated'. There is also a disagreement concerning the fate of TTS. According to (52) TTS is continuously created, leading to a steady-state thickness. According to (54) TTS may disappear in wear, depending on the conditions of wear (since thick debris beds may lower the surface shear below the point of TTS being generated, but not supressing wear).

Given these incongruous observations, it would be advantageous to observe TTS in-situ during wear. Since metallography is obviously inapplicable in this case, diffractive methods can be used as an alternative. X-ray and electron diffraction have been used ex-situ on TTS with success (52; 55; 54); since the equipment needed for X-ray diffraction is to some degree overlapping with that needed for X-ray computed tomography, the is the opportunity to apply both techniques at the same time.

6.1 Proof of concept

The wear samples generated in the pilot tomography experiment could, in principle, be 'recycled' for diffraction experiments. However, the samples were not designed for a diffraction experiment and did not have a clear beam path: the beam would pass through the plastic tube, both sides of the aluminium annulus and through the plastic tube again, creating a multitude of diffraction signals from various points. Instead, annular steel samples from the experiments discussed in section 4.2.2.1 were reused. Samples had an internal diameter of 66 mm and 2 mm thick wall; having been worn under different conditions, they experienced different levels of wear (see Table 8):

Sample name	Normal load in wear (N)	Wear cycle amplitude (°)	Number of wear cycles	Total sliding distance (mm)
1200N/900°	1200	900	8	7800
2500N/900°	2500	900	8	7800
600N/900°	600	900	8	7800
4000N/2.5°	4000	2.5	1600	6900

Table 8: Wear parameters of the samples used in diffraction experiment.

The shape of the samples made it very straightforward to create a geometry favourable to diffraction, yet representative of the components in-situ: a large ring segment was removed, which was then cut in half and the parts stacked on top of each other with the worn surfaces touching. The pair was clamped in a sample holder sitting perpendicular to the diffraction beam, thus being in the same position as the components were on the wear machine. The X-ray beam entered the sample from the concave side, with the detector being located on the convex side. The large radius of the sample compared with the small diffraction region reduced the effects of the sample curvature. The design of the sample holder is discussed in section 3.3.1. The position of sample in the sample holder and the path of the diffraction beam is shown in Figure 97.

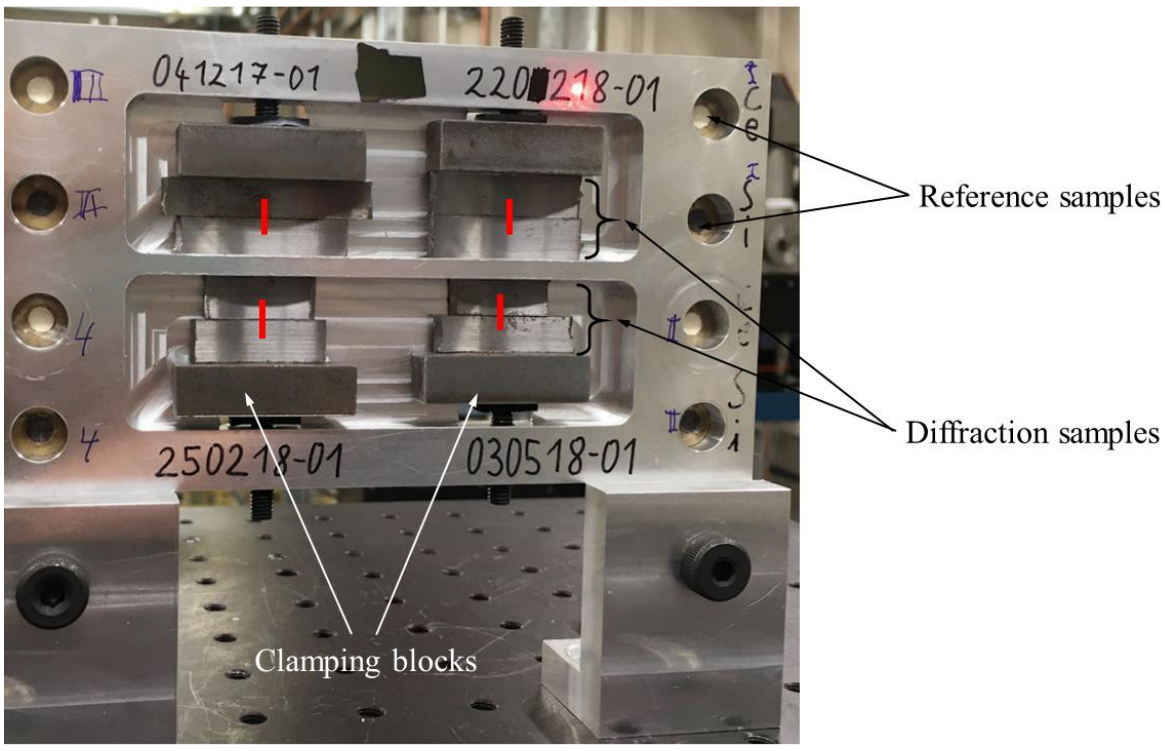

Figure 97: Assembled sample holder (seen from the beam side) with samples. Red lines show the approximate position of vertical diffraction scan lines.

6.2 Experiment

The experiment took place on the I12 beamline at Diamond Light Source. Experimental hutch 1 (155) was used, applying a monochromatic beam with energy of 90 keV and a Pilatus3 X CdTe 2M plane detector, which measures 1475x1679 pixels in size, with each pixel being 172x172 μm. According to (191) the mass attenuation coefficient for pure iron is approximately 0.5 cm^2g^{-1} at X-ray energy of 100 keV. A mild steel (over 99% Fe) wall 2 mm thick would therefore absorb about 54% of incoming X-rays, with absorption being slightly larger at 90 keV. This was judged to be optimal for the experiment.

The sample holder was aligned using a gamma camera and the centres of each sample noted in the coordinates of the sample table. Two main sets of scans were performed: 4 line scans over the vertical centre line of each sample and 4 area scans that mapped a 1x2 mm area around the centre of each sample pair. In addition, some 'ad hoc' scans were made to study the responses observed. In all cases a 'letterbox' shaped beam was used, measuring 250 μm horizontally and 50 μm vertically. The beam was moved vertically in 25μm steps. The diagram of the experimental setup in shown in Figure 98A.

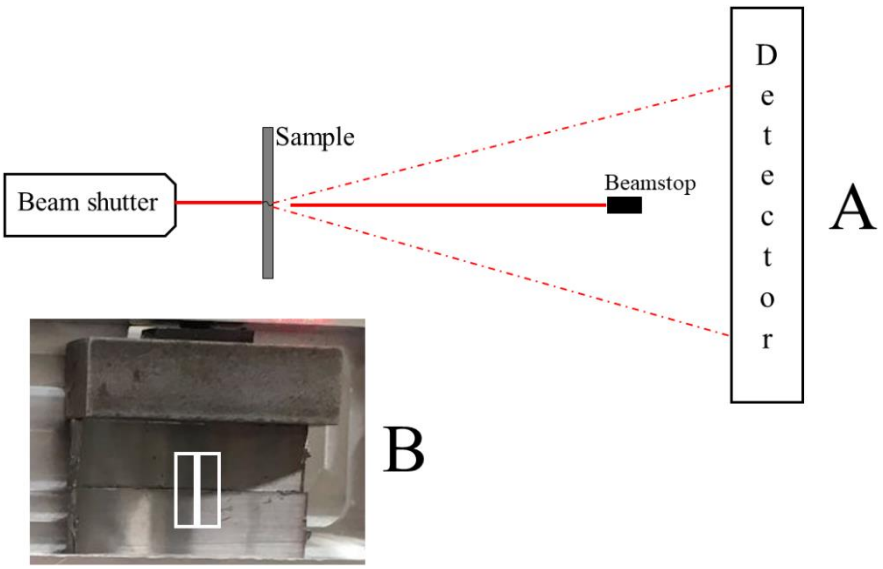

Figure 98: The diagram of the diffraction experiment set-up A) The close-up of a diffraction sample, the central line represents the vertical line scan, the rectangle the area scan B).

6.3 Results

Raw diffraction data was collected as a series of .tiff files showing the diffraction rings (example in Figure 99).

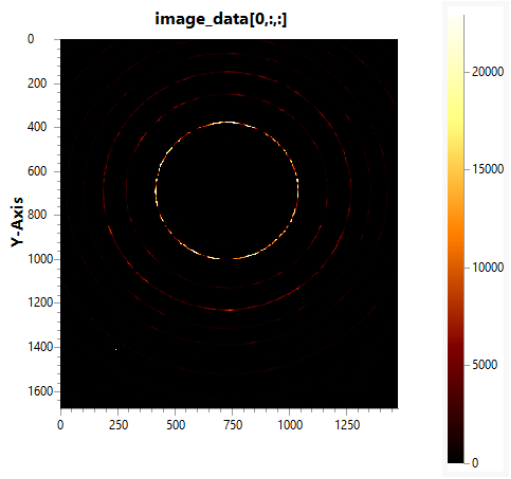

Figure 99: Diffraction pattern of undeformed bulk material.

Azimuthal integration and preliminary data processing were performed using DAWN software. Figure 100 shows the diffracted spectrum of undeformed bulk material.

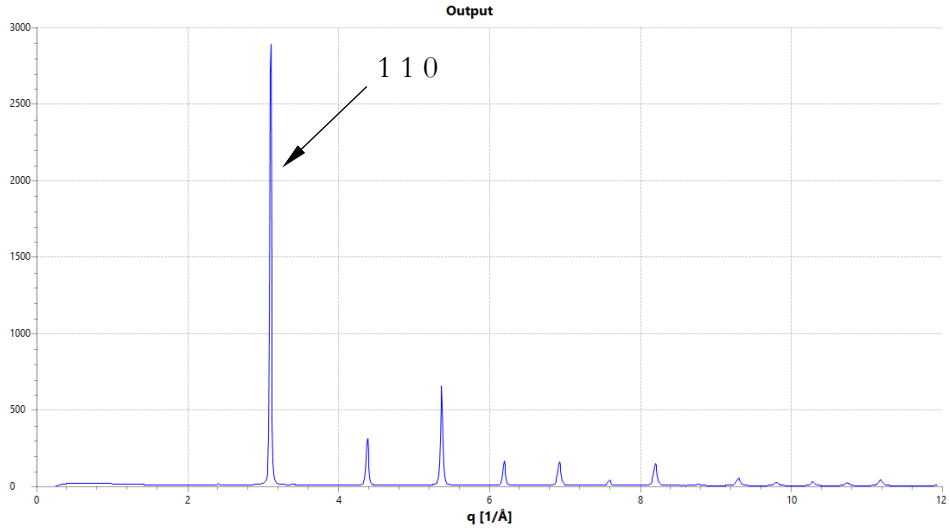

Figure 100: X-ray diffraction spectrum of undeformed sample material.

By comparing the spectrum on Figure 100 with materials provided by Bhadeshia (192) it was concluded that the sample material is overwhelmingly consisting of ferrite. Correspondingly, the very large first peak is related to the 110 crystal plane. For peak fitting, the fitting region around the 110 peak was iteratively adjusted until a satisfactory agreement was found between the integrated spectrum and the shape of the peak generated. Pseudo-Voigt peak shape was used in the first instance; if there were issues with the calibration or frequent noise spots a Gaussian or another pseudo-Voigt profile was used as comparison.

6.3.1 Preliminary examination of line scans

Figure 101 and Figure 102 show the variation in position of the 110 diffraction peak and full width at half-maximum (FWHM) as a function of the vertical position within the sample.

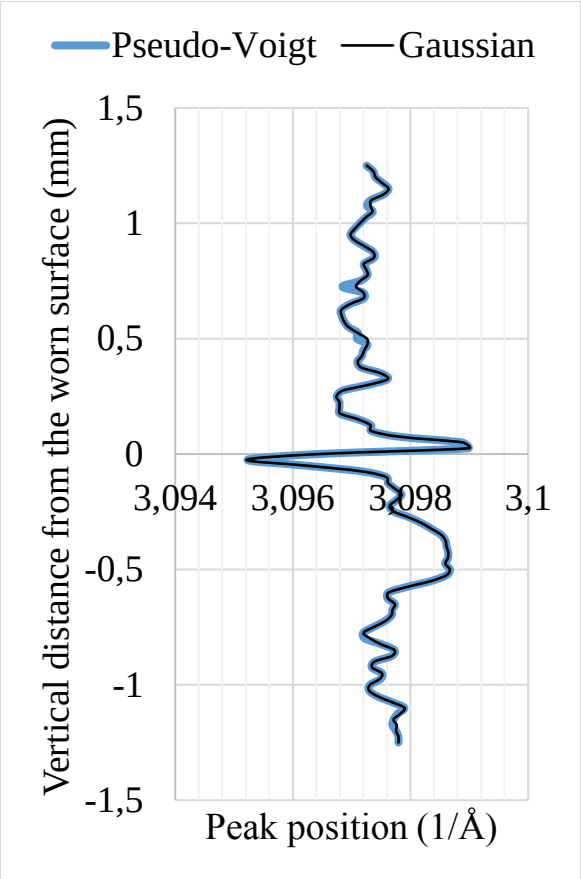

Figure 101: Peak position as a function of vertical position for the wear sample 4000N/2.5°.

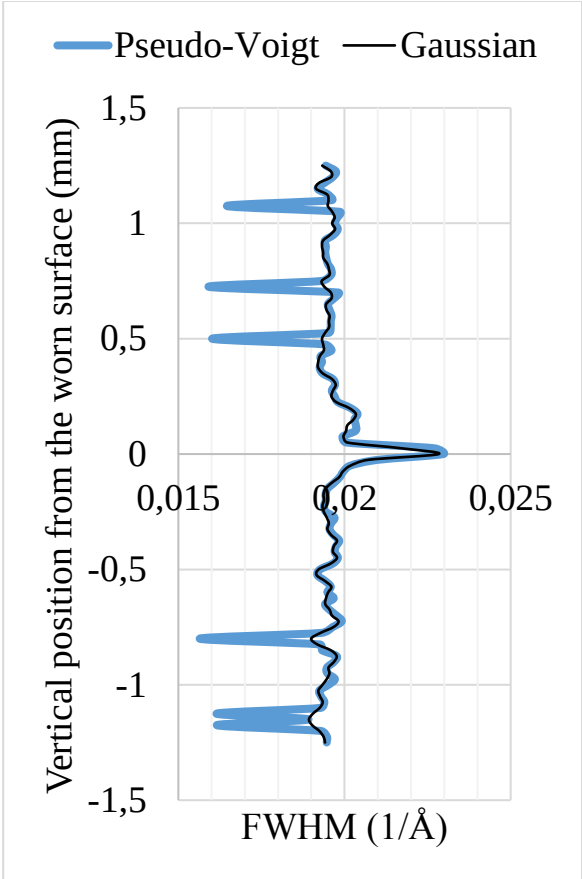

Figure 102: FWHM as a function of vertical position for sample 4000N/2.5°.

The close agreement between the Pseudo-Voigt and Gaussian fit lines indicates that the variations observed are not caused by differences in peak fitting. Occasionally, sudden changes appear in the integrated signal (see the Pseudo-Voigt line in Figure 102). The fact that these changes only occur in one point at a time and change in position (if they appear at all) with the type of fit used, indicates that these outliers are caused by sporadic failures of the peak-fitting algorithm to process individual integrated spectra. As these outliers are not caused by any physical process, they can be removed from the data. Peak position and shape both exhibit a significant disturbance at the mid-point of the scan, where the wear surface is located, with smaller, seemingly random, variations observed elsewhere.

To confirm that the disturbance in the central region is not a random variation, ad hoc scans were done, extending the length of the scan line to a total length of 8 mm, as seen in Figure 103 and Figure 104. Figure 103 shows consistent measurement noise in regions far away from the worn surface, with a significant spike in the position corresponding to the worn surface. Similarly, Figure 104 shows significant noise, with a sharp reversal, at the worn surface. While several sharp decreases in FWHM are observed, these can be attributed to calibration, since they only appear when using one peak profile, but not the other. The central disturbance on the other hand, sees FWHM rise regardless of peak fit and is different both in shape and size compared to the oscillations observed far from the worn surface. This shows that the worn region induces a characteristic change in the diffraction signal.

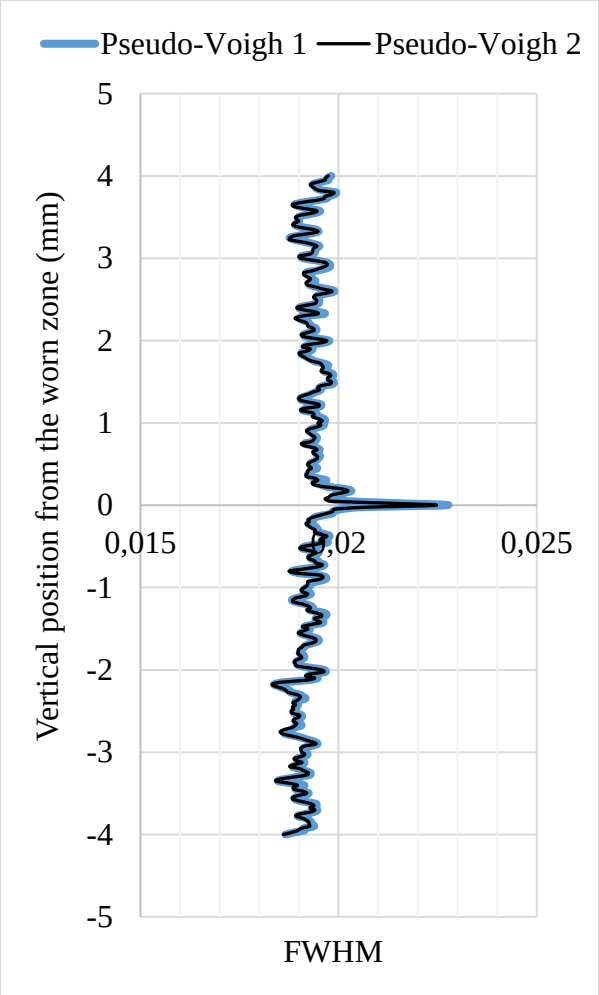

Figure 103: FWHM for the 4000N/2.5° sample with the scan line extended. Outliers have been removed.

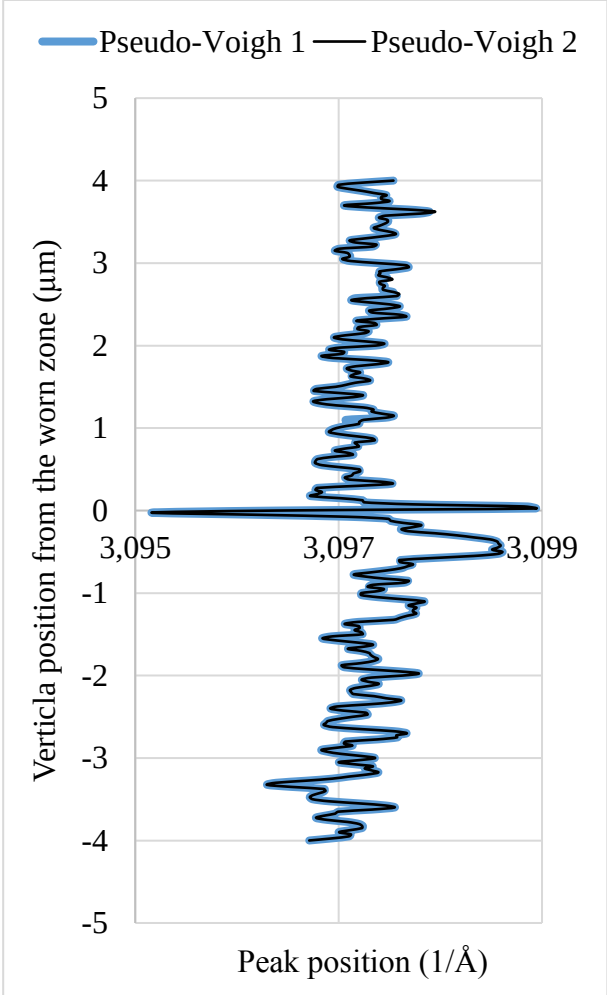

Figure 104: Peak position as a function of vertical position for sample 4000N/2.5° with the scan line extended.

By plotting the FWHM profiles onto the same graph, we can observe effects of different wear conditions. Figure 105 shows FWHM as a function of vertical position for all four samples studied. For example, the distance over which the peak broadening rises above the experimental noise is similar in all three cases where very large amplitudes of wear motion were applied, but smaller when a small wear displacement was used. Conversely, the magnitude of peak broadening observed decreases with increasing normal load i.e. broadening is most severe in sample 600N/900° (worn at 600 N), lower in sample 2500N/900° (worn under otherwise identical conditions, but using 2500 N) and much lower in sample 4000N/2.5° worn at 4000 N and a lower displacement.

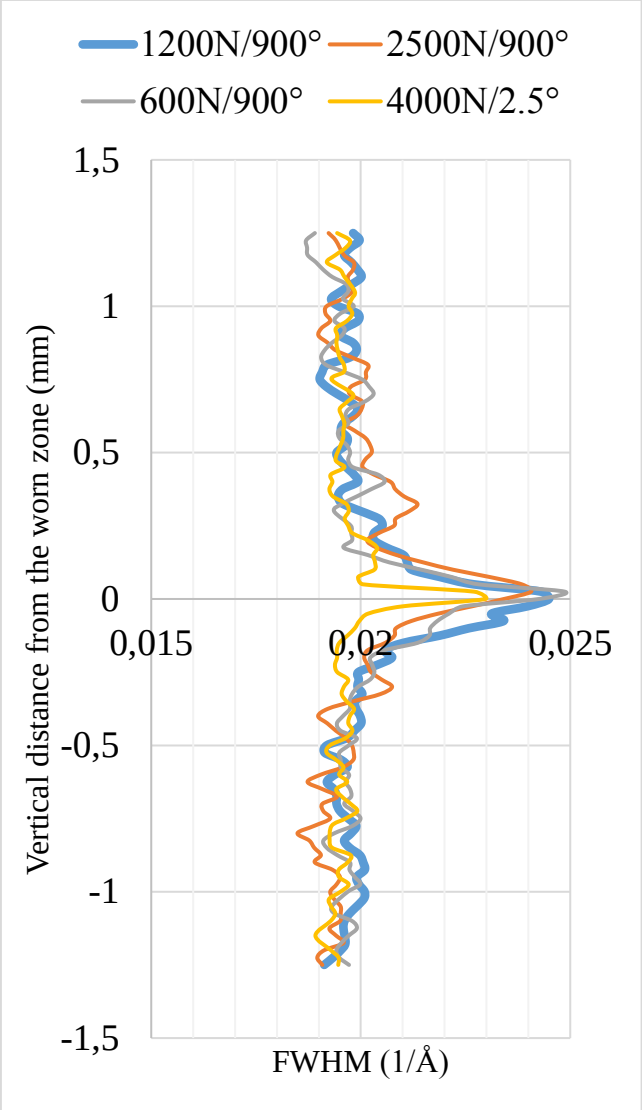

Figure 105: FWHM as a function of vertical position for all four samples. Outliers have been removed.

In both cases a significant change is observed at the contact. The worn surfaces are rough, making it impossible for them to contact fully, causing a part of the diffraction volume to be unfilled. To assess the effect this has on diffraction results, we plot the peak area (which serves as the measure of the intensity of the diffraction signal) as a function of vertical position (Figure 106). As may be observed, the intensity of the diffraction peak drops by roughly 50%, but is still well above zero and manual examination of the raw diffraction patterns confirmed the presence of a clear signal. This indicates that while the contact of worn surfaces does create partially unfilled diffraction volumes, there is no completely empty volume. To observe the effects of the partially filled volume, the peak position and peak area are plotted on the same graph (Figure 107, only the region close to the worn surface shown).

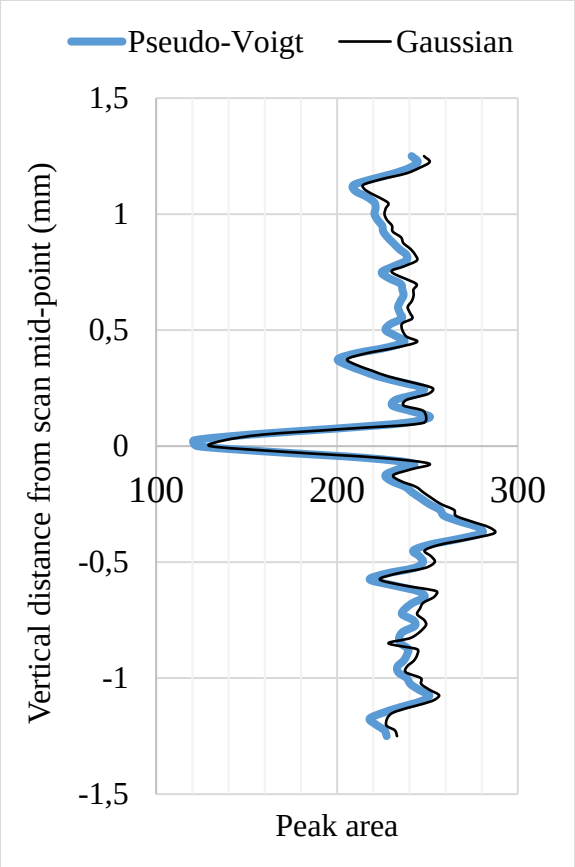

Figure 106: Peak area as a function of vertical position for the sample 4000N/2.5°.

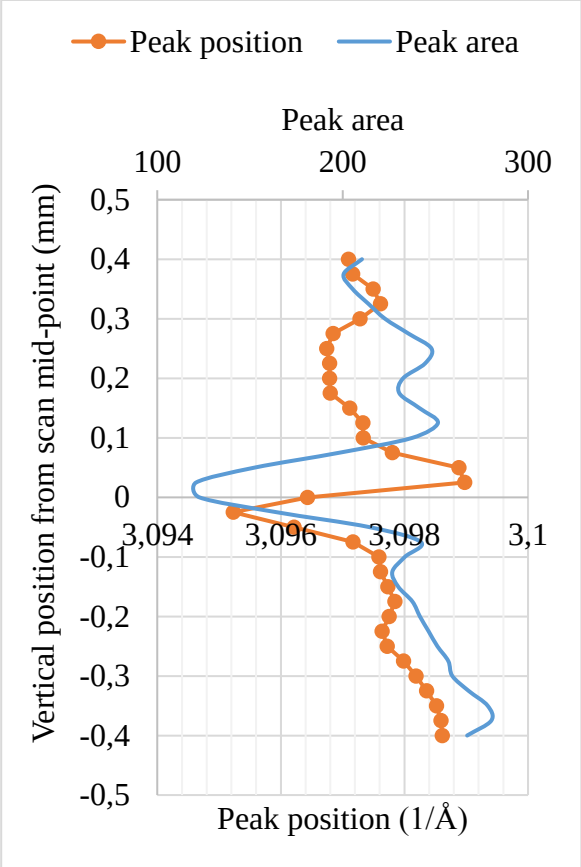

Figure 107: Peak position and peak area for sample 4000N/2.5° (focused on the interface region).

An average of peak area values was taken in the region far away (>0.25 mm) from the interface. If data points where the peak area deviates more than 2σ from the average are eliminated, Figure 108 and Figure 109 are obtained. While the large disturbance in peak position occurs almost exclusively when the decrease in peak area is largest (Figure 107, Figure 109), peak broadening occurs over a wider positional range, so even after removal of data points corresponding to lower peak area, the increase in peak width remains clearly visible in three samples.

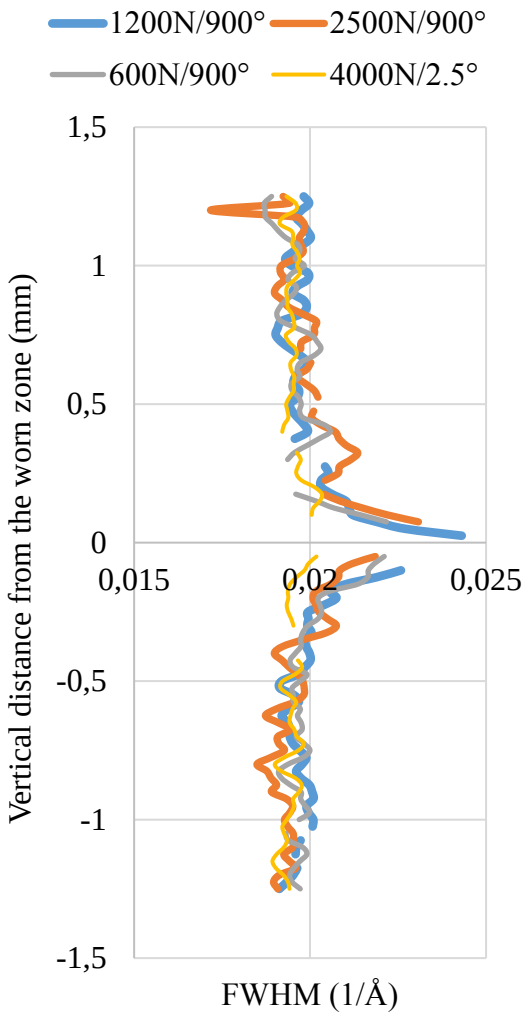

Figure 108: FWHM as a function of vertical position for all four samples. Only data points where peak area deviates from far-away average by less than 2σ are shown.

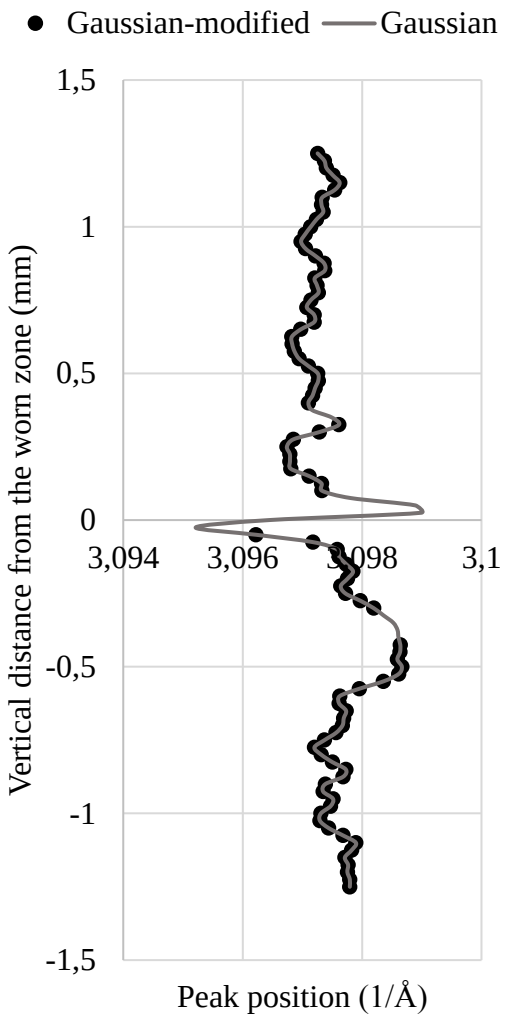

Figure 109: Peak position as a function of vertical position for sample 4000N/2.5°. Modified Gaussian shows only data points where peak area is more than 2σ below average.

6.3.2 Preliminary examination of mesh scans

The mesh scans are comprised of four line scans, running in parallel, 250 μm apart. The same beam size was used as in line scans discussed in section 6.3.1. The mesh scans conclusively show that the features observed in line scans are present throughout the volume of the sample. Figure 110 and Figure 111 show the distribution of peak area in two samples. The worn interface is clearly visible as a horizontal 'belt' of significantly lower diffraction signal. Despite significant noise occurring in the wear-unaffected region, the change is consistent both in position (relative to the sample) and magnitude.

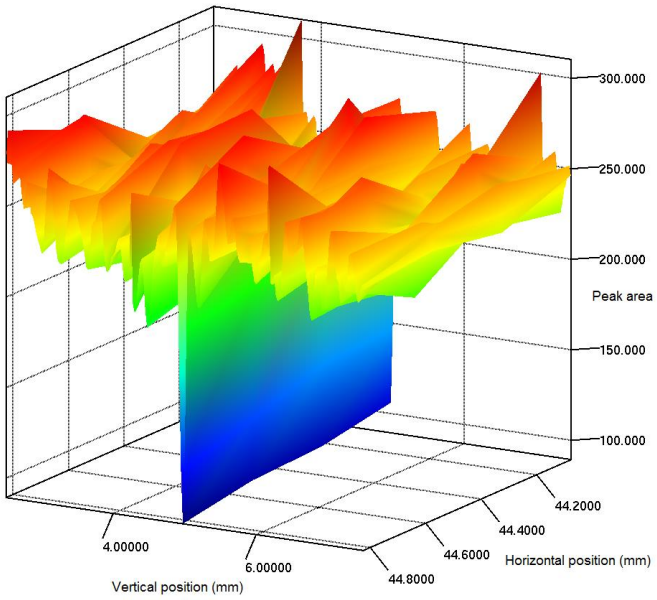

Figure 110: Peak area in a 2x1mm region in sample 1200N/900°. Note that the interface is located at 5mm of vertical position.

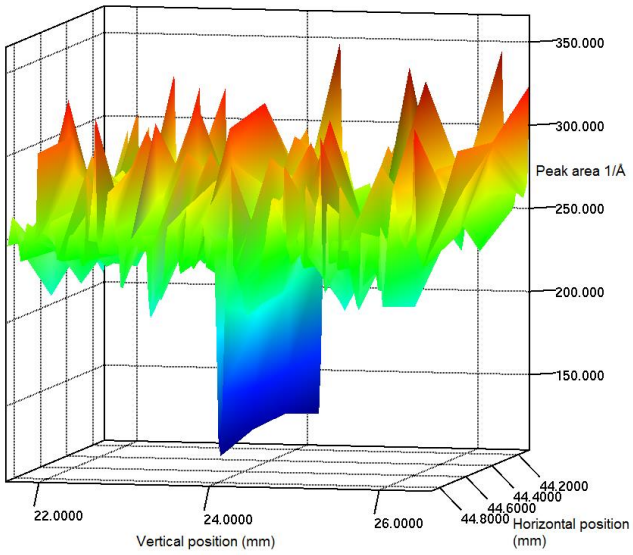

Figure 111: Peak area over a 2x1mm region in 4000N/2.5°. Note that the interface is located at 24mm of vertical position.

Unfortunately, significant experimental noise persists in some cases, as seen in Figure 112.

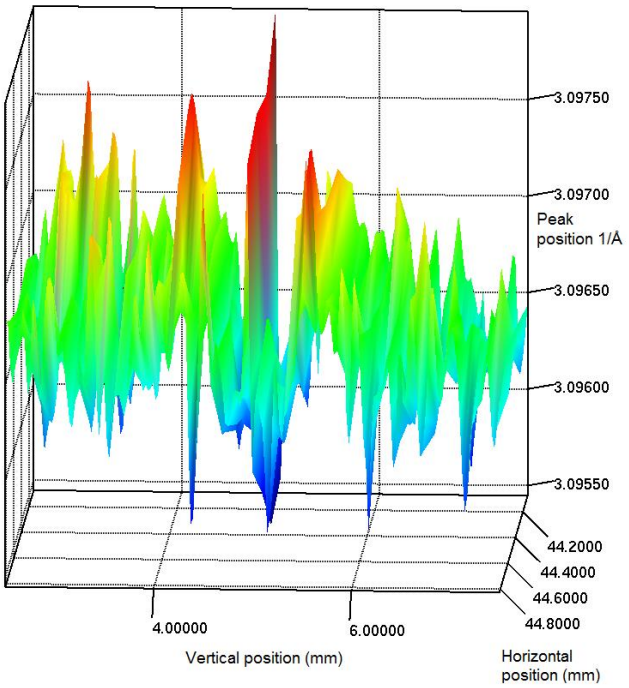

Figure 112: Peak position over area of 2x1mm in sample 1200N/900°. Note that the interface is at 5mm of vertical position.

These outcomes indicate that it is possible to identify the position of the wear zone (via peak weakening) and show that the shapes of the peak shift and peak broadening graphs from line scans are consistent within individual sample, which indicates a layer of plastically deformed material existing underneath and along the length of the worn surface.

Peak position shows a 'double reversal' shape which is unexpected, but consistent across the sample and appears in all samples tested. It seems most likely that this is an artefact of the imperfect experiment geometry. Let's suppose the sample elements are not mounted dead square to the beam, which causes the contact interface to be tilted. If so, then as the sample is scanned past the beam, the beam will first see the gap as a hole on one side of the sample (say the detector side), thus biasing the sampled material away from the detector, and shifting the peak position. As the gap in the sample passes the beam window, the beam will finally see the gap as a hole on the opposite side, now biasing the sampled volume position the opposite way. The result should be a wobble in peak position with a roughly centrally inverted symmetry and amplitude bounded by the ratio sample thickness-detector distance. This ratio was approximately 1:500, which is consistent with the amplitude of the observed wobble.

6.4 Comparison with traditional metallography and other techniques

The great advantage of starting with an ex-situ experiment is that a direct comparison between diffraction, metallography and other techniques applied to the same sample can be made; this enables a better assessment of the applicability of synchrotron X-ray diffraction. It is of particular interest to determine, if some data concerning the worn profile of the surface could be deduced from the diffraction data.

For example: the decrease of peak area at the worn interface has been explained through 'porosity' of the diffraction volume which is caused by the roughness of the worn surface causing the worn bodies not to be in perfect contact. This would indicate that there could exist a link between the worn surface profile and the length over which the peak area decreases.

To gather surface profile data, Alicona InfinteFocus optical profilometer was used to observe the topography of the worn surface on the diffraction samples. The surface profile was sampled at 8 locations. Each sampling region was 250 μm wide, containing 125 separate line profiles measuring 1.3 mm in the radial direction. The values of individual line profiles were averaged to obtain average maximum primary profile deviation (defined as the magnitude of the largest deviation from the profile centreline) and primary profile Rq, Ra and Rz roughness values for each region. In the context of Figure 113, 'Min' means the smallest out of 8 averaged values measured on each sample, 'Max' means the largest out of 8 averaged values and 'Average' means the average of the 8 values. It should also be born in mind that the distance over which the peak intensity decreases can only be multiples of 25μm, which is approx. 30% of the distances observed. This means that variations in the profile parameters smaller than 30% cannot be accurately reflected in the diffraction data. Figure 113 shows the relationship between the

maximum primary profile deviation and the vertical distance over which the diffraction signal weakens.

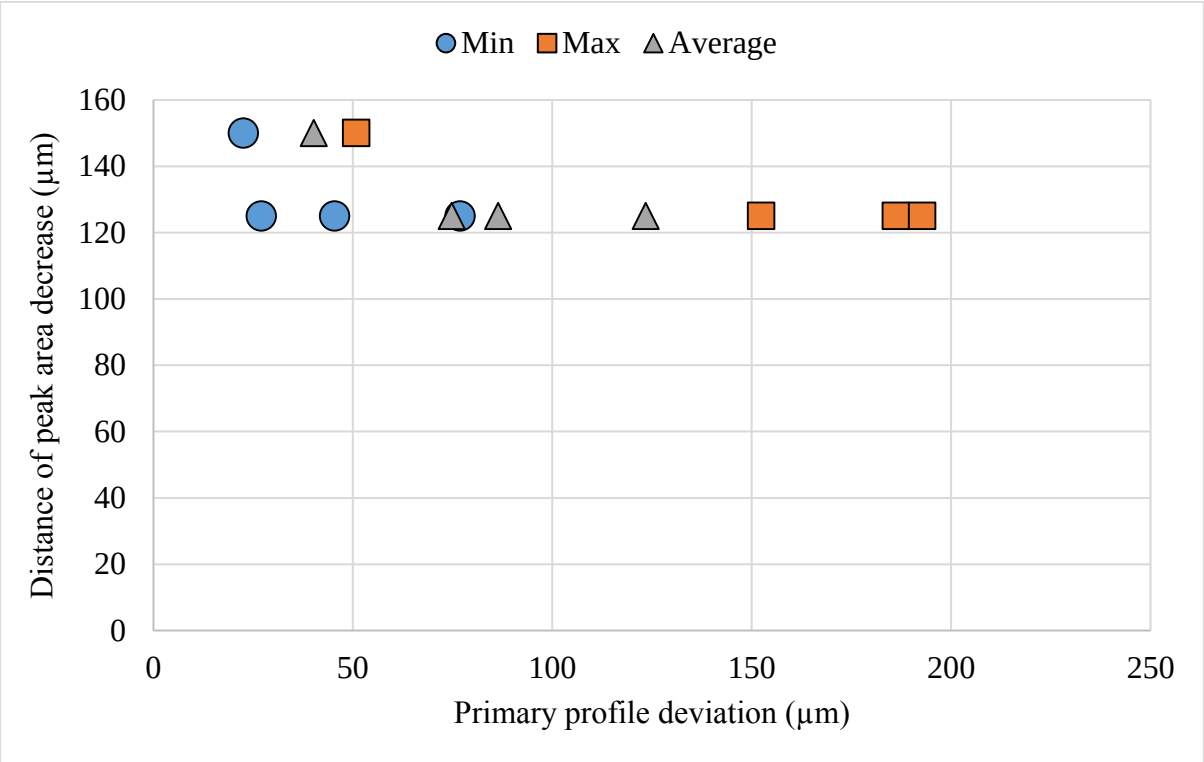

Figure 113: Relationship between the distance of peak area decrease and the largest worn profile deviation.

In three cases out of four, the values of the largest primary profile deviations observed in each sample roughly corresponds to the magnitude of the vertical distance of the peak intensity decrease. This is not surprising, since the surfaces cannot approach closer than the height of the largest asperities. Ra, Rq and Rz plots show identical trends, and are not shown, since they do not appear to contain any additional information. However, the number of data points is very low.

For metallography the samples under study were sectioned using a diamond saw, polished and etched with Nital to observe the microstructure. Images obtained are shown in Figure 114-Figure 122. The direction of the wear motion was perpendicular to the page. Each figure is oriented so that the undeformed material is at the bottom. As it may be observed, the undeformed material consists primarily of ferrite, with some pearlite colonies and globular inclusions, which are probably slag (Figure 114). This is consistent with the diffraction data from Figure 100, which a spectrum characteristic of ferrite. Ferrite grains typically measure 50 µm or more. The wear-damaged zone consists of thin layers (2-5 µm) running roughly parallel to the worn surface.

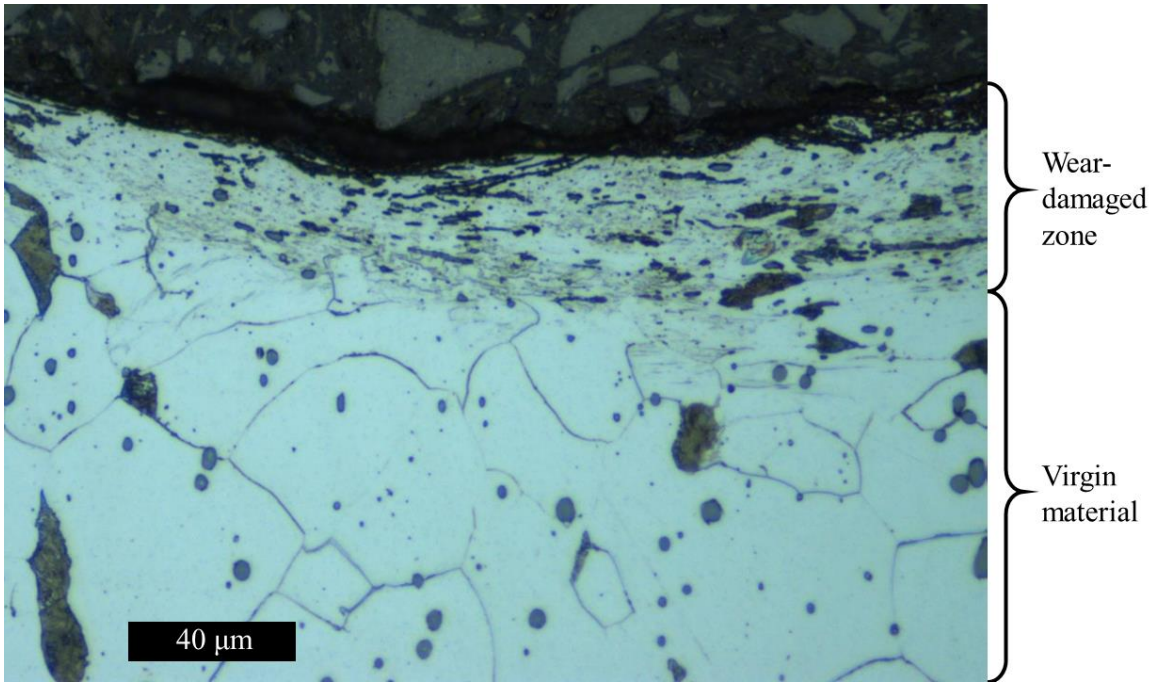

Figure 114: Typical example of worn sample microstructure. The virgin material with large ferrite grains and inclusions and the material deformed and damaged by wear are clearly visible.

It was difficult to conclusively determine whether the layers are single crystals flattened or whether they comprise of many crystals from optical micrographs, however the literature (52; 68; 55; 65) and some observations would point to the latter possibility (see Figure 123). The thickness of this layer can vary significantly (even on the same sample), from under 10 µm in some places on sample 4000N/2.5° (Figure 115) to over 50 µm on sample 600N/900° (Figure 117).

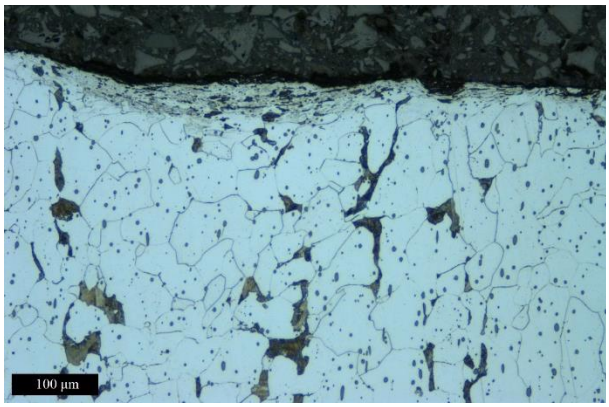

Figure 115: Crystal structure of sample 4000N/2.5° magnified 20x.

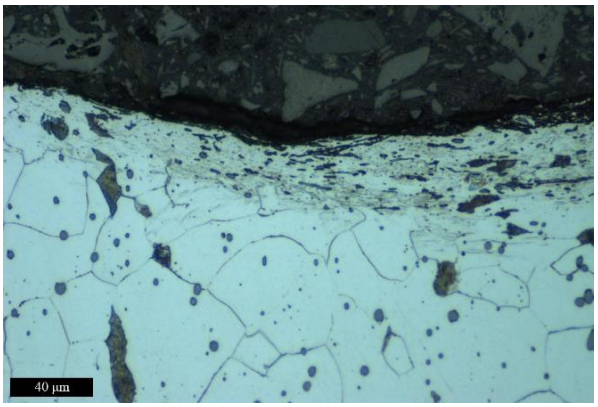

Figure 116: Crystal structure of sample 4000N/2.5°, magnified 50x.

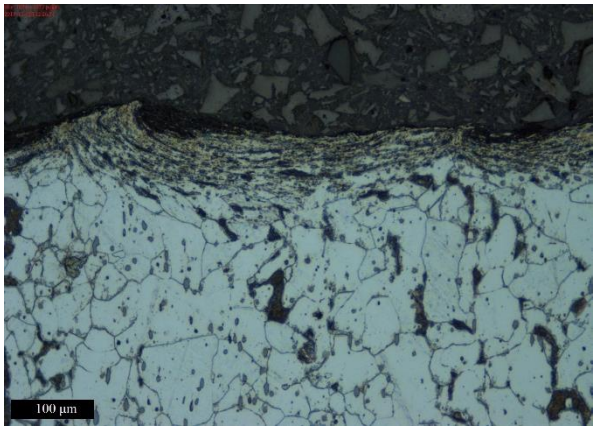

Figure 117: Sample 600N/900° magnified 20x.

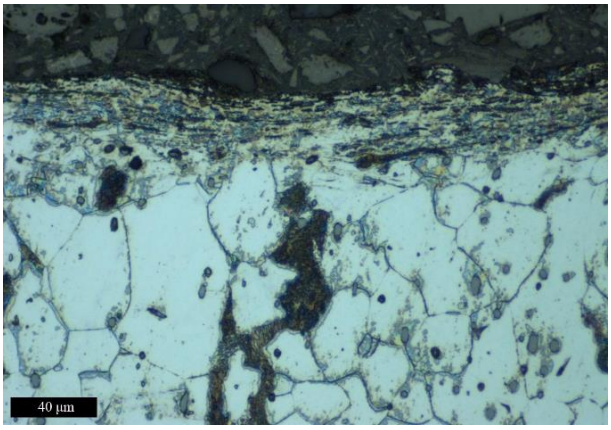

Figure 118: Sample 600N/900° magnified 50x.

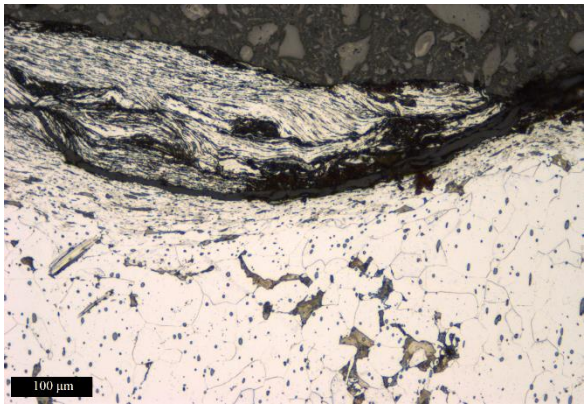

Figure 119: TTS in the sample 1200N/900° magnified 20x.

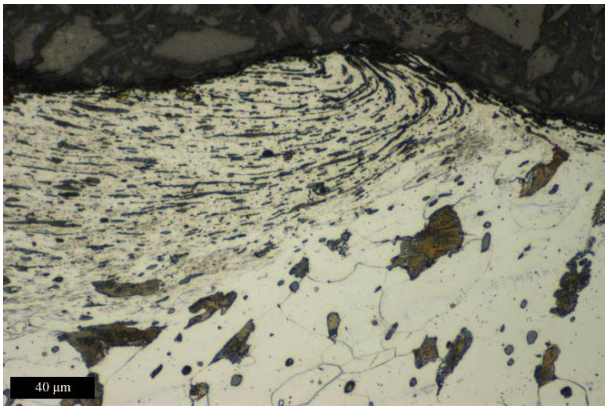

Figure 120: TTS in the sample 1200N/900° magnified 50x.

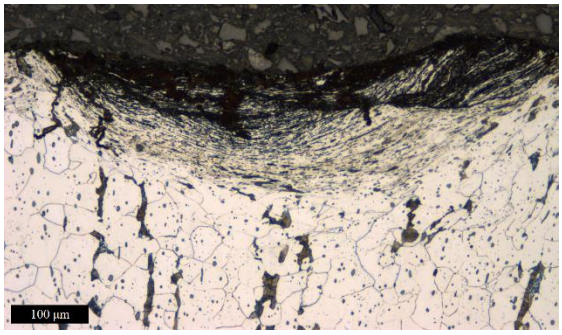

Figure 121: Sample 2500N/900° magnified 20x.

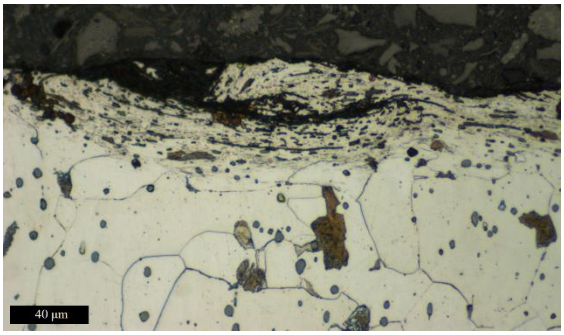

Figure 122: Sample 2500/900° magnified 50x.

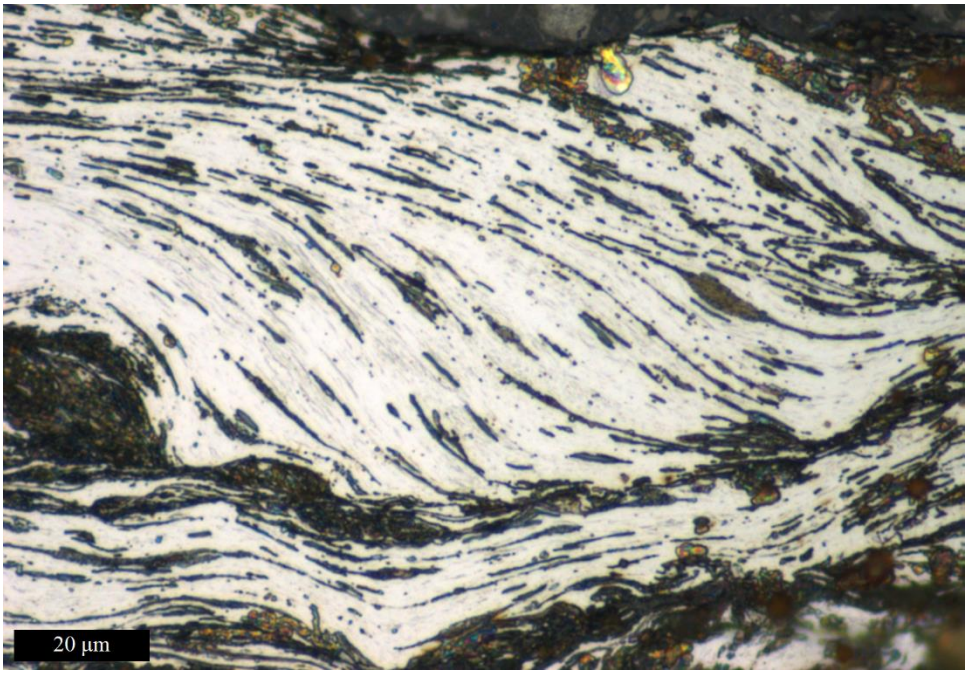

Figure 123: TTS layer in sample 2500N/900° magnified 100x.

Can the thickness of the deformed layer be linked to the FWHM of the diffraction peak? Figure 108 shows that FWHM begins to rise even before the diffraction signal drops off due to contact porosity (except in sample 4000N/2.5°). The region where FWHM increases above noise, but remains outside the region of excess signal drop was isolated manually (except for sample 4000N/2.5° where there appears to be no change in FWHM above noise until signal begins to weaken). The thickness of the peak broadening region on both sides of the sample is averaged to obtain the average length of the peak broadening region (Table 9). The peak broadening region is comparable in thickness to the maximum observed thickness of the physical TTS. The only exception is the sample 4000N/2.5°. However, the maximum thickness stated in Table 9 for this sample is observed only once, in all other regions, TTS is a lot thinner, seldomly exceeding 20 µm and 40 µm only once. This could explain why there exist a disparity between the diffraction and metallographic observations in this case.

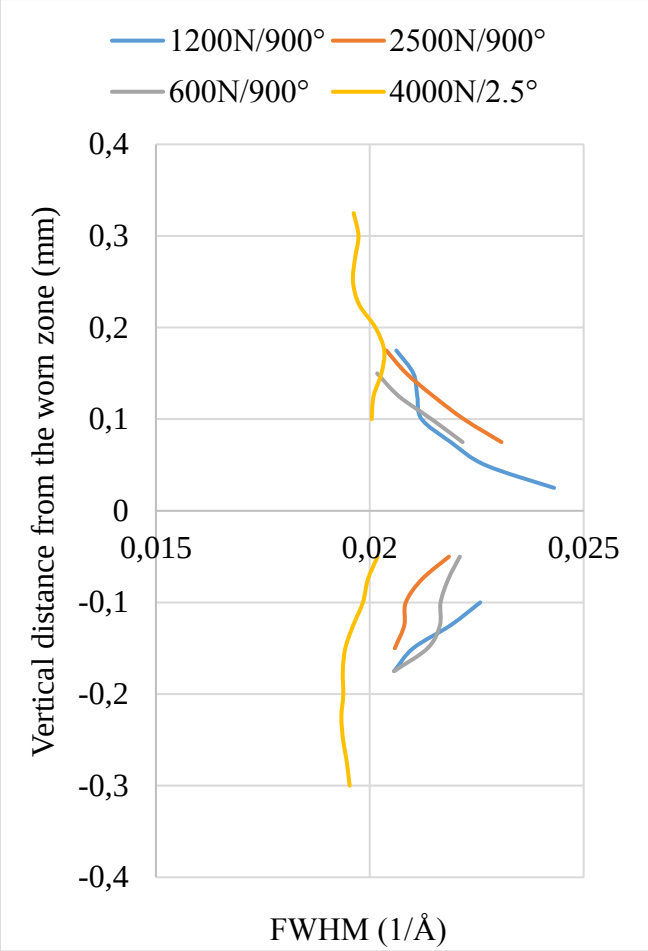

Figure 124: Isolated regions of peak broadening.

Experiment name	Maximum TTS thickness (µm)	Average region of peak broadening (µm)
4000N/2.5°	60	0
600N/900°	100	100.0
1200N/900°	110	112.5
2500N/900°	120	100.0

Table 9: TTS thickness and width of the peak broadening region.

6.5 Detailed analysis

In an attempt to extract more information from the diffraction data, the diffraction patterns were integrated across a 45° angle in various orientations to determine, if there is some spatial distribution to the diffraction signal.

With respect to peak area, the diffraction signal drops uniformly in all directions at the interface (Figure 125, Figure 126). These two examples are representative of the general pattern.

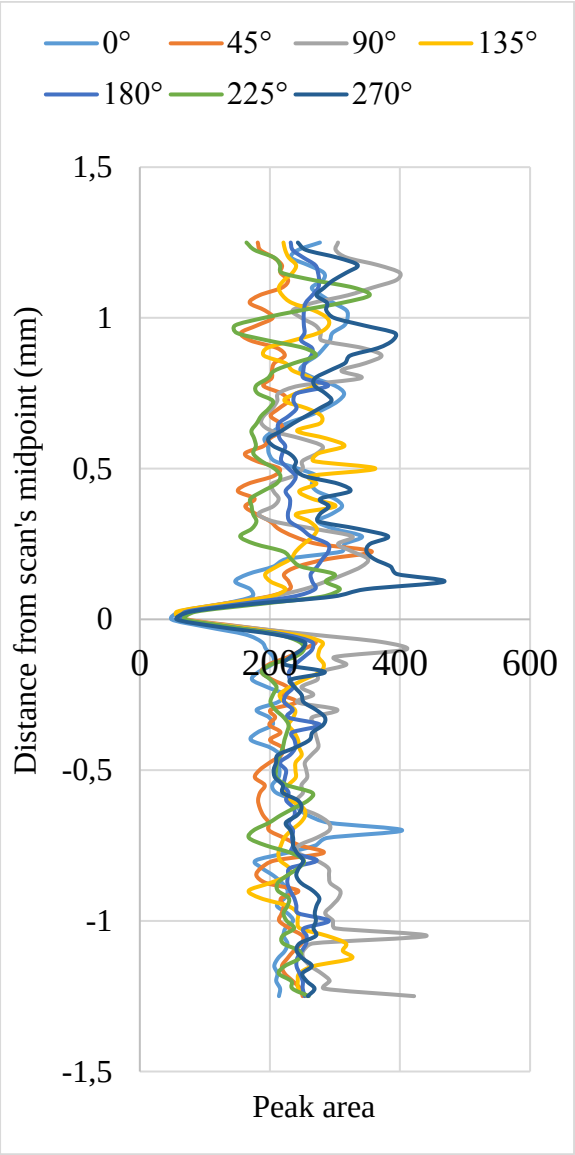

Figure 125: Peak area integrated over 22.5° of either side of the given azimuthal angles in sample 600N/900°.

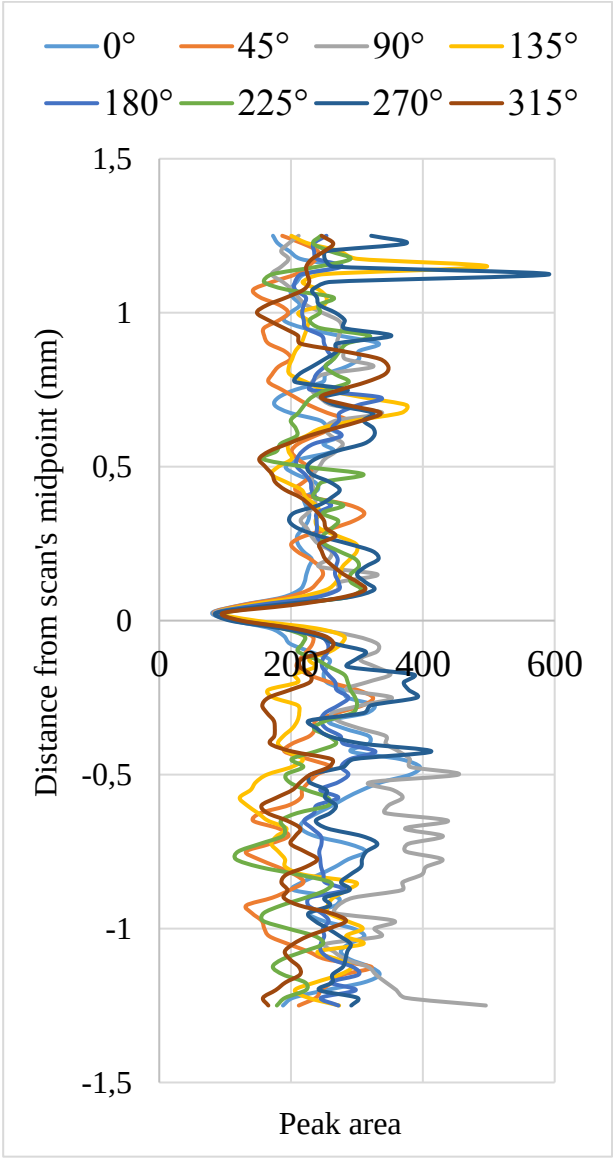

Figure 126: Peak area integrated over 22.5° of either side of the given azimuthal angles in sample 2500N/900°.

As before, there is substantial noise and the signals show the same general behaviour as the fully integrated results. With respect to peak position it is notable that when signal is integrated in directions roughly parallel with the worn surface (azimuthal angles 0° and 225°) the peak position is the highest, while directions perpendicular the worn interface (azimuthal angles 90° and 270°) shows the lowest values (Figure 127, Figure 128).

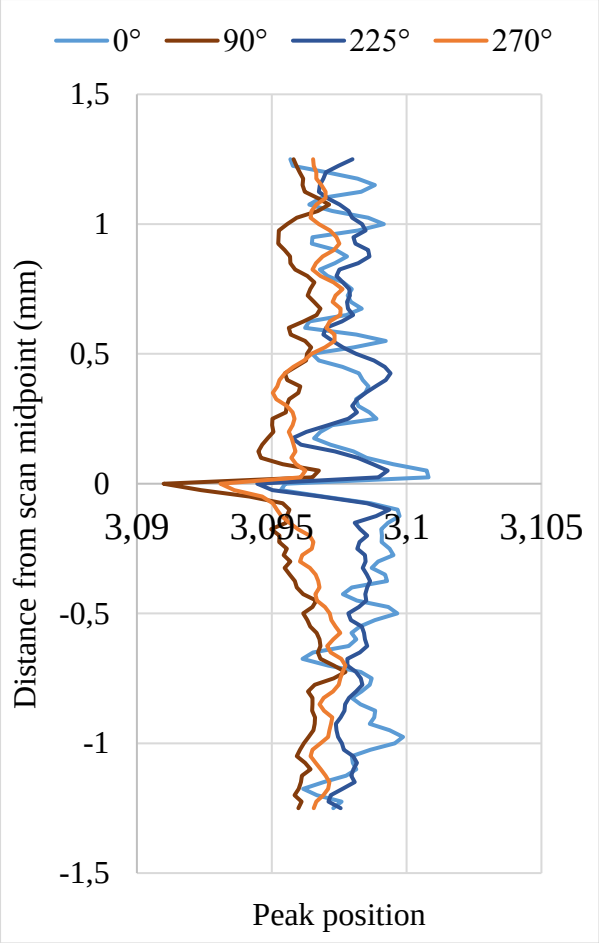

Figure 127: Peak position in sample 600N/900° integrated over 22.5° of either side of the given azimuthal angles.

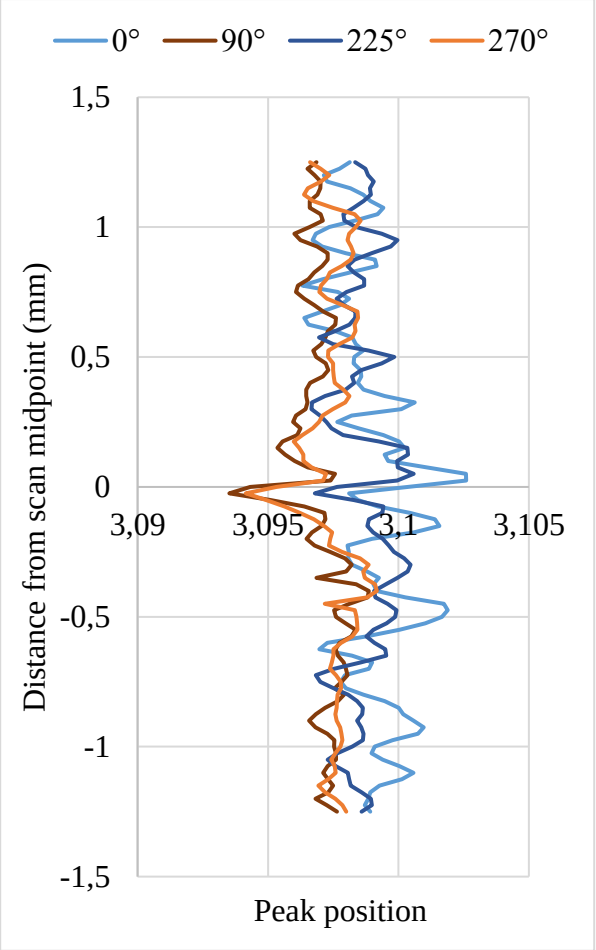

Figure 128: Peak position in sample 030518-01 integrated over 22.5° of either side of the given azimuthal angles.

This could indicate a texturing/straining of the material in the horizontal direction i.e. in the direction of sliding. This is consistent with the structure of the TTS as shown in Figure 115-Figure 123, however a further point of interest can be made. While the metallography shows a thin, heavily deformed layer immediately below the worn surface, the lines associated with orthogonal azimuthal angles in Figure 127 and Figure 128 remain separated over a much greater distance (in Figure 128, the 0° and the 270° line do not cross over about 0.5 mm). This would indicate that some sort of a wear-induced change extends approximately 250 µm into the material, despite the visible damage on the crystal-level being only limited to the TTS.

6.6 Pilot diffraction - Outcomes

In the experiments presented, the location of the interface between the worn surfaces could be reliably observed using the diffraction data, since the wear affected zone caused a characteristic disturbance of the diffraction signal in terms of peak shift and peak broadening. In the examples studied, the peak broadening rises above the noise over a distance of 0.325 mm-0.500 mm

suggesting a region of residual strain due to the formation of a plastically deformed zone during the wear process.

The peak position is more difficult to interpret; metallographic observations have revealed a thin, subsurface layer with refined grain size. However, the thickness of this layer is smaller than the prominence of the surface asperities and is comparable to the vertical beam size used (50 μm, which is also the lower limit of the instrument). Despite this, the maximum thickness of the tribologically transformed layer observable through ex-situ metallography can be linked to the distance over which peak broadening is observed. Accurate identification of the grain size in this experiment was not attempted, since there were only four samples to examine and deconvoluting the effects of strain, texture and grain refinement was judged to be too complex relative to the importance of data that could be potentially gathered.

Together, these observations indicate, that X-ray diffraction applied to an annular contact in-situ is both technically possible and practically valuable, as it enables observations of the plastic straining associated with wear to be made, without upsetting the wearing contact. If chapter 0 demonstrated the viability of using X-ray computed tomography for observing the topography of the worn contact, this chapter demonstrates the possibility of observing subsurface effects of wear. Combining both approaches into one experiment can therefore be expected to give an extremely powerful approach to observation and quantification of wear, meriting further development in this direction.

7 Advanced X-ray studies of wear[4]

Results presented in chapter 5 and published in (2) demonstrate both the viability and utility of using X-ray computed tomography for observations of wear. Application of X-ray diffraction to a worn geometry at a synchrotron facility was demonstrated in the pilot diffraction work presented in chapter 6. Applying both techniques simultaneously, promises a possibility to study wear between two metallic bodies in greater depth. Processes such as roughening and folding of surfaces (70), creation, accumulation and transport of wear debris (97; 98), chemical reactions of the wear debris and wearing bodies with the atmosphere and/or lubricants (43; 42; 193; 57), as well as subsurface changes, such as recrystallization and grain refining (194; 56; 195; 62; 196) are all of great interest to tribologists and further exploration of techniques capable of investigating them without disturbing the contact is a valuable pursuit in itself. Ideally, the X-ray study of the wear process would take place in-situ, so that the same wear sample is examined several times during the wear process.

In the past X-ray methods have been successfully used to quantify wear-related phenomena. Zanini et al. (33) and Hejjaji et al. (34) measured post-wear surface profiles using ex-situ X-ray computed tomography showing that appropriately fine resolution can be obtained, discussion of X-ray diffraction for studying crystal structure changes in wear are provided by Lee (197), with examples of in-situ diffraction on wear affected structures being published by Reid et al. (198) demonstrating the ability to observe wear-related stresses. Between 1998-2000 a number of studies (80; 81; 82; 83) appeared, proving the viability of 2D X-ray radiography for observing wear between a variety of optically opaque materials. Zhang et al. (184; 185) applied X-ray computed tomography to observe the real area of contact between artificially textured surfaces. The ability to establish the real area of contact through X-ray imaging is of particular interest, since this appears to be beyond the reach of traditional approaches. While mathematical models linking surface profiles and real area of contact exist (199), see also discussions in (200; 201) as well as finite element modelling of Zhang et al. (184; 185), they require knowledge of both the surface profiles and material properties. Establishing post-wear surface profiles traditionally requires separation and cleaning of the wear bodies, removing the influence of wear debris accumulation on the final result. Establishing the stiffness, yield point and other properties of wear-deformed material as well as the thickness of the wear affected zone is in turn a yet more

[4]This chapter is based on manuscript titled *Use of Synchrotron X-rays for Imaging and Diffraction Studies of Worn Contacts – Towards Direct Observation of Wear Damage in Optically-opaque Contacts* submitted for review to Tribology International in May 2022.

complex operation, requiring sectioning of samples for purposes of metallography and micro-indentation.

Direct observations of wear through X-ray methods thus represent a powerful alternative to traditional approaches. In addition, X-ray observations can be used to test models predicting processes such as initiation of wear, growth of debris bed, generation of tribologically transformed structure etc. As an extensive discussion of the model of Fillot, Iordanoff & Berthier has been presented in previous chapters (sections 2.3.2, 4.1) using the X-ray approach to test this model is a natural further step.

This chapter presents the results of an advanced proof-of-concept work aimed at demonstrating the application of X-ray computed tomography and X-ray diffraction at a synchrotron beamline. Due to COVID-19 restrictions, the use of a wear machine at the beamline was not possible. The experiment was thus designed with separate wear and X-ray parts, with the wear samples bonded in epoxy putty to preserve the worn-in condition. The experiment therefore straddles the boundary between in-situ and ex-situ approaches, since the wear and X-ray examinations are separate, but the contact remains undisturbed and can be examined as if worn directly on the beamline. In this manner a series of samples can be examined, each standing in for a separate point in the development of the wear process. This approach is sufficient to demonstrate the viability of applying X-ray tomography and diffraction to a worn contact at several different points during the progression of wear; the design and application of a machine needed for a full in-situ experiment is a technical, rather than a physical, limitation.

7.1 Use of a synchrotron

Laboratory-scale X-ray devices often have limited brightness, leading to very long exposure times (up to 8 hours in the pilot work of (2)). Observing wear repeatedly during the wear process means that a relatively large amount of data needs to be collected, automatically leading to (prohibitively) long experimental times. In addition, laboratory-scale devices can simply lack the space needed to accommodate a wear rig, capable of applying the desired loads and movements to the wear sample, preventing an in-situ experiment from a practical perspective. Synchrotron facilities on the other hand, enable much higher brightnesses and therefore shorter experimental times. Synchrotron beamlines are also often equipped with a variety of sensors easily enabling the application of different techniques. Limits to the weight and size of the experimental equipment are also typically much wider (202; 155; 203; 204), making the use of a synchrotron facility much more conducive to investigation of wear through X-ray techniques.

7.2 Advanced X-ray studies of wear - experimental strategy

The objective of the work presented here was to prove the viability and practicality of carrying out a wear experiment combining X-ray tomography and X-ray diffraction at a synchrotron beamline for the purpose of investigating wear with minimum interruption to the wear process. Although the use of a synchrotron enables very short exposure times (this study used 0.05 s per projection), the large number of projections result in total imaging time of the order of minutes; this makes observing wear through tomography (although possibly not through 2D radiography) in real time impractical, since the tomographic process would need to be completed in a fraction of the time needed to complete one wear cycle. In case of reciprocating/fretting wear this would require very low (<0.01 Hz) reciprocation frequencies, which translate into extremely low wear rates. It is therefore necessary to stop the wear motion (while still applying the normal load), while the tomography and diffraction observations are being made. The effects of such stoppage(s) on the progress of wear are not know for certain at this time. However, it can be expected that some of the elastic deformation created by the last wear cycle will be released through localized slip and potentially creep and also that the bulk temperature of the wearing bodies will decrease somewhat, due to absence of frictional heating in the wear zone.

Since the in-situ wear experiment must be of a stop-start nature, it can be simulated effectively by a set of samples, each worn to a different level and examined after the completion of wear. For the purpose of this study, two sets of samples were prepared, each set representing a wear experiment running at a constant normal force, with each sample representing one point in the development of wear from the unworn to steady-state wear condition. Samples were worn using a Zwick-Roell Z100 compression-torsion loading frame (Zwick-Roell, Germany). X-ray experiments were carried out at the I12 beamline at Diamond Light Source[5]. Due to the capacity of the chosen detectors (imaging module 3 (155)), the worn region of the sample had to be smaller than 8x8 mm. For diffraction experiments, the same 2D area diffraction detector was used as in diffraction experiments described in chapter 6 (size of 1475x1679 pixels, each pixel being 172x172 μm).

[5]The experiments and data reconstruction were carried out by beamline staff members Dr O.V. Magdysyuk and Dr S. Michalik in coordination with the author.

As in the work of Aleksejev et al. (2), an annular contact was used, but the dimensions were increased to an external diameter of 7.5 mm and internal diameter of 5.5 mm. Aluminium alloy 6082T6 was chosen as the material in the belief, that its low density and resulting low X-ray attenuation would contribute to expediency of the experiment. This was the same material as used for aluminium samples in experiments described in sections 4.2.2.3, 4.3.1 and 5.3.1. At the end of wear, the sample elements were bonded using UniBond Express Repair epoxy putty while under full normal load and allowed to set, to create a bonded wear sample. A schematic of the sample is shown in Figure 129. The details of sample preparation are described in section 3.4.2. Stages of the sample preparation are shown in Figure 58.

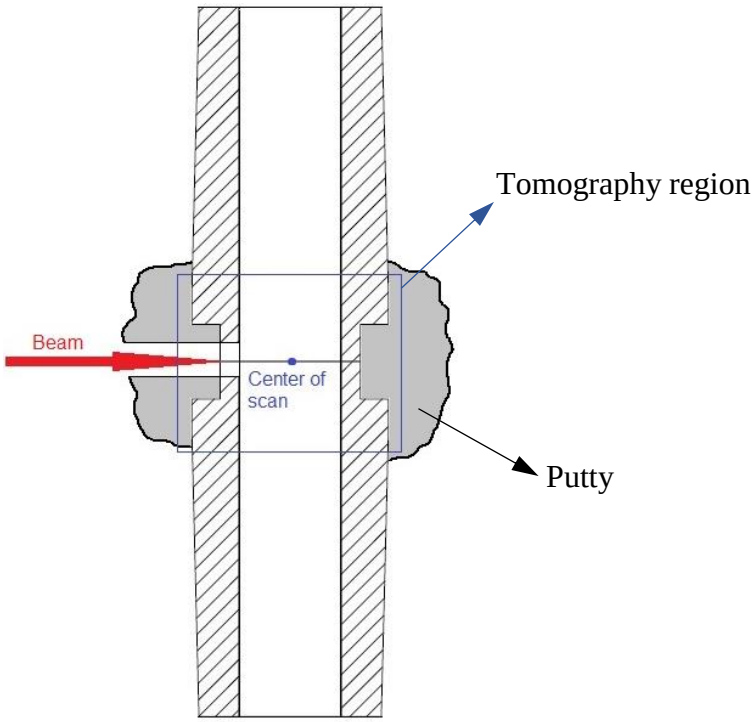

Figure 129: Schematic of the bonded sample.

A sample of the hardened putty was submitted to energy dispersive X-ray spectroscopy to determine its composition[6]. The chemical composition is shown in Figure 130.

[6]**The procedure was performed by Dr Kalin Dragnevski of Laboratory for In-situ Microscopy and Analysis at the Department of Engineering Science, University of Oxford.**

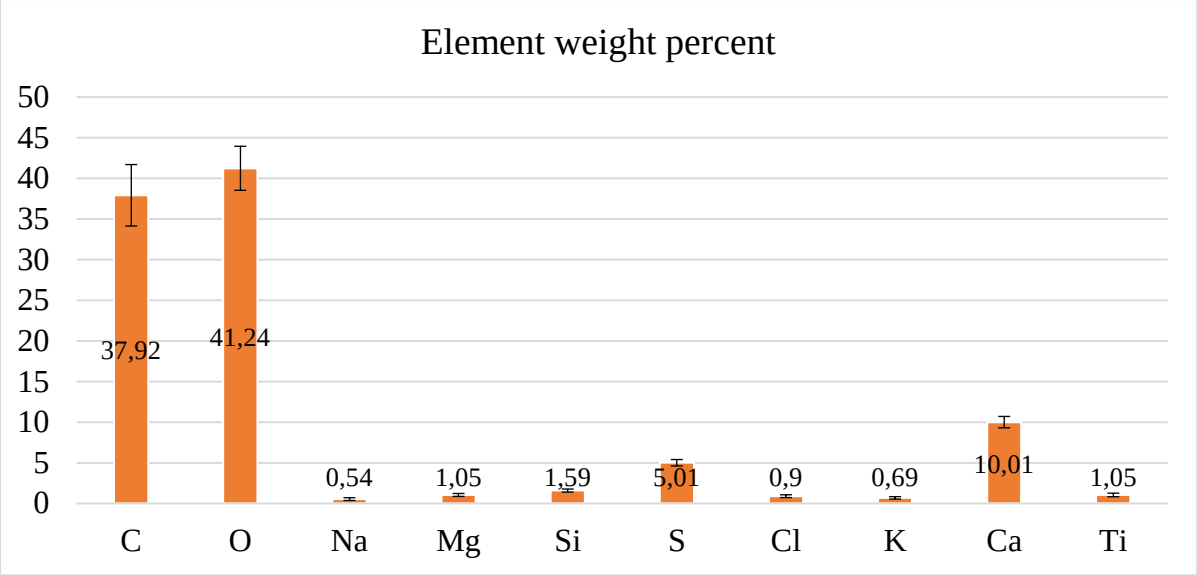

Figure 130: Chemical composition of the epoxy putty.

Mapping of elemental concentration showed an even distribution of small spots containing high concentrations of Ca, Mg and Si. The results are consistent with an organic polymer filled with powdered calcium carbonate and possibly calcium sulphate, with small addition of magnesium carbonate, silicon dioxide and some titanium compound, most likely titanium oxide, as it is commonly used as a white pigment. The presence of crystalline material in the binding putty caused additional diffraction signals to appear in the diffraction experiments. Special approaches were taken to separate the diffraction signals from the metal and the binding putty.

7.2.1 Wearing the samples

A total of 15 wear samples were prepared. Seven were worn at a normal force of 510 N (which corresponds to the nominal contact pressure of 25 MPa) for 50, 100, 200, 500, 1000, 2500 and 5000 cycles respectively. Seven extra samples were worn at normal force of 300 N (corresponding to nominal contact pressure of 15 MPa) for 50, 100, 200, 500, 1000, 2500 and 5000 cycles. In a full in-situ experiment this would correspond to only two samples, examined at different numbers of wear cycles. One sample was bonded under normal force of 510 N without any wear, to produce the control sample. As there was no wear, it was assumed that this sample represents the initial (unworn) condition for both sets of samples.

In all cases, wear was generated by applying a reciprocating rotating motion, using an angular amplitude of 3° (which corresponds to imposed linear amplitude of 170 μm at median radius) at a frequency of 0.5 Hz. Each sample was then labelled and stored securely, before being shipped to Diamond Light Source.

7.2.2 Beamline set-up

The sample holder was attached to the sample table. Each sample was placed into the sample holder and aligned so that the axis of the sample was perpendicular to the beam and the beam coaxial with the radial hole.

For diffraction, a monochromatic beam with an energy of 58.7 keV was used, combined with a CdTe Pilatus area detector and the sample-detector distance of 691.07 mm. With the beam shining through the radial hole, a 1.5 mm high line scan was made by translating the sample in the beam-path in the vertical direction across the worn region. A beam size of 0.25 x 0.05 mm was used and the beam was moved in steps of 0.02 mm to generate 76 diffraction points across the worn region on one side of the sample. The exposure time was 10 s per diffraction point. Program DAWN (205) was used to precisely determine a sample-detector distance, X-ray energy, position of a beam centre on the 2D detector and a tilt of the detector with respect to the direct X-ray beam using LaB6 standard sample data, and then to azimuthally integrate 2D patterns. For X-ray computed tomography, a field of view of 8 x 5.5 mm was covered by a PCO.edge camera with module 3 optics, an image size of 8 x 5.5 mm was used, with 1800 projections taken for each sample, using an exposure time of 0.05 s per projection. Sample-to-camera distance was 500 mm. Tomography was repeated at 58.7 and 53 keV, with tomography results obtained at 53 keV judged to be superior in quality, due higher contrast. This also indicates that there is ample reserve of capacity for studying wear in more attenuating materials, such as ferrous alloys. The voxel size for tomography was 3.24 μm. Diamond Light Source-developed program Savu (206) was used for reconstruction of tomography data, applying the FBP algorithm (207) as a part of Astra Toolbox (208).

7.3 Advanced X-ray studies of wear - Results

The most valuable application of empirical results is to formulate and test mathematical models of the process under study. A good model of wear must account for the behaviour of the wear debris bed and its interactions with the wearing bodies (8).

The general trajectories of mass removed from the wearing bodies, mass ejected from the contact (which are not the same, since some of the debris is entrapped in the contact) and the thickness of the wear debris bed as predicted by the model of Fillot, Iordanoff & Berthier model are shown in Figure 131. Mass removed from the first bodies is obtained by integrating eqn. 17, mass ejected by integrating eqn. 18 and debris bed thickness by solving eqn 19.

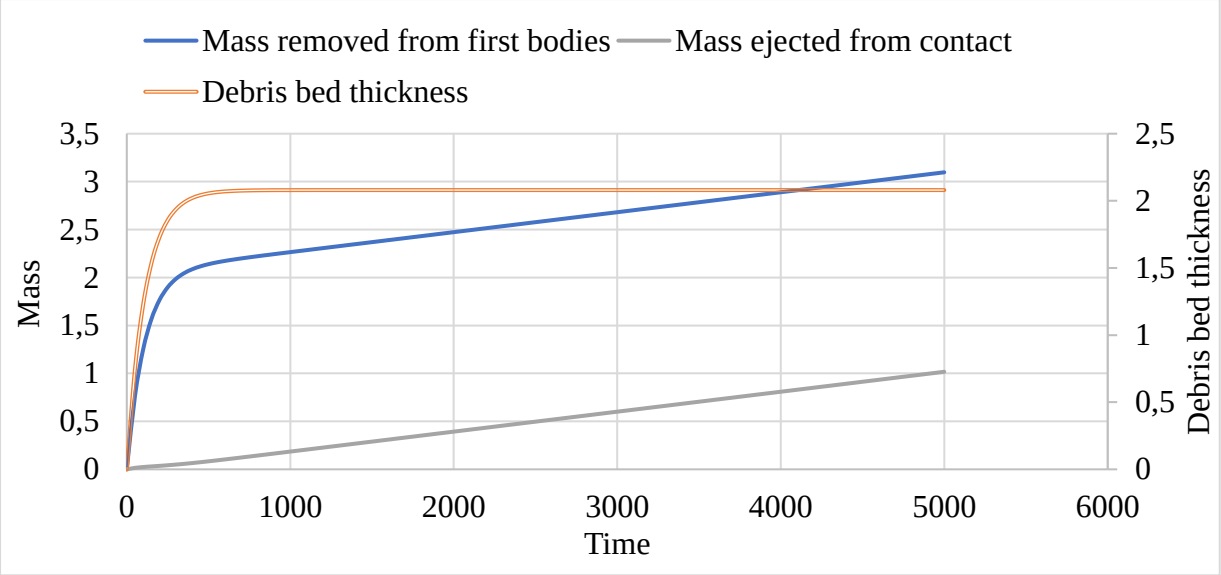

Figure 131: General trajectories of total masses and debris bed thickness associated with wear process according to the model of Fillot, Iordanoff & Berthier (drawn after (15), units are arbitrary).

In a fretting wear experiment performed at a fixed frequency, time can be replaced with a number of wear steps, as there is a fixed relationship between the two. Material density likewise links mass and volume, enabling the mass to be interpreted as a volume and vice-versa. In this work, the experimental data collected is compared with the model of Fillot, Iordanoff & Berthier to observe, if this model can be used to explain the observations made.

7.3.1 Quantity of wear

The quantity of wear was measured directly from the output of the Zwick-Roell machine: during the wear process, the separation of the sample holders changes due to sample shape being impacted. The sample holder separation is measured at the beginning and the end of the wear experiment, the difference between them is multiplied with the nominal contact area, to give the volume of material displaced by the wear process from the wearing bodies (Figure 132). This method of measuring wear is crude from a practical standpoint, however, measuring mass lost in wear was not possible on account of the use of putty to bond the contact. In a full in-situ experiment, weighing the sample would require the removal of samples, thus defeating its purpose.

It is apparent that the changes in total quantity of wear are not significantly dependent on the normal force. This is consistent with experimental evidence of Hintikka et al. (86; 109) showing that wear in full annular contacts is independent of normal force. Since the difference between data points collected at 300 N and 510 N is within the experimental scatter of the data, the model of Fillot, Iordanoff and Berthier (15) was manually fitted to both datasets, giving a reasonable agreement, given the scatter.

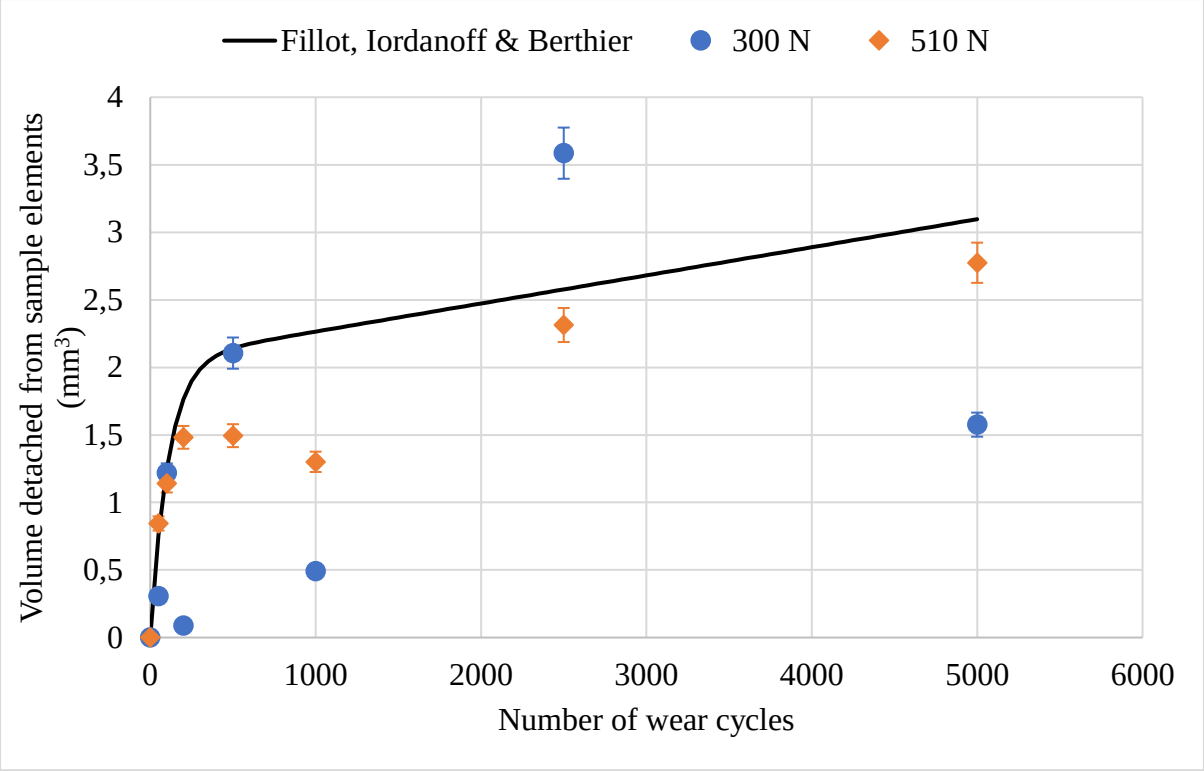

Figure 132: Volume detached from the sample elements as measured, with the model of Fillot, Iordanoff & Berthier fitted.

It should be borne in mind, that in a true in-situ experiment (rather than a simulated one, as presented here) each data point would be the result of the wear process continuing from the *previous* data point. In practice this means than in a true in-situ experiment it would be impossible for there to be less volume loss after 1000 cycles than after 500 (as it occurred when using normal force of 510 N) or that there would be more wear after 2500 cycles than after 5000 (as it occurred here when using 300 N). The scatter encountered here, while unfortunate, further illustrates the sensitivity of the wear process to a variety of factors and therefore the value of being able to directly observe the progress of wear within one wear sample.

7.3.2 Tomography results

X-ray tomography enables the worn contact to be observed 'from the inside' which is important in detemining how and where the wear initiates and how it progresses. A typical example of an axial tomography slice is shown in Figure 133, showing the three principal regions of the tomograph (putty, aluminium sample and air), the radial hole drilled through the side of the sample and the wear damage. A radial tomography slice is shown in Figure 134. Approximate positions of slices A and E relative to the wear zone (as shown in Figure 135-Figure 137) are also indicated. The relatively long sample-to-camera distance used caused noticeable phase contrast artifacts to occur. Where a sharp edge between two materials exists in the sample, the sharp change in X-ray refraction coefficient creates a local signal perturbation, causing the more

strongly-attenuating material to appear in a lighter shade than normal near the edge and reverse for the less-attenuating material.

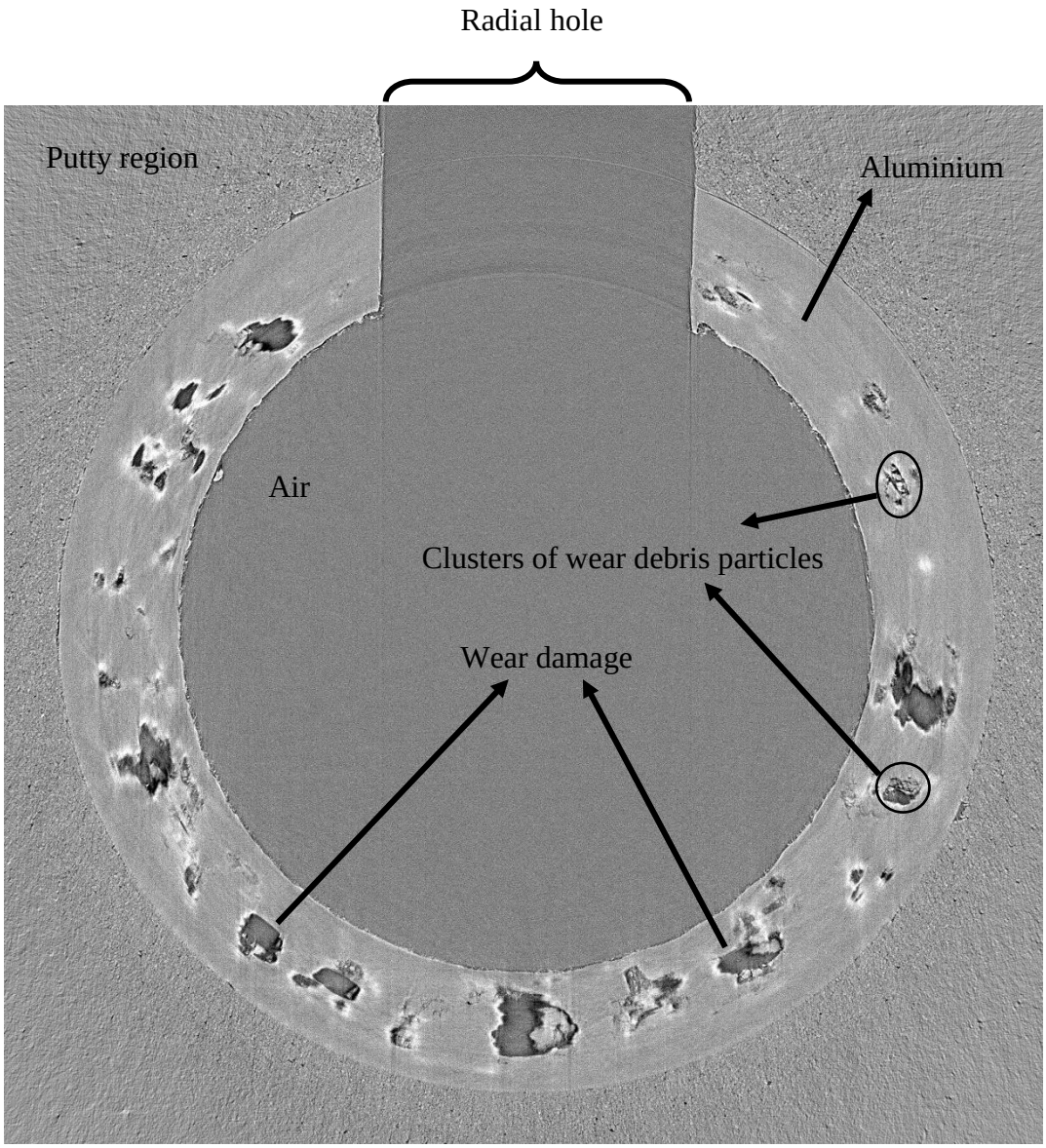

Figure 133: Axial tomography slice, showing characteristic components.

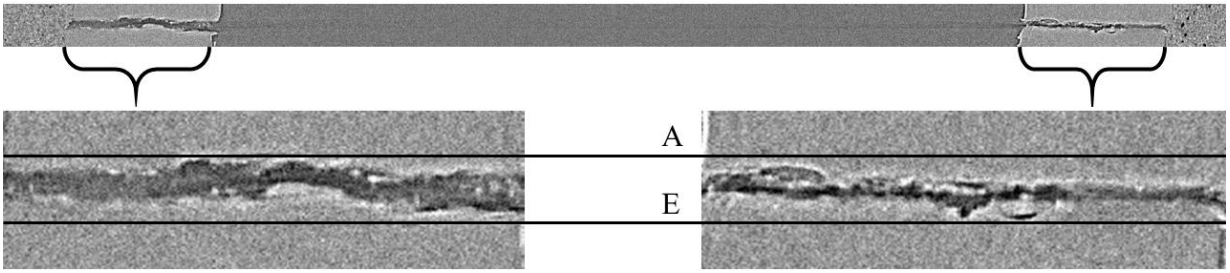

Figure 134: Radial tomography slice. The entire tomography area is at the top. The worn regions are zoomed in below. Lines A and E are approximate locations of slices A and E in Figure 135-Figure 137.

Figure 135 shows a series of axial slices through the wear zone in two samples, both worn for 50 wear cycles. Slice A lies just at the top of the wear zone, slice E just at the bottom. As might be observed, the wear initiates evenly around the inner edge of the annulus and is limited to a narrow strip of material close to the edge, where roughening and folding of the surface occur. This is consistent with modelling work of (25), who demonstrated that in axially loaded annular contacts with straight walls, there exists a radial pressure gradient with the highest contact pressure occurring at the inner edge. Figure 136 shows wear after 100 cycles; the wear damage can be seen spreading in the radial direction (compare Figure 136-C2 with Figure 135-C2). After 500 wear cycles (Figure 137), wear damage extends almost across the entire annular surface (Figure 137-C1 and Figure 137-C2).

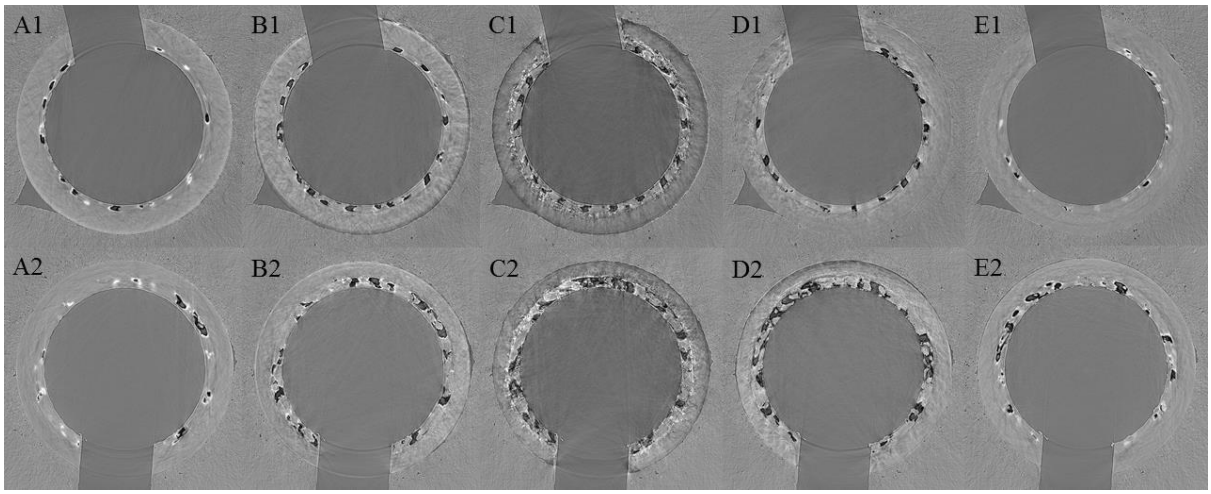

Figure 135: Axial sections of the worn region after 50 wear cycles; images are 10 slices (32.4 μm) apart. A1-E1 show wear at 300 N, A2-E2 wear at 510 N.

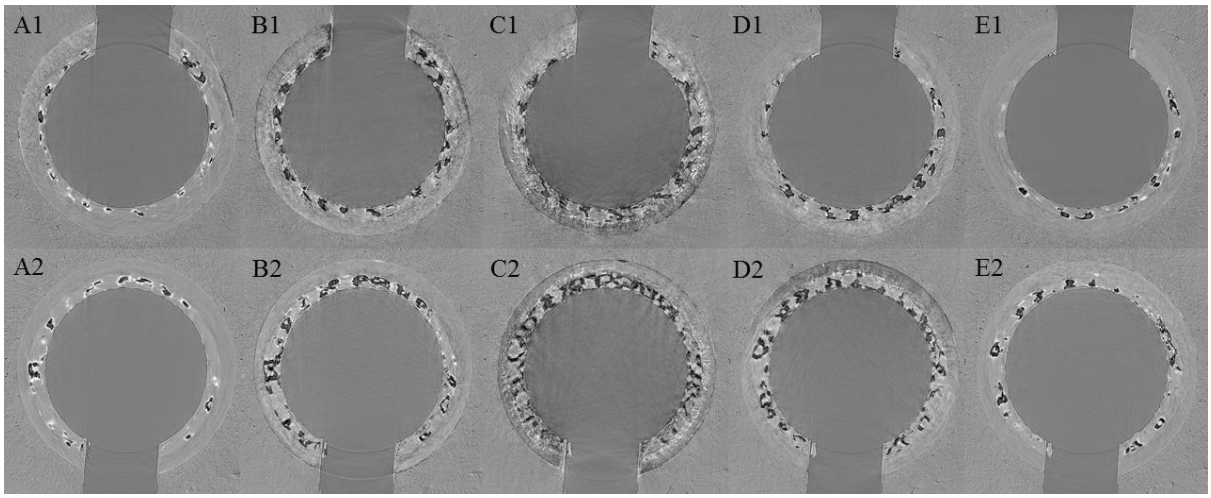

Figure 136: Axial sections of the worn region after 100 wear cycles; images are 10 slices (32.4 μm) apart. A1-E1 show wear at 300 N, A2-E2 wear at 510 N.

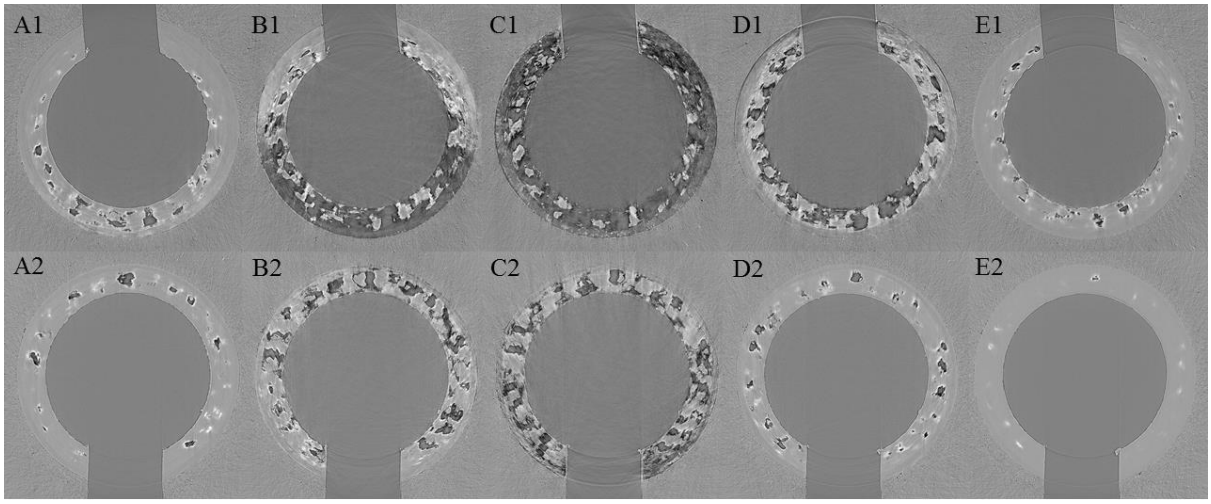

Figure 137: Axial sections of the worn region after 500 wear cycles; images are 15 slices (48.6 μm). A1-E1 show wear at 300N, A2-E2 wear at 510 N.

Using the MATLAB code developed in the Department of Material Science, University of Oxford (209), the tomographs can be 'unwrapped', making the cylinder appear as a block, which enables additional sections to be made, not possible on the initial tomograph. Figure 138 thus shows a section made along the median circumference of the tomographs shown in Figure 137, showing the undulating surface created by 500 wear cycles. Figure 139 shows a similar section of samples worn for 2500 cycles, with the worn zone showing both more wear debris and comparatively smoother surfaces.

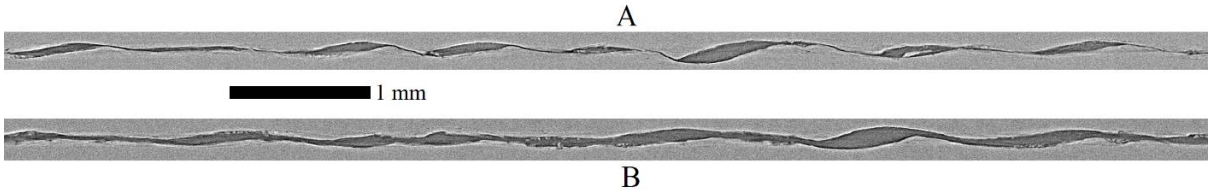

Figure 138: 'Unwrapped' tomography data, showing radial cross-section of the worn zone along the median circumference of the sample. Wear after 500 cycles as 510 N A) Wear after 500 cycles at 300 N B)

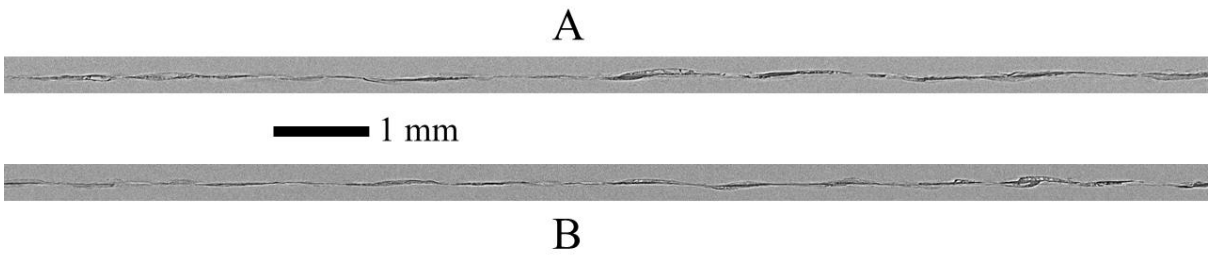

Figure 139: 'Unwrapped' tomography data, showing a cross-section of the worn zone along the median circumerence of the sample. Wear after 2500 cycles at 510 N A) Wear after 2500 cycles at 300 N B)

Progress of wear with number of wear cycles can be clearly seen in Figure 140 and Figure 141. Each slice shown is equidistant from the edges of the wear zone in their respective samples. Wear damage spreads radially from the inner towards the outer edge. The steady state wear conditions are reached somewhere between 500 and 1000 cycles. In the initial stage of wear the surface roughens, reducing the contact area between the wearing bodies (see Figure 140-D, Figure 141-C). In a full in-situ experiment, each image would represent the condition of the same sample at different stages of wear.

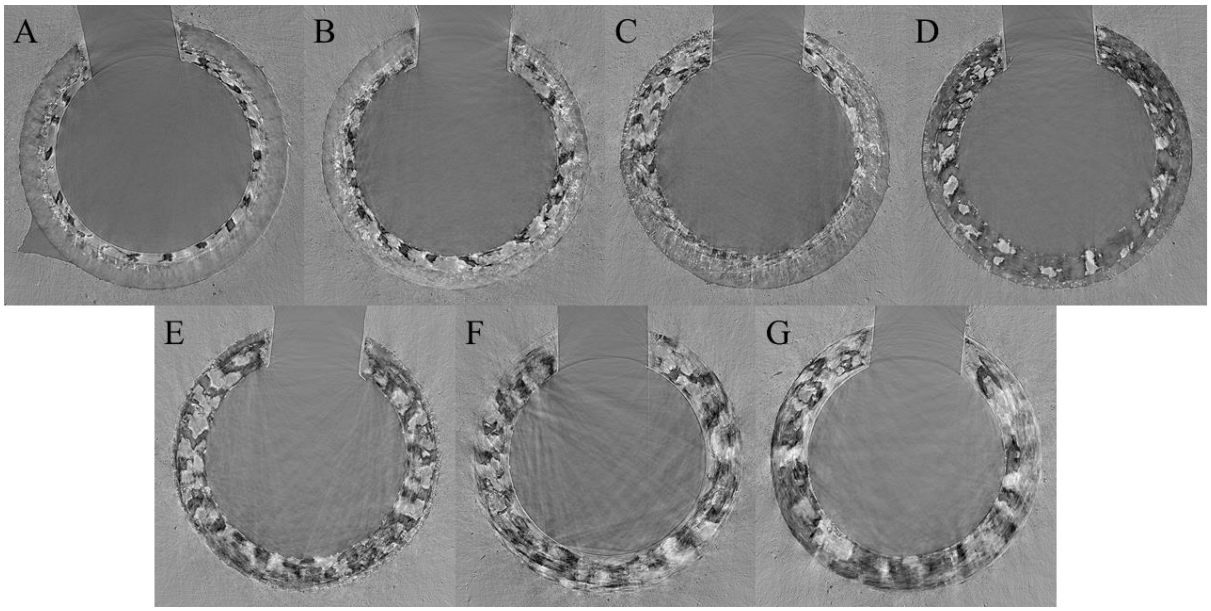

Figure 140: Axial cross-sections through the middle of the worn zone (normal force 300 N); 50 cycles A) 100 cycles B) 200 cycles C) 500 cycles D) 1000 cycles E) 2500 cycles F) 5000 cycles G).

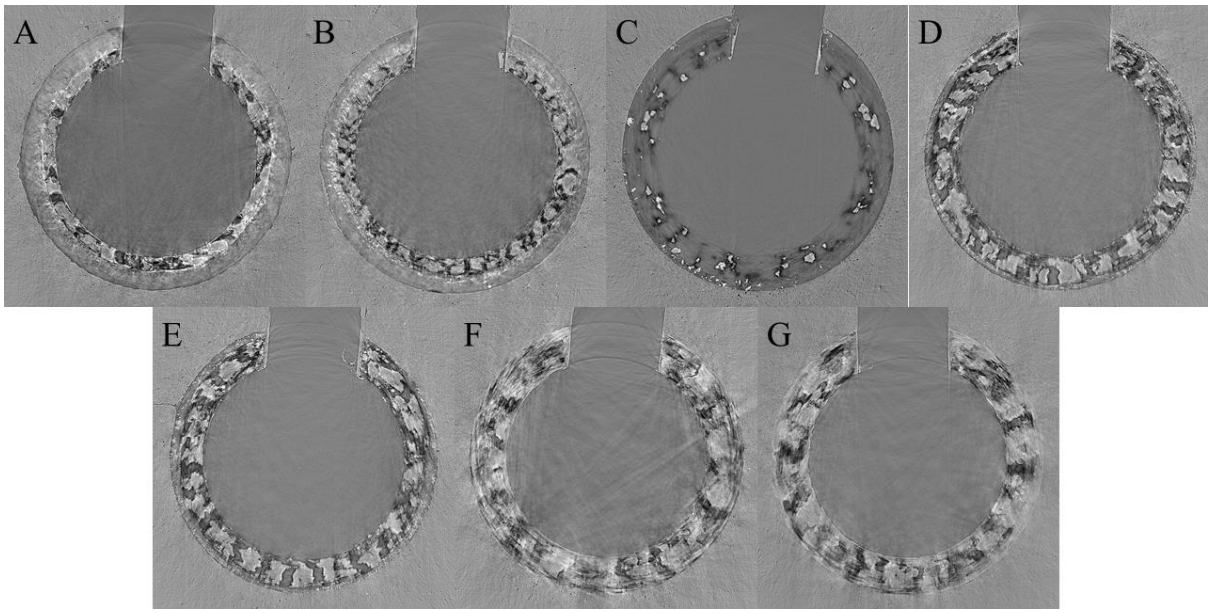

Figure 141: Axial cross-sections through the middle of the worn zone (normal force 510 N); 50 cycles A) 100 cycles B) 200 cycles C) 500 cycles D) 1000 cycles E) 2500 cycles F) 5000 cycles G).

Despite being worn to different degrees, the wear zones shown in Figure 140 and Figure 141 all show a common type of patterning: the wear zone is comprised or irregularly-shaped islands of material, giving the appearance of leopard spots. The patches are roughly periodic, appearing at regular intervals around the circumference. As before, unwrapping the tomography data can help visualize this trend. Axial sections shown in Figure 140D and Figure 141D have been unwrapped (Figure 142).

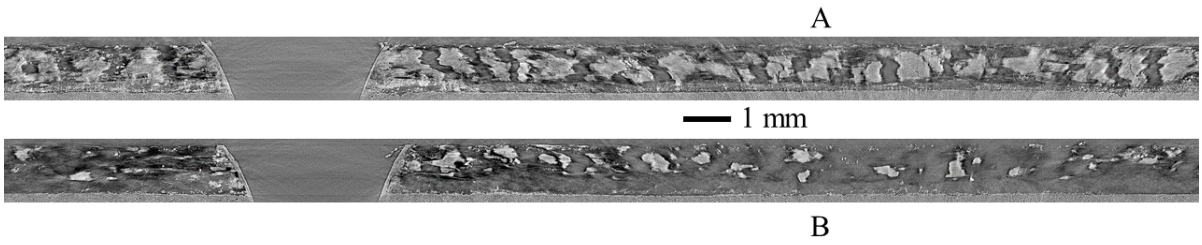

Figure 142: Unwrapped tomography data. Unwrapped Figure 141D A) Figure 142D B)

While a roughly even distribution of material around the circumference is not unexpected (if the material piled-up in one end of the contact, the surfaces would become angularly misaligned, which is not possible due to stiffness of the sample mount) there is no immediately apparent reason for such periodicity. To investigate this further, the angular separation between the centres of raised patches in the wear zone was measured on each wear sample, using the sections shown in Figure 140 and Figure 141. The frequency distribution of the observed separation angles is shown in Figure 143, indicating approximate periodicity with period 10°-30°.

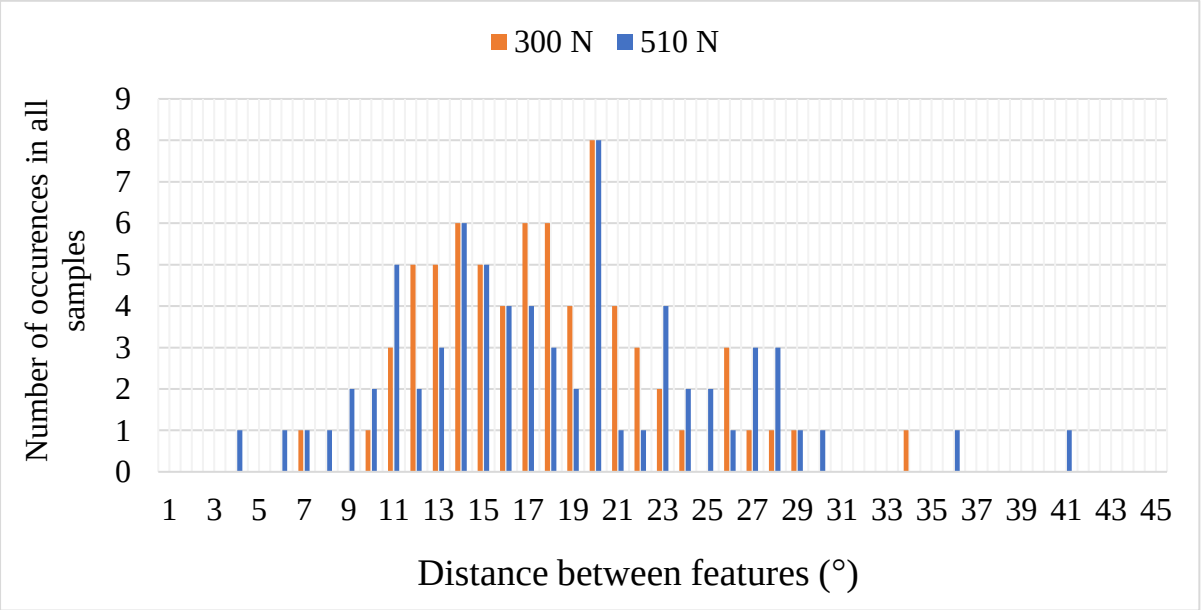

Figure 143: Frequency distribution of angles measured between the material patches at both levels of normal force.

The most commonly encountered angles are 14 and 20 angular degrees, occurring 6 and 8 times respectively in both experimental runs. Superficially, it would appear that a higher normal force promotes somewhat larger separation of features; however, the average angular separation is 17.7 degrees for samples worn at 300 N and 18.0 degrees for samples worn at 510 N. The fact that the most common angles observed are close to multiples of imposed displacement (3°, see section 7.2.1) suggests that the observed periodicity is not coincidental. However the exact mechanism operating is difficult to determine: in the initial stage of wear, the wear zone is formed of large patches of material, separated by narrow gaps (see Figure 140A for example), this transforms to small 'islands' of material separated by large gaps (Figure 141C for example) with large patches with small gaps reappearing at higher numbers of wear cycles (Figure 140E, Figure 141E). This development does not suggest some straightforward relation between the size or distribution of the patches and imposed displacement.

When examining the tomographs shown in Figure 135-Figure 142 it becomes apparent, that while debris particles can definitely be seen in the contact, the wear scar isn't filled with a continuous wear debris bed. As observed already in section 5.4 most of the contact is in fact empty. This raises the question of whether the concept of debris bed thickness, used by Fillot, Iordanoff and Berthier is indeed widely applicable and what is its precise physical meaning in contacts which do not form continuous debris beds.

Examining the axial slices could also be useful for monitoring the quality of alignment in the wear rig. Unevenness in wear pattern would indicate that the contact pressure is uneven across the contacting surface (see Figure 137-B1, Figure 140-C). In an in-situ experiment, examining the wear zone could be used for adjustments of rig alignment during the experiment or to obtain more accurate judgment on the quality of the experimental run.

7.3.3 Total depth of the wear scar

By counting the number of axial slices in the worn zone, the total depth of the wear scar can be determined (as already discussed in section 5.4.2). Identification of where the wear zone begins/ends has an error of about two slices, creating an absolute error of ± 4 slices. As each slice is 3.24 μm thick, the absolute error is thus ±12.96 μm. The total wear scar depth is the upper bound on the thickness of the debris bed layer and while the exact relation between their values is unclear at present, a linear proportionality is assumed as a first approximation. Total depth of wear scar is shown in Figure 144. The values used to generate the Fillot, Iordanoff & Berthier model plot in Figure 132, were used to plot the development of debris bed thickness according to their model (eqn 9), which was found to roughly match the development of total

wear scar depth in both shape and magnitude (also compare with the relevant trace in Figure 131). However, the empirical measurements of total depth show a 'hump' peaking at about 200 cycles, rather than a monotonic increase predicted by the model. This trajectory is very similar to typical trajectories of friction coefficient during the wear experiment (see section 2.2.5) and could indicate, that the relation between the total wear scar depth and the debris bed thickness is not perfectly linear.

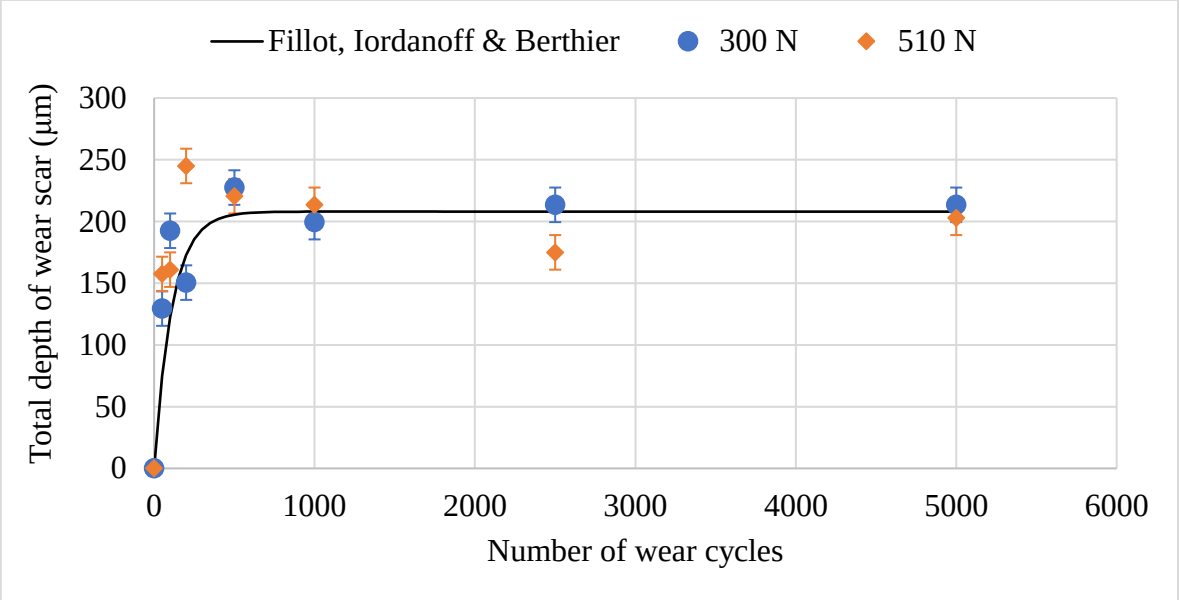

Figure 144: Total thickness of wear scar as measured and predicted by the model of Fillot, Iordanoff & Berthier.

7.3.4 Contact porosity

By examining the radial slices through the worn zone, the contact porosity can be established. In this section, contact porosity is defined as the percentage of the wear zone volume which is not metal nor metal oxide. The wear zone volume is defined as the nominal contact area multiplied with the total wear scar thickness. For the purpose of porosity calculations, 16 radial slices were taken from each tomograph and submitted to thresholding in ImageJ to determine the area not corresponding to metal or metal oxide. The mean porosity values for each of the samples are shown in Figure 145. The primary source of error is the scatter in the values used to calculate that mean. The error bars show the standard error associated with each mean. Contact porosity increases significantly in the initial stage of wear, before decreasing again to a low, steady-state value (≈10%).

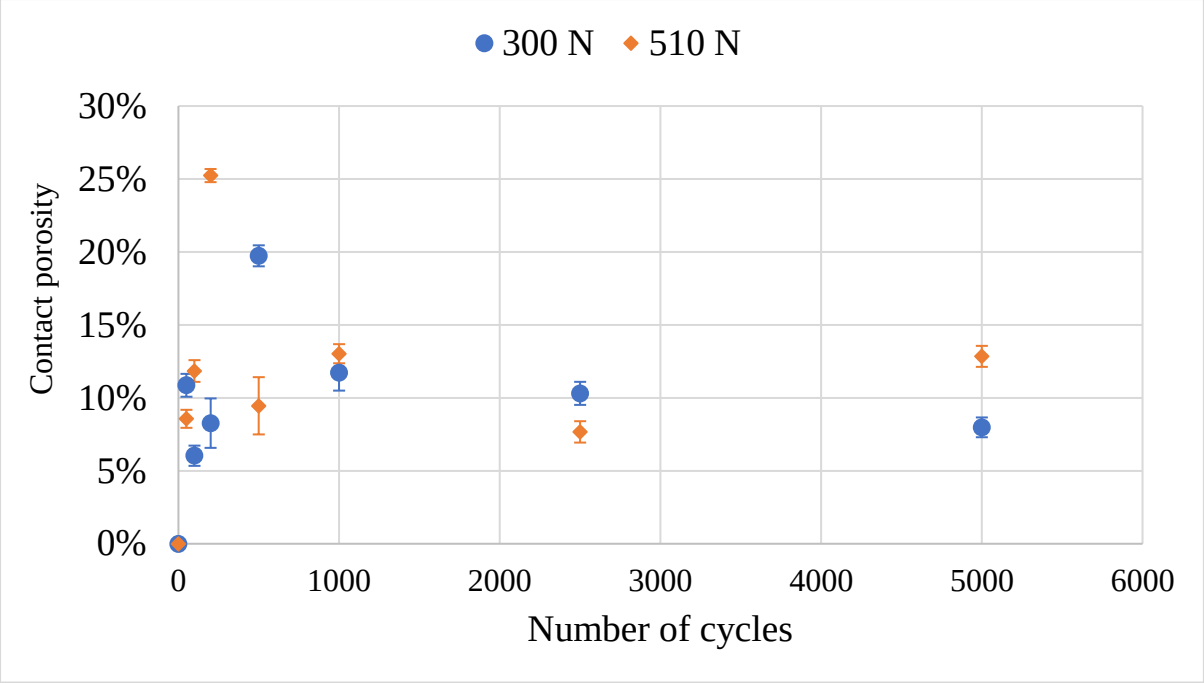

Figure 145: Contact porosity.

7.3.5 Real area of contact

Using the method described in (2), the real area of contact between the worn surfaces can be estimated. Using Avizo software, the air region of the tomograph can be visualized. The gaps in the air region, when viewed along the axis of the sample, represent the contact between the sample elements. Selected examples of real areas of contact are shown in Figure 146.

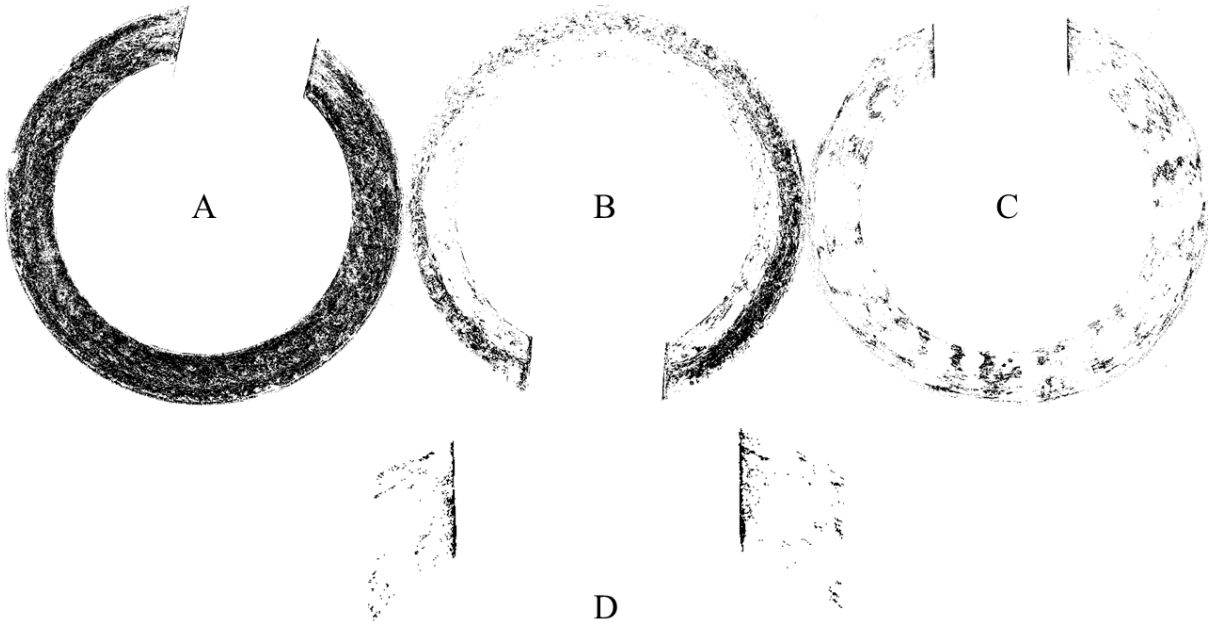

Figure 146: Real areas of contact, black showing the metal-to-metal contact. Unworn contact A), Normal force 510 N, 100 wear cycles B), Normal force 510 N, 5000 wear cycles C), Detail of the area around radial hole D).

At the edges of the radial hole there exists a 'line' of contact area. This is certainly an artefact of the drilling operation, since it appears consistently in all samples and there is no reason why material would pile in this particular area during wear. For this reason, a thin region at the edge of the hole was excluded from the calculation of the contact area. The results are shown in Figure 147.

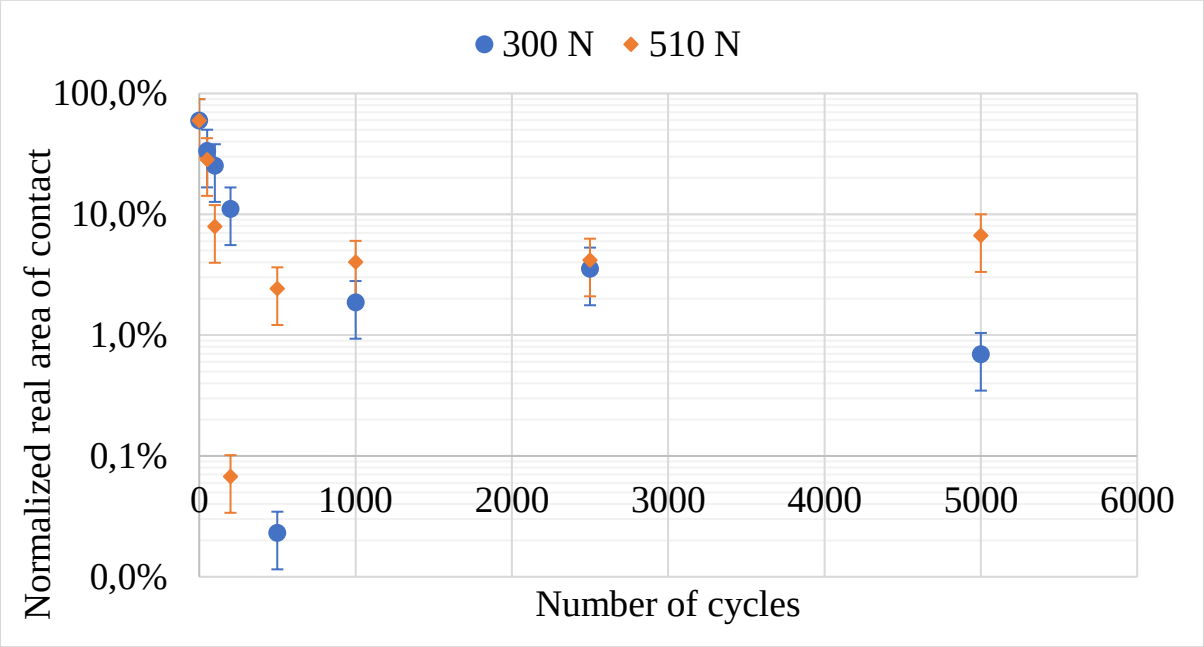

Figure 147: Real contact area expressed in % of nominal contact area.

The real area of contact is largest before the start of wear, but it is not 100% due to initial surface roughness. With the progress of wear and associated surface roughening and debris generation, the real contact area is reduced quickly to near zero (≈0.5% of nominal contact area) before increasing again to a low steady-state value (≈5%), which could indicate the gradual reduction of the large asperities created during the initial roughening of the surface.

Estimating the real area relies on manually thresholding the tomography data in Avizo software, which inevitably includes a human decision factor in the end result. The analysis was repeated three times; points in Figure 147 show results at the threshold judged optimal by the analyst. The threshold was then moved 1000 points above and below the chosen value (which conservatively represents the range of realistic threshold values), areas recalculated and the larger of the two deviations from the initial value used to calculate the relative error for the data point.

7.3.6 Diffraction results

In this experiment X-ray diffraction was used to determine what changes have occurred under the worn surface of the material as a result of wear. Numerous researchers have demonstrated that wear typically causes restructuring of the material immediately underneath the worn region (54; 52; 55; 196; 57; 62) characterised by extensive plastic straining, work hardening and grain refinement. It was hoped that X-ray diffraction would enable the observation of these changes in-situ.

The set-up of the experiment introduced a challenge to diffraction data analysis, since the X-rays diffract both from the sample, as well as the mineral fillers in the binding putty. However, owing to the relative strength of the respective signals, deconvoluting them is not overly demanding. Using the lattice parameter for pure aluminium provided by Straumanis (210) the theoretical positions of diffraction peaks for 111, 200, 220 and 311 planes were calculated and strong peaks were discovered in corresponding places in the empirical diffraction spectra (example shown in Figure 148).

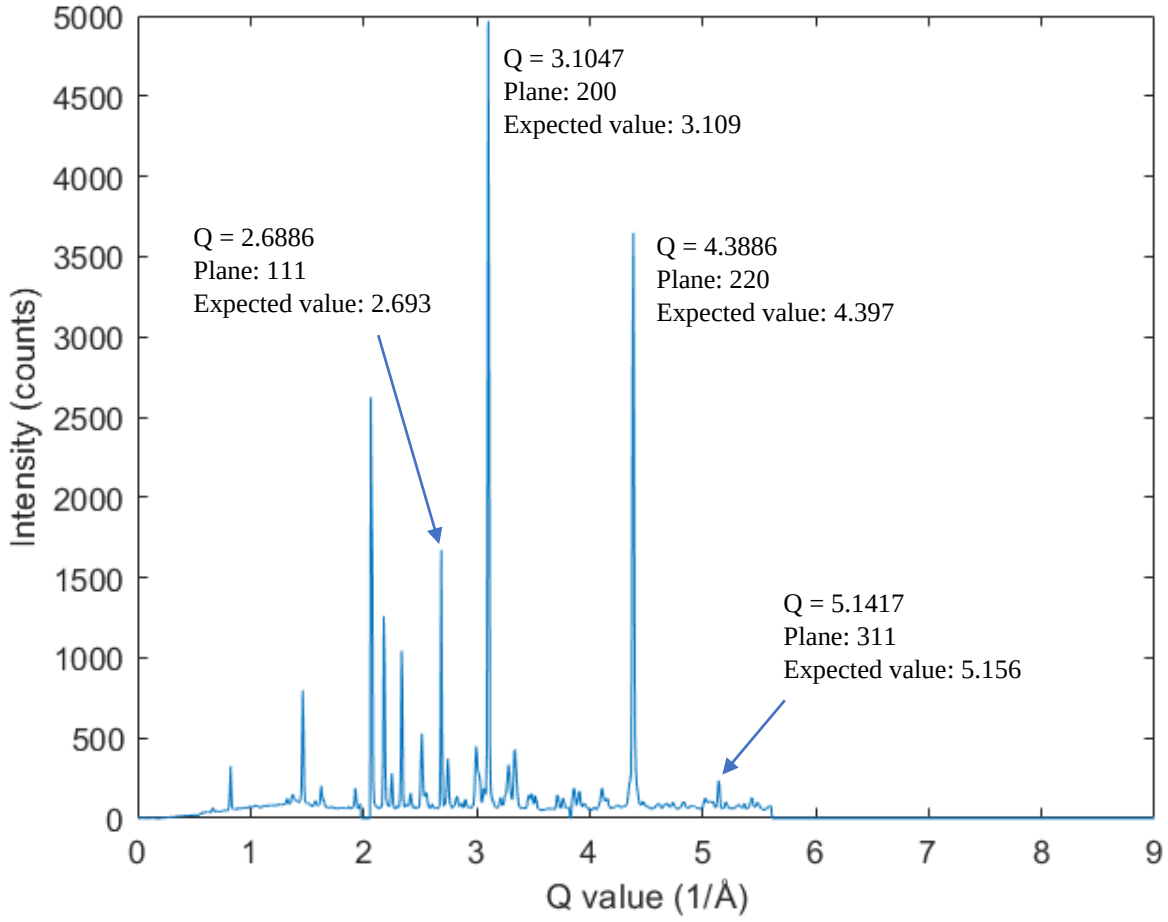

Figure 148: Diffraction spectrum for undeformed sample material. Location of peaks from specific planes is marked.

As described in section 7.3.4, the worn contact is porous, causing the intensity of the diffraction signal to drop when the beam moves through the worn region. Figure 149 and Figure 150 show peak intensities for two crystal planes, when the diffraction signal is integrated over an angle of 7.5° of either side of azimuthal angle of 0°. Choosing a small angle of integration enables the texture of individual sample elements to be studied. For example, in one sample (Figure 150) peak intensity rebounds for 220 family of planes, but not for the 200 family, indicating that one sample element has fewer 200 planes oriented so as to diffract within the chosen angle of integration. Texturing of the unaffected material is likely due to the samples being machined from a drawn/extruded aluminium bar; the texture being the artefact of the production process.

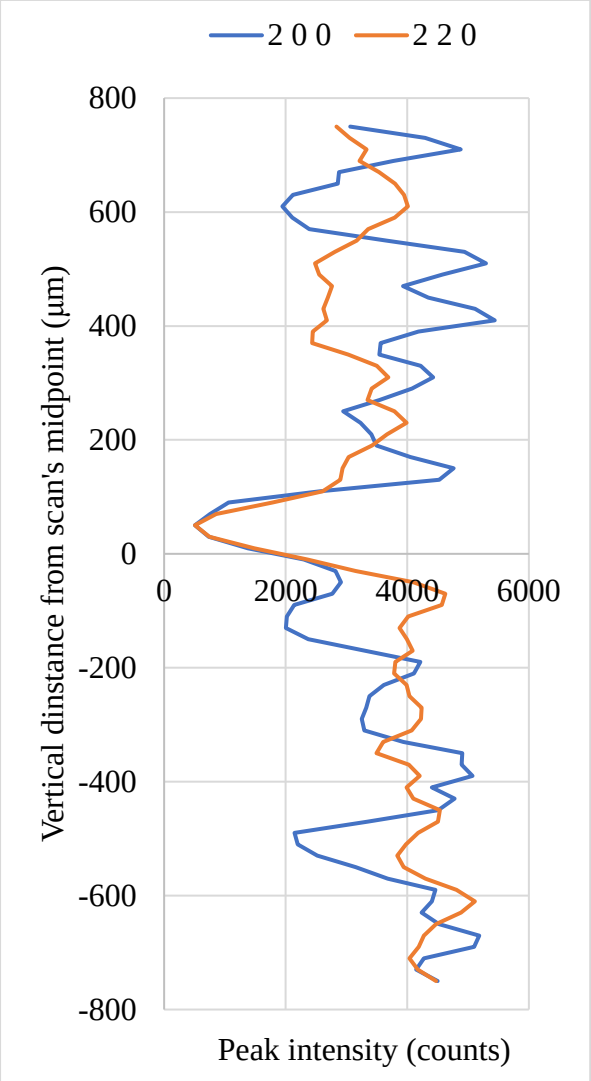

Figure 149: Peak intensities for 200 and 220 crystal planes as a function of position within sample. Normal force 300N, 5000 cycles.

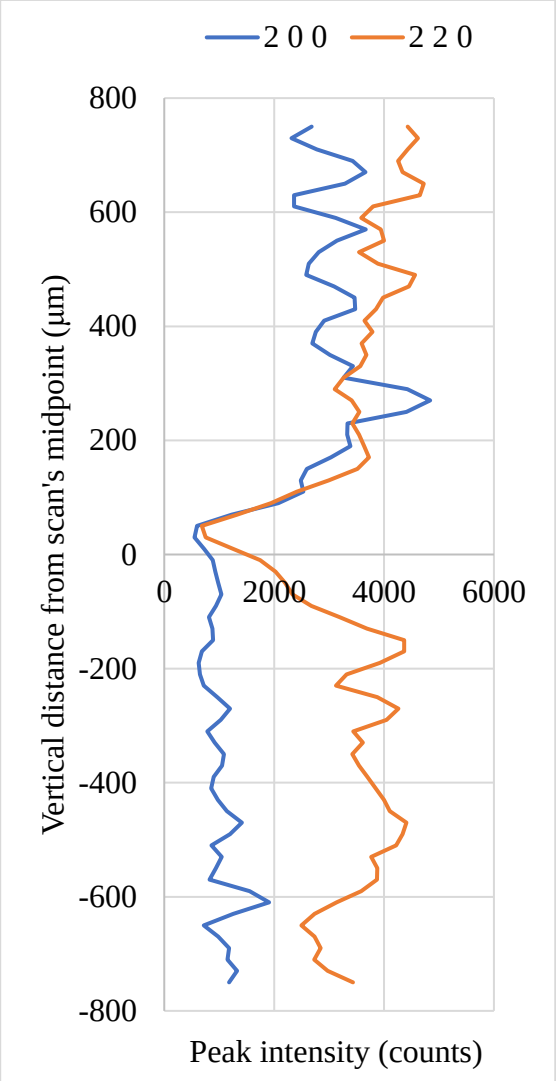

Figure 150: Peak intensities for 200 and 220 crystal planes as a function of position within sample. 510N, 5000 cycles.

The residual elastic lattice strain was determined through the analysis of the diffraction data for the 220 peak, as this peak was least affected by the experimental noise. While it would be in principle beneficial to analyse several peaks, the unpredictable oscillations of their intensity made this a challenging endeavour which was judged to exceed the immediate needs and timescale of this work. As before, the diffraction signal was integrated over an angle of 7.5° of either side of azimuthal angle of 0° to give strain in the direction of sliding. By rotating the azimuthal angle around which the integration of spectra is performed, the spatial distribution of strain could be obtained. As before, this was not attempted on account of time limitations, since the hoop strains measured were judged to be of greatest interest. The application of Williamson-Hall anaylsis to peak width data was attempted however, with the intention of obtaining additional information concerning grain size in the strained layer. Unfortunately, these attempts have not been successful, as of time of submission.

In each collected spectrum, the peak and its immediate surrounding (area of ± 1/Å relative to the peak position) were extracted and a peak shape comprised of a sum of seven basic Gaussian peaks fitted using the least square method[7]. Residual lattice strain can be inferred from the changes of the peak position. It was assumed that material far away from the wear region has zero residual strain; 30 far-away data points were averaged to obtain a strain-free reference. Representative examples of the spatial distribution of residual lattice strain are presented in Figure 151 and Figure 152.

[7]The associated calculations and relevant Mathlab code were performed and developed by Marcus Williamson of Department of Materials, University of Oxford.

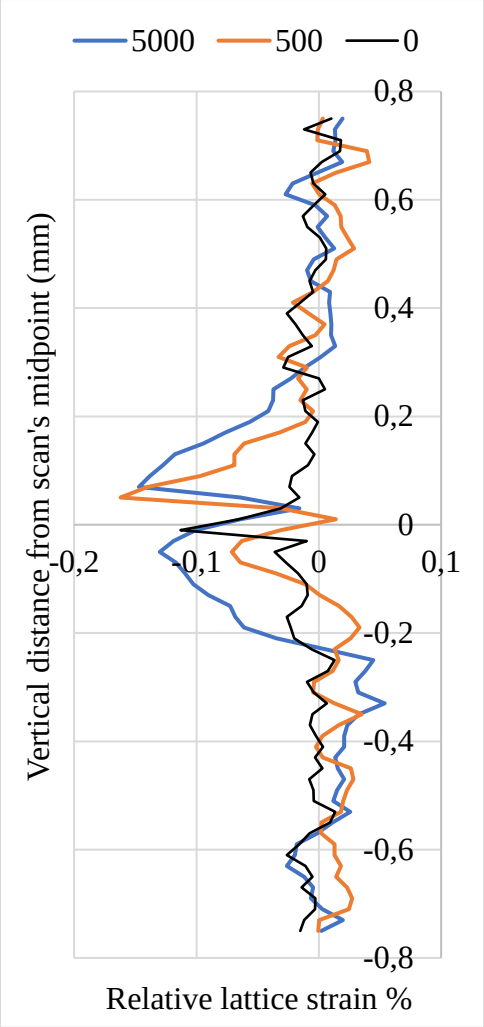

Figure 151: Residual lattice strain at normal force of 510 N as a function of number of cycles.

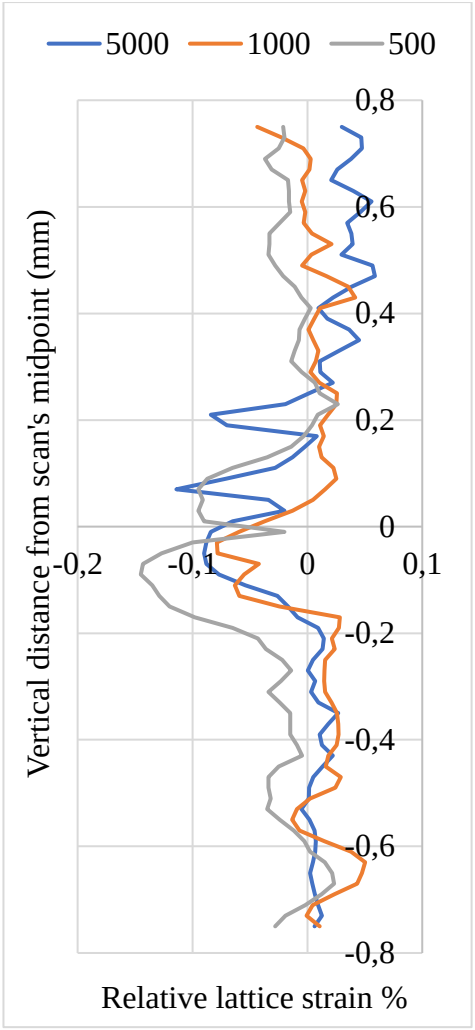

Figure 152: Residual lattice strain at normal force of 300 N as a function of normal force.

In worn samples, the distribution of residual strain commonly shows a 'double dip' in the contact region (see for example the 5000 cycle line in Figure 151). The position of the central 'spike' which divides the dip in two, corresponds exactly with the location of maximum decrease in signal intensity, indicating that this is the artefact caused by signal loss due to contact porosity. The left and right sides of the dip would therefore represent changes caused by sub-surface changes to the material. The maximum relative strain magnitudes for each sample are shown in Figure 153. The maximum strain reaches a peak at around 500 cycles, before decreasing slightly. In the early stages of wear there were oscillations in the observed peak strain value. In the early stages of wear there were oscillations in the observed peak strain value.

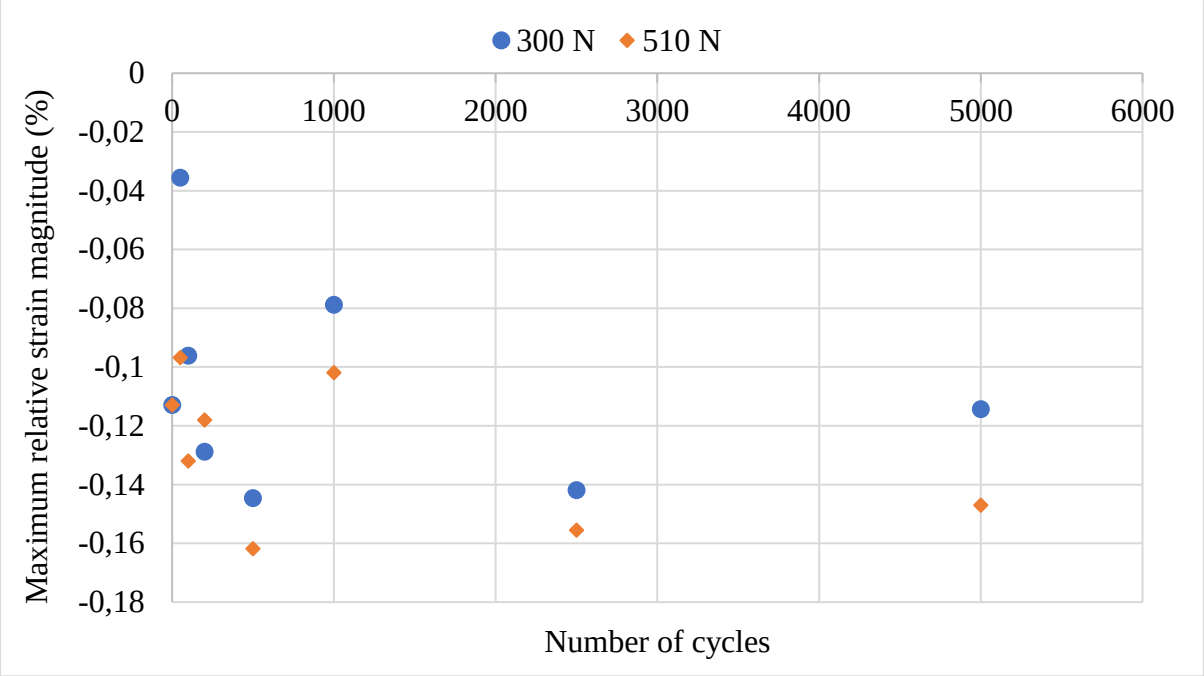

Figure 153: Maximum relative strain observed in each sample as a function of cycle number.

The development of the residual strains suggests different wear processes occurring at different stages. In the initial stage, the surface is roughened by surface folding and/or material transfer (possibly in a manner suggested by (70)) causing large asperities to form (this is consistent with the appearance of the wear zone as shown in Figure 140C-D and Figure 141C). These are eventually worn away as the debris bed builds, with a strained layer being formed underneath the surface, possibly through the debris indenting the virgin material. The thickness of the strained layer under the worn surface can be estimated by firstly measuring the length over which the strain raises more than three standard deviations of the average value for the undeformed material, subtracting the local wear scar thickness in the diffraction volume and dividing by two. The elastically strained layer is not necessarily equal in thickness to the tribologically transformed structure; as demonstrated in section 6.5 changes to the diffraction signal can extend deeper into the material than the visible damage to the crystal structure does. Results are shown in Figure 154, with the strained layer's thickness increasing with the number of cycles.

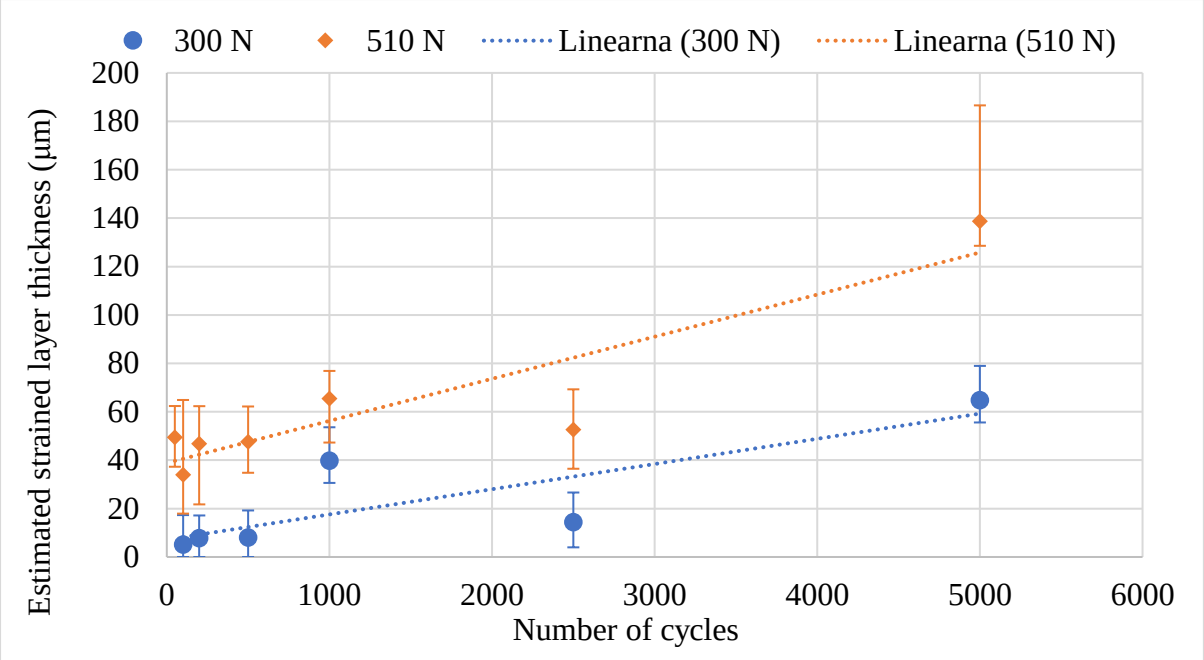

Figure 154: Estimated thickness of the strained layer created by wear as a function of number of cycles.

7.4 Advanced X-ray studies of wear - Outcomes

The tests presented have yielded considerable data, enabling the wear in metal-metal contacts to be studied without disassembling them. Since an in-situ experiment would dispense with the use of binding putty or drilling holes through the contact region after wear, thus in some sense simplifying the process, it can be concluded that an in-situ imaging/diffraction experiment is both possible and appropriate for its desired purpose: to observe and quantify the condition of the wearing contact at different stages of the wear process. The principal consideration for design of an in-situ experiment is the use of an appropriate beamline-compatible wear rig. This, however, is not an unsurmountable obstacle; use of loading frames, furnaces and other large and bulky equipment for applying mechanical forces, as well as specific thermal and chemical environments to samples during synchrotron studies is a widespread practice, demonstrating that capacity in terms of space and weight exists in many facilities.

Beside demonstrating the viability of using synchrotron for tribological studies, this work also demonstrates the value of this approach:

- The progress of wear has been successfully observed without any mechanical disturbance to the contact.
- Loss of volume due to wear was quantified, compared to a theoretical model proposed by Fillot, Iordanoff & Berthier and an acceptable agreement obtained.
- Using the same model parameters, the general trend of the wear scar development was also predicted, meaning the approach of Fillot, Iordanoff and Berthier is capable of predicting the development of two separate wear-created features with reasonable accuracy.
- Contact porosity and real area of contact were quantified; these are properties which could be valuable in studying permeability of contact to fluids, heat or electrical currents.

It appears unlikely that such rich information could be obtained with traditional techniques. In this study only 15 data points were gathered, however a full in-situ experiment could collect many more, with only one sample per level of normal load. This would require the use of a wear machine compatible with the synchrotron beamline. If annular contacts were used, a biaxial compression-torsion rig would suffice and synchrotron-compatible models are in fact commercially available (as discussed in section 3.4.1). An experimental rig using Hertzian contacts or other common open contact geometries would probably need to be designed and made from the ground up. At any rate, cylinder-on-flat, flat-on-flat and similar geometries appear much more conducive to 2D radiography (with the X-ray beam being perpendicular to the wear zone) than tomography (since they are not rotationally symmetric and it might be very difficult to prevent the samples being shaded by parts of the wear rig).

8 TRANSITION TO THE OPEN CONTACT

In section 2.4.1, the model of Fillot, Iordanoff & Berthier was identified as a promising starting point for developing an improved model of wear. A series of experiments were used to examine the effects of contact geometry on parameters of this model, using a closed contact geometry that served as a physical representation of the idealized geometry FI&B originally simulated (117; 15; 133). It was also demonstrated (section 4.3.2.2), that in the annular geometry studied, the model of FI&B predicts a non-monotonic dependence of wear on normal force, which is consistent with experimental observations for that contact geometry, but had not been explained until now. In section 7.3 wear in annular geometry was examined through X-ray computed tomography, with the quantity of material detached from the worn sample and the total thickness of the wear scar (the latter being assumed to be proportional to the debris bed thickness) both following the trends predicted by FI&B model.

Given the relative successes of this model it is worthwhile to attempt to expand it to an *open* contact geometry. If this can be done successfully, it would represent a major development since it is at present unclear, how can wear in one geometry be inferred from measurements of wear in another geometry. In this chapter we shall attempt to find a global wear model for an open geometry, based on the idea of the tribological circuit (see section 2.3.2).

The first step is to find a form of FI&B model applicative to an open contact geometry. In order to achieve this, the parameters of the FI&B model need to be linked to the contact geometry and the contact conditions, such as normal force (F_N), relative sliding velocity (v_r) and amplitude of sliding (D; for reciprocating or fretting wear). The core relations of this FI&B model have already been given in previous chapters, but are restated again for clarity:

$$Q_d(t) = C_d \cdot \left(H_{max} - H(t)\right) \quad (37)$$

$$Q_e(t) = C_e \cdot H(t) \quad (38)$$

$$\varrho_d \cdot S \cdot \frac{dH(t)}{dt} = Q_d(t) - Q_e(t) \quad (39)$$

where ϱ_d and S denote the debris density and contact area respectively. In steady state, the debris bed thickness (H) becomes stable ($H(\infty)=H_{stab}$) and debris creation (Q_d) and ejection rates (Q_e) become equal.

The values of steady state debris bed thickness and steady state wear rate (for initially clean and perfectly flat surfaces) are given by (117; 15):

$$H_{stab}=\frac{C_d}{C_d+C_e}\cdot H_{max} \quad (40)$$

$$Q_d(\infty)=Q_e(\infty)=Q_{stab}=\frac{H_{max}}{\frac{1}{C_e}+\frac{1}{C_d}} \quad (41)$$

The role and meaning of H_{max} is discussed in 4.3.2.4. FI&B also argued, that if $C_e>>C_d$ (which would apply for example if the wear debris was aggressively removed by some process), Q_{stab} is described by the Archard wear law. As $C_e>>C_d$ makes $C_e^{-1}+C_d^{-1}\approx C_d^{-1}$ we may rewrite eqn 41. as

$$Q_{stab}(C_e\gg C_d)=C_d H_{max}=kF_N v_r \quad (42)$$

Where k is the wear constant, F_N the normal force and v_r the relative sliding velocity of the wearing bodies.

8.1 Wear model for an open contact geometry – Expanding the approach of Fillot, Iordanoff and Berthier

In open contacts, C_e can be at least partially determined from geometrical constraints. Consider a rectangular block sliding along a flat surface with a constant velocity v_r. The block measures L in the direction of sliding and l perpendicular to the direction of sliding. This geometry is identical to the one used by the sponsor (see description in section 1.1, Figure 4, Figure 155).

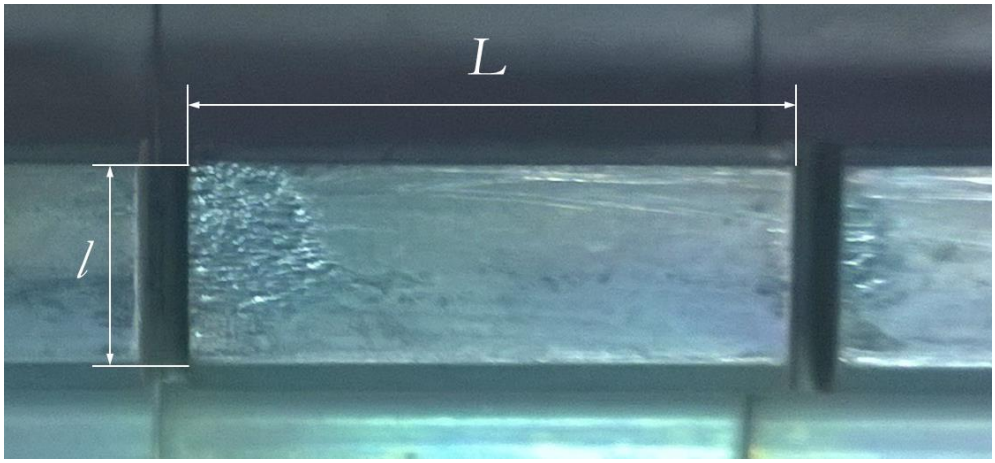

Figure 155: Contact patch at the root of the compressor blade. In service, the patch oscillates left-to-right, rubbing against the seat. Dimensions *l* and *L* are marked for reference.

A debris bed of some thickness H exists between the contacting surfaces. It is assumed that the debris is ejected through a gap, measuring H by l in area with an average ejection velocity of v_e.

Debris ejection rate can therefore be written:

$$Q_e(t)=v_e l H(t)\varrho_d \quad (43)$$

By comparing eqn. 43 with eqn. 38 we determine, that for a flat-on-flat contact in unidirectional sliding with some constant velocity, C_e is given as:

$$C_e=v_e l\varrho_d \quad (44)$$

The relationship between relative sliding velocity v_r and the ejection velocity v_e depends on the properties of the debris and its interaction with the surfaces. If the debris is strongly adhered to the moving body, very little may be ejected. If debris behaves as a Newtonian fluid there will exist a linear velocity profile within the debris bed, with v_e being half of v_r. The velocity profile in the debris bed is usually unknown and is influenced by many variables (see for example (211; 137)) however, regardless of the actual shape of the steady state velocity profile, v_e can be written as a multiple of v_r:

$$v_e=\frac{1}{H}\cdot\int_0^H v(h)\,dh=P\cdot v_r \quad (45)$$

The parameter P introduced in this fashion takes a value between 0 and 1, depending on $v(h)$. Through this mechanism, changes in the debris properties (for example particle-to-particle adhesion, sintering of particles, particle size distribution etc.) translate into changes in wear.

Eqns. 42-44 are not limited to sliding of rectangular blocks, as any shape of some fixed width l will leave the same wear scar area, if rigidly translating along a plane with a fixed velocity v_r for some time t.

A transition from unidirectional sliding to a reciprocating case can now be made. If velocity changes direction, the quantity of ejected material should not be affected significantly, since the contact is open at both ends and the debris bed thickness is considered to be uniform. While it is true, that the steady state velocity profile in the debris bed will take some time to develop, these times are likely to be very short, since the 'viscosity' of the wear debris is very high, ensuring quick momentum transfer. In one wear cycle, the accumulated slip is 4 times the imposed

displacement D. A cycle takes time t_c to complete. We can therefore approximate a reciprocating contact as a unidirectional one by writing:

$$v_r = \frac{4D}{t_c} \quad \textbf{46}$$

Assuming a constant reciprocation frequency and the contact already being in steady-state condition, we can expand eqns. 39 and 40 with eqns. 43, 44 and 45:

$$H_{stab} = \frac{C_d}{C_d + \frac{4D}{t_c} Pl\varrho_d} H_{max} \quad \textbf{47}$$

$$Q_{stab} = H_{stab} \frac{4D}{t_c} Pl\varrho_d \quad \textbf{48}$$

Inserting eqn. 46 into eqn. 41 and uniting this with eqns. 47 and 48 we can calculate the mass lost in one steady state wear cycle:

$$M_{cycle} = \frac{k F_N \frac{4D}{t_c}}{C_d + \frac{4D}{t_c} Pl\varrho_d} \frac{4D}{t_c} Pl\varrho_d \cdot t_c = D \frac{4Pl\varrho_d}{C_d t_c + 4DPl\varrho_d} k F_N 4D \quad \textbf{49}$$

By inserting the expression for C_d from eqn. 42 eqn. 49 is obtained, expressing the mass lost in one steady-state cycle:

$$M_{cycle} = \frac{k F_N \frac{4D}{t_c}}{\frac{k F_N \frac{4D}{t_c}}{H_{max}} + \frac{4D}{t_c} Pl\varrho_d} \frac{4D}{t_c} Pl\varrho_d \cdot t_c = \frac{k F_N 4DPl\varrho_d}{\frac{k F_N}{H_{max}} + Pl\varrho_d} \quad \textbf{50}$$

Eqn. 50 describes wear as increasing linearly with imposed displacement and being to some degree non-linearly dependent on normal force and width of the contact. Dependence on imposed displacement D is therefore the same as in Archard's law. As discussed in section 2.3.1 of the literature survey, the literature is inconclusive, with some researchers reporting linear and others (for example (95; 41; 40; 107; 105)) a quadratic dependence on D (see also eqns. 4-6).

Let us investigate dependence on contact width l and normal force F_N. It is obvious, that the magnitude of other parameters will have significant effect on the behaviour, making it necessary to establish the ranges in which these are most likely to occur. Ranges typical for laboratory fretting experiments are listed in Table 10.

Parameter	Typical range	Source/explanation
ϱ_d	10^3 (kg/m^3)	Bulk material is in 10^3-10^4 range
k	10^{-10}-10^{-5}	(104; 10)
D	10^{-4} (m)	(95; 31; 30; 29)
l	10^{-4}-10^{-2} (m)	In sphere-flat contacts l is the same range as D. For cylinder-flat; flat-flat contacts (95; 92; 31; 29)
P	0-1	Eqn. 45
F_N	10^2-10^4 (N)	(95; 40; 107; 30; 109)
H_{max}	10^{-4} (m)	Debris bed thicknesses measured are in 10^{-2}-10^{-1} mm range.

Table 10: Typical ranges of experimental parameters in laboratory fretting wear experiments

Using a similar approach to the one from section 4.3.2.2, general order of magnitude values can be inserted into eqn. 50 to enable the dependence on l and F_N to be tested

Line	k	D	l	ϱ	H_{max}	F_N
A	10^{-5}	10^{-4}	N/A	1000	10^{-4}	1000
B	10^{-5}	10^{-4}	N/A	1000	10^{-4}	3000
C	10^{-6}	10^{-4}	N/A	1000	10^{-4}	1000
D	10^{-5}	10^{-4}	N/A	500	10^{-4}	1000
E	10^{-5}	10^{-4}	10^{-2}	1000	10^{-4}	N/A
F	10^{-5}	10^{-4}	$2 \cdot 10^{-2}$	1000	10^{-4}	N/A
G	10^{-6}	10^{-4}	10^{-2}	1000	10^{-4}	N/A
H	10^{-5}	10^{-4}	$3 \cdot 10^{-2}$	500	10^{-4}	N/A

Table 11: Magnitudes of parameters used in traces in Figure 156 and Figure 157

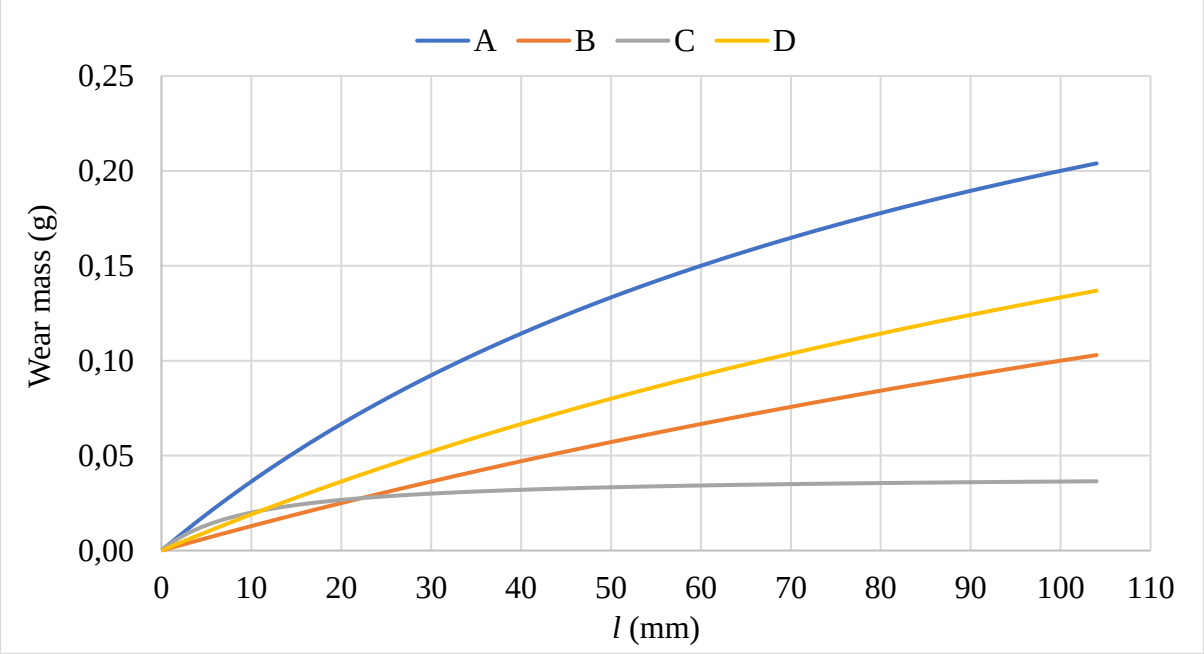

Figure 156: Wear mass accumulated in 10^5 cycles as a function of l according to model in eqn. 50. Lines A, B, C, D correspond to parameters stated in Table 11.

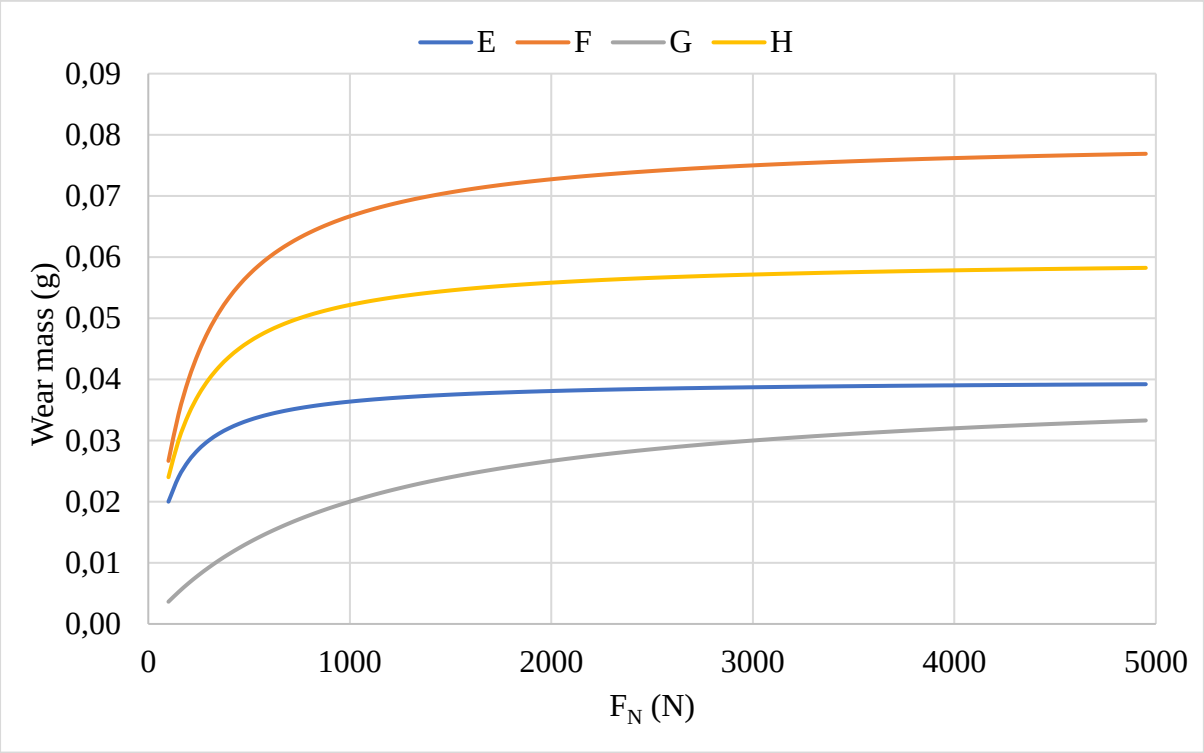

Figure 157: Wear mass accumulated in 10^5 cycles as a function of F_N according to eqn. 50

There is little, if any evidence of fretting/reciprocating wear in open contacts under typical laboratory conditions showing the trends from Figure 156 and Figure 157. It would appear that the approach of Fillot, Iordanoff & Berthier has encountered a limit for further development, at least with the assumptions used.

8.2 Experiments with castellated samples.

In an attempt to gain further insight into the *mechanical* circumstances of the wear process, a series of experiments were performed using castellated annular samples.

8.2.1 Experimental work (constant *L*, varying *D*)

A sample with outside diameter 84 mm and inside diameter 80 mm was used. On one sample element, the wearing surface was divided into 16 sectors, separated by 5 mm wide gaps. When such a sample is pressed against a full annulus and rotated axially, we obtain what are essentially 16 flat-on-flat contacts running in parallel, making the end result an aggregate of 16 runs. Initially, the angular displacement was varied from 0.6° to 3°. Normal force was 5300 N (i.e. 331.25 N per contact patch, giving nominal contact pressure of 20 MPa). The experimental procedure was the same as described in section 4.3.1. Again, linear dependence of mass loss on imposed amplitude was observed (Figure 158). To observe the behaviour of mass displaced by wear (which is known from previous tests to increase more rapidly than merely mass loss) the samples were carefully machined to remove burrs and re-weighed. The dependence was also linear.

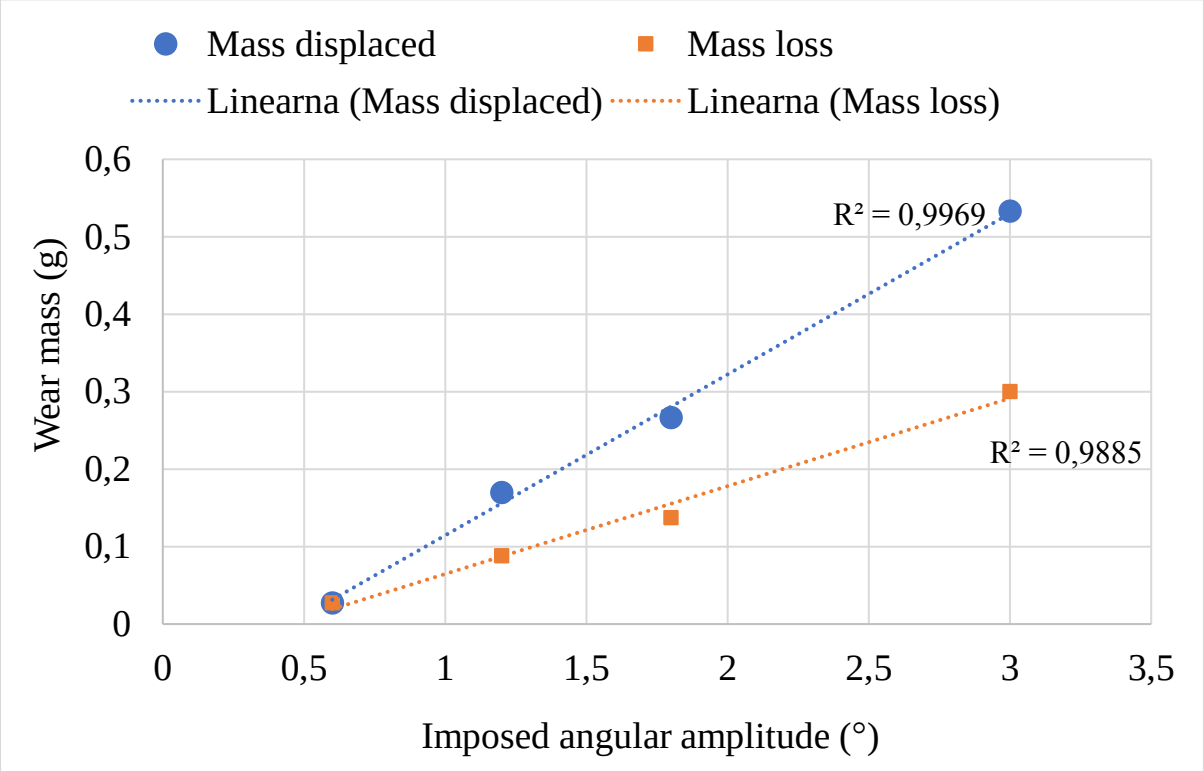

Figure 158: Mass lost and mass displaced as a function of imposed amplitude with respective R^2 values.

A similar experiment was attempted, using smaller imposed amplitudes (0.1° to 0.6°). Expecting smaller amounts of wear, the normal force was increased to 7100 N and number of cycles was increased from 3500 to 7000 in order to increase the total amount of wear. The results are shown in Figure 159. Two regions can be observed, with wear increasing at a different rate at low displacements than at high displacement. The first three data points were plotted vs the square of imposed displacement *D* and were found to fall on a straight line (Figure 160).

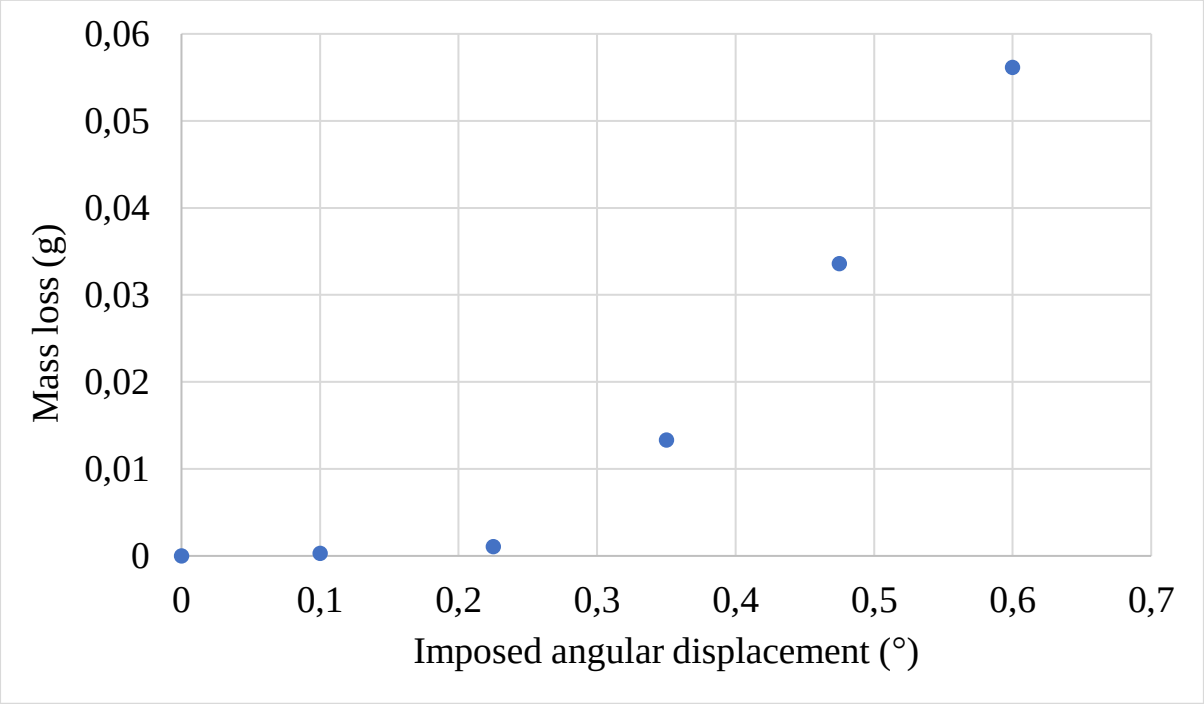

Figure 159: Dependence of mass loss on imposed displacement.

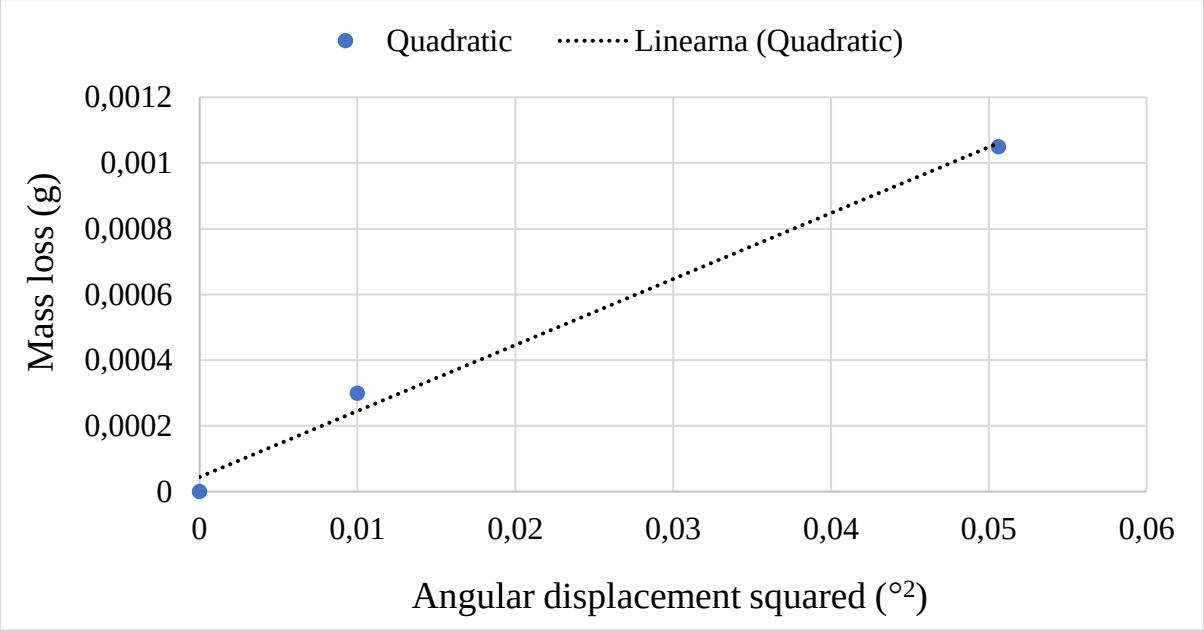

Figure 160: Mass lost for the first three experiments as a function of displacement squared.

A similar progression was reported by Fouvry et al. (21), which the authors identified as being the result of a partial-to-full slip transition, with the non-linear relationship between imposed displacement and wear appearing in partial slip and linear relationship in the full slip regime. Lack of care in determining the exact nature of the slip regime could explain at least some cases, where quadratic (rather than linear) dependence of wear on imposed displacement was observed. The pseudo-quadratic dependence of wear in partial slip on imposed displacement could be (perhaps somewhat speculatively) explained through a change in imposed displacement causing a proportional change both in the size of the slip region and in the amount of wear in the slip region. The effects of increasing imposed displacement are thus multiplied with themselves, until full slip is reached and the wear zone can no longer expand, leaving the proportional increase in wear with imposed *D* as the only remaining effect. To confirm that partial slip has occurred in this experiment, the fretting loops were examined (Figure 161). As it can be seen, the lowest values of imposed *D* correspond to fretting loops that are consistent with nearly stuck condition. Increasing *D* beyond approx. 0.4° caused a full-slip condition to occur.

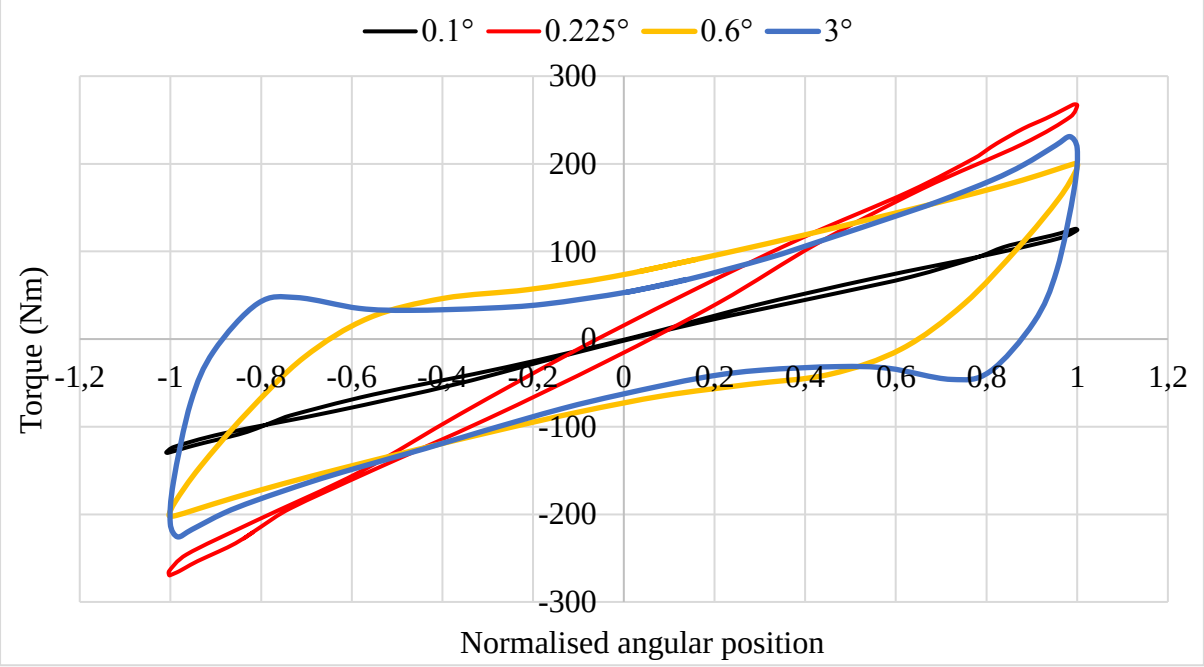

Figure 161: Typical steady-state fretting loops for experiments with constant *L* and different values of imposed *D*.

8.2.2 Experimental work (constant *D*, varying *L*)

To study the effects of *L* on wear, three series of experiments were performed. A pairing of a castellated and a full ring was used. The number of segments was 3, 6, 12 or 24 (see Figure 46 in section 3.2.9). Since the ring diameter was the same, this gives a wide range of contact sizes.

In each series, 4 experimental runs were made, one with 3, 6, 12 and 24 segments respectively. Imposed angular displacement was 0.6° (corresponding to $D \approx 430\mu m$) in all cases, with imposed frequency being 4 Hz and the number of cycles 10000.

In the first series, the normal force applied to the sample was kept constant at 5200N: as the number of contact patches was increased from 3 to 24, the total contact area remained the same, giving constant contact pressure, but decreasing normal force *per contact*.

In the second series, the normal force was increased with the number of contacts, to maintain a constant normal force of 833 N, so the only variable remaining should be L. However, this was strictly not the case. Examination of the video footage of the experiment using the sample with 24 contacts showed the sample flexing under torsional load, meaning that a large part of the imposed displacement was absorbed by elastic deformation of the sample, instead of through relative sliding. The sample design was such that the sample stiffness decreased with decreasing L, causing the *effective* amplitude to drop, even if the imposed amplitude remained the same. Fretting loops were examined to observe the extent of this effect (Figure 162).

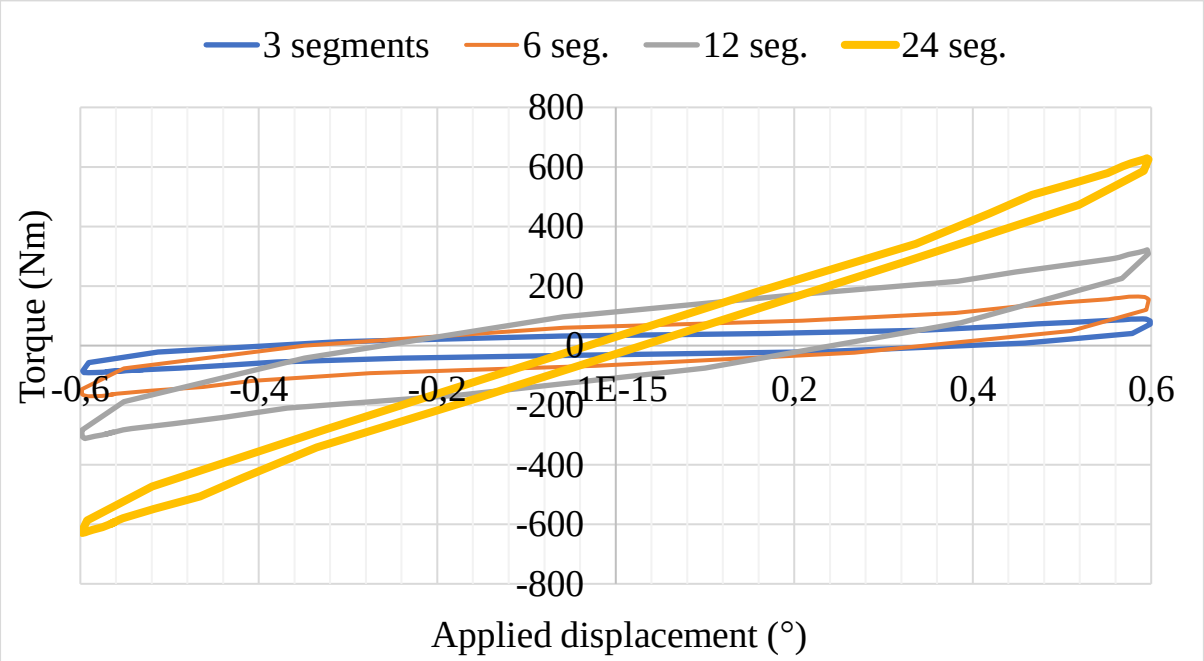

Figure 162: Fretting loops for the 6550th cycle in the second experimental series.

As it may be observed, the loops change with increasing number of contacts per sample, showing a decrease in stiffness. The sample with 24 contacts operates in almost fully stuck condition, with very little relative movement between the surfaces. The effective displacement was calculated using the approach described in (158) for further use in wear model development.

The third series had the same experimental parameters as the second series, but the sample was of a different design to increase its torsional stiffness. In the third series a different sample design was used, that had lower segments (2 instead of 5 mm, see Figure 47) with segment sides cut in a stepped profile. Debris entrapment rings were used in an attempt to force debris ejection solely in the direction of sliding.

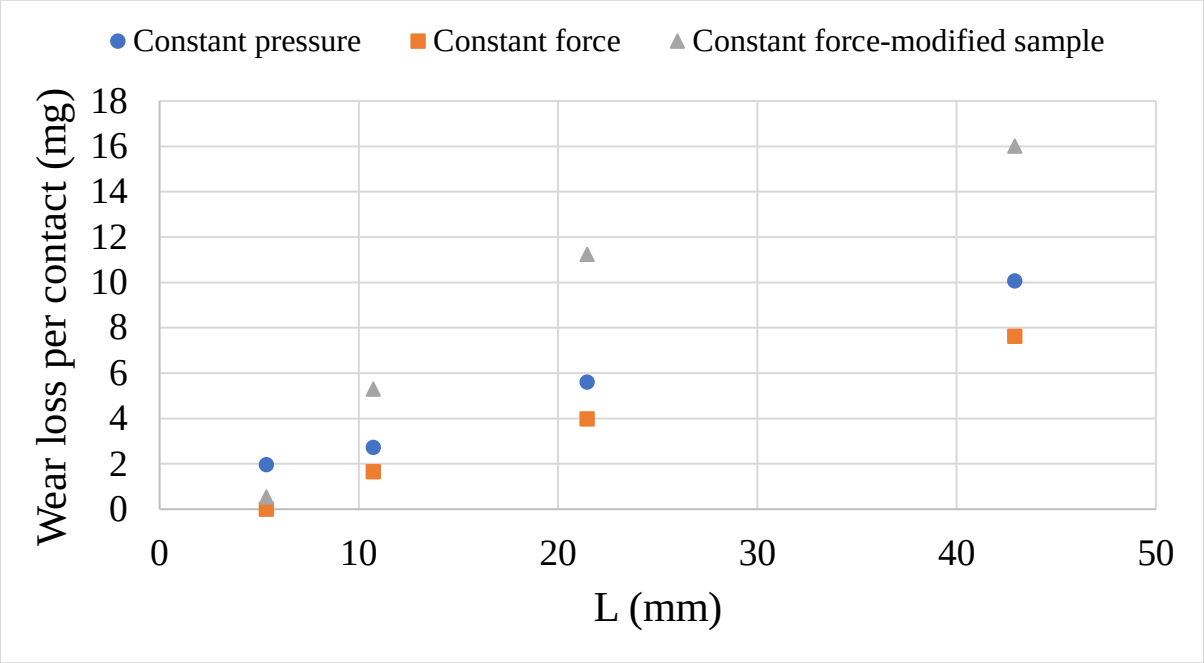

Figure 163: Wear mass loss measured in all three experimental series.

Figure 163 shows the measured wear mass loss in all three experimental series as a function of *L*. The first and second experimental series follow each other closely, but the third, using the modified sample has a different trajectory and generally exhibits more wear. In total, the third experimental series was not a significant improvement over the second one. The increase in sample stiffness was smaller than expected, however, the use of entrapment rings did enable an important observation to be made. The entrapment rings were used in the attempt to prevent any ejection of wear debris in the radial direction. It was therefore expected, that the debris will accumulate in the relief cuts between the wear surfaces. This was not the case (Figure 164). Instead, a significant quantity of wear debris was pushed up between the sample wall and the entrapment rings (Figure 164-Figure 166)

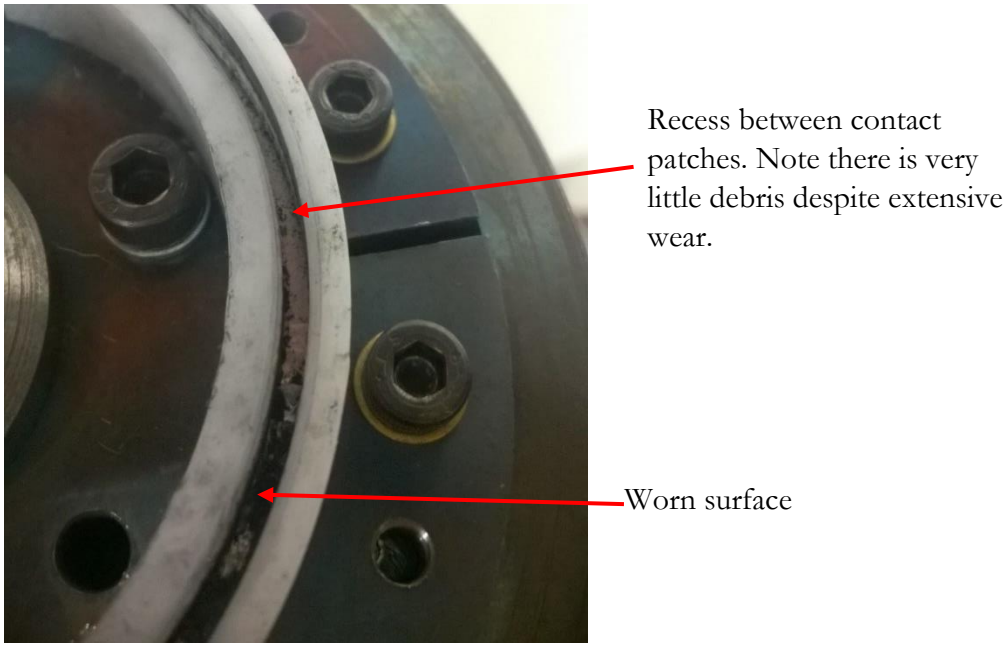

Figure 164: The wear sample with the entrapment rings. Notice the lack of wear debris in the recess between the contact patches.

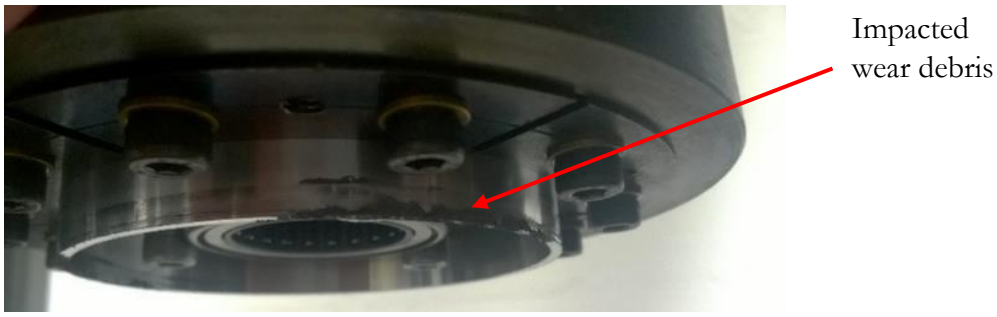

Figure 165: The top sample element showing the accumulation of wear debris above the contact patch

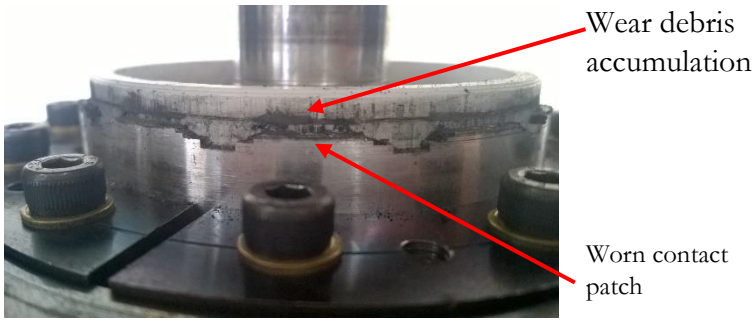

Figure 166: Bottom sample element; note the accumulation of wear debris on the entrapment ring above each contact.

In other words, the wear debris was ejected primarily along the shortest path available (in this case radially) and *not* the one which was kinematically favourable (in this case, tangentially). No such observation is known from the literature studied. Indeed, at a glance, this may appear to be in contradiction with the literature; Leheup & Pendelbury (115) established that the debris can be driven in the radial direction with an interstitial air flow, Aleksejev et al. (1) that the ejection can be independent of the length of the ejection path and Zhu, Shipway & Sun (31) based their wear

model on the assumption that ejection occurs in the direction of sliding. However, these are not contradictions; (115; 1) studied full annular contacts where radial ejection was the only possibility, while in experiments of (31) width of the contact l was approximately two orders of magnitude larger than length in the direction of sliding L, meaning that the ejection in the direction of sliding was the shortest route for the debris to be ejected.

Based on these observations it can be concluded that the open contact wear model must account for debris ejection in all directions, unless the wear geometry strongly prefers ejection in a particular direction.

8.3 Derivation of wear model for open contacts – Ejection in multiple directions

In this section, a derivation of a wear model taking account of debris ejection both in and across the direction of sliding is attempted. As before, a rectangular contact area is assumed, measuring L in the direction of sliding and l perpendicular to the direction of sliding (see Figure 155). The work of Archard and FI&B is invoked as a starting point. According to Archard, the volume of material removed is proportional to the total distance slid and normal force F_N, as well as inversely proportional to the material hardness Υ. Multiplying with the debris density ϱ_d gives the mass removed. In one wear cycle, the total slid distance equals four times the imposed displacement. The wear volume according to Archard ($V_{Archard}$) and wear mass according to Archard ($M_{Archard}$) are thus:

$$V_{Archard} = \frac{k_V F_N 4D}{\Upsilon} \qquad 51$$

$$M_{Archard} = V_{Archard}\varrho_d = \frac{k_V F_N 4D \varrho_d}{\Upsilon} \qquad 52$$

According to FI&B, the quantity of material detached from the wearing bodies decreases linearly from maximum with growing debris bed thickness H. Restating eqn. 37 in terms of total masses rather than mass flow rates, the mass of particles detached in one wear cycle (M_d) can thus be written as:

$$M_d(H) = K_d\left(H_{max} - H(n)\right) \qquad 53$$

K_d in this case being the constant of proportionality and n being the number of the cycle in question. If $H(n)=0$ (which is typical for example for the first wear cycle or if the debris is aggressively removed by some mechanism), the maximum possible mass is removed; the maximum being equal to $M_{Archard}$:

$$K_d H_{max}=M_{Archard}=\frac{k_V F_N 4D\varrho_d}{\Upsilon} \qquad 54$$

Using eqn. 54 the final form of the equation for M_d can be obtained:

$$M_d(H)=\frac{k_V F_N 4D\varrho_d}{\Upsilon H_{max}}\left(H_{max}-H(n)\right) \qquad 55$$

The mass ejected from the contact in one wear cycle can be treated similarly, but taking into account the ejection of the wear debris both in the direction of sliding and perpendicularly to it. When the contact slips for D during the cycle an area lD of wear debris bed is uncovered, representing a mass of $lDH\varrho_d$ of debris. Some of this material may not be ejected from the contact (for example on account of being attached to the moving surface or on account of being reingested), but suppose a fraction β of the uncovered material is permanently ejected. In each cycle $4\beta lDH\varrho_d$ of debris is ejected at the leading and trailing edge of the contact. At the same time, debris is being ejected at the sides of the contact, which have a total length of $2L$. Let us assume that the debris is driven out of the contact by the relative motion of the slipping surfaces, such that the side ejection in a cycle, per unit length of the contact edge, is proportional to $4D$ (α being the constant of proportionality). Suppose that the side ejection increases linearly with the depth of the debris bed, H, giving a total mass ejected (M_e) per cycle:

$$M_e=4\beta lDH\varrho_d+4D\alpha\cdot 2LH\varrho_d \qquad 56$$

The change in debris bed mass can be written as:

$$\varrho_d Ll\frac{dH}{dn}=M_d-M_e=\frac{k_V F_N 4D\varrho_d}{\Upsilon H_{max}}\left(H_{max}-H(n)\right)-4\beta lDH(n)\varrho_d-4D\alpha\cdot 2LH(n)\varrho_d \qquad 57$$

Setting $h=H/H_{max}$ the differential equation 57 can be simplified:

$$\frac{dh}{dn}=\Omega-(\Omega+\Psi)h \qquad 58$$

Where:

$$\Omega=\frac{k_V F_N 4D}{\Upsilon H_{max} l L} \quad (59)$$

$$\Psi=\frac{4D}{L}\left(\beta+2\alpha\frac{L}{l}\right) \quad (60)$$

With the boundary condition $H(0)=0$, the differential equation 58 can be solved. The solution includes critical number of cycles n_c which divides the wear into the initial stage dominated by debris generation and steady-state stage controlled by debris entrapment:

$$h(n)=n_c\Omega\left(1-e^{-\frac{n}{n_c}}\right) \quad (61)$$

$$n_c=(\Omega+\Psi)^{-1} \quad (62)$$

The total mass of material removed in N fretting cycles can be established through integration (remembering the definitions of Ω and $h=H/H_{max}$):

$$M_{total}=\int_0^N M_d dn=\int_0^N \frac{k_V F_N 4D\varrho_d}{\Upsilon H_{max}}(H_{max}-h(n)H_{max})dn=\int_0^N \frac{k_V F_N 4D\varrho_d}{\Upsilon}\left(1-h(n)\right)dn \quad (63)$$

$$M_{total}=\int_0^N \Omega H_{max} l L \varrho_d\left(1-h(n)\right)=H_{max} l L\Omega\varrho_d\left(N-n_c\Omega\left(N-n_c\left(1-e^{-\frac{N}{n_c}}\right)\right)\right) \quad (64)$$

Data collected in experiments from sections 8.2.1 and 8.2.2. can now be reinterpreted using the new model. For the material in question, the hardness is Υ=101 HV (Table 3 in section 4.2). If yield strength of the material rather than hardness is the property affecting the wear resistance (as it is suggested by some of the authors discussed in section 2.3.1) this does not affect the derivation significantly, since both properties have the same unit.

Parameters k_V, α and β were varied until a satisfactory fit was established (the chosen values being k_V=0.0006, $\alpha=8\cdot10^{-5}$ and β=0.01). The maximum debris bed thickness was assumed to be H_{max}=0.1 mm. The comparison between the model and the measured results for sample with 16 contacts (L kept constant, D varying, original results shown in Figure 158) is shown in Figure 167. The effective angular displacements were calculated using the method published by (158) with effective linear displacements calculated from them and fed into the model.

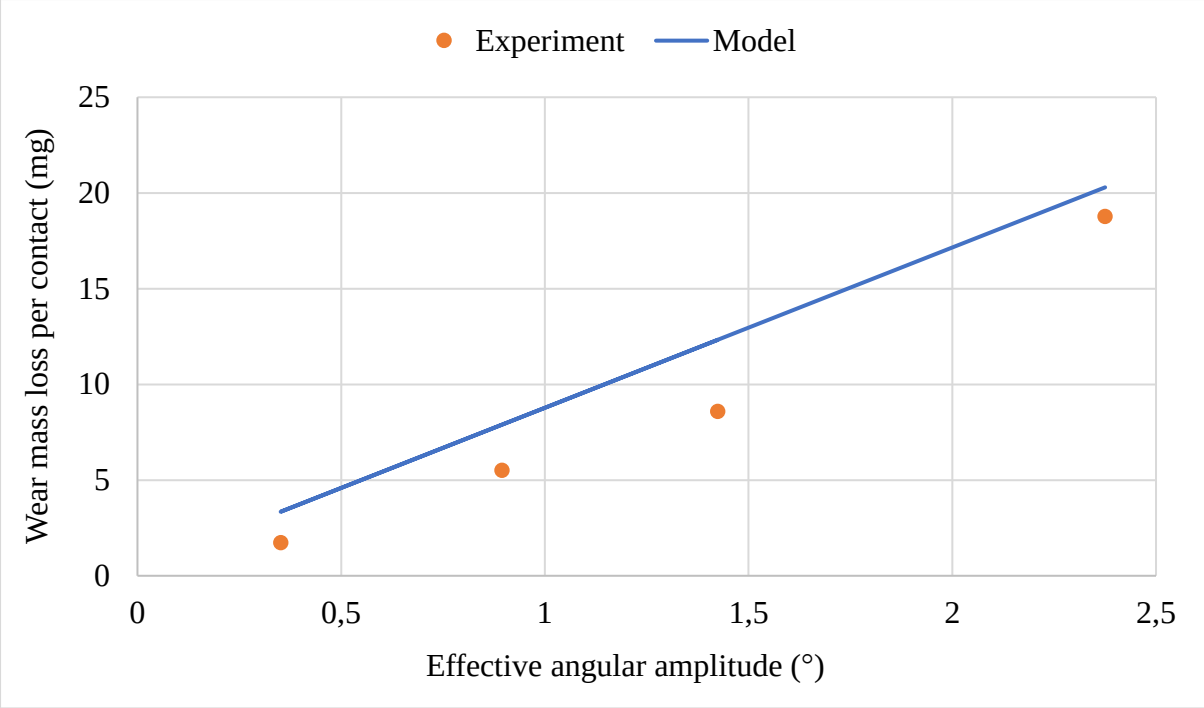

Figure 167: Measured and predicted mass losses at constant *L* and different values of *D*.

The comparison between the model and the data obtained at constant nominal contact pressure (first shown in Figure 163) is shown in Figure 168. The comparison between the model and the data obtained at constant force (again, the model is fed effective displacement) is shown in Figure 169.

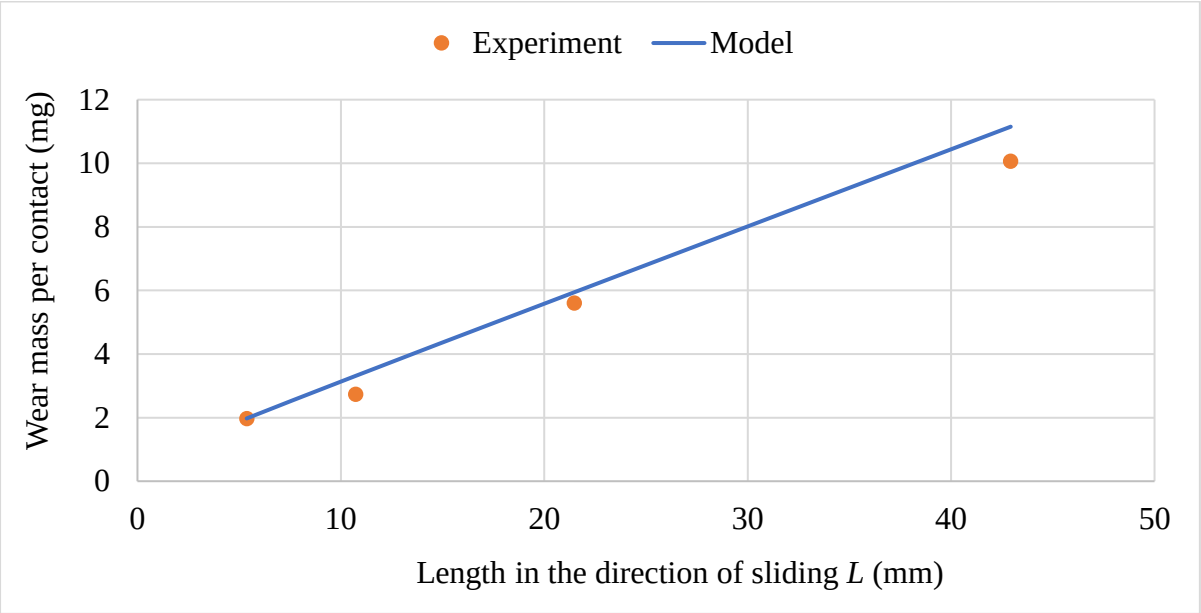

Figure 168: Improved model and experimental data (constant nominal contact pressure)

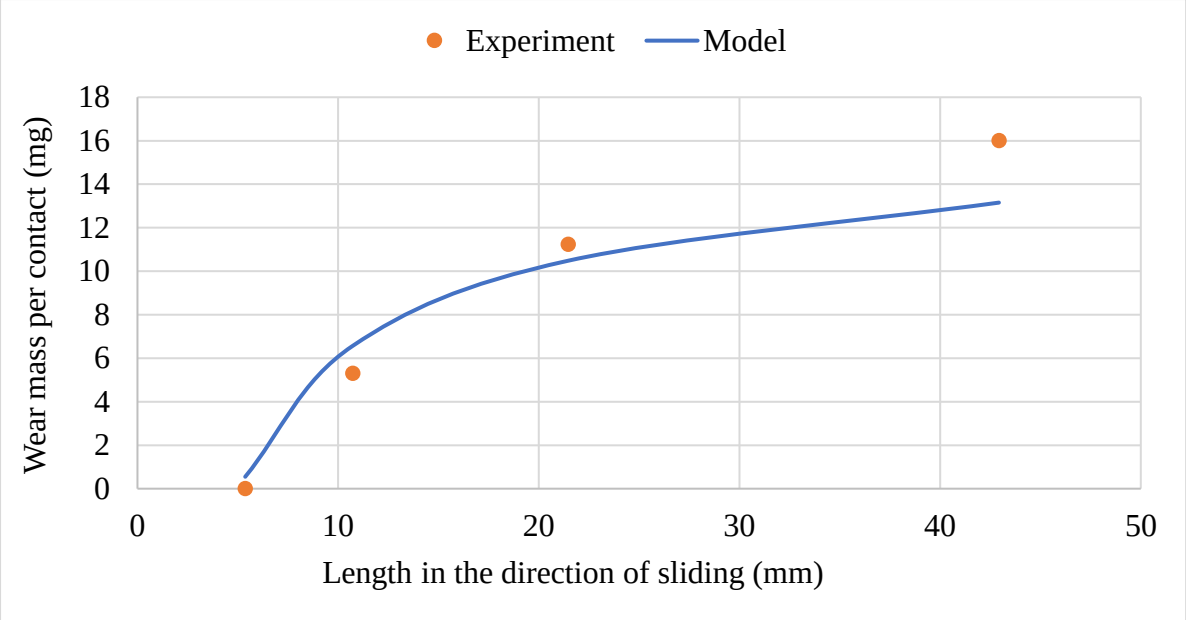

Figure 169: Model and experimental data at constant force per contact

The model presented can reliably predict (using only one set of parameters) wear across a range of displacements (effective displacements from 18 to 1700 μm), three separate sets of wear conditions and five different open flat-on-flat geometries. It also appears to be one of the relatively few that considers the bi-axial nature of the debris ejection (especially given that the models taking debris ejection into account at all are rare).

8.4 Debris bed properties – preliminary numerical modelling

As demonstrated by modelling work of Fillot, Iordanoff & Berthier on effects of debris particle adhesion on wear (133) debris properties may have significant effect on progress of wear. Likewise, eqn. 45 links the quantity of debris being ejected to the velocity profile in the debris bed, which is likely to depend on the interactions between the debris particles. The parameters α and β introduced in eqn. 56 also appear to be at least somewhat connected to debris properties. In turn, the behaviour of the debris could conceivably depend on pressure the contact is submitted to, the size of debris particles produced, material properties of the particles (metal oxides typically have stiffness and hardness different than the metal itself) and parameters of particle-particle interaction (particle surface roughness, particle-particle friction coefficient, particle cohesion etc.) These properties and parameters in turn may depend on temperature, with the temperature of the debris bed depending not only on the bulk temperature of the wearing bodies, but also on heat generation in wear and the rate of its dissipation, creating an extremely complex series of interactions, which are at present very poorly understood. In the light of this, it is all the more interesting, how little attention has been paid to studies of debris properties. It is

quite rare to see a wear study describing the distribution of debris particle sizes and the chemical composition of the debris. Studies concerning the development of debris properties with wear or properties such as compressibility of debris (which could be established by compressing a sample of ejected debris) or friction between particles (which is linked to the angle of repose, which could be measured straighforwadly, if a sufficient quantity of ejected debris was available) are rarer still. For a comprehensive and advanced study of wear debris see (141; 57).

As explained in the literature survey (section 2.2.7) there is a body of experimental work concerning the effects of bulk temperature on wear which agrees that higher temperatures (to a point) promote particle cohesion through sintering, reducing debris ejection and therefore wear. However, no studies which would investigate the effects of temperature on wear debris in isolation from the first bodies were found. In the literature survey (section 2.3.3.3) several studies where numerical modelling to study the behaviour of compacted debris beds and disintegration of material into debris were discussed. These were, for the most part, done on a conceptual level, but did nevertheless give insight (or at least presented a possible path to gaining insight) into debris behaviour. In principle, realistic behaviour of debris could be obtained by simulating a series of physical tests involving debris using DEM and iteratively adjusting the model parameters until the simulation results correspond with the outcome of the physical model. A very similar approach was pursued by (137).

An attempt was made to expand this approach and simulate shearing of the debris bed using the discrete element (DEM) approach. The intention was to study the relationship between the relative sliding velocity of the surfaces and the average particle velocity in the same direction (defined in eqn. 45 as P) as a function of particle shape, contact pressure and particle interaction parameters. A commercially available DEM software packaged called EDEM was used. True simulation of wear was not attempted, since this software lacked the capacity to apply appropriate boundary conditions needed for wear simulation.

Two particle shapes were simulated: a sphere (Figure 170) with a radius of 0.05 mm and a more realistic flake (Figure 171; see Figure 68 for images of real debris particles), comprising of three bonded spheres (with radius of 0.025 mm each) placed at the points of an equilateral triangle with a side of 0.0308 mm. The flake particle was treated as a complete and indestructible body, since the code used could not accommodate particles containing breakable bonds.

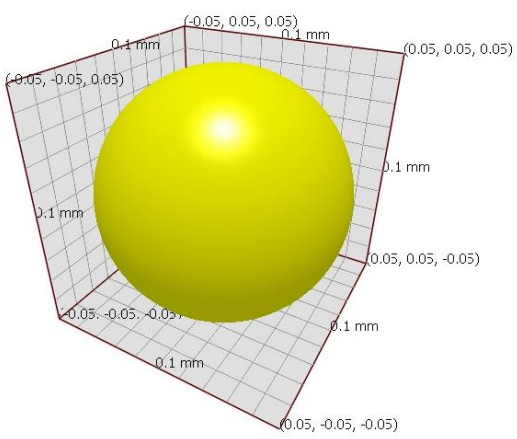

Figure 170: The spherical particle used in EDEM simulations

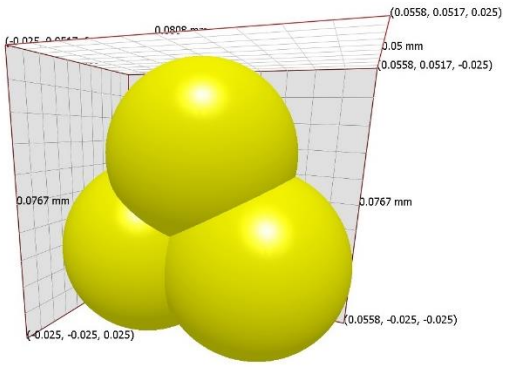

Figure 171: The flake particle used in EDEM simulations

Material properties of the particles are given in Table 12. The properties chosen were those for aluminium metal, with coefficients of restitution, static and rolling friction being set to arbitrary, but broadly realistic values.

Property	**Value**
Elastic modulus	$70 \cdot 10^9$ Pa
Poisson ratio	0.32
Coefficient of restitution	0.9
Density	2700 kgm^{-3}
Coefficient of static friction	1.1
Coefficient of rolling friction	0.05

Table 12: Material properties of particles used in EDEM simulations

All simulations were carried out using a compression/shear cell (Figure 172) measuring 4 by 2 mm in size. Gravitational acceleration of 9.81 ms^{-2} was applied in -Z direction. Periodic boundary conditions were applied on walls perpendicular to the X and Y directions, essentially simulating an endless particle bed.

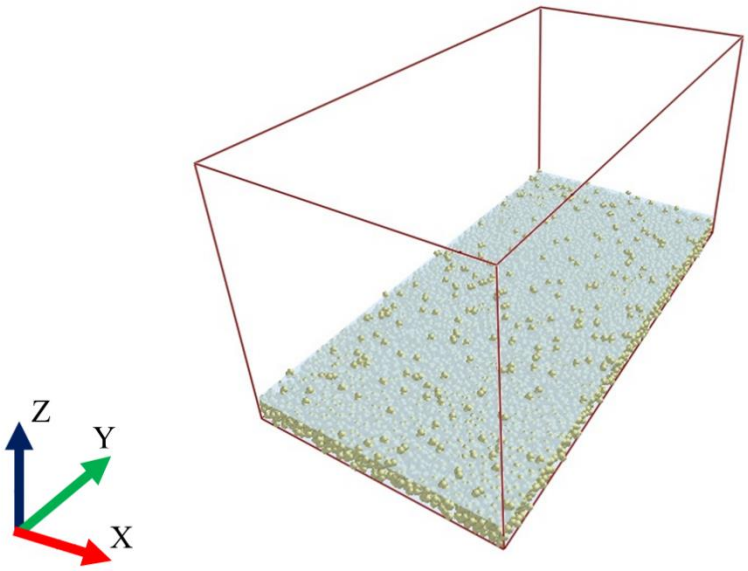

Figure 172: Compression/shear cell with flake particles

The simulation procedure was in two parts. In the first part, the box cell is generated and particles seeded throughout its volume and allowed to settle to the bottom. Periodic boundary conditions are then applied to the appropriate walls and a compression/shear plate added on top. The plate is moved downwards (-Z direction) and a conveyor kinematic is imposed in the Y direction, compressing and shearing the bed. The purpose of this is to determine the relationship between the pressure on the plate and its vertical position, since EDEM does not allow pressure boundary conditions to be imposed. This has proved to be a serious deficiency of the software, since the response of the bed was extremely sensitive making it impossible in practice to achieve values close to the desired target pressure.

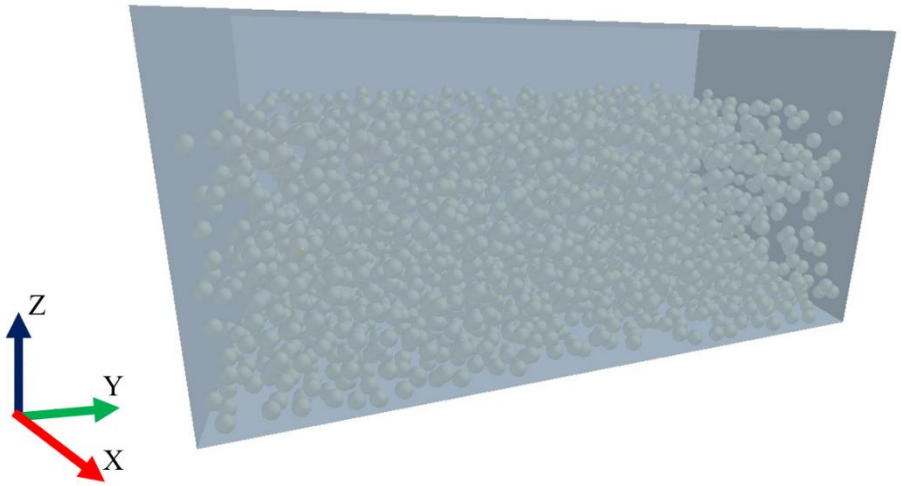

Figure 173: Spherical particles settling

The second part begins with a settled particle bed (the same in all simulations using the same particle shape). The compression/shear plate is rapidly moved down to the position corresponding to the desired pressure level for the simulation at hand. Conveyor translation at a desired speed was then applied to shear the particle bed.

This enables the observation of two principal quantities:

- ❖ cell pressure at the end of the simulation;
- ❖ the dependence of *P* on pressure, particle shape and particle interaction parameters.

8.4.1 Results - Spherical particles

A number of simulations were made studying the effect of different sliding velocities (range of 1-15 m/s) and contact pressures. The particle shape shown in Figure 171 was used, with 2500 particles in the bed. Results are shown in Figure 174; *P* is calculated as the ratio of the average particle velocity in the Y direction in the last step of the simulation and the relative sliding velocity being simulated. Some anomalies can be observed, including one instance of negative *P* (particles move against the direction of shearing) and two instances of *P* over one (particles on average moving faster than relative sliding velocity). This could be because the average velocity is extracted in one moment of the simulation, rather than averaged over a number of simulation steps. The majority of simulated values of *P* oscillate around the value of 0.3.

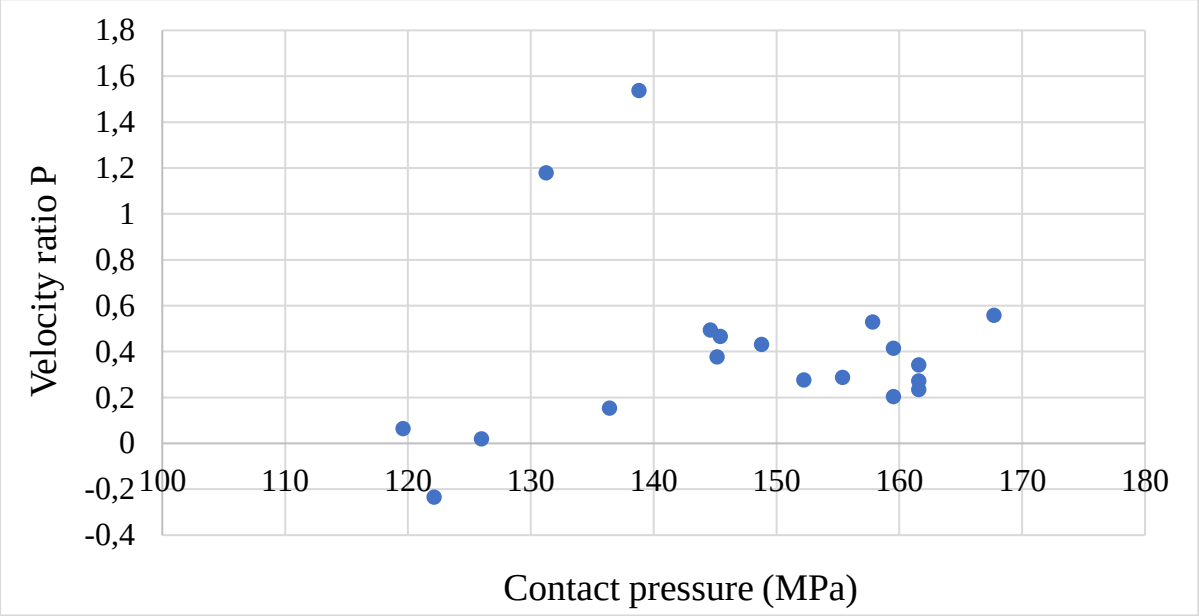

Figure 174: Velocity ratio *P* as a function of pressure for spherical particles.

The effects of static and rolling friction were also studied. Properties and parameters from Table 12 were still used, but the coefficients of static or rolling friction were varied. The relative sliding velocity of 10 m/s was used. The limitations of the software limited control over the pressure simulated, causing a very wide range of pressures occurring when simulating the effects of different friction coefficients, despite the friction coefficient being the only variable changed. Results showing *P* and the simulated shear cell pressure as a function of particle-particle static friction coefficient are shown in Figure 175 and Figure 178.

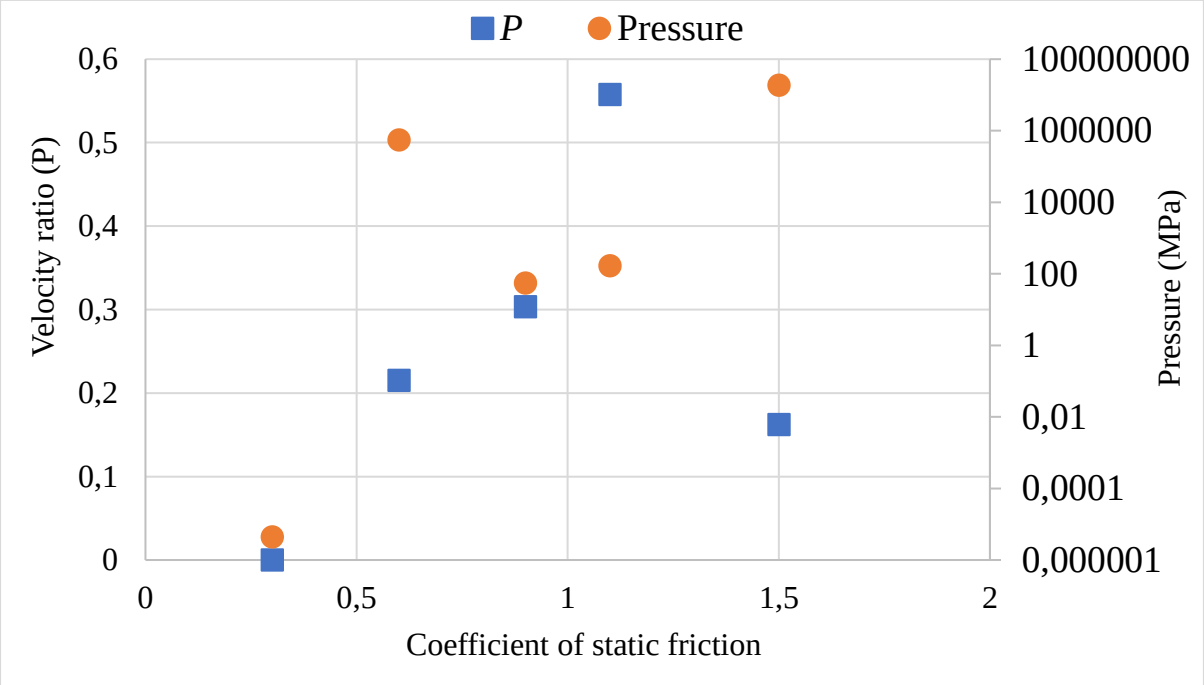

Figure 175: *P* and cell pressure as a function of coefficient of static friction.

With the particle-particle friction coefficient of 0.3, almost no pressure can be built in the cell, resulting in very little momentum transfer from the shear/compression plate to the particles. No such problems were encountered at higher values and there appears to be no obvious connection between the value of *P* and the cell pressure over a very large range of values for the latter.

The results of simulations studying the effect of particle-particle rolling friction are presented in Figure 176. As it may be observed, the pressure achieved is not significantly dependent on the coefficient of rolling friction, with *P* being between 0.35 to 0.55 in all cases.

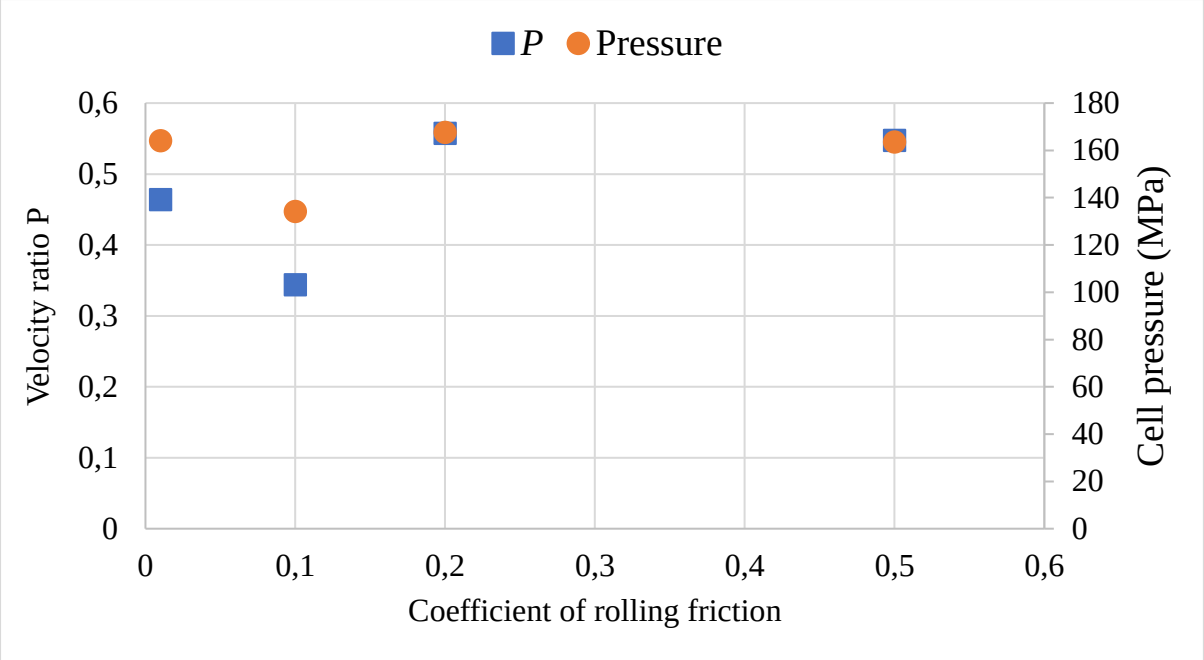

Figure 176: *P* and simulated cell pressure as a function of rolling friction coefficient.

8.4.2 Results – Flake particles

A number of simulations were made studying the effect of different sliding velocities (range of 1-15 m/s) and contact pressures. The particle shape shown in Figure 171 was used, with 5000 particles in the bed. The number was higher than the number of spheres in simulations discussed in section 8.4.2 in order to insure roughly equivalent debris bed thickness (due to different shape, flake particles form thinner beds). Results are shown in Figure 177; *P* is calculated as the ratio of the average particle velocity in the Y direction at the end of the simulation and the relative sliding velocity being simulated. As it might be observed, the majority of values lie around 0.4. It would also appear that *P* is only weakly dependent on pressure above nominal contact pressure of about 1500 kPa.

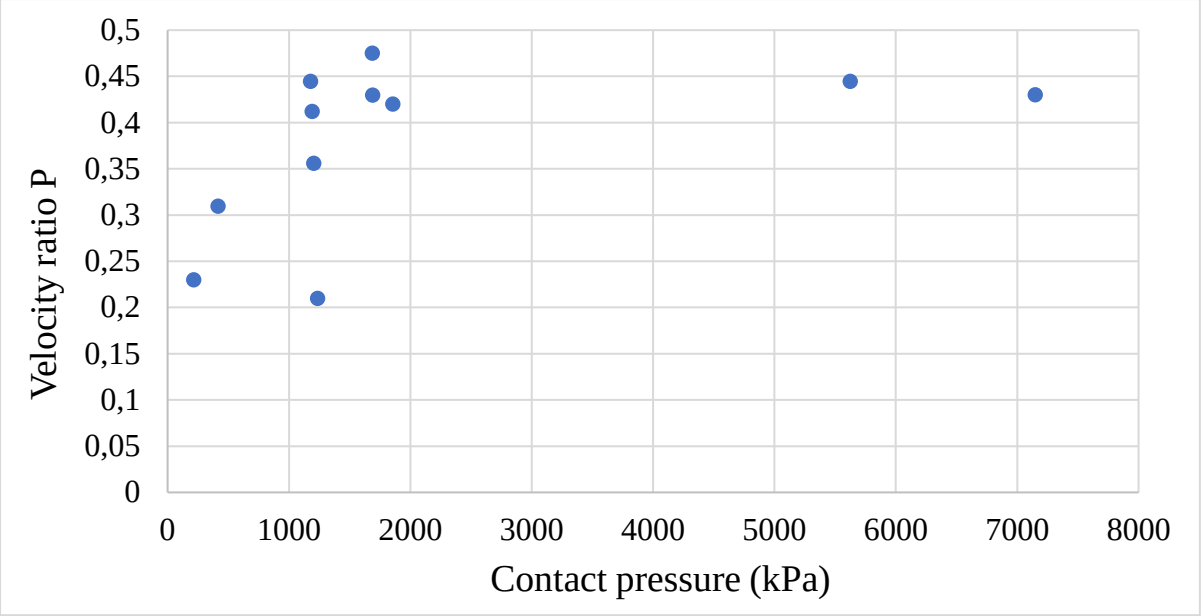

Figure 177: Ratio of relative sliding velocity and average particle velocity in the Y direction.

Further simulations were made to study the effects of static and rolling friction. Properties and parameters from Table 12 were still used, but the coefficient of static or rolling friction were varied. The relative sliding velocity of 10 m/s was used. Results showing *P* as a function of particle-particle static friction coefficient are shown in Figure 178. As before, the values oscillate around 0.4, except for one, when the coefficient was set to 0.3.

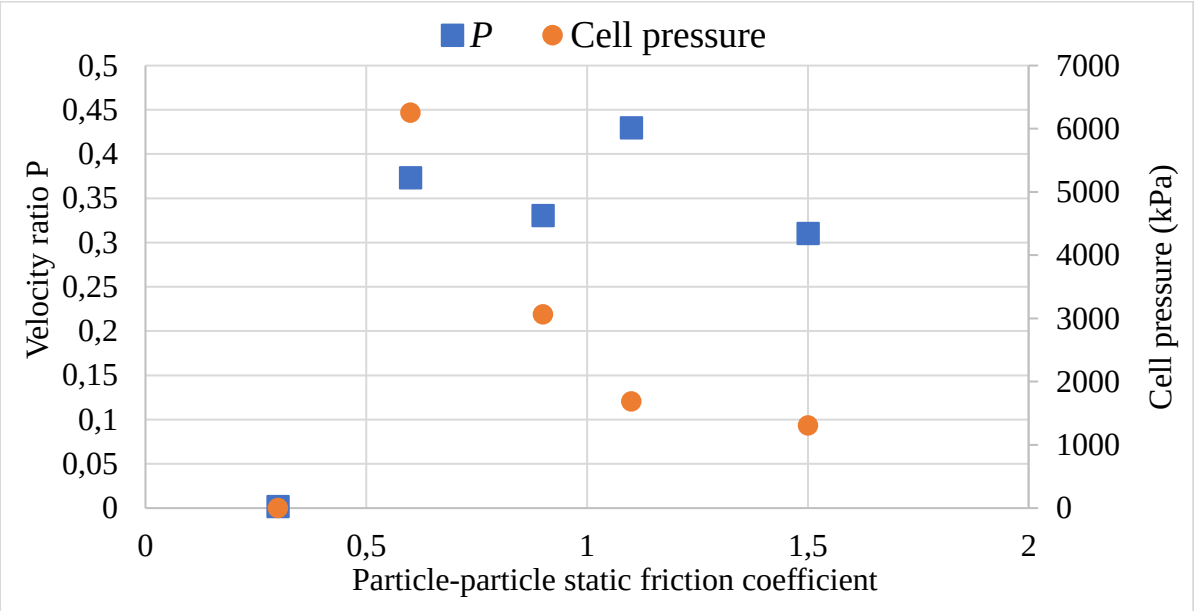

Figure 178: *P* as a function of static friction coefficient for flake particles

This can be explained by the near absence of a pressure build-up in the shear cell, when the friction coefficient is set to 0.3. With no pressure on the particles, there can be only little transfer of momentum from the compression/shear plate to them, explaining the very low value of *P*. Whether the lack of a pressure build-up is the result of some simulation error or is a genuine result of low particle-particle friction is not clear at this point.

Results of the simulations using different coefficients of particle-particle rolling friction are shown in Figure 179.

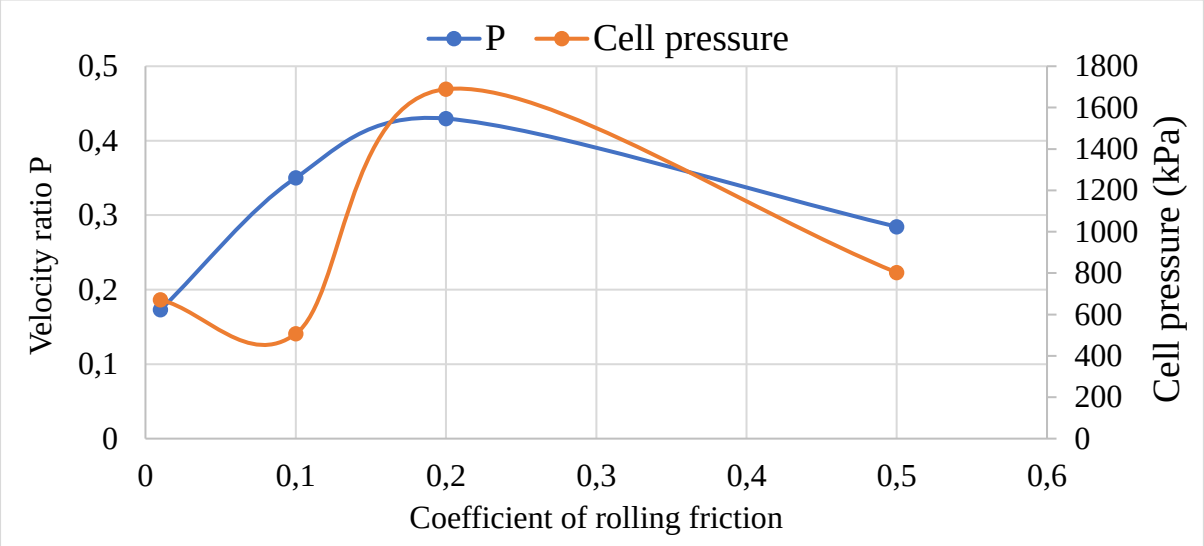

Figure 179: *P* and achieved cell pressure as a function of coefficient of rolling friction

8.4.3 Preliminary DEM modelling - Conclusions

While the number of simulations was quite small and the control over the simulation parameters was less precise and direct than would be ideal, some patterns nevertheless emerge:

The large variation in cell pressures generated in simulations with uniform spherical particles indicate that such particles form exceptionally stiff debris beds; the simple switch to 'flake' particles made the bed more 'pliable' indicating that realistic debris particle shapes and size distributions would lead to beds with relatively low stiffness.

In most cases, regardless of the particle shape, using 0.4 as a value of *P* is a reasonable approximation. Most exceptions found through the simulations occur when the simulated cell pressure is below 1000 kPa, when the values of *P* are much lower. This is a pressure which is generally considered 'low' by standards of laboratory wear experiments, where contact pressures of 10-100 MPa range are common. If this is a general pattern of wear, keeping the contact pressure below 1000 kPa could be an effective wear-retarding tactic, however no significant evidence for or against such a hypothesis has been found at present.

Generally, the behaviour of the bed appears to be more sensitive to the static particle-particle friction coefficient than the rolling friction coefficient. This can be explained by considering that the static friction coefficient represents the limit to the magnitude of force that can be transmitted from one particle to another, whereas the rolling friction coefficient only describes the extent of energy dissipation in rolling over each other, having no direct connection to the amount of momentum being transferred in this process. This indicates that additional studies on what material (chemical composition, hardness, stiffness) and geometrical (surface roughness, particle shape, size) parameters of the wear debris influence the static friction coefficient could be very valuable.

8.5 Transition to open contacts – outcomes

Formulating a reliable wear law for any geometry and a wide range of contact conditions has been beyond the powers of tribological science and remains so: the law would need to explicitly account for effects of geometry, atmosphere, wear parameters, material, temperature and possibly some other factors. Despite a large number of publications (sections 2.2.8-2.3.1) these dependencies remain mostly unclear at this point, even if studied in isolation from one another.

Experiments using castellated samples demonstrated that a torsional wear rig can be used for studies of open contacts. However, the combination of the material studied, the sample design and the particular rig used has shown itself to lack torsional stiffness, which complicated the experimental work, requiring the actual displacements to be calculated from the wear data. To a degree, these could probably be rectified by more sophisticated sample design or a stiffer sample material, but such simple improvements would quickly hit both material and machining limits. Despite this, additional insights were generated. The observations of Fouvry et al. (21) were confirmed (although the geometry used was different) showing that dependence of wear on imposed displacement changes with the slip regime. More importantly, it was discovered, that the wear debris ejects along the shortest available path (section 8.2.2) even if the debris movement is not kinematically driven. This explains, at least in part, why the first attempt to apply the law of Fillot, Iordanoff and Berthier (117) did not work. An effective wear model should account ejection both in the direction of movement and perpendicular to it. In contacts with rectangular contact areas, formulating the debris ejection expression is relatively straight-forward. In other geometries, such as ball-on-flat where edges are not always parallel or perpendicular to the imposed movement, this would be more difficult and might require deliberate measurement of the debris ejection pattern.

A more advanced wear model was produced taking this into account. Using two additional debris ejection parameters to account for debris being ejected from all sides of the contact a satisfactory fit with the data from castellated samples was obtained. The model was based on the reasoning introduced by Fillot, Iordanoff & Berthier, but is not a direct derivation from their published work. Further testing of this approach could be fruitful, especially in combination with additional studies of the debris bed. As noted in section 5.5 and again in section 7.3 there exists at least some cases where the contact is mostly empty and no truly continuous debris layers exists. Treating the debris bed as some uniform, coherent body can therefore be overly simplistic in at least some cases. It is not clear how the voids in the debris bed affect the ejection or how to determine the density of the debris in the bed, where it might be less compacted than in a density measurement after ejection. It should be noted, that Fillot, Iordanoff & Berthier initially expressed their model in terms of *debris bed mass* and only restated it in terms of *debris bed thickness* (*H*) half-way through their 2005 publication (117). This in turn created a slightly misleading situation, which was carried through this work as well, due to its reliance on the terminology and assumptions in (117).

The advanced wear model obtained in this chapter assumes that ejection perpendicular to the motion increases in proportion to displacement, but it is presently unclear why it would be so or what the ratio of ejection along and across the imposed motion is or what controls it. A study of what governs the α and β parameters appears to be a relatively simple step in this direction. By using a sample shaped like a truncated pyramid, rubbing against a flat, the debris ejected in every direction would fall along separate paths and could be collected using appropriate containers, thus enabling ejection in specific directions to be measured.

9 Discussion and Conclusions

The issue of wear is complex with many questions still open despite decades of extensive efforts. As noted by Godet (14), tribology exists at an intersection of mechanical engineering and material science, but also fluid mechanics and chemistry, meaning that great advances require a combination of skills and perspectives which only rarely occurs.

The subject of study is one of immense complexity, with variables known to influence wear including dimensional (such as size of the contact or size of debris particles), material (hardness, yield strength), chemical (composition of the materials and atmosphere), thermal (bulk temperature) as well as loading variables (speed of sliding, normal force etc.) Their effects are often difficult to deconvolute or to study in isolation.

This work focused on the effects of dimensional and loading variables in an attempt to shed further light on their effect and, if possible, to develop a more general model ('law') enabling the prediction of dry, reciprocating/fretting wear.

9.1 Fundemantal limitations to effective wear predictions.

Modelling of wear aims to answer two questions: namely how much material has been removed and what the exact shape of the worn geometry is. Unfortunately, answering the second question is, in practice, extremely difficult, since that requires a local model of wear. While such models do exist, they usually only account for events like shearing of individual asperities (as in the original Archard's formulation (104)), effects of thermal expansion (51) on asperities etc. But as it was demonstrated both by the literature (sections 2.3.1, 2.3.2) and by the experimental work performed (section 4.2) macroscopic changes to contacts can induce changes to where and how is material removed. In other words, the contact appears to 'feel' macroscopic changes down to the local level.

It is useful to use an analogy with a pipeline: the flow conditions (flow velocity, velocity profile, pressure of the fluid, temperature etc.) may be studied at a particular point, but the quantities measured are affected by changes far away from the observation point (lengthening the line can cause the flow rate to decrease due to higher pressure drop, manipulation of valves upstream may induce turbulence, changes in temperature can cause changes in fluid viscosity and density etc.)

For this reason, this work pursued a purely macroscopic approach, aiming to improve/develop a method for predicting the total amount of wear, but not the localized loss of material.

9.2 Expanding the model

Through the survey of literature, a then relatively obscure wear model proposed by of Fillot, Iordanoff & Berthier (132; 117; 15; 133) was identified as fruitful for further research. The FI&B wear model takes into account both the creation and ejection of wear debris and links the two processes together. In this manner a relatively advanced model of wear is produced and can be developed still further by determining the factors affecting debris creation, transport within the contact and ejection. As such, it is a conceptually powerful model and its mathematical form lends itself to application to different geometries.

9.2.1 Observations in favour of FI&B model

The FI&B model is supported by a number of observations and analyses. Indirectly, the model is supported by its ability to accommodate a number of observed effects into its framework. It has been demonstrated that increasing debris entrapment decreases wear, see for example the work of Hintikka, Lehtovaara & Mäntylä (109), Zhu, Shipway & Sun (31) and Zhu & Shipway (212). It has also been demonstrated that changing the debris properties can change the wear rate, for example under the influence of temperature (see discussion in section 2.2.2). The FI&B model explains this through changes in debris ejection causing changes in the quantity of debris entrapped in the contact, thus changing the rate of particle detachment.

More directly, this model is supported by the fact that wear expressions very similar to it have been developed by independent experimental and analytical studies (37; 118). Also, the functional dependency of the amount of material removed from the wearing bodies on time as predicted by FI&B (see Figure 131) corresponds well with experimental observations published by (31; 212; 141; 56; 100; 213) as well as advanced tomography experiments presented in this work (section 7.3.1) and numerical study of Li et al. (136). In section 4.3.2.2 it was demonstrated that in the contact geometry (annular contact of an infinite radius) studied by Fillot, Iordanoff & Berthier wear should become independent of normal force, if the force is sufficiently large. Such behaviour was observed in real annular contacts (i.e. those with finite radii) as reported in (86; 109). It was confirmed in this work as well (section 4.3.2.1) and is not readily explainable within the limits of traditional wear models.

9.2.2 Testing the FI&B model

However, at the start of this work, the model of FI&B was not widely discussed in the tribological community, nor was it extensively studied. In this thesis, several facets of this model were investigated.

In section 4.2, the hypothesis of Fillot, Iordanoff & Berthier (117), that wear entrapment is affected by the length of the ejection path, was examined. The set of experiments carried out using two different metals indicates that the length does affect the ejection (1) but only if the worn surface roughness is large enough. If the roughness is low, the length of ejection path does not affect entrapment (eqn. 28). This outcome shows the importance of worn surface roughness as a self-generating lengthscale affecting wear. This further complicates any prospective wear law, since the mechanisms governing the worn surface roughness need to be established in order to enable correct prediction of debris entrapment.

In section 4.3, the factors governing the maximum debris bed thickness were investigated. The results of experiments indicate that with the wear debris bed fully developed, release of the particles into the debris bed requires a certain (high) value of coefficient of friction in the contact. It was experimentally demonstrated that in contacts where debris ejection is artificially restricted, the average coefficient of friction for the contact is below the theoretically calculated threshold needed for particles to be released into the bed. This indicates that sufficiently thick debris beds can lower the coefficient of friction to levels which are insufficient to support release of the wear particles into the bed. The bed, having no outflow of particles (due to restricted ejection) and no inflow (due to lack of detachment), thus stabilizes at a certain maximum thickness. However, the exact dependence of coefficient of friction for the contact on the accumulation of debris is generally not known, meaning that predicting the magnitude of H_{max} without experimental measurements is not straightforward with the current level of understanding. As a very rough approximation, values of 0.05-0.1 mm appear to serve well, based on the data gathered (see chapter 4).

In chapter 8, an attempt was made to expand the FI&B model to an open geometry. Through experimentation it was determined that the debris is ejected preferentially along the shortest ejection path, even if debris transport is driven mechanically along other paths. Taking account of this observation, a new model was developed using the concept of the tribological circuit (section 8.3) and applied to a flat-on-flat rectangular contact. Good agreement was achieved over a wide range of effective displacements, normal forces and contact aspect ratios, demonstrating the resilience and power of this approach. While the model was not tested on other open geometries, there is no reason to suspect it would not be applicable. The relatively low stiffness of the experimental rig used was taken into account, implying that the model should apply to data from rigs of different stiffnesses and behaviours consistent with FI&B-type model was already observed in other geometries (31; 212; 141; 56; 100). Use of more traditional open-

geometry experimental rigs could also be beneficial due to their smaller samples and higher stiffness (in comparison to the rotary rig used here) being conducive to higher resolution of weight loss measurements and greater repeatability. However, formulation of debris ejection equation could also be challenging in contacts where edges are not parallel or perpendicular to the motion (such as in ball-on-flat or crossed-cylinders wear geometries). In some cases, evolution of contact width and contact length with wear would also need to be accounted for.

9.3 Use of X-rays for observing wear

An interesting, but highly important side achievement of the work was the application of computed X-ray tomography to the observations of wear (chapter 0, published in (2), chapter 7). This appears to be the first such attempt and has enabled an optically opaque contact to be investigated without disturbing it. While a complete in-situ experiment where the progress of wear would be observed through X-ray was not possible due to external factors, a detailed replacement experiment at a synchrotron facility (chapter 7) did demonstrate that it is possible to apply X-ray CT and X-ray diffraction to a worn contact simultaneously. Since the machine needed to wear the sample used is within the load-bearing and radiological constraints of the same beamline, it seems certain that the progress of wear could be observed directly by means of X-ray CT.

This is of significance for a number of reasons. In an engineering/industrial sense, it opens the possibility of monitoring worn contacts without dismantling them, possibly leading to shorter inspection times. In an academic/research sense, this is a tool enabling the progress and development of wear between most material pairs to be visualized accurately. Models predicting the development of the wear scar can be directly tested and new insights into the mechanism(s) of wear made. This was demonstrated in sections 7.3.1 and 7.3.3, where the FI&B model was successfully compared to the data collected through tomography.

In addition, many quantitative and qualitative observations concerning wear are very difficult to make relying exclusively on traditional tribological methods. For example, the real area of contact between worn opaque surfaces appears to be almost impossible to assess with any certainty, without resorting to X-ray methods. As discussed in section 5.4.4, mathematical models used rely on many assumptions and may not take into account the presence of the debris bed. X-ray tomography also revealed more information about the wear debris bed. The formulations used in the FI&B model, especially the concept of the debris bed thickness, imply that the bed is a continuous or a quazi-continous entity, separating the surface. Instead, observations revealed

wear debris mostly filling the depressions in a heavily-roughened and mostly empty contact zone. The exact implications of this for the model are not known at the moment.

Similarly, the porosity of the wear region appears difficult to establish through conventional methods. Real area of contact and porosity are of interest in studies of thermal/electrical conduction normally through the contact and flow/material transfer radially through the contact. Use of computer X-ray tomography enables the development of such features to be monitored with the progress of wear. As demonstrated in section 5.4.3 worn surface profiles can be also be obtained through this approach which is very significant, given their importance to debris ejection.

9.4 Wear mitigation strategies

While accurate modelling of wear might remain some time away, some methods for mitigating wear can nevertheless be identified.

As first identified by Hintikka, Lehtovaara & Mäntylä (86) wear in annular contacts (and possibly other closed contacts) becomes independent of normal force. This has been explained through the application of the law proposed by Fillot, Iordanoff & Berthier (117) (see section 4.3.2.2). In practical terms this means that increasing loads on annular contacts can result in disproportionally smaller or even no extra increase in wear. Conversely, decreasing the normal force might result in a smaller reduction in wear than expected.

Most existing wear models predict wear to increase (linearly or otherwise) with displacement. Reducing the effective displacement D experienced by the contact is thus an effective way for reducing the amount of material lost. This can be achieved for example be packing/fixing components more tightly, reducing the amplitude of vibrations experienced etc. It should also be born in mind that the effective displacement is not directly related to the imposed displacement. In some of the experiments conducted (see section 8.2) the imposed displacement was the same, but the effective changed significantly, since the stiffness of the wearing components decreased. Forcing the contact to operate in a fully or at least partially stuck condition can serve as an effective way to mitigate wear, since the motion of the components is accommodated through elastic deformation, rather than sliding. This can be accomplished by decreasing shear stiffness of the components and/or with suitably large *increases* in normal force; as stated by Vingsbo & Söderberg (19): '*…fretting wear and oxidation may be inhibited by increasing the normal force until mixed stick-slip conditions, or even stick conditions, once again are obtained.*' This seemingly counter-intuitive approach is further emphasized by the wear maps published by Heredia & Fouvry (157).

However, such approach is not without risk. High loads and small displacements increase the possibility of components failing through fatigue-induced cracking rather than wear: '*Fretting with small amplitude and high load usually leads to fretting fatigue, while large-amplitude and low-load fretting typically leads to wear.*' (72) Improper application could result in more wear, for example, if the normal force applied wasn't large enough to force the contact into sufficiently low effective displacement.

Some analysis indicates that materials with negative coefficient of thermal expansion can be highly resistant to wear (51). In such a material, rubbing asperities retract from each other, reducing local stresses, thus supressing wear. Additional research into using materials with very low coefficients of thermal expansion (such as invar alloy) or materials with negative coefficient of thermal expansion as anti-wear liners and/or coatings appear a relatively simple way to test a potentially fertile method for wear reduction.

There exists an agreement in the literature (see section 2.2.2) that *in steels worn in air* increasing the temperature of wearing bodies can significantly (factors of ≈10 are reported) decrease wear. Observations of this nature have been reported since at least as early as 1973 (214) and have been extensively confirmed since (106; 87; 92; 93; 30). For wearing steel components in air, maintaining their bulk temperature at above 200-250°C appears to be an exceptionally effective wear-suppression mechanism, albeit one which might be difficult to apply in practice. For some materials, higher susceptibility to fretting fatigue (as opposed to fretting wear) at higher temperatures is also reported (94).

9.5 Most effective wear simulation strategies

While the model of Fillot, Iordanoff & Berthier has been confirmed as a viable way for modelling wear, many of its constant remain impossible to calculate from first principles, making the practical application dependent on experimental measurements. Also, the model is not local, meaning that it cannot predict the shape of the wear scar.

To predict the exact shape of the wear scar, some other method is needed. As discussed before, linking the microscopic and macroscopic wear processes is very difficult. The use of discrete element modelling however bypasses this issue, since it is not based on a wear model per se, but models wear as a result of material interaction from particle to macroscopic levels.

This is a rather novel approach, but it appears to resolve most challenges associated with numerical modelling of wear. The approach presented by Li et al. (136) appears particularly strong in this respect. Paired with a realistic model for simulating both bulk material and loose

debris behaviour, a model like the one presented appears ideally suited to predict both the total amount of material lost and the post-wear morphology, without the need for a macroscopic or local wear law.

With the computing capacity available to researchers rising continuously, it can be hoped that computational limitations (discrete element method is computationally expensive) will diminish with the passage of time. The crucial limitation thus remains the relatively weak knowledge of the debris properties. Further studies on particle morphology, size distribution, chemical composition, particle-to-particle friction appear very valuable to further attempts to develop DEM for tribological simulations.

9.6 Opportunities for future work

Opportunities for further work can be divided into two main groups:

9.6.1 Material charaterisation of wear

- This work has failed in carrying out a true in-situ imaging of wear through X-rays. Further development of the application of X-ray methods in tribology appears to be both highly promising and technologically relatively straight-forward option for other wear researchers to pursue.

- An important product of the efforts mentioned above would be observations concerning the properties of the wear debris beds. How thick they normally are? What % of the worn zone volume do they occupy and what governs this value? In which contacts (if any) are there continuous debris beds?

- The scope of analysis applied to X-ray diffraction data collected in this study (see section 7.3.6) was relatively modest. Any future in-situ X-ray diffraction experiments would benefit from a more detailed analysis to obtain a comprehensive picture of strain distribution and additional information about grain refinement in the wear region.

- The properties of wear debris are poorly studied at present. A comprehensive study of wear debris, including its physical (complete with compressibility and particle-to-particle friction coefficient values) and chemical charaterisation, as well as development of debris properties with progress of wear would undoubtedly be much welcome in the tribological field, especially if additional interest in wear models based on tribological circuits appears.

- In section 8.3 several assumptions are made concerning the ejection of wear debris in multiple directions. It would be very interesting to directly measure the partitioning of the total quantity of debris ejected between the directions of ejection.

- Despite some efforts, the exact mechanism governing the magnitude of H_{max} remains unknown. Further study on how exactly does H_{max} stop growing and how to measure it reliably would be of great value in answering this question.

9.6.2 Development of wear models

- Given the relative success of the expanded model discussed in section 8.3 in flat-on-flat geometries, it could be fruitful to expand it to other open geometries. This would require formulation of debris ejection expressions for specific geometries.

- In principle, the model described in section 8.3 should apply to annular contacts as well, if the dimension L was made infinite. Calculating the dependence of the model on L (all other things being constant) and comparing the theoretical response to an experimental one would help to confirm or infirm the model proposed.

- Development of direct modelling of wear through DEM appears worthy of further exploration. The first step in this would be the development of methods for achieving realistic bulk material and particle behaviour. For bulk material, that would probably require the inclusion of plasticity in the model.

- Given the importance of surface roughness to debris ejection (see section 4.2.2.3) a model for predicting the development (or at least final magnitude) of worn surface roughness appears vital to predicting wear. How such a model could be developed is however not clear at present.

9.7 Conclusions

In short, the main conclusions of research can be summarized as follows:

- Present methods for modelling wear are insufficient to predict wear reliably from information concerning contact geometry, materials and loadings. A different method for predicting wear is needed.

- The model of Fillot, Iordanoff & Berthier is consistent with experimental results available in the literature and based on firm physical principle of mass conservation. It

satisfies the basic condition for a universal wear model, namely accounting for the three principal mechanisms in wear: debris generation, entrapment and ejection.

- FI&B model implies a strongly non-linear dependence of wear on normal force in annular contacts, which is consistent with experimental results reported for this type of contact and currently lack any other explanation.

- Worn surface roughness and debris bed size are dimensions governing the ejection of wear debris from the contact. They are not open to direct control, as they are self-establishing length-scales.

- X-ray CT can be effectively used to observe wear between metal surfaces. This includes quantification of worn roughness if the resolution is sufficient and observation of the real area of contact.

- With X-ray methods, wear can be extensively observed and quantified with the worn elements remaining in contact and under load. This indicates that with an appropriate wear machine, wear can be observed in-situ in (pseudo)real-time. This appears to be the first time such capability was demonstrated.

- The development of wear observed in the X-ray imaging tests could be explained in terms of FI&B model.

- In open contact geometries, debris is ejected along the shortest path, not the one which is mechanically driven (unless it also the shortest). This behaviour was not known previously.

- With the point above taken into account, the model of FI&B can be expanded to an open geometry. In the work presented, it was possible to fit the model developed to results of three separate experiments using one set of fitting parameters.

While wear remains a surprisingly unwieldy subject to study, some additional insights have been obtained nevertheless. The work performed and published on annular contacts has drawn attention to this relatively rarely studied type of contact geometry, which possesses many desireable properties for the experimental tribologist. While perhaps at a very early stage, the global wear model based on the work of Fillot, Iordanoff and Berthier has shown its strengths and will hopefully be developed further in the future. Its ability (long considered elusive) of being transmittable between the wear geometries is particularly encouranging in this respect. A

novel method for examining wear through X-rays has been developed, further expanding the number and power of tools available to the tribological community.

10 Acknowledgments

The author wishes to thank:

Professors John Huber and David Hills for their continuous support as supervisors and mentors.

Dr Robert Paynter for his extensive help with the operation of Zwick-Roell loading frame.

Dr Diana Passmore and Dr Kalin Dragnevski for help with the preparation of metallography samples, as well as the use of optical and electronic microscopes.

Professor Clive Siviour and Dr Maureen Aceveses Lopez for their help with testing the Instron loading frame.

Professors James Marrow and Felix Hofmann for the access to XRadia Versa and their contribution to the design of X-ray experiments and 3 successful Diamond Light Source research proposals.

Yijun Lim who operated the Xradia Versa X-ray machine during the pilot imaging work.

Dr Oxana V. Magdysyuk and Dr Stefan Michalik of I12 beamline at Diamond Light Source for their support during pilot diffraction and synchrotron X-ray tomography imaging experiments.

Yang Chen and Marzena Tkaczyk for their extensive help with Avizo software, image processing and related advice.

Professor Jin-Chong Tan and his doctoral students for help with high-precision weight scales.

Professor Jeroen Bergmann for his extensive and meticulous support during the transfer and confirmation of status stages.

Dr Igor Dyson for his help with measuring the properties of the used materials and useful discussions.

Marcus Williamson for the support with X-ray diffraction analysis and preparation of experiments.

Cleveland Williams and the staff of the Staff/student workshop for support with machining operations and manufacturing.

Simon Hills and the staff of Oxford University workshops for their machining work, design advice and practical support.

This work was supported through Rolls Royce Plc contract number 4800000925 and the Cornerstone prosperity partnership. Felix Hofmann acknowledges funding from the European Research Council (ERC) under the European Union's Horizon 2020 research and innovation programme (grant agreement No 714697). Xradia and Avizo facilities were funded through the EPSRC Grant EP/M02833X/1 "University of Oxford: experimental equipment upgrade".

11 References

1. *Experimental investigation of debris entrapment in annular contacts.* Aleksejev, J., et al. 2020, Journal of Engineering Tribology, Vol. 235, pp. 687-697.

2. *In-situ X-ray tomography of wear – A feasibility study.* Aleksejev, J., et al. 2020, Tribology International, Vol. 150. 106355.

3. *The Mechanisms of Fretting - A Review.* Hurricks, P. I. 1970, Wear, Vol. 15, pp. 389-409.

4. *Wear Patterns and Laws of Wear - A Review.* Zmitrowicz, A. 2006, Journal of Theoretical and Applied Mechanics, Vol. 44, pp. 219-253.

5. *Wear Debris: A Review of Properties and Constitutive Models.* Zmitrowicz, A. 2005, Journal of Theoretical and Applied Mechanics, Vol. 43, pp. 3-35.

6. *Experiments and observations on the various alloys, on the specific gravity, and on the comparative wear of gold.* Hatchett, Charles. 1803, Philosophical Transactions of the Royal Society, Vol. 93, pp. 43-194.

7. Jost, P.H. *Lubrication (tribology): education and research, a report on the present position and industry's needs.* London : H.M. Stationery Office, 1966.

8. *Wear models and predictive equations: Their form and content.* Meng, H. C. and Ludema, K. C. 1995, Wear, Vols. 181-183, pp. 443-457.

9. *How common is the steady-state? The implications of wear transitions for materials selection and design.* Blau, Peter. 2014, Wear, Vols. 332-333, pp. 1120-1128.

10. *The Wear of Metals Under Unlubricated Conditions.* Archard, J. F. and Hirst, W. 1956, Proceedings of the Royal Society of London, Vol. 236, pp. 397-410.

11. *Role of Wear Particles in severe-mild wear transition.* Hiratsuka, K and Muramoto, K. 2005, Wear, Vol. 259, pp. 467-476.

12. *High-temperature sliding wear of metals.* Stott, F.H. 2002, Tribology International, Vol. 35, pp. 489–495.

13. *Wear-mechanism Maps.* Lim, S.C. and Ashby, M.F. 1987, Acta Metallurgica, Vol. 35, pp. 1-24.

14. *Third bodies in Tribology.* Godet, M. 1990, Wear, Vol. 136, pp. 29-45.

15. *Wear modelling and the third body concept.* Fillot, N, Iordanoff, I and Berthier, Y. 2007, Wear, Vol. 262, pp. 949-957.

16. *Determination and prediction of the fretting crack initiation: introduction of the (P, Q, N) representation and definition of a variable process volume.* Proudhon, H., Fouvry, S. and Yantio, G.R. 2006, International Journal of Fatigue, Vol. 28, pp. 707-713.

17. *A simple model for friction evolution in fretting.* Hirsch, M.R. and Neu, R.W. 2013, Wear, Vol. 301, pp. 517-523.

18. *Fretting wear mapping: the influence of contact geometry and frequency on debris formation and ejection for a steel-on-steel pair.* Warmuth, A.R., Shipway, P.H. and Sun, W. 2015, Proceedings of the Royal Society, Vol. 471. 20140291.

19. *On Fretting Maps.* Vingsbo, O. and Söderberg, S. 1988, Wear, Vol. 126, pp. 131-147.

20. *Progress in fretting maps.* Zhou, Z.R., et al. 2006, Tribology International, Vol. 39, pp. 1068-1073.

21. *An energy description of wear mechanisms and its applications to oscillating sliding contacts.* Fouvry, S., et al. 2003, Wear, Vol. 255, pp. 287-298.

22. *Elastic spheres in contact under varying oblique forces.* Mindlin, R.D. and Deresiewicz, H. 1953, Journal of applied mechanics, Vol. 63, pp. 327–344.

23. *A quantitative approach of Ti–6Al–4V fretting damage: friction, wear and crack nucleation.* Fouvry, S., Duó, P. and Perruchaut, Ph. 2004, Wear, Vol. 257, pp. 916-929.

24. *Study on transition between fretting and reciprocating sliding wear.* Chen, G.X. and Zhou, Z.R. 2001, Wear, Vol. 250, pp. 665–672.

25. *Stable and unstable friction in fretting contacts.* Hintikka, J., et al. 2019, Tribology International, Vol. 131, pp. 73-82.

26. *A modelling approach for the nonlinear dynamics of assembled structures undergoing fretting wear.* Armand, J., et al. 2019, Proceedings of the Royal Society A, Vol. 475. 20180731.

27. Stachowiak, G., Batchelor , A. and Stachowiak, G. *Experimental Methods in Tribology.* 1. s.l. : Elsevier Science, 2004. Vol. 44.

28. *Effect of hardness differential on metal-to-metal fretting damage.* Budinski, K.G. 2013, Wear, Vol. 301, pp. 501-507.

29. *The influence of surface hardness on the fretting wear of steel pairs—Its role in debris retention in the contact.* Lemm, J.D., et al. 2015, Tribology International, Vol. 81, pp. 258-266.

30. *The role of frictional power dissipation (as a function of frequency) and test temperature on contact temperature and the subsequent wear behaviour in a stainless steel contact in fretting.* Jin, X., Shipway, P.H. and Sun, W. 2015, Wear, Vols. 330-331, pp. 103–111.

31. *The dependence of wear rate on wear scar size in fretting; the role of debris (third body) expulsion from the contact.* Zhu, T., Shipway, P.H. and Sun, W. 2019, Wear, Vols. 440-441. 203081.

32. *Quantification of Wear and Deformation in Different Configurations of Polyethylene Acetabular Cups Using Micro X-ray Computed Tomography.* Affatato, S., Zanini, F. and Carmignato, S. 2017, Materials, Vol. 10.

33. *Uncertainty determination for X-ray computed tomography wear assessment of polyethylene hip joint prostheses.* Zanini, F., et al. 2018, Precision Engineering, Vol. 52, pp. 477-483.

34. *Surface and machining induced damage charaterization of abrasive water jet milled carbon/epoxy composites speciments and their impact on tensile behaviour.* Hejjaji, A., et al. 2017, Wear, Vols. 376-377, pp. 1356-1364.

35. Belin, M., et al. Micro-scale Real-Time Wear Dynamics Investigated by Synchroton Radiation. [book auth.] M. Dienwiebel and M.I. De Barros Bouchet. *Advanced Analytical Methods in Tribology.* s.l. : Springer, 2018.

36. *Continous Control as Alternative Route for Wear Monitoring by Measuring Penetration Depth.* Zivic, F., et al. 2011, Journal of Alloys and Compounds, Vol. 509, pp. 5748-5754.

37. *Tracing wear debris pathways via ion-implanted indium-111.* Warner, J.A., et al. 2010, Wear, Vol. 268, pp. 1257-1265.

38. *Applications of radioactive tracer technology in the real-time measurement of wear and corrosion.* Eberle, D.C., Wall, C.M. and Treuhaft, M.B. 2005, Wear, Vol. 259, pp. 1462-1471.

39. *The Influence of temperature on friction and wear of unlubricated steel/steel contacts in different gaseous atmospheres.* Velkavrh, I., et al. 2016, Tribology International, Vol. 98, pp. 155-171.

40. *A tribo-oxidation abrasive wear model to quantify the wear rate of a cobalt based alloy subjected to fretting in low-to-medium temperature conditions.* Dréano, A., Fouvry, S. and Guillonneau, G. 2018, Tribology International, Vol. 125, pp. 128-140.

41. *A combined friction energy and tribo-oxidation formulation to describe the high temperature fretting wear response of a cobalt-based alloy.* Dreano, A., Fouvry, S. and Guillonneau, G. 2019, Wear, Vols. 426-427, pp. 712-724.

42. *Comparison of different theoretical models for flash temperature calculation under fretting conditions.* Kalin, M. and Vižintin, J. 2001, Tribology International, Vol. 34, pp. 831-839.

43. *Influence of flash temperatures on the tribological behaviour in low-speed sliding: a review.* Kalin, M. 2004, Materials Science and Engineering A, Vol. 374, pp. 390-397.

44. *The role of geometry changes and debris formation associated with wear on the temperature field in fretting contacts.* Jin, X., Sun, W. and Shipway, P.H. 2016, Tribology International, Vol. 102, pp. 392-406.

45. Shore, H. *Tool and Chip Temperatures in Machine Shop Practice.* Cambridge, MA : MIT, 1925.

46. *Physical Properties of Surfaces III—The Surface Temperature of Sliding Metals The Temperature of Lubricated Surfaces.* Bowden, F.P. and Ridler, K.E.W. 1936, Proceedings of the Royal Society, Vol. 154, pp. 640-656.

47. *Interface Tempreature Measurements in the Fretting of a Medium Carbon Steel.* Sproles, Jr., E.S. and Duquette, D.J. 1978, Wear, Vol. 47, pp. 387-396.

48. *Flash temperature measurement during dry friction process at high sliding speed.* Sutter, G. and Ranc, N. 2010, Wear, Vol. 268, pp. 1237-1242.

49. *Surface temperatures and fretting corrosion of steel under conditions of fretting contact.* Ghasemi, H.M., Furey, M.J. and Kajdas, C. 1993, Wear, Vols. 162-164, pp. 357-369.

50. *The Influence of Thermal Expansion on the Friction and Wear Process.* Barber, J.R. 1967, Wear, Vol. 10, pp. 155-159.

51. *Suppression of wear in dry sliding friction induced by negative thermal expansion.* A.S., Grigoriev, et al. 2020, Physical Review E, Vol. 102. 042801.

52. *Tribologically transformed structure in fretting.* Sauger, E, et al. 2000, Wear, Vol. 245, pp. 39-52.

53. *Nanostructure formation on the surface of railway tracks.* Lojkowski, W., et al. 2001, Materials Science and Engineering, Vol. 303, pp. 197–208.

54. *Nucleation and early growth of tribologically transformed structure (TTS) induced by fretting.* Zhou, Z. R., et al. 1997, Wear, Vol. 212, pp. 50-58.

55. *Study of the tribologically transformed structure created during fretting tests.* Sauger, E., et al. 2000, Tribology International, Vol. 33, pp. 743-750.

56. *Effect of surface chemistry on the mechanical response of metals in sliding tribocorrosion systems.* Bidiville, A., et al. 2007, Wear, Vol. 263, pp. 207-217.

57. *The effect of frequency on both the debris and the development of the tribologically transformed structure during fretting wear of a high strength steel.* Kirk, A.M., et al. 2019, Wear, Vols. 426-427, pp. 694-703.

58. *Characterization of cracks formed in large flat-on-flat fretting contact.* Juoksukangas, J., et al. 2019, International Journal of Fatigue, Vol. 124, pp. 361-370.

59. *EBSD, SEM and FIB characterisation of subsurface deformation during tribocorrosion of stainless steel in sulphuric acid.* Perret, J., et al. 2010, Wear, Vol. 269, pp. 383-393.

60. *The comparative study on nanostructured tribolayers of Alloy 690TT subjected to fretting wear under different oxygen contents.* Xin, L., Lu, Y. and Shoji, T. 2017, Material Charaterisation, Vol. 131, pp. 157-167.

61. *EBSD studies on wear-induced subsurface regions in LIGA nickel.* Prasad, S.V., Michael, J.R. and Christenson, T.R. 2003, Scripta Materialia, Vol. 48, pp. 255-260.

62. *The formation and characterization of fretting-induced degradation layers using quenched and tempered steel.* Nurmi, V., et al. 2019, Tribology International, Vol. 131, pp. 258-267.

63. *Effect of counterface materials on dynamic recrystallized structure and wear resistance of nanostructured Cu.* Yao, B. and Han, Z. 2017, Tribology international, Vol. 113, pp. 426-432.

64. *Comparison of various high-stress wear conditions and wear performance of martensitic steels.* Valtonen, K., et al. 2019, Wear, Vols. 426-427, pp. 3-13.

65. *High Pressure Torsion of Rail Steels.* Wetscher, F., et al. 2006, Material Science Forum, Vols. 503-504, pp. 455-460.

66. *The mechanism of formation of nanostructure and dissolution of cementite in a pearlitic steel during high pressure torsion.* Ivanisenko, Y., et al. 2003, Acta materialia, Vol. 51, pp. 5555-5570.

67. *An attempt to produce ex situ TTS to understand their mechanical formation conditions – The case of an ultra high purity iron.* Descartes, S., Busquet, M. and Berthier, Y. 2011, Wear, Vol. 271, pp. 1833–1841.

68. *Formation conditions of mechanically modified superficial structures for two steels.* Busquet, M., Descartes, S. and Berthier, Y. 2009, Tribology International, Vol. 42, pp. 1730–1743.

69. *Tribologically transformed structure of titanium alloy (TiAl6V4) in surface fatigue induced by repeated impacts.* Sekkal, A.C., Langlade, C. and Vannes, A.B. 2005, Materials Science and Engineering, Vol. 393, pp. 140-146.

70. *Surface folding in metals: a mechanism for delamination wear in sliding.* Mahato, A., et al. 2014, Proceedings of Royal Society A, Vol. 470. 20140297.

71. *Nano-indentation mapping of fretting-induced surface layers.* Liskiewicz, T., Kubiak, K. and Comyn, T. 2017, Tribology International, Vol. 108, pp. 186-193.

72. *Dynamic changes of mechanical properties induced by friction in the Archard wear model.* Liu, Y., Liskiewicz, T.W. and Beake, B. 2019, Vols. 428-429, pp. 366-375.

73. *An experimental study on fretting wear behavior of cross-contacting Inconel 690 tubes.* Chung, I. and Lee, M. 2011, Nuclear Engineer and Design, Vol. 241, pp. 4103-4110.

74. *Experimental and numerical modelling of the ignition of solid propellant.* Charlery, R., et al. 2015, Tribology International, Vol. 82, pp. 330-342.

75. *Fretting: Load Carrying Capacity of Wear Debris.* Colombie, C., et al. 1984, Transactions of ASME, Vol. 106, pp. 194-201.

76. *Self-Protection of High Wear Materials.* Play, D. and Godet, M. 1977, ASLE Transcations, Vol. 22, pp. 56-64.

77. *Coexistence of different wear mechanisms in a simple contact.* Play, D. and Godet, M. 1977, Wear, Vol. 42, pp. 197-198.

78. *Research on in-situ microscopic observation of dynamic contact and reciprocating sliding friction of GM-3 lining interface.* Feng, C., et al. 2017, Tribology International, Vol. 115, pp. 179-190.

79. *Fretting wear behaviour of polymethylmethacrylate under linear motions and torsional contact conditions.* Briscoe, B.J., et al. 1998, Tribology International, Vol. 31, pp. 701-711.

80. *Study on fretting wear behavior of laser treated coatings by X-ray imaging.* Fu, Y., Batchelor, A.W. and Loh, L.L. 1998, Wear, Vol. 218, pp. 250-260.

81. *Revealing the hidden world of fretting wear processes of surface coatings by X-ray imaging.* Fu, Y.Q., Batchelor, A.W. and Loh, N.L. 1998, Surface and Coatings Technology, Vol. 107, pp. 133-141.

82. *In situ observation of sliding wear tests of butyl rubber in the presence of lubricants in an X-ray microfocus instrument.* Chandrasekaran, M. and Batchelor, A.W. 1997, Wear, Vol. 211, pp. 35-43.

83. *Direct observation of frictional seizure of mild steel sliding on aluminum by X-ray imaging Part I: Methods.* Chandrasekaran, M., Batchelor, A.W. and Loh , N.L. 2000, Journal of Material Science, Vol. 35, pp. 1589-1596.

84. *In situ fretting fatigue crack propagation analysis using synchrotron X-ray radiography.* de Pannemaecker, A., et al. 2017, International Journal of Fatigue, Vol. 97, pp. 56-69.

85. *Investigation of non-Coulomb friction behaviour in reciprocating sliding.* Mulvihill, D.M., et al. 2011, Wear, Vol. 271, pp. 802-816.

86. *Fretting-induced friction and wear in large flat-on-flat contact with quenched and tempered steel.* Hintikka, J., Lehtovaara, A. and Mäntylä, A. 2015, Tribology International, Vol. 92, pp. 191-202.

87. *The effect of temperature on wear and friction of a high strength steel in fretting.* Pearson, S.R., et al. 2013, Wear, Vol. 303, pp. 622-631.

88. *The Genesis of Friction.* Suh, N. and Sin, H. 1981, Wear, Vol. 69, pp. 91- 114.

89. *An Experimental Study Of Fretting.* Feng, I.M. and Rightmire, B.G. 1956, Proceedings of the institution of mechanical engineers, Vol. 170, pp. 1055-1064.

90. *Atmospheric characteristics in friction and wear of metals.* Mishina, H. 1992, Wear, Vol. 152, pp. 99-110.

91. *Torsional fretting behaviours of LZ50 steel in air and nitrogen.* Cai, Z., et al. 2009, Tribology international, Vol. 42, pp. 1676-1683.

92. *Effect of test conditions on the temperature at which a protective debris bed is formed in fretting of high speed steel.* Hayes, E.K. and Shipway, P.H. 2017, Wear, Vols. 376-377, pp. 1460-1466.

93. *Fretting wear of stainless steels under variable temperature conditions: Introduction of a 'composite' wear law.* Rybiak, R., Fouvry, S. and Bonnet, B. 2010, Wear, Vol. 268, pp. 413-423.

94. *Temperature-dependent fretting wear damage of high strenght stainless steel sheets.* Hirsch, M.R. and Neu, R.W. 2016, Wear, Vols. 346-347, pp. 6-14.

95. *Fretting wear rate evolution of a flat-on-flat low alloyed steel contact: A weighted friction energy formulation.* Baydoun, S., et al. 2019, Wear, Vols. 426-427, pp. 676-693.

96. *Wear particle analysis - utilization of quantitive computer image analysis: A review.* Raadnui, S. 2005, Tribology International, Vol. 38, pp. 871-878.

97. *An Attempt to Provide a Unified Treatment of Tribology Through Load Carrying Capacity, Transport, and Continuum Mechanics.* Godet, M., Play, D. and Berthe, D. 1980, Journal of Lubrication Technologies, Vol. 102, pp. 153-164.

98. *The Third-body Approach: A Mechanical View of Wear.* Godet, M. 1984, Wear, Vol. 100, pp. 437-452.

99. *Velocity Accommodation in Friction.* Berthier, Y., Godet, M. and Brendle, M. 1989, Tribology Transactions, Vol. 32, pp. 490-496.

100. *On the physical nature of tribolayers and wear debris after sliding wear in a superalloy/steel tribosystem at 25 and 300 °C.* Rynio, C., et al. 2014, Wear, Vol. 317, pp. 26-38.

101. *A numerical simulation of fretting wear profile taking account of the evolution of third body layer.* Arnaud, P., Fouvry, S. and Garcin, S. 2017, Wear, Vols. 376-377, pp. 1475-1488.

102. *A Numerical Study on the Effect of Debris Layer on Fretting Wear.* Yue, T. and Wahab, M.A. 2016, Materials, Vol. 9, pp. 597-611.

103. *Semi analytical fretting wear simulation including wear debris.* Done, V., et al. 2017, Tribology International, Vol. 109, pp. 1-9.

104. *Contact and Rubbing of Flat Surfaces.* Archard, J. F. 1953, Journal of Applied Physics, Vol. 24, pp. 981-988.

105. *A New Machine for Studying Surface Damage Due to Wear and Fretting.* Kusner, D., Poon, C. and Hoeppner, D.W. Philadelphia : ASTM, 1982.

106. *Fretting Wear.* Waterhouse, R.B. 1984, Wear, Vol. 100, pp. 107-118.

107. *Experimental and modelling aspects of abrasive wear of a A357 aluminium alloy under gross slip fretting conditions.* Elleuch, K. and Fouvry, S. 2005, Wear, Vol. 258, pp. 40-49.

108. *Wear analysis of A357 aluminium alloy under fretting.* Elleuch, K. and Fouvry, S. 2002, Wear, Vol. 253, pp. 662-672.

109. *Third Particle Ejection Effects on Wear with Quenched and Tempered Steel Fretting Contact.* Hintikka, J., Lehtovaara, A. and Mäntylä, A. 2016, Tribology Transactions, Vol. 60, pp. 70-78.

110. *The sliding wear behaviour of steels with the same hardness.* Zambrano, O.A., et al. 2019, Wear, Vols. 418-419, pp. 201-207.

111. *The Relationship Between The Abrasive Wear Resistance, Hardness and Microstructure of Ferritic Materials.* Moore, M.A. 1974, Wear, Vol. 28, pp. 59-68.

112. *Effects of composition and microstructure on the abrasive wear performance of quenched wear resistant steels.* Ojala, N., et al. 2014, Wear, Vol. 317, pp. 225-226.

113. *Experimental Evidence for Friction and Wear Modelling.* Berthier, Y. 1990, Wear, Vol. 139, pp. 77-92.

114. *Rheology and flows of solid third bodies: background and application to an MoS1.6 coating.* Descartes, S. and Berthier, Y. 2002, Wear, Vol. 252, pp. 546–556.

115. *Unlubricated reciprocating wear of stainless steel with an interfacial air flow.* Leheup, E. R. and Pendlebury, R. E. 1991, Wear, Vol. 142, pp. 351-372.

116. *Graphite wear against rough surfaces - the effects of sliding distance and interface gas flow.* Gordelier, S.C. and Skinner, J. [ed.] D. Dowson, M. Godet and C.M. Taylor. Leeds : Mechanical Engineering Publications Limited, 1976. The wear of non-metallic materials: proceedings of the 3rd Leeds-Lyon Symposium on Tribology.

117. *Simulation of Wear Through Mass Balance in a Dry Contact.* Fillot, N., Iordanoff, I. and Berthier, Y. 2005, Journal of Tribology, Vol. 127, pp. 230-237.

118. *Wear Modeling Revisited Using Electrical Analogy.* Hanief, M. and Wani, M.F. 2017, Journal of Tribology, Vol. 139. 064502-1.

119. *Modeling and simulation in tribology across scales: An overview.* Vakis, A.I., et al. 2018, Tribology International, Vol. 125, pp. 169-199.

120. *Numerical tribology of a dry contact.* Renouf, M., et al. 2011, Tribology International, Vol. 44, pp. 834-844.

121. *Finite element simulation and experimental validation of fretting wear.* McColl, I.R., Ding, J. and Leen, S.B. 2005, Wear, Vol. 256, pp. 1114-1127.

122. *Wear by plastic ratchetting.* Kapoor, A. 1997, Wear, Vol. 212, pp. 119-130.

123. *A stress based damage mechanics model to simulate fretting wear of Hertzian line contact in partial slip.* Ghosh, A., Leonard, B. and Sadeghi, F. 2013, Wear, Vol. 307, pp. 87-99.

124. *The Quasi-Hydrodynamic Mechanism of Powder Lubrication—Part III On Theory and Rheology of Triboparticulates.* Heshmat, H. 1995, Tribology Transactions, Vol. 38, pp. 269-276.

125. *Grain flow as a fluid-mechanical phenomenon.* Haff, P.K. 1983, Journal of Fluid Mechanics, Vol. 134, pp. 401-430.

126. *Flow Characteristics of a Powder Lubricant Sheared Between Parallel Plates.* Zhou, L. and Khonsari, M.M. 2000, Journal of Tribology, Vol. 122, pp. 147-155.

127. *Lubrication With Granular Flow: Continuum Theory, Particle Simulations, Comparison With Experiment.* Sawyer, W.G. and Tichy, J.A. 2001, Journal of Tribology, Vol. 123, pp. 777-784.

128. *Granular Flow Lubrication: Continuum Modeling of Shear Behavior.* Higgs, C.F. and Tichy, J.A. 2004, Journal of Tribology, Vol. 126, pp. 499-510.

129. *Granular Collision Lubrication: Experimental Investigation and Comparison to Theory.* Elkholy, K.N. and Khonsari, M.M. 2007, Journal of Tribology, Vol. 129, pp. 923-932.

130. *A Review of Dry Particulate Lubrication: Powder and Granular Materials.* Wornyoh, E.Y.A., Jasti, V.K. and Higgs, C.F. 2007, Journal of Tribology, Vol. 129, pp. 438-449.

131. *Kinetics of particle detachment: contribution of a granular model.* Fillot, N., Iordanoff, I. and Berthier, Y. [ed.] G. Dalmaz, et al. Lyon : INSA de Lyon, 2003. Proceedings of the 30th Leeds-Lyon Symposium on Tribology.

132. *A Granular Dynamic Model for the Degradation of Material.* Fillot, N., Iordanoff, I. and Berthier, Y. 2004, Journal of Tribology, Vol. 126, pp. 606-614.

133. *Modelling third body flows with discrete element method - a tool for understanding wear with adhesive particles.* Fillot, N., Iordanoff, I. and Berthier, Y. 2007, Tribology International, Vol. 40, pp. 973-981.

134. *Modeling Wear for Heterogeneous Bi-Phasic Materials Using Discrete Elements Approach.* Champagne, M., Renouf, M. and Berthier, Y. 2014, Journal of Tribology, Vol. 136. 021603-1.

135. *A numerical framework for discrete modelling of friction and wear using Voronoi polyhedrons.* Mollon, G. 2015, Tribology International, Vol. 90, pp. 343-355.

136. *Fretting damage modelling of liner-bearing interaction by combined finite element-discrete element method.* Li, W., et al. 2013, Tribology international, Vol. 61, pp. 19-31.

137. *A study of abrasive wear on high speed steel surface in hot rolling by Discrete Element Method.* Phan, H.T. , et al. 2017, Tribology International, Vol. 110, pp. 66-76.

138. *Discrete element method to simulate continous material by using the cohesive beam model.* Damien, Andre, et al. 2012, Computer methods in applied mechanics and engineering, Vols. 213-214, pp. 113-125.

139. *Tensile test simulation of high-carbon steel by discrete elements.* Chen, G., Schott, D. and Lodewijks, G. 2016, Engineering Computations, Vol. 33, pp. 1224-1245.

140. *Normal contact between rough surfaces by Discrete Element Method.* Jerier, J.F. and Molinari, J.F. 2011, Tribology International, Vol. 47, pp. 1-8.

141. *An exploration of debris types and their influence on wear rates in fretting.* Blades, L., et al. 2020, Wear, Vols. 450-451.

142. *Effect of plastic deformation on the evolution of wear and local stress fields in fretting.* Hu, Z., et al. 2016, International Journal of Solids and Structures, Vol. 82, pp. 1-8.

143. *Effect of grain size and hardness on fretting wear behavior of Inconel 600 alloys.* Li, J., et al. 2015, Tribology International, Vol. 81, pp. 215-222.

144. *Fretting of fuel cladding materials for Pb cooled fast reactors—Approach to long term prediction using fretting maps.* Del Giacco, M., Weisenburger, A. and Müller, G. 2014, Nuclear Engineering and Design, Vol. 280, pp. 697–703.

145. *Slippage effect on rolling contact wear and damage behavior of pearlitic steels.* Zhou, Y., et al. 2016, Wear, Vols. 362-363, pp. 78–86.

146. *A study of debris and wear damage resulting from fretting of Incoloy 800 steam generator tubes against AISI Type 304 stainless steel.* Soria, S.R., Tolley, A. and Yawnya, A. 2016, Wear, Vols. 368-369, pp. 219–229.

147. *Mechanisms of incursion accommodation during interaction between a vibrating blade and an abradable coating.* Mandard, R., et al. 2015, Wear, Vols. 330-331, pp. 406-418.

148. Fillot, N. Personal communication. Lyon : s.n., 2019.

149. Clark, Z. Systematic Wear Testing. Oxford : University of Oxford, 2017.

150. Alicona Imaging GmbH. *IFM Manual - IFM 2.1.5. EN.* Grambach : Alicona Imaging, 2008. p. 73.

151. Ren, Z. and Glodež, S. *Strojni elementi I. del.* Maribor : Založništvo Fakultete za strojništvo Maribor, 2011. pp. 170-172.

152. R+W Precision couplings. [Online] [Cited: 30 October 2020.] https://www.rw-couplings.com/products/precision-couplings/metal-bellows-couplings/bk1/.

153. Henkel Adhesives. *Locktite 638 TDS.* [Online] [Cited: 21 June 2019.] http://tds.henkel.com/tds5/Studio/ShowPDF/243%20NEW-EN?pid=638&format=MTR&subformat=REAC&language=EN&plant=WERCS.

154. Paganin, D. *Coherent X-Ray Optics.* Oxford : Oxford University Press, 2006. ISBN 9780198567288.

155. Diamond Light Source. *I12-EH1.* [Online] [Cited: 25 February 2020.] https://www.diamond.ac.uk/Instruments/Imaging-and-Microscopy/I12/Experiments-in-EH1.html.

156. *Introduction of a power law formulation to quantify the contact size effects on friction and wear responses of dry oscillating sliding contacts: Application to a chromium steel interface.* Fouvry, S. and Merhej, R. 2013, Wear, Vol. 301, pp. 34–46.

157. *Introduction of a new sliding regime criterion to quantify partial, mixed and gross slip fretting regimes: Correlation with wear and cracking processes.* Heredia, S. and Fouvry, S. May 2010, Wear, Vol. 269, pp. 515-524.

158. *Is the wear coefficient dependent upon slip amplitude in fretting? Vingsbo and Söderberg revisited.* Pearson, S.R and Shipway, P.H. 2015, Wear, Vols. 330-331, pp. 93-102.

159. *Third Body Effects on Friction and Wear During Fretting of Steel Contacts.* Diomidis, N. and Mischler, S. 2011, Tribology International, Vol. 44, pp. 1452-1460.

160. *Effect of iron oxide debris on the reciprocating sliding wear of tool steels.* De Oliveira, M.M., et al. 2019, Wear, Vols. 426-427, pp. 1065-1075.

161. *Effect of Debris Size on the Reciprocating Sliding Wear of Aluminium.* Costa, H.L., Oliveira, M.M. and De Mello, J.D.B. 2017, Wear, Vols. 376-377, pp. 1399-1410.

162. The Engineering Toolbox. *Friction and Friction Coefficient.* [Online] [Cited: 23 June 2021.] https://www.engineeringtoolbox.com/friction-coefficients-d_778.html.

163. Fuller, D.D. Coefficients of Friction. [ed.] D.E. Gray. *American Institute of Physics Handbook, 3rd edition.* s.l. : McGraw-Hill, 1972, 2d, p. 43.

164. Engineers Edge. *Coefficient of Friction Equation and Table Chart.* [Online] [Cited: 23 June 2021.] https://www.engineersedge.com/coeffients_of_friction.htm.

165. Engineering Library. *Coefficient of Friction.* [Online] [Cited: 23 June 2021.] https://engineeringlibrary.org/reference/coefficient-of-friction.

166. *The effects of surface texture in reciprocating contacts – An experimental study.* Vladescu, S., et al. 2015, Tribology International, Vol. 82, pp. 28-42.

167. *Signatures of granular microstructure in dense shear flows.* Mueth, D.M., et al. 2000, Nature, Vol. 406, pp. 385-389.

168. *Using advanced tomography techniques to investigate the development of White Etching Cracks in a prematurely failed field bearing.* Gould, B., et al. 2017, Vol. 116, pp. 362-370.

169. *Dynamic wear evolution and crack propagation behaviors of steel wires during fretting-fatigue.* Wang, D., et al. 2016, Tribology International, Vol. 101, pp. 348-355.

170. *Crack formation within a Hadfield manganese steel crossing nose.* Dhar, S., et al. 2019, Wear, Vols. 438-439. 203049.

171. *2D and 3D characterization of rolling contact fatigue cracks in manganese steel wing rails from a crossing.* Dhar, S., et al. 2019, Wear, Vols. 436-437. 202959.

172. *Verification of the use of Micro-CT scanning to assess the features of entire squat type defects.* Earl, S., et al. 2019, Wear, Vols. 438-439. 203074.

173. *Charaterisation of fretting fatigue damage using synchrotron X-ray micro-tomography.* Proudhon, H., Buffiere, J.Y. and Fouvry, S. 2006, Tribology International, Vol. 39, pp. 1106-1113.

174. *Three dimensional imaging of damage in structural materials using high resolution micro-tomography.* Buffiere, J.Y., et al. 2005, Nuclear Instruments and Methods in Physics Research, Vol. 238, pp. 75-82.

175. *Tribological mechanisms involved in friction wood welding.* Cornuault, P. and Carpentier, L. 2020, Tribology International, Vol. 141. 105963.

176. *Debris development in fretting contacts – Debris particles and debris beds.* Kirk, A.M., et al. 2020, Tribology International, Vol. 149. 105592.

177. *Fiji: an open-source platform for biological-image analysis.* Schindelin, J., et al. 2012, Nature Methods, Vol. 9, pp. 676-682.

178. *Modelling of real area of contact between tool and workpiece in metal forming processes including the influence of subsurface deformation.* Nielsen, C.V., Martins, P.A.F. and Bay, N. 2016, CIRP Annals - Manufacturing Technology, Vol. 65, pp. 261-264.

179. *Heat partition and surface temperature in sliding contact systems of rough surfaces.* Waddad, Y., et al. 2019, International Journal of Heat and Mass Transfer, Vol. 137, pp. 1167-1182.

180. *Temperature rise of diamond-like carbon during sliding: Consideration of the real contact area.* Yamamoto, S., et al. 2019, Tribology International, Vol. 131, pp. 496-507.

181. *The Flash Temperature Concept.* Blok, H. 1963, Wear, Vol. 6, pp. 483-494.

182. *Effect of displacement and humidity on contact resistance of copper electrical contacts.* Sung, I.H., et al. 2016, Tribology International, Vol. 95, pp. 256-261.

183. *Wear debris and electrical resistance in textured Sn-coated Cu contacts subjected to fretting.* Trinh, K.E., et al. 2015, Wear, Vols. 344-345, pp. 86-98.

184. *Experimental and finite element analyses of contact behaviors between non-transparent rough surfaces.* Zhang, F., et al. 2019, Journal of the Mechanics and Physics of Solids, Vol. 126, pp. 87-100.

185. *A discussion on the capability of X-ray computed tomography for contact mechanics investigations.* Zhang, F., et al. 2020, Tribology International, Vol. 145. 106167.

186. *Evaluation of the real contact area in three-body dry friction by micro-thermal analysis.* Stempfle, Philippe, et al. 2010, Tribology International, Vol. 43, pp. 1794-1805.

187. *Temperature Maps for Frictional Heating in Dry Sliding.* Ashby, M.F., Abulawi, J. and Kong, H.S. 34, 1991, Tribology Transactions, Vols. 577-587.

188. *Application of X-ray micro-computed tomography on high-speed cavitating diesel fuel flows.* Mitroglou, N., et al. 2016, Experiments in fluids, Vol. 57. 175.

189. *Fast X-ray imaging of cavitating flows.* Khlifa, I., et al. 2017, Experiments in fluids, Vol. 58.

190. *X-ray computed tomography of cavitating flow in a converging-diverging nozzle.* Jahangir, S., et al. Baltimore : ASME, 2018. 10th International Symposium on Cavitation. pp. 1104-1108.

191. National Insitute of Standards and Technology. [Online] [Cited: 28 February 2020.] https://physics.nist.gov/PhysRefData/XrayMassCoef/ElemTab/z26.html.

192. Phase Transformations & Complex. *Austenite and Ferrite (Crystallography and Diffraction).* [Online] 2003. [Cited: 02 March 2020.] https://www.phase-trans.msm.cam.ac.uk/2003/Lattices/iron.html.

193. *Contact size, frequency and cyclic normal force effects on Ti6Al4V fretting wear processes: An approach combining friction power and contact oxygenation.* Fouvry, S., et al. 2017, Tribology International, Vol. 113, pp. 460-473.

194. *Microstructural characterization of Ti-6Al-4V subjected to fretting.* Swalla, D.R., Neu, R.W. and McDowell, D.L. 2004, Journal of Tribology, Vol. 126, pp. 809-816.

195. *Dependence of tribofilm characteristics on the running-in behavior of aluminum–silicon alloys.* Stoyanov, P., et al. 2015, Journal of Material Science, Vol. 50, pp. 5524–5532.

196. *Cracks and degradation layers in large flat-on-flat fretting contact with steels and cast iron.* Juoksukangas, J., et al. 2020, Tribology International, Vol. 145.

197. *Analysis of sliding wear mode on annealed steelby X-ray diffraction technique.* Lee, H. 2004, Wear, Vol. 256, pp. 657-663.

198. *Measurement of strain evolution in overloaded roller bearings using energy dispersive X-ray diffraction.* Reid, A., et al. 2019, Tribology International, Vol. 140.

199. *Contact of Nominally Flat Surfaces.* Greenwood, J.A. and Williamson, J.B.P. 300-319, 1966, Proceedings of the Royal Society A, Vol. 295.

200. *Prediction and Measurement of True Area of Contact Between Solids.* O'Callaghan, P.W. and Probert, S.D. 1987, Wear, Vol. 120, pp. 29-49.

201. *The coefficient of proportionality k between real contact area and load, with new asperity models with new asperity models.* Paggi, M. and Ciavarella, M. 1020-1029, 2010, Wear, Vol. 268.

202. Advanced Photon Source. *Beamline 1-ID-B,C,E: High-energy X-ray Scattering.* [Online] [Cited: 6 August 2021.] https://www.aps.anl.gov/Beamlines/Directory/Details?beamline_id=2.

203. Diamond Light Source. *I13 beamline.* [Online] [Cited: 7 August 2021.] https://www.diamond.ac.uk/Instruments/Imaging-and-Microscopy/I13.html.

204. European Synchrotron Radiation Facility. *ID19 beamline.* [Online] [Cited: 07 August 2021.] https://www.esrf.fr/cms/live/live/en/sites/www/home/UsersAndScience/Experiments/StructMaterials/ID19.html.

205. *Data Analysis Workbench (DAWN).* Basham, M., et al. 2015, Journal of Synchrotron Radiation, Vol. 22, pp. 853-858.

206. Wadeson, N. and Basham, M. *Savu: a Python-based, MPI framework for simultaneous processing of multiple, N-dimensional, large tomograhpy datasets.* 2016.

207. *Three dimensional reconstruction from radiographs and electron micrographs: Application of convolution instead of Fourier transforms.* Ramachandran, G.N. and Lakshminarayanan, A.V. 1971, Proceedings of Natural Academy of Sciences, Vol. 68, pp. 2236-2240.

208. *Iterative methods for the reconstruction of three-dimensional objects from their projections.* Gilbert, P. 1972, Journal of Theoretical Biology, Vol. 36, pp. 105-117.

209. University of Oxford, Department of Material Science. *Marrow Group.* [Online] https://sites.google.com/site/marrowgroupwiki/home/how-to/avizo-visualisation/tube-unwrap-in-matlab?authuser=0.

210. *The Precision Determination of Lattice Constants by the Powder and Rotating Crystal Methods and Applications.* Straumanis, M.E. 1949, Journal of Applied Physics, Vol. 20, pp. 726-734.

211. *Solid Third Body Analysis Using a Discrete Approach: Influence of Adhesion and Particle Size on Macroscopic Properties.* Iordanoff, I., Seve, B. and Berthier, Y. 2002, Journal of Tribology, Vol. 124.

212. *Contact size and debris ejection in fretting: The inappropriate use of Archard-type analysis of wear data and the development of alternative wear equations for commonly employed non-conforming specimen pair geometries.* Zhu, T. and Shipway, P.H. 2021, Wear, Vols. 474-475.

213. *The effects of external loading on low displacement wear rates of unlubricated steels.* Blades, L., et al. 2022, Wear, Vols. 490-491.

214. *Structure and mechanism of formation of the "glaze" oxide layers produced on N-based alloys during wear at high temperature.* Stott, F.H., Lin, D.S. and Wood, G.C. 1973, Corrosion Science, Vol. 13, pp. 449 - 469.